**Inherently Adaptive Structural Materials**[*]

**Technova Corporation**

1232 Mizzen Drive
Okemos, MI 48864-3480
USA


Phone/Fax: 517-485-9583
Email: tchnv@aol.com

**November 2002**

# CONTENTS

**ABSTRACT**

A new generation of structural materials and systems are under development, which mimic the adaptive, self-healing and structural features of the skeletal system. These systems utilize the input energy of service loads in order to synchronize their structural configuration with their service environment. They also possess the ability to concentrate material resources in damaged areas to render self-healing effects. The process of self-adaptation involves:

1. Conversion of the mechanical energy imposed by load and damaging effects into electrical energy to drive the self-adaptation process (which is guided by electrical signals).
2. Electrostipping of substance from less stressed areas, to be transported through a solid electrolyte and electrodeposited at highly stressed areas, yielding an optimum distribution of available material resources for normalizing the stress distribution.

The new biomimetic structural materials comprise functional and structural nanolayers built onto an open-cell base system. The versatility of cellular precursors in terms of geometric complexity and scale, complemented with the ability of modern membrane-mimetic processes to build hybrid nanolayers onto these structure, yielding gradient structures with strucdtural substance concentrated along load paths promise a new generation of highly efficient and versatile structural systems with unique adaptive/self-healing qualities. The functional constituents responsible for adaptive qualities of the system are piezoelectric, solid electrolyte and structural nanolayers; multiple assemblies of these nanolayers are built upon the struts of open-cell precursor thorugh ionic self-assembly. The piezoelectric effect converts the mechanical energy input of service loads to electrical energy, which in turn electrostirps, transports and electrodeposits structural substance to tune the structure to service laods and damaging effects.

The fundamental principles of this new material system were validated through an integrated analytical/experimental effort which: (1) developed analytical methodologies for design of the new system to meet structural and adaptive requirements; (2) applied the ionic self-assembly process towards build-up of piezoelectric, solid electrolyte, metallic and ceramic nanolayers which are key functional and structural constituents of the system; (3) demonstrated the electrostripping and electrodeposition phenomena within solid electrolytes, and verified the ability of piezoelectric effect to drive these henomena; (4) designed integrated structural materials and system with adaptive qualities, and established the geometric constraints associated with viable adaptive features; and (5) experimentally validated the adaptive phenomenon in a basic integrated system. It was concluded that assembled nanolayers of piezoelectric, solid electrolyte and structural constituents provide a viable basis for development of adaptive and self-healing structural materials and systems. The concept of hybrid layered composites built onto open-cell precursors was also shown to promise distinctly high levels of structural efficiency. Commercial viability of the technology is supported by: (1) the low cost and energy-efficiency of the ionic self-assembly process; (2) the potential to develop complex, integrated structural components and systems with distinctly high efficiency; (3) the low cost and availability of the required raw materials; and (4) the positive impact of adaptive and self-healing qualities on structural design philosophies, which promise to complement enhanced safety with gains in initial and life-cycle economy.

# CHAPTER 1

## INTRODUCTION

Inherent adaptation and self-healing qualities of biological matter make critical contributions towards autonomous, efficient and sustainable operation of living beings. Our approach, inspired by the self-healing and adaptive qualities of bone, seeks to develop new synthetic materials which are inherently capable of adapting to new service environments and damaging phenomena. These systems strive to relieve highly stressed areas and assume a normalized stress condition through redistribution of mass. Piezoelectricity is employed to signal highly stressed areas and also to drive the mass transfer process. The piezoelectric effect generates electric potentials and charges in response to stress gradients, which guide and drive the mass transfer processes. Piezoelectricity essentially converts the mechanical (strain) energy built into material systems under service loads into electrical energy to drive the self-healing and adaptation processes. Build-up of mechanical energy generally represents a damaging effect on structural materials; in our approach, however, this damaging effect is turned into a constructive phenomenon. The actual transfer of mass is accomplished through electrolysis in the context of a solid electrolyte. This process electrostrips, transfers and electrodeposits mass under electrical effects which reflect on stress gradients. Electrodeposition occurs in highly stressed areas, thus lowering the elevated stresses generated under damaging effects or altered service loads.

Our approach involves consolidation of different structural and functional constituents into an integrated material system. The topological constraints relevant to self-healing and adaptation phenomena require introduction of functional (e.g., piezoelectric and solid electrolyte) constituents in the form of nanolayers. We have adapted the ionic self-assembly process as a practical and low-cost means of building up these nanolayers. We have further chosen to build the nanolayers upon the struts which constitute cellutar (open-cell) material systems. Hybrid nanolayered composites buit onto open-cell structures promise to complement self-healing and adaptation qualities with uniquely high levels of structural efficiency (performance-to-weight ratios).

The work reported herein towards development of theoretical and desing principles and experimental validation of above concepts covers the following topics:

1. Review of the structure and the adaptive / self-healing qualities of bone.
2. Review and experimental implementation of the ionic self-assembly process for build-up of structural and functional nanolayers which are relevant to our application.
3. Review of the functional constituents, development of theoretical concepts, and basic experimental evaluation of the self-healing and adaptive principles.
4. Design and experimental validation of integrated adaptive and self-healing structural materials.
5. Theoretical modeling and experimental validation of the structural qualities of the material system.

# CHAPTER 2

# BONE: THE INSPIRATION FOR THE NEW MATERIAL SYSTEM

## Introduction

The new material system is inspired by the structural and functional qualities of bone. It employs piezoelectricity to convert the mechanical energy built into the system under service loads into electrical energy, which drives electrolysis phenomena in the context of a solid electrolyte to produce electrolysis phenomena which render adaptive and self-healing effects. A biomimetic process, "ionic self-assembly," is adapted to process the hybrid composite system. The new material also mimics the structure of bone; it assumes a hybrid nanostructure comprising multiple nanolayers built onto an open-cell structure, offering high levels of structural efficiency. The system maintains its efficiency by adapting its structure to the prevalent service environment and any structural damage and deterioration over time.

## Bio-Inspiration: Structural and Functional Qualities of Bone

### The Basic Structure of Bone

At the lowest level, bone is a composite material consisting of fibrous protein, collagen, stiffened by an extremely dense filling of calcium phosphate. Collagen is a common structural protein which, in the case of bone, undergoes a thorough transformation into a mineralized skeletal structure. Collagen is an aggregation of the protein molecules "tropocollagens," which have an inherent tendency to combine together to form microfibrils, which are stabilized by intermolecular crosslinks. Microfibrils, in turn, aggregate to form fibrils.[1] Impregnating the collagen, in fully mineralized bone, is the bone salt which is some variety of calcium phosphate. A key bone mineral is a version of calcium phosphate called hydroxyapatite, with its unit cell (the smallest part of a crystal that is repeated uniformly throughout the crystal) containing $Ca_{10}(PO_4)_6(OH)_2$. There is some evidence that calcium and phosphate are initially deposited as an amorphous calcium phosphate, and then transformed more and more into a form like apatite.[2] The resulting mineral is neither amorphous nor perfectly crystalline. The mineral is initially deposited in spaces between tropocollagen molecules. The particular conformation of collagen molecule allows it to act as a nucleation site, permitting precipitation of lumps of mineral which, without the presence of energetically favorable sites, could not come out of solution.[3] Subsequently, the mineral is deposited all over the collagen fibrils and, to some extent, within them. The precipitation is not random; one of the long axes of mineral plates is always fairly well aligned with collagen fibrils. Finally, mineral is deposited between the fibrils, in the amorphous and rather tenuous ground substance.

Above the level of collagen fibril and its associated mineral, mammaline bone mostgly occurs in lamellar form.[4] The collagen and its associated mineral are arranged in sheets (lamellae) about 5 micron thick. Fibrils lie within the plane of the lamella, rather than passing from one to the next. The division between one lamella and the next is abrupt, and there seems to be a sheet of interlamellar bone, about 0.1 micron thick, with a rather high mineral content and little collagen, between the pairs of lamellae. Although all the collagen fibrils in one lamella do not point in the

same direction, it does seem, on passing from one lamella to the next, that the preferred direction of fibrils changes.  This is seen very clearly in fracture surfaces that cut across lamellae.  This change in direction has mechanical consequences.

At the next higher order of structure, there is the mechanically important distinction between cancellous bone(Figure 2.1a) and compact bone (Figure 2.1b).  Compact bone is solid, with relatively small spaces for capillaries, erosion sites, etc.  In cancellous bone, on the other hand, there are large spaces.  The difference between the two types of bone is visible to the naked eye.  The material making up cancellous bone of adults is usually primary lamellar bone.  The simplest type of cancellous bone consists of randomly oriented cylindrical struts, about 0.1 mm in diameter, each extending for about 1 mm before making a connection with one or more other struts.  In a variation of this pattern, the cylindrical struts are replaced by little plates.  The amount of variation ranges from a cancellous bone in which there is just the occasional plate among struts, to a canellous bone in which there is just the occasional strut among plates.  In another cancellous bone, the plates may be considerably longer, up to several millimeters.  When this happens, there is a higher level of anisotropy; these longer plates are not randomly oriented but are preferentially aligned in one direction.  These different versions of cancellous bone are found in characteristically different places.  Roughly, the type made of cylindrical struts, with no preferred orientation, is found deep in bones, well away from any loaded surfaces, while the more oriented types, made of many plates or completely of plates, are found just underneath loaded surfaces, particularly where the pattern of stress is reasonably constant.  The porosity of cancellous bone is the proportion of the total volume that is not occupied by bone tissue.  Usually, it will be occupied by marrow, but in birds there may be gas.  The porosity varies from being effectively complete, where there is only the occasional tentative strut sticking into the marrow cavity, down to about 50%.  If the porosity is less than about 50%, it cannot be easily distinguished from compact bone with many holes in it.  However, it is interesting that the change from compact to cancellous bone is usually clear and takes place over a small distance.

Bone grows by accretion on pre-existing surfaces.  Long bones have cancellous bone at their ends; compact bone often forms in regions where cancellous bone already exists.  The old cancellous bone is not replaced; new bone is merely wrapped around the struts of cancellous bone, producing a structure with no obvious grain, called "compact coarse-cancellous bone" (Figure 2.1c).[5]  The original bone, comprising a cancellous network, is shown plain in Figure 2.1c.  As the bone grows in length, bone tissue is eroded (or deposited) in directions shown by arrowheads in Figure 2.1c where ordinary lamellar bone is added near the surface, but among the trabeculae, compact coarse-cancellous bone  is formed.
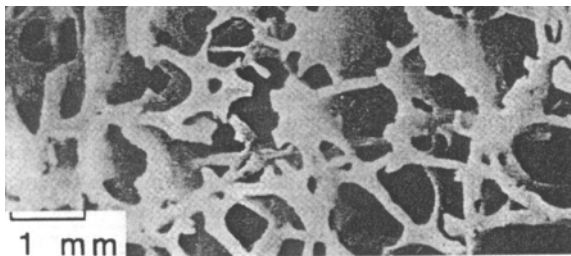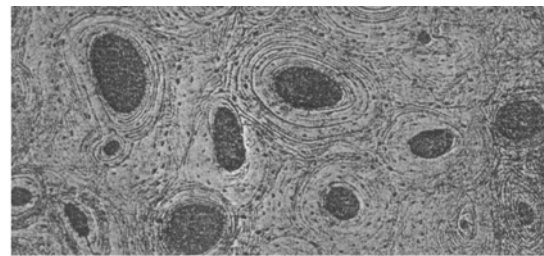


*(a) Cancellous Bone*                    *(b) Compact Bone*
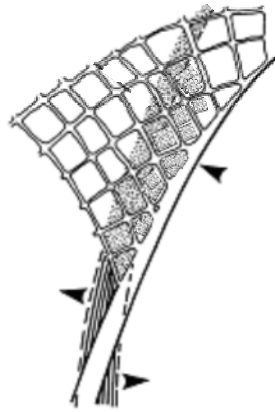
*(c)  Production of Compact Coarse-Cancellous Bone Near the End of a Long Bone.*[5]

*Figure 2.1.  Cancellous and Compact Bones, and Production of Bone.*

*Basic Principles and Experimental Evidence of the Adaptive Qualities of Bone*

Bones have quite intricate shapes, yet they also have a general size and build that is adapted to the loads they bear.  It is well known that bed rest[6] and weightlessness, as in space flight,[7,8] lead to a reduction in bone mass and reduced growth rate of bone.  The morphological changes resulting from weightlessness reduce the strength, stiffness, and energy absorption capacity of bone.[9]  Similarly, intensive loading of a bone can result in an increase in mass.  The arm bones of professional tennis players are larger on the racket-holding side than on the other,[10] and middle-aged runners have more mineral in their bones than do sedentary people.[10]  It is inconceivable, on the other hand, that the shapes of bones could result merely from mechanical adaptation to loads placed on them. This was shown to be the case by many experiments starting in the 1920's.  For instance, it has been shown in as early as 1920's that a small fragment of the limb bud of a chick embryo, grafted into the chorioallantois of another older embryo, developed into a recognizable femur with a head even though there was no pelvis with which it could articulate.[11]  Bones, therefore, develop at least partly without reference to the loading system.  However, their final build is dependent in some way on the mechanical environment in which they find themselves, whether during development or in maturity.  The form of bones, lying latent in the genes, is the result of natural selection acting in the past on mechanically functioning skeletons.  Figure 2.2 summarizes the process through which the shape and size of bones are affected by the forces acting on them during life.  Loads are applied to a bone, resulting in strains and stresses.  Bone senses these strains (stresses), and compares them against some desirable (allowable) levels.  If the actual strains (stresses) deviate from the desirable level, either at all or by some threshold amount, bone is added to surfaces or removed from them.  This reconstruction alters the build of bone, so that same forces will now result in different and (if the reconstruction has been correct) more acceptable strains (stresses) in bone.  It is probable that bone will, sooner or later, actually be removed unless information is given to the remodeling system (which makes it adaptive) for it to remain in place or to be increased in amount.
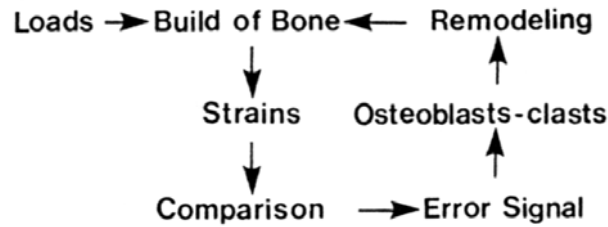
Figure 2.2. The Adaptive System Operating in Bone.

Different experiments have been performed in which the strain in the living bone has been monitored before and after remodeling. Two classic experiments are reviewed here. Goodship, et al (1979)[12] removed part of the ulna of pigs (Figure 2.3). This removal resulted in roughly a doubling of the peak strain on the radius during walking, as measured by strain gages attached to the surface of bone, when compared with strains on the control side. An explosive growth of the bone followed, the bone became rounded rather than ellipsoidal in cross section, and the difference in peak strain became less. In three months, the strain on each side was about the same. This seems a good example of the control system involved when remodeling works properly. The other classic experiment (Lanyon, et al, 1982)[13] on the forelegs of sheep showed that the strain at the end of a year was somewhat lower in the radius whose ulna had been removed than in the radius on the other side.
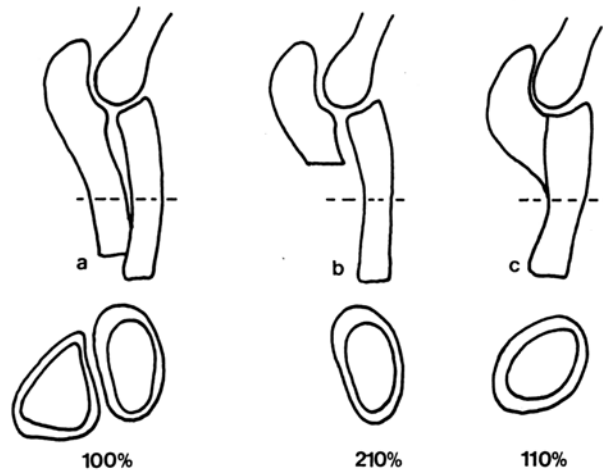


Figure 2.3. A Classic Experiment on Remodeling of Bone (strain on the radius in walking is shown at bottom).[12] (a) Normal limb of a pig with ulna present, 100% strain; (b) Ulna partially removed, more than doubling the strain; (c) After three months the radius has changed shape, and strain is about the same as on the control side.

If bones are subjected to an altered loading regime, there are two ways they might respond: by altering their build or architecture, or by altering the quality of bone tissue in some way. Experiments have been conducted on the effect of shielding a dog's femur against stress by screwing a plate to it, so that its stiffness is artificially increased. After a year, strips of bone were taken from control animals and also from animals that had attached to them either stiff plates made of cobalt chrome alloy or more flexible plates made of graphite fibers in polymethylmethacrylate matrix.[14] The maximum bending moment and the area under the load-

deformation curve (a measure of energy absorption capacity) were measured for strips of standard length and width (their depth, however, was determined by the thickness of the cortex). It was found that the control, non-plated strips were stronger and absorbed more energy than strips from the stiff-plated bones; the strips from the flexible-plated bones, however, were barely affected, behaving just like the controls. Calculation of the Young's modulus and tensile strength of the bone materials indicated that these properties were unaffected. The cortical thickness had been reduced in stiff-plated femora, and this accounted for all observed changes in properties. The contrary experiment, of increasing the level of activity well above normal, has been performed on pigs. The control animals were allowed to do what pigs like doing, which is nothing much and a lot of eating. The experimental animals were trained to trot for about 40 kilometers a week, and this was kept up for 8 months. Again, strips were tested, and marked differences found in the load the strips could bear and the energy they were able to absorb; these properties were enhanced in the exercised animals. However, there was again no different in the Young's modulus and tensile strength, nor in mineral or organic constitutes of these strips. In these long-term experiments, therefore, it seems that the bone that was laid down (if bone mass is increased) or removed is very similar to the original bone. This is what one would expect, because there is no reason for supposing that a different type of bone material would be more suitable for dealing with the altered loading regime. Of course, if bone is laid down during remodeling, its constitution will be different initially from that of the original bone because new bone has a lower mineral content than older bone.

Mechanisms of Bone Adaptation

Adaptive remodeling of bone involves two basic phenomena: (1) measurement of bone strains; and (2) adaptive measures are taken in response to strain. The strain-related messages must be read and acted upon locally. Although bone resorption or deposition, mediated through parathyroid hormone or calcitonin, may affect some parts of the skeleton more than others, there seems to be no good evidence that these effects are localized differently according to the differing mechanical needs of various parts of the skeleton.

Electrical effects are the likely mode of information transfer between bone strains and the cells in bone. Application of potential differences across bones, which causes a current flow, has been observed to result in new bone formation taking place to a greater extent than in the absence of such potentials.[15] It is also known that electrical potentials can be developed in bone by deforming it; this effect is called piezoelectricity. Some crystals have a lattice structure such that, when strained, there is a net separation of charges. This results in a potential difference being set up between opposite ends of the crystal, which happens because the crystals have no center of symmetry. Apatite has a center of symmetry and, so, does not exhibit piezoelectricity. Dry collagen does show it, however, though wet collagen barely does, probably because when wet it has little shearing stiffness. However, wet collagen, stiffened by mineral, is reportedly responsible for the stress-generated potentials of bone.

Besides piezoelectricity, streaming potential could also play a role in signaling bone strain conditions. If a solid surface in contact with a polar liquid (e.g., plasma) has a surface charge, then the fluid will have a concentration of oppositely charged ions near the surface. Many of these ions will be firmly bound to the surface, others less so. If the fluid is made to flow with

respect to the surface, the less rigidly bound ions will be made to move, and such a net movement of charges is a current; therefore, a potential difference must appear between the upstream and the downstream parts of fluid;[16] some question the significance of streaming potentials to adaptive phenomena in bone.[17]

If a specimen of wet bone is loaded in bending, the potential difference that appears is transient. The tension side will become positively charged with respect to the compression side (Figure 2.4). The peak difference depends upon both the strain and the strain rate,[18] and is of the order of 5 to 10 mV. When bone is held at a constant deformation, potential decays quite quickly, going to near zero in about two seconds.[19] If the bone is unloaded, so that it returns to its original shape, a potential of equal magnitude and opposite sign appears, and decays as quickly.
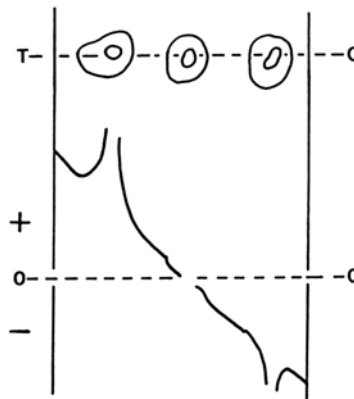


*Figure 2.4.  Diagram of the Electrical Potential Gradient in a Bending Specimen.*

Theoretical treatment of bone shows that the hydrostatic stresses in osteocycles could be quite high; it has been suggested that these transient high pressures may be a stimulus to remodeling.[20] Some suggest that remodeling is mediated through cells on free surfaces, not by the osteocytes;[21] hydrostatic stresses are thus unlikely signals for remodeling, unless enclosed cells signal to cells on surface which do the remodeling.

Once the local state of  bone strain is signaled, the next question is: how does bone react adaptively to this information?  Bone remodels so as to fit it to its function.  Pioneers in this field suggested that bone cells respond to change in curvature of surfaces.[22]  If, on the application of load, a surface becomes more concave, bone would be laid down on it.  If it becomes more convex, it would be eroded.  It is, however, difficult for cells to measure changes in surface curvature, while they can measure changes of strain with depth.[23]  A bone cell would lay down bone on its local surface if, on application of load, strains deep to it become more tensile with depth.  It should remove bone if strains become less tensile with depth (Figure 2.5).  This explains why the trabeculae in cancellous bone are arranged more or less along the lines of principal strain; this effectively eliminates bending stresses.  The way this could come about has been analyzed.[23]  Figure 2.6 shows the deformation occurring in a strut, set diagonally between two sheets, which are being forced toward each other.  There will be changes of curvature, which could be removed by remodeling process.  A portion of canellous bone that had spaces set at random in it would come to be regularly and effectively arranged in relation to loads imposed on

it (Figure 2.7).  Indeed, it looks as if such a fairly simple method of control produces structures that are good approximations to optimum structures of minimum weight.
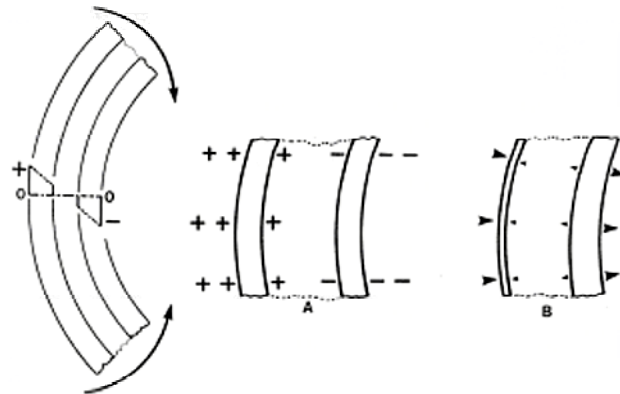


*Figure 2.5.  Section of a Hollow Bone Loaded in Bending (cells measure the change of strain with depth): (A) Strain-induced potentials; (B) Direction of bone remodeling, and the resulting asymmetric thickness of cortical walls.*
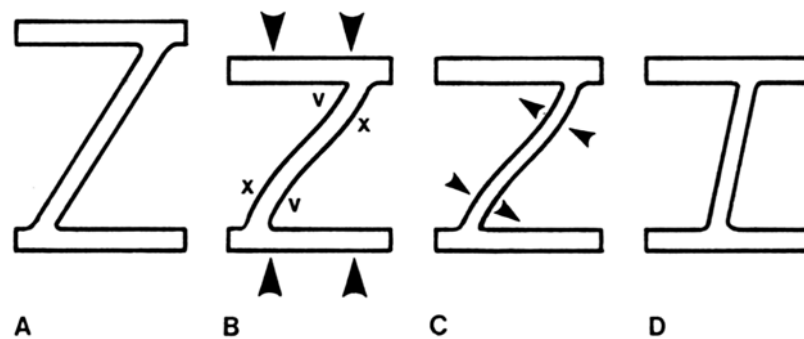


*Figure 2.6.  Remodeling of Cancellous Bone: (A) The original shape: two sheets joined by a diagonal strut; (B) A load (large arrows) is applied, making some strut surfaces more convex (x) and others more concave (v); (C) The direction of remodeling occurring; (D) Shape after some remodeling.*
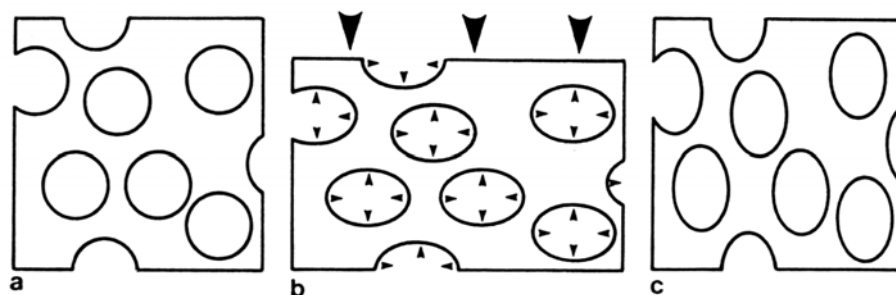


*Figure2. 7. Remodeling of Cancellous Bone: (a) A portion of cancellous bone with circular spaces set more or less randomly; (b) On loading, bone deforms and erosion occurs at surfaces that become more convex, with those becoming more concave added to (small arrowheads show the direction of reconstruction); (c) After reconstruction, bone has a better shape to resist the applied loads.*

Experiments have been performed on tibiae of rabbits subjected to continuous (static) bending loads for many months.[24]  The force producing bending was occasionally adjusted so that the maximum bending stress in bone remained effectively constant, at about 60 MPa,.  The results showed that constant stress has very little effect on bone over many months.  In experiments involving intermittent loading, bending stresses of about the same magnitude as in static experiments were applied at about 0.5-1 Hz for 1-3 hours each day.  Results were quite clear; there was considerable extra bone deposited under intermittent loading conditions.

Because stress-generated electric potential declines quite quickly after the bone is loaded, the rate of strain is important in determining the magnitude of the potential evoked.  Experiments on the potential produced in the radii of sheep during normal locomotion indicate that, as expected, the maximum strain in bones increased with speed of locomotion; strain-generated potentials, however, increased much more rapidly than strains with speed.[25]  When the sheep walked slowly, although strains could be clearly recorded, strain-generated potentials were small and irregular, with no recongnizable strain-linked patterns.  In other words, strain rates must be high for strain-generated potentials to reach reasonably high values.  It has been suggested that as activity in old people decreases, strain rates imposed on bones fall to a level at which the resulting strain-generate potentials are small and incapable of initiating bone deposition.  If, as seems to be the case, bone is removed unless it is actively protected, this level of strain-generated potential will result in bone being removed even though stresses and strains in bone become higher and higher as a result.  Experimental results confirm that bone remodeling is indeed much more sensitive to strain rate than to maximum strain.[26]

The general thrust of experimental programs reported above is that bones are adapted to loads exerted  on them, so that the strains they experience are brought to some reasonable level – in fact, that they have some safety factor.  If this is accepted, the subtlety of the process becomes apparent, because different bones in the same skeleton will need to have different strains as the "desired" level of strain.  This is because the variability of loading is different for different bones.  In the case of human skeleton, if the control system in tibia produces a strain of 0.002 during day-to-day locomotion, a sensible safety factor may well result.  But if bones in vault of skull were remodeled so that day-to-day strains were 0.002, the top of human skull which is only trivially loaded by muscle action would have to be very thin indeed if normal activities were to produce strains as great as 0.002.  But a very thin skull would be useless against the occasional sharp blow to which skull is subjected.  One should thus assume that the control system in some bones of skull has a different set point from that in other bones.  The case of deer antlers is even more striking, because while antlers are growing they are covered by a periosteal "velvet." This is richly supplied with blood, and deer seem to do their best to prevent any load application on the antler.  When growth has finished, the velvet is shed, and no more growth is possible.  Only then are the antlers loaded in earnest, in fights.  The whole growth process seems especially designed to prevent any adaptive remodeling, yet deer can fight fairly successfully, and their antlers do not break all the time, nor yet are they over-designed; they seek in fact to have a sensible safety factor.  There is thus some way of modifying, or even overriding, the control system in particular bones and even in different parts of the same bone.  Another aspect of this subtlety concerns bones that are liable to fail by buckling.  If a bone is long and slender, it may collapse suddenly by Euler buckling.  The problem for a signaling system designed to prevent such buckling is that strains at any point in bone give little information about whether the bone is

near collapse. In a column loaded very nearly along its long axis (there is bound to be some deviation of the line of action of force from the long axis), local stress may become large only just before failure occurs. If, however, more bending is imposed on such a slender bone, two phenomena occur: (a) the load that will cause collapse decreases, but (b) the greatest stresses in bone give a better warning of the likelihood of collapse. Some bones may be loaded in bending when they could be loaded in direct compression;[27] while this may be viewed as inefficient skeletal design, such bending may increase "perfusion of tissues" or maintain a "healthy flux of strain-generated potentials." However, it may be that imposing apparently gratuitous bending on slender bones may not directly help bones resist the loading, but may help the remodeling system to respond more effectively by giving a greater warning of collapse. Another problem for local signaling systems is to produce useful remodeling when deformation of the bone must be restrained in some way. If, for instance, a bone is loaded as a cantilever, then deformation at free end depends much more on strains near the fixed end when compared with those near the free end (Figure 2.8). It would, therefore, be adaptive to have quite low strains near the fixed end, while strains near load cold be higher without greatly affecting total deformations. For the remodeling system to work properly in such a bone, the local signal producers should have information about the loading system as a whole.
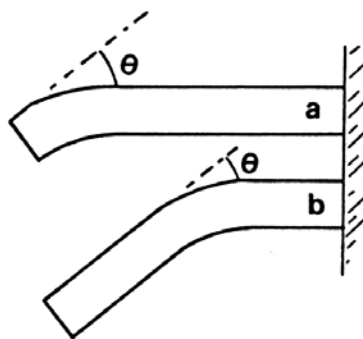


*Figure 2.8. Effect of Similar Curvature Near Free Versus Fixed End on Deformation at Free End of A Cantilever Beam.*

Internal Remodeling

Internal remodeling is primarily concerned with Haversian systems (osteons) especially in cortical bone. The essence of internal remodeling of osteons is central removal of osteonic bone followed by its replacement. Bone removal is through the usual osteoclastic method, and takes place on the perimeter of the Harvesian canal which is transformed into a widened tunnel-like longitudinal space. This is often followed by internal deposition of lamellar bone by osteoblasts lining the tunnel. Osteogenesis is carried out progressively and the tunnel narrows and may or may not return to the usual diameter of Haversian canals. Bone formation may stop for a time and later recommence. In reconstructed tunnels, cessation of osteoclastic activity is often marked by a scalloped reversal line, while temporary termination of bone deposition is characterized by an arrest (or resting) line. During bone deposition, narrow ostoid seams rim the new mineralized matrix. The speed of tunneling is usually much greater than that of the subsequent osteogenesis, partly accounted for by the concentration of osteoclasis at the end of the tunnel, and new bone deposition over the whole internal surface. Tunneling is often

concentric to the canal or part of the canal, but it may be eccentric or even extend into the solid compactum of adjacent osteons.  Through osteonic remodeling after birth, the primary osteons of pre-natal life are replaced by larger secondary osteons, and it is the latter which are in continuous process of remodeling throughout adult life.  In forming osteons, the linear rate of bone deposition is deemed to be about 1 micron per day.  Estimates of the rate of renewal of osteons in the skeleton of adult dogs vary from 2% to 11%, and are even higher for certain bone-like ribs.  In the aging skeleton, osteogenesis does not keep up with tunneling, and the result is wider Haversian canals which may culminate in an osteoporotic cortical pattern.  One of the remodeling functions seems to be the ready provision of minerals for metabolic needs, and this is supported by osteons exhibiting varying degrees of mineralization, ranging from incompletely calcified new osteons to fully  calcified old ones.  The former are sometimes referred to as metabolic bone, and the latter as structural bone.  There is little doubt, however, that mechanical factors are important to remodeling; inactivity results in widened Haversian canals and porotic bone, while stresses (especially longitudinal ones) result in a more solid compactum.  It is important to recognize that the processes involved in physiological internal remodeling are essentially those which take place under pathological conditions.  Tunneling succeeded by internal bone deposition are also characteristic of the creeping repair, which occurs in avascular nektonic compact bone following fracture, and osteonic tunneling is also responsible for the porosis which so commonly develops in the viable cortex of fractured bones.

Internal modeling involves formation of new Haversian systems which seem to have no straightforward mechanical advantage over primary bone.  It is possible, however, that they could reorient the grain of bone if altered loading systems make the present grain inappropriate.  They could also repair microcracks, remove dead bone, and have a function in calcium or phosphorus metabolism.  These aspects of internal remodeling are discussed below.

*Grain Alteration*

It is true that, when imposed forces change direction in relation to the grain of bone, Haversian remodeling can alter the grain of bone adaptively.  This has been observed under large muscle insertions and during fracture repair.[28]  It has been argued that the Haversian remodeling seen under muscle insertions results in muscles having firm attachments to the bone even when muscle insertion is migrating during growth, and also during erosion of the bone surface when the shape of bone is being altered.[29]  Compact coarse-cancellous bone is often badly oriented, and replacing it with well-positioned Haversian systems might be mechanically advantageous.  However, the usual orientation of Haversian systems makes it certain that improving the grain of bone is not their only function.  Quite simply, many Haversian systems developing in long bones do not materially alter the grain of bone, because they have a mainly longitudinal, though very gently spiraling, course, and the blood channels they replace have the same orientation.[30]  Furthermore, in human being and animals that undergo many generations of remodeling, there does not seem to be any general change of direction between earlier and later system generations.  Certainly, the longitudinal orientation of systems in long bones is appropriate for the force systems usually acting, but no more appropriate than that of primary laminate they replace.  The only effect that might possibly be important occasionally is the reduction in the anisotropy of bone.  Fibrolamellar bone seems to be rather weak when loaded in tension radially to the long

axis of bone; Haversian bone is somewhat stronger. However, long bones can be loaded in this way only with great difficulty, and it can hardly be important in life.

*Microcrack Removal*

It has been suggested that Haversian systems form at the end of microcracks and thereby blunt them.[31] When a crack enters the vicinity of a Haversian system, it will tend to travel around the cement sheath, because this is a zone of weakness, relieving the bone inside the system of stress (Figure 2.9a). As a result, local bone cells will become osteoclasts and destroy the bone around them – the usual response to a marked reduction of stress in bone. When the cavity becomes filled in, a new Haversian system will appear. This simplification of microcrack control in bone can be geometrically inconsistent. A damaging crack front in a long bone is likely to travel in a radial direction and to be oriented normal to the long axis of bone. Havesian systems are generally oriented with their long axis normal to such a crack front, and so there will be no great tendency for the crack front to travel around the cement sheet (Figure 2.9b). Still, this simplified interpretation of the crack removal effect associated with Haversian bone formation highlights the role that stresses, or lack of them, near a crack front may have in locally inducing reconstruction.
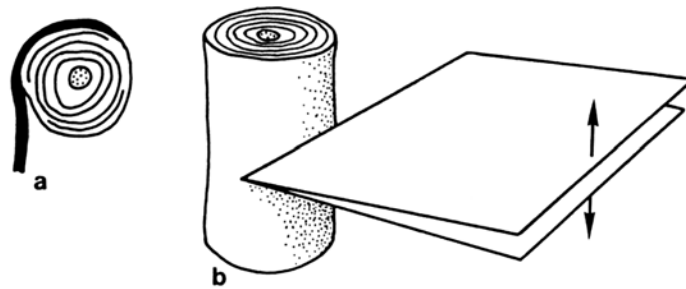


*Figure 2.9. Interaction of Microcracks with Haversian Bone: (a) A microcrack, shown black, tends to get caught by a cemen tsheath around a Haversian system; (b) However, most damaging cracks have the orientation shown here, with tensile forces, arrows, producing cracks traveling in the plane normal to the axis of Haversian system.*

*Dynamics of Bone Mineral*

Nucleation, crystal formation, crystal growth, solubility and reactivity are key factors influencing the dynamics of bone mineral. The fact that bone mineral is difficultly soluble is of far-reaching physiologic significance. This property not only determines the deposition of the bone mineral; it preserves the structure and rigidity of bone. Moreover, it is of critical significance in maintaining the balance of minerals between the skeleton and the fluids of body. Calcification is essentially the deposition within a soft organic matrix of a difficultly soluble compound of calcium. For calcification to occur, certain fundamental conditions must be present. These divide themselves naturally into: (1) humoral; and (2) local conditions. Humoral conditions embrace the supply and transport of the minerals necessary for calcification and their delivery to the locus of calcification in the concentrations required. Local conditions include whatever it is that differentiates a calcifiable form a non-calcifiable tissue. This is at times referred to as the local factor. Since, however, several interrelated factors, enzymatic and non-enzymatic, appear

to be involved, it will be convenient to refer to these collectively as the local mechanism. In considering the humoral conditions for calcification, it is apparent that in spite of the difficulties in defining the solubility relationships of bone mineral, its deposition and its maintenance in the solid state depend primarily upon its solubility.

Bone Tissue, Electrical Control and Fracture Healing

Bone healing is a complex and dynamic affair with a succession of changes commonly culminating in restoration of the part. Following a proliferation of cells and blood vessels, bone tissue is produced, and often fibrous elements and cartilage too. The new osseous tissue is different from that in the bone and it is a provisional structure. It is subsequently removed and much of it replaced by osseous tissue similar to that in undamaged bone. At the same time, any cartilage formed undergoes replacement ossification in a manner reminiscent of that which occurs during osteogenesis at the epiphyses during the growth period. Consequently, an understanding of bone repair requires a knowledge of bone as a tissue, of the different kinds of bone tissue in man and the composition and inter-relationshipos of their components.

Bone is a complex, highly organized and specialized connective tissue. It is characterized physically by its hardness, rigidity and strength, and microscopically by relatively few cells and much intercellular substance formed of mineralized fibers and cement. The hard nature of bone is deceptive in its intimate details. Inorganic material comprises about two-thirds of the weight of dried defatted bone. Most of it is a complex of calcium and phosphte, but there are also carbonate, citrate, potassium, sodium, magnesium and other materials in the intercellular substance. Some of the mineral is probably amorphous calcium phosphate but much or most is in the form of very tiny ultramicroscopic crystals. The mineralization process of bone is highly complex. Calcification of specific tissues like bone would seem to depend on two main factors, namely the local development of a calcifiable matrix and conditions which promote local super-saturation of the minerals so as to exceed the solubility product of the crystals. Calcification is likely to depend on the acquisition by matrix of nucleation or seeding centers. These are sites where the initiation of crystal formation is catalyzed. The seeding could occur after prior deposition of calcium or phosphate ions in a specially oriented arrangement so as to allow the crystal lattice to form and then grow by epitaxy. Calcification must also involve the movement of calcium and phosphate ions to the sites of nucleation. Intracellular movement of calcium and phosphate ions and their expulsion into the calcifiable milieu is necessary to maintain the local supersaturation needed for crystal growth. This could involve cellular membrane barriers between bone spaces and extravascular spaces. The activity of these cellular membranes in transmitting the mineral ions to the calcifiable matrix is likely to be under the control of hormones. The mineral elements are deposited within the organic matrix of intercellular substance. The organic matrix is produced by bone-forming cells or osteoblasts and has two components, fibers of collagen and a soft material known as ground substance or cement. These are intimately related. Collagen is a fibrous protein, ubiquitous in extraosseous body tissues where it is formed by fibroblasts. It is formed by osteoblasts in bone where it is the main protein constituent of osseous tissue and where it is more densely packed than in any other tissue. Collagen accounts for 20-30% of the dried, defatted weight of bone, and for about 90% of dried, defatted demineralized tissue (organic matrix). The strength of bone is largely due to its collagen and not its minerals, and the architectural arrangements of fibers within osteons and trabeculae of

adult bone are conducive to great strength with structural efficiency. This is also of great importance in fracture repair where bulky callus, though often important, is not necessarily equivalent to strong healing. The relative contributions of collagen and minerals to bone strength are readily demonstrated by comparison of decalcified bone samples in which the soft tissues remain, with those of macerated specimens from which collagen and other soft tissues have been removed by alkali or other treatment, leaving the mineral structure unaffected. Though decalcified bone is no longer hard, it resists tension and compression and even torsion, while macerated bone, though hard, is weak and often quite fragile like chalk. Figure 2.10 shows the collagen fiber orientation in a single lamellated osteon. The interweaving arrangement and coarse nature of collagen bundles in woven bone under polarized light are illustrated in Figure 2.11. Regular crossbanding of individual collagen fibrils at intervals of about 640 Angstrom is characteristic of all mammalian collagen. Another specific feature is its hydrolysis by the enzyme collagense.



*Figure 2.10. Osteon of Compact Bone Cut Obliquel.*[35]
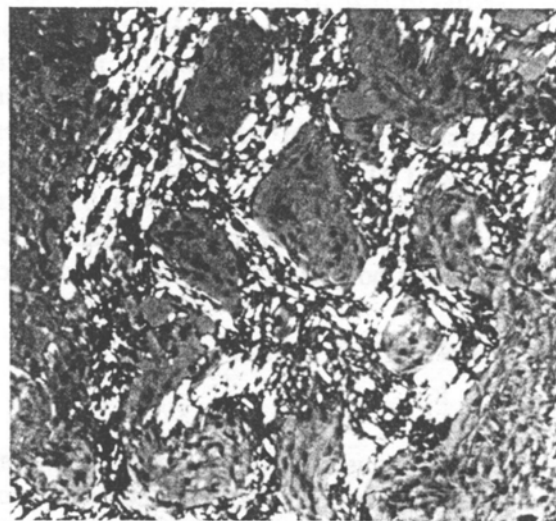


*Figure 2.11. Weaving of Coarse Collagen Bundles.*[35]

The basic unit of collagen is a rigid rod 3000 by 14 Angstrom in size with a molecular weight of about 300000. Structurally, it is a triple coil with a double helical twist; the chains have lateral association (cross-linking). Bone collagen is cross-linked rapidly and extensively during its formation, and this probably adds to the strength of bone. These tropocollagen units link

together to form collagen filaments and fibrils which are about 100 Angstrom in diameter and increase in thickness by accretion to form the individual fibers which then collect into bundles, commonly 3–5 micron thick. The ground substance or cement in bone is the non-collagenous part of bone matrix. It is a complex viscous material in which the collagen is embedded. It is estimated to form about 8% of the organic matrix.[36] Its best known components are proteoglycans (protein- polysaccharides). In these compounds the polysaccharide and protein are linked by strong covalent bonds. Ossification in bone is brought about by a secretory cell, the osteoblast, which produces all the organic matrix of bone and may also play a part in its mineralization. The precursors of osteoblasts are knows as osteogeneic cells which have limited multipotency. Under appropriate conditions in tissue culture, they can differentiate into osteoblasts, chondroblasts and fibroblasts, and this is also evident during bone repair. After appropriate stimulation in vivo (e.g., by fracture), they divide by mitosis once or twice and differentiate into osteoblasts. New electronegative potentials arising within bone upon fracture may stimulate this division and subsequent maturation.[35] Although all bone tissue in mammals contain cells, fibers and cement, their relative amounts and arrangements vary. The primary classification of bone types is based on the arrangements and thickness of fibers in matrix. Two types of bone are of paramount importance for understanding normal structure and repair: (1) woven bone; and (2) lamellar bone. Woven bone is architecturally arranged as a close network of fine trabeculae. This is because it is formed within the interstices of a vascular field so that the trabeculae come to have a honeycombed or sponge-like arrangement separated by vessels with their accompanying cells (Figure 2.12). The trabeculae are small and the network is quite a fine one compared with the relatively open network of lamellated trabeculae even in canellous bones like the pelvis (Figure 2.13). Structurally, woven bone is distinguished by its osteocytes which tend to be plump and irregularly distributed in the matrix, and by the coarse bundles of fibers in its matrix which usually form an interwining pattern, hence the alternative names of coarse fiber and woven bone. During its formation, new woven bone can appear in two forms. One kind is characterized by a relatively homogeneous condensed matrix tending to obscure the fibers and these trabecula are lined by well defined membranes of osteoblasts. The other kind is characterized by much fibrillar matrix and relatively few lining osteoblasts. The different appearances suggest that scretion of cement and fibers by osteoblasts are not simultaneous, and also perhaps that part of the fibrillary component of woven bone is derived from condensations of pre-formed connective-tissue fibrils in the ostogenetic field. Woven bone is the immature bone formed during rapid ostogenesis such as in intra-uterine life and during the active growth period in children. It is always a temporary or provisional structure to be removed and often replaced by bone with a lamellar structure. Nearly all the bone in fracture callus has a woven structure. Woven bone distinguishes the osteogenesis of certain benign osseous tumours and osteogenic sarcomata, though their malignant nature produces special cellular fractions. Lamellar bone is distinguished histologically by its multilayered structure. Compact lamellar bone superficially resembles plywood in section (Figure 2.13) as if numbers of thin plates were cemented together, and a series of concentric plates characterize the cross-sectional appearance.[35] In lamellar bone, the lacunae with their osteocytes are relatively small and oval, and are spaced in the matrix in an orderly fashion at regular intervals. Lamellar bone is characteristic of the adult skeleton though it is also said to be present in extinct reptiles such as dinosaurs. Unlike woven bone, lamellar bone is formed as a deliberate long-lasting structure. It is the tissue with great strength which replaces not only the woven bone produced during fracture repair and other pathological states, but also fine-fibered bone formed in the fetus and that

formed initially during endochondral ossification. Lamellar bone is deposited by an additive process in an orderly manner on existing bone by the layer of osteogenic cells which line its surface. When the accretion occurs on trabeculae surrounding a centrally placed blood vessel, a concentrically arrange osseous structure is created. This is the architecture which distinguishes the Haversian system (osteons). Osteons are the architectural units of compact bone. They are elongated, almost solid cylinders largely directed in the long axis of the bone. Each osteon is made up of a series of thin lamellae about 3 micron thick concentrically arranged around a central canal known as the Haversian canal.

Remodeling through bone removal and formation around Haversian canals is a structural alteration involving successive cycles of resorption and deposition of bone. Resorption widens the canals into spaces, and longitudinal tunneling can involve other osteons. Much or even all the osteon is destroyed, and then osteogenesis resumes, a cement line marking the transition. Now the space is filled in by concentric (or sometimes eccentric) new bone deposition by the lining osteoblasts to form a new secondary osteon. The mean rate of bone deposition in a forming osteon is estimated as 0.5-1.5 micron per day. From rib biopsies in adults it is estimated that the average turnover of cortical bone is about 5% per year. The lifetime of osteons varies between spaces and between bones, but the mean lifetime in adult man is of the order of 15 years. Cortical bone is not all osteons and their remnants from remodeling. Several layers of circumferential lamellae cover the surface of cortices having been formed by the osteogenic cells of the periosteum. This is how cortices grow in width. The circumferential lamellae are demarcated from the underlying osteons by cement lines, sometimes referred to as accretion lines to indicate the manner of bone deposition. Many parts of these lamellae subsequently become involved in nearby osteonic tunneling and their locations become part of the seats of new osteons. Not all osteons are equally mineralized. Younger osteons and the younger central parts of forming osteons are less mineralized than the older ones, containing about 70% of the calcium in the latter. The initial calcification is rapid but subsequent mineralization is slow, taking months to reach the maximum. Local changes in the composition of the organic matrix also take place. The younger, less mineralized matrix has been referred to as metabolic bone and the older, less active but more mineralized matrix as structural bone. The latter forms 95% or more of skeletal bone. Metabolic bone (labile bone) is more reactive and is said to play an important part in regulating body's requirements for calcium through hormonal means utilizing ostoclastic resorption for the ready availability of calcium ions. Cortical bone also contains a series of canals which traverse the whole thickness of the cortex from the medulla to the periosteum crossing osteons and their Haversian canals in their course. Each contains a blood vessel which communicates with and supplies the vessel in the Haversian canal which it crosses. This is of paramount importance in the blood supply of cortical bone. The nature of lamellation of cortical bone is determined by the general orientation of its collagen fibers which is constant in each lamella; the general fiber direction alternates abruptly from one layer to the next such as successive longitudinal and circular orientation in the cross-section appearance. The lamellae are not separated by cement lines, and there are many fiber connections between successive layers.
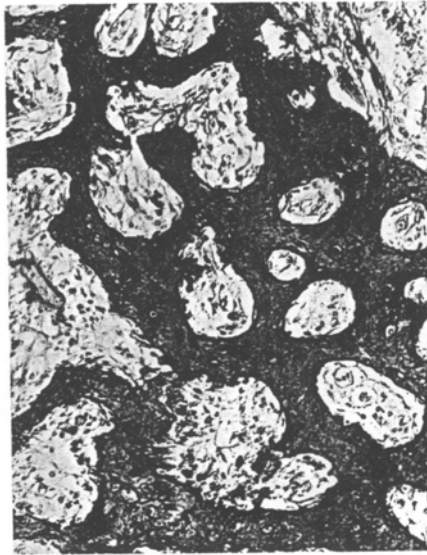
*Figure 2.12. Woven Bone with Closely Arranged Spongy Network Formed Around Vascular Cellular Tissue.[35]*



*Figure 2.13. Cancellous Bone in the Pelvis Containing An Abundance of Red Marrow.[35]*

Electrical Control and Fracture Healing of Bone

Strengthening of particular parts of a bone to meet functional demand is carried out through self-regulating mechanisms initiated by mechanical stress. Since the discovery in bone of selective electrical potentials promoted by bending, these signals have been considered to trigger the activity of particular bone-forming and bone-removing cells, thus determining the placement and orientation of new osseous tissue and selective removal of the old. Tiny electrical potentials develop in both living bone and (in a modified form) in dead bone under bending. Areas under

compression become electro-negative, and those in tension electro-positive. The potential is generated immediately on bending, and a steady potential can be achieved when it is maintained, though it may leak away. An opposite potential is briefly induced on removing the stress. The potentials are piezoelectric in origin; bone also possesses intrinsic electrical potentials from the streaming properties of its blood flow (streaming potentials), from metabolic activity, and from surrounding muscles. Long bones at rest have a characteristic electrical pattern on the surface; the metaphysis is electro-negative with respect to the epiphysis and the diaphysis is essentially isopolar.[46] The pattern is altered after fracture when the shaft, especially over the fractured part, becomes electro-negative until the fracture is healed. These intrinsic and endogenous potentials are likely to be important in fracture healing while those externally induced by stresses are likely to determine subsequent remodeling. Osteogenesis has been demonstrated in bone, especially at the cathode when tiny electrical currents were passed through it, and the effective magnitudes of the currents required are comparable with those produced by deforming the bone. Moreover, when an intact long tubular bone is kept compressed, periosteal callus forms around the bone between the points under compression. The phenomena support the hypothesis that local generation of electrical potentials is concerned with the functional reconstruction of bone including remodeling after fracture; that the potentials for reconstruction are generated within the bone largely by mechanical stresses put upon it; and that they operate on bone cells, modifying their activity, triggering them when and where to proliferate and to form or remove bone matrix. The system can be envisioned as a negative feed-back cycle set in motion by an external force. This stimulates an osseous transducer determined by the electrical properties of bone which in turn stimulates an electrical signal in proportion to the force exerted. This signal affects cellular and extracellular transducers which influence the activity of bone cells and the orientation of new collagen. Thereby, bone structure is modified in a direction tending to neutralize the effect of the external force.

Environmental changes in bone – mechanical, chemical or thermal – produce potentials which act on osteogenic cells and can stimulate them to form bone. The development of electrical potentials in bone subjected to stress occurs in dead bone and decalcified bone as well as living bone, and are partly piezoelectric in nature. Piezoelectricity is a property related to structural deformation, and was originally demonstrated in crystals when they were mechanically deformed. In bone, it is derived by deformation of its collagen fibers, and is unrelated to the hdroxyapatite and mineral content.[35] Collagen is known to have piezoelectric properties as it becomes electrically charged on stretching or other deformations. Since piezoelectricity is dependent on deformation stresses, its relationship to fracture healing is complex. Bone also receives electrical potentials from other sources which are also important to fracture repair. These are endogenous potentials from the streaming properties of flowing blood (streaming potentials) and from metabolic activity, and currents are also transferred to bone from the surrounding muscles. In intact bones, growth zones and the vascular metaphysis are electro-negative, and the diaphsis is essentially isopolar. Potential changes on bone surfaces after surgical interference are derived from injury potentials from surrounding soft tissues, especially muscle; hence, potential is greatly reduced when bone is insulated from surrounding tissues, and rise again when the insulation is removed as if the surface of bone acted as a pathway for currents produced by trauma to surrounding muscles.[37] This helps explain the pattern of electrical changes in bone following fracture.

The fact that new bone can form by electrical stimulation of an intact or fractured bone is now well established.  The osteogenesis occurs or begins at the cathode when small electrical currents are passed and the effective magnitudes of currents are comparable with those produced by bone deformation.  The phenomenon was originally demonstrated in the intact rabbit's femur utilizing vitallium electrodes and a current of 1 micro-ampere applied continuously for 3 weeks from a 1.5 volt battery.[38]  A ridge of periosteal callus formed between electrodes, more in the region of electro-negative electrode (cathode) than elsewhere.  Increased osteogenesis at the cathode has been amply confirmed not only in intact bone but also in experimental fractures.[39]   The electrodes used and the currents applied have varied.  Some used direct current, others pulsed currents of various shapes and frequencies; direct currents seem as effective as pulsed currents, and stimulating currents generally range between 5 and 25 micro-amperes.  Some practical applications of these phenomena involve use of external pulsating electromagnetic fields whereby currents are induced through non-invasive means, and the use of electret film on a bone surface to induce callus formation.  Elecret is a material with permanent electrical polarization analogous to the magnetic polarization of a magnet.  It has a weak electrical field, and utilizing an electret made from Teflon film, bony periosteal callus has been produced in the femur of rats wrapped by the film.  Bone damage can occur with relatively large currents or relatively high voltage.  Bone destruction has been noted when the stimulating current is greater than 1 milli-ampere; bone architecture develops an abnormal Pagetoid pattern after passing a current of 7-10 micro-amperes with 150 milli-volts for 1 to 6 months.

Electrical stimuli influence the behavior of osteogenic and other cells, possibly by transduction of the signal to a biochemical message.  Fracture repair tissue in frogs is formed by nucleated red cells in the haematoma which undergo a remarkable series of nuclear and cytoplasmic changes prior to forming callus cartilage.  Similar changes are produced in vitro when frogs' red cells are stimulated by very weak electrical currents.  Electrical potentials following fracture have been found responsible for the changes produced in red cells, with their messenger RNA so altered by the new electrical field that it changes from an inactive or coiled form to an active, extended form.[40]

The above findings have led to efforts to increases osteogenesis and speeding the union of recent fracture through electrical stimulation, and to heal old defects, ununited fractures and pseudo-arthroses.[35,39,40]  The overall results are encouraging for treatment of non-union when electrical stimulation is combined with prevention of movement at the site.  However, surgeons will hesitate before subjecting a patient to an open operation to implant electrodes, so that the non-invasive techniques of external stimulation would seem more practical. Pulsing electro-magnetic fields produced outside the body to induce changes in electrical potential within the affected bone are in use.  It cannot be assumed that any improvement in fracture healing from electrical stimulation is necessarily derived from a concurrent increase in the amount of new bone formed.  Bulky callus may or may not produce provisional union.  The speeding of bridging between the fragments and increasing its mechanical strength are more significant.  The strength of a bone is related to its gross and microscopic architecture including the orientation of trabeculae and the arrangement of collagen fibers.  Experiments in vitro suggest that small electrical potentials help to control collagen synthesis and fiber orientation.  The formation of collagen has been observed to increase when fibroblasts are cultured in an interrupted electrostatic field,[41] and the orientation of fibers polymerizing from solution was influenced by applying small electrical currents.[42]

These findings are consistent with the dipole properties of collagen which carries a net negative charge and will migrate in an electrical field. A distinction between osteogenesis and strength of fracture union has been found experimentally. In electrically stimulated fracture healing of rabbit's fibula, the resistance to bending after union was significantly better in stimulated bones compared with controls, though histological differences in healing between the two groups were not impressive.[43] Studies of the effects of electrical stimulation on osteotomies in rabbits have concluded that bulky callus obtained with currents of a certain value was associated with a lower tensile strength of the healing bone compared with that in unstimulated bones.[44] Lowering the current strength produced stronger healing with less callus. The increased bone strength seemed to be due to better orientation of the healing trabeculae. In normal healing which proceeds well, there might be marginal gains associated with electrical stimulation;[45] the most important application of electrical stimulation is likely to be for prolonged non-union to which certain fractures, especially those of the tibia, are prone.

There are changes produced by fractures on the resting potentials in a bone and those which occur during natural unstimulated healing. A characteristic alteration in the electrical pattern of skin overlying long bone fractures in rabbits and man have been demonstrated.[46] The whole shaft became electro-negative especially the area over the fracture, and changes occurred immediately after injury. Obviously, the initial electrical change was not the result of healing, and much of the new electrical pattern may have arisen from potentials derived from injury to muscles around the fracture.[47] The electrical potential continued to be negative until the fracture was judged healed by radiography, and the last part to revert to its normal isopolar state was the fracture site. Presumably repair processes were responsible for the prolonged electro-negative pattern but the relative contributions from bone healing and soft tissue repair are uncertain. Assuming that the same cellular activity is involved in normal bone repair and in that stimulated by electrical forces, it is possible that the driving force to normal bone healing is the spontaneous electro-negative pattern in the fracture area produced by injury. This may come from the bone injury or from trauma to surrounding muscles or from both sources. On the other hand, severe damage to muscles around a fracture is believed to be deleterious for fracture healing or at least fracture union. Consequently, any extra electrical stimulation to bone repair from muscle-derived potentials might be regarded teleologically as a compensatory reaction to the muscle trauma. Movement, stability, compression and tension are all known to affect the healing of fractures and their ultimate union, and it is not unlikely that they operate in part through the production or suppression of endogenous electrical stimuli at the fracture site.

All important injuries make demands on body's economy; most injuries, not just fractures, produce a hypermetabolic state accompanied by loss of weight and tissue cataboliss. At the same timehealing needs energy, synthetic intermediates of metabolism, and vitamin C and a good blood supply. Moreover, calcium, phosphorus and vitamin D are required for mineralization of osteoid matrix created during fracture healing. Repair occurs ultimately through the courtesy of body nutrition, but it has a high biological priority and proceeds even during starvation.

When a bone is fractured, the part becomes swollen, painful and tender from ecchymosis and inflammatory changes. These resolve clinically usually in few days, and in most cases a special connective tissue known as callus develops subsequently on either side of the fracture, externally

and internally.  This becomes firm and then hard from the formation of bone and cartilage.  The broken fragments often become anchored to each other by external callus, and in many long bones this is commonly the stage of functional or clinical union.  In due course, bony union generally takes place across the fracture gap; the callus is reconstructed and the fracture area is remodeled, strengthened and restored to something like its previous state.  Fractures in man can generally heals and unites through: (1) acute changes of local haemorrhage, inflammation and necrosis; (2) proliferation of repair tissue and osteogenic cells; (3) formation of new bone, fibrous tissue and often cartilage around and on either side of the fracture gap; (4) union of the fracture gap; and (5) remodeling of the callus and the original structure of bone.

# CHAPTER 3

# BIOMIMETIC PROCESSING OF HYBRID NANOSTRUCTURES

## Background Review

### Introduction

Nanosized materials or nanostructures have dimensions, as their name implies, in the 1-100 nanometer range. It is in this size regions that the interaction between biology, chemistry, and physics is the most synergistic. Consequently, it is also an area which may yield truly advanced materials. Nanostructures are, literally, facts of life in biology. Proteins, viruses, and bacteria are nanosized, three-dimensional structures which have been self assembled from smaller subunits. Although individual atoms in the subunits (polypeptides, for example) are covalently linked, assembly of the subunits is maintained by non-covalent (van der Waals, hydrogen-bonding, electrostatic, and hydrophobic) interactions. As far as the chemist is concerned, nanosized materials are huge macromolecules (with molecular weights of the order of $10^6$ to $10^{10}$) constructed from millions of atoms. Atom-by-atom synthesis of nanostructures, via covalent bond formation, is a formidable task which has not as yet been achieved by synthetic chemists. Covalent polymerization is the best that chemists have done thus far. Chemists have made spectacular progress, however, in forming self-organized and supermolecular materials in the size domain of nanostructures by the non-covalent bond assembly of molecules. Nanosized materials are synthesized in nature by a process known as biomineralization. Efforts to mimic biomineralization involve crystal growth in association with surfactant monolayers, noting that the precipitation of inorganic solids within living organisms, termed biomineralization, generally occurs in association with organic matrices; monolayer systems were considered to provide an excellent opportunity for investigating the influence of an organic matrix on crystal growth.[49] Most naturally occurring nanostructured materials are hierarchical composites and are often referred to as hierarchically organized materials. This term implies an organization of materials in discrete steps, ranging from the atomic to the macroscopic scale. At each step, the components are held together by specific interactions and are organized for optimal overall performance. Tendons, which are responsible for connecting muscles to bones, provide a good illustration of hierarchical construction. A second example is the abalone shell with a "brick-and-mortar" hierarchical architecture. Calcium carbonate (aragonite) bricks are bonded by soluble acidic proteins and poly saccharaide which are present in the abalone wall. This design, schematically presented in Figure 3.1, imparts a great deal of structural strength to the shell and reduces the risk of cracking. Architectural lessons to be learned from nature are illustrated by these two examples.[7]
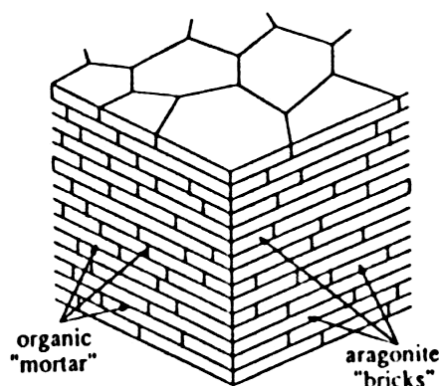


*Figure 3.1  Schematic Structure of the Nacre of Red Abalone Shell.*[54]

Most modern materials are formed empirically by solid-state methods.  These methods generally involve more processing activity than chemical synthesis (for example, sintering of ceramic powders, modifying concrete by polymers, thermo-mechanical processing of alloys, layering polymeric membranes for special applications, implanting ions into semiconductors, and growing crystals).  The industrial production of ferrofluids (liquid magnets) serves to illustrate the crudest end of materials processing.  The development of a new generation of advanced materials demands innovative chemical tailoring, a task firmly based upon a fundamental understanding of the interactions and reactions involved at the atomic level.  Chemists have already risen to the occasion and have contributed significantly to materials science.  Colloid chemistry is particularly well suited for advancing materials science since:

- It has matured and has become quantitative and predictive thanks to both the vast number of new techniques being utilized and theories being developed;
- The sizes and behaviors of many advanced materials enable them to be colloidal
- Materials processing often involves reactions at solid-solid, solid-liquid, or solid-gaseous interfaces (of which the manufacturing of ceramic membranes by the sol-gel process is an obvious example);
- Colloidal aggregates have served as containers and/or templates for the generation of advanced materials;
- Most significantly, many biominerals, which constitute Mother Nature's response to advanced materials, can be considered to be colloidal systems; indeed, the mimetic approach to biomineralization is clearly centered upon colloid chemistry.

Colloid chemistry is thus pervasive to materials science and continues to make an ever-increasing contribution to the field.  Construction of nanostructured advanced materials, using modern "wet" colloidal chemical techniques, is central to our activities.  Our approach has been based on membrance-mimetic chemistry and inspired by biomineralization..  Advantage has been taken of membrane-mimetic systems to provide chemical, spatial and dimensionality control for in situ generation and stabilization of ultra-small metallic, ceramic and polymeric particulate films.  In particular, ionic self-assembly has been used to process membrane-mimetic systems.  Our system of ionic self-assembly yields nanoparticles that are incorporated into or generated in situ between the apposing head-groups of thin films.

The membrane-mimetic approach to advanced materials, adapted here, is inspired by biomineralizaiton.  Precipitation and/or cluster formation, occurring in biological cells, are nature's way of constructing teeth, bone, shells, and direction-finding equipment.  Intense efforts have been exerted for the rationalization of biomineralization in terms of known colloidal, crystallographic, and solid-state principles.  The availability of appropriate precursors in appropriate concentrations and the presence of a matrix has been suggested to determine the outcome of nucleation and subsequent particle growth.  Compartmentalization provided by membranes and cells has been considered to be responsible for the inflow of ionic precursors and for the imposition of shape and size control over the incipient crystal growth.  Proteins have been recognized as playing a paramount role in directing biomineralization.[54]  Biological membranes are intimately involved in biosyntheses, energy transduction, information transmission, and cell recognition.  They define the very existence of the cell.  The ardent desire to understand the structure and properties of membranes is not surprising.  Insight has been obtained from studies of biomembranes and their constituents, in vivo and in vitro, as well as from the examination of a variety of membrane models.  Investigation of models has led to the rationalization of many properties, including osmotic activity, phase transition, phase separation, dissymmetry, fluidity, permeability, fusion and substrate mobilities into and out of membranes.  There are, of course, no perfect models, and no single model can faithfully reproduce all of the complexities of the membrane ensemble in vitro.  A subtle, but important, difference exists between modeling and mimicking.  Modeling implies a more or less faithful duplication of the original in a scaled-down version, whereas mimicking suggests only the imitation of the essential features.  No

attention is paid in mimicking to the faithful duplication or reconstitution of cell membranes. Only the essential components of membranes are placed on the chemist's canvas. An often-quoted motto has been a caution against the slavish and needless copying of Mother Nature.[54] Substantial alteration of reaction products, rates, stereochemistries has been observed in relatively simple surfactant assemblies which mimicked aspects of the biological membrane.

The layer-by-layer self-assembly (adsorption) of oppositely charged polyelectrolytes, polyelectrolytes/nanoparticles, polyelectroltes/graphite oxide, polyelectrolytes/layered α-zirconium phosphate nanopartiles, and polyelectrolytes/clay platelets have provided an eminently suitable biomimetic approach to the construction of complex nanostructures. That any number of layers of nanoparticles (or platelets) of any composition can be adsorbed in any desired order ensures the versatility of nanolayered composite construction by the self-assembly method. Ionic self-assembly is an effective processing methodology for the emerging interdisciplinary area between supramolecular chemistry, nanobiology and nanomaterials; it is represented in Figure 3.2 by the gray section. The region of nanosructures also encloses the level of structural complexity in which life science separates from materials science, although both rely on the same molecular components. Complex properties can only be realized within a certain length scale of structured matter. Consequently, a higher level of complexity is reached by combination of smaller functional entities. However, the new properties of such an assemblage cannot be predicted form the properties of its constituents. Whereas scientists have accumulated tremendous knowledge in manipulating matter both on the levels of atoms and molecules (length scale from 0.01 nm up to 2.0 nm) and in the macroscopic world (length scale from 0.5 micrometer up to 100 m), there is very little understanding of the structures and processes occurring on a length scale of 2.0 nm up to 0.5 micrometer. This area of supramolecular aggregation and nanostructures, which also encloses the size range of prebiotic chemistry and early subcellular life, is the regions where materials science and life sciences separate. Whereas new levels of complexity in biological systems are always reached by combining smaller subunits, man has also achieved more complex systems by the combination and miniaturization of existing units (silicon technology, integrated circuits). However, the length scale of nanomaterials can hardly be addressed by making things smaller, so the creation of well defined organic nanostructures has become a challenge for materials science at the supramolecular level.[51]

Among modern technologies, the methods for preparing specially organized nanostructures are acquiring an ever growing importance.[56] Moreover, the study of the structure and the methods for obtaining such organized macromolecular assemblies is also of great importance for fundamental sciences and for better understanding of the principles of organization and self-organization of molecules into natural or designed assemblies (aimed, in the final analysis, at certain technological purposes).

Figure 3.3 compares the methods used for assembly of nanostructures with various degrees of molecular order and stability. The optimum combination of molecular order and stability of nanostructures obtained usually determines the usefulness of these technologies. The most ordered nanostructures are free-standing liquid-crystal films with a thickness of several molecular layer, but these films are very unstable. Better results are obtained if films are transferred onto substrates. Then they acquire a structure close to that of Langmuir-Blodgett films, although they can also be built by molecules of thermotropic liquid crystals. The Langmuir-Blodgett (LB) method, which allows one to obtain monolayers of amphilic molecules on the water surface and to transfer them onto substrates, is one of the most widely used techniques for obtaining films with thicknesses ranging from 50 to 5000 Angstrom. These films are studied intensely. Each year, hundreds of new articles on these studies are published. Another method that acquires a great popularity is chemical assembly of molecules obtained in specific chemical reactions between alternating monomolecular layers. A widely used method for industrial manufacturing of ultrathin films is deposition from solutions onto rotating substrates (spin coating) and thermal deposition of macromolecules onto substrates. Unfortunately, unlike the methods considered above, the latter methods do not allow one to control the molecular order in the films. Finally, there is a method for

molecular assembly due to adsorption of oppositely charged macromolecules (polyion-polyion assembly). This method provides for build-up of monolayers of various substances growing in a preset sequence on various substrates at a growth step of about 10 Angstrom. These films are characterized by a slightly lower molecular order than LB or free standing films (in particular, they are disordered in the planes of molecular layers) but have the advantage of high physical and chemical strength and easy preparation. Our work employs and expands the technology of preparation of such anostructures.
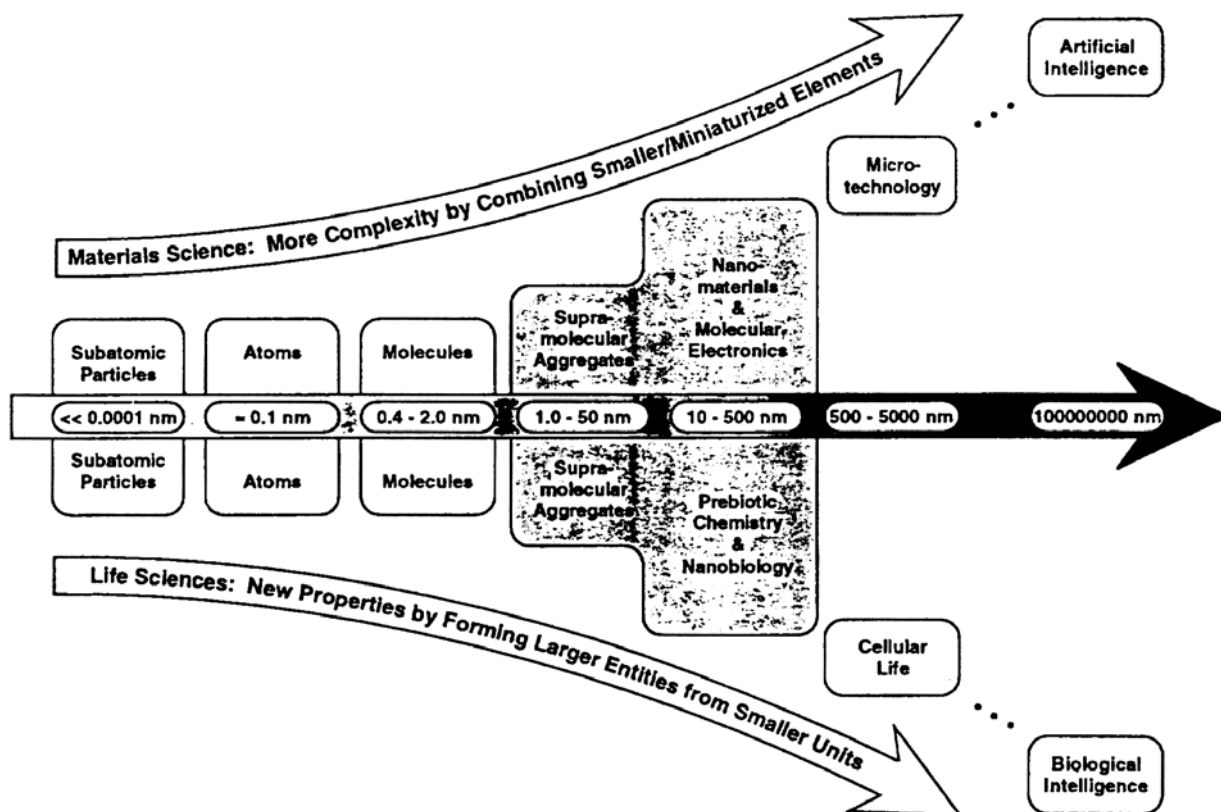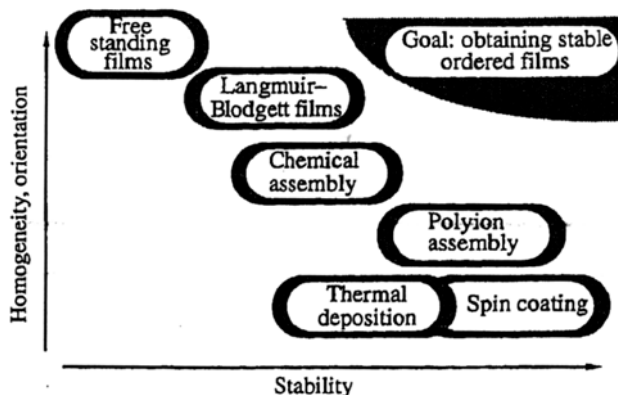


*Figure 3.2. Length Scale of Ionic Self-Assembly.*



*Figure 3.3. Comparing Various Technologies for Preparing Ultrathin Organic Films.[9]*

In assembly of nanolayers it is important to be able to control the layer sequence and individual parameters such as layer thickness, density and roughness. The most common methods for the preparation of ultrathin multilayer films have been the Langmuir-Blodgett (LB) technique and the molecular self-assembly technique, which is based on chemisorption.[51] In recent years, a self-assembly technique has been established for ultra-thin film preparation that is based on physisorption from solution and exploits electrostatic attraction between opposite charges. The key to a successful buildup of multilayer assemblies in a layer-by-layer fashion is the inversion and subsequent reconstruction of surface properties (Figure 3.4). The adsorption of a single polymer layer can modify the surface of the substrate in three different ways (Figure 3.4a). All functional groups (i.e., negative charges) are adsorbed to the surface, whose charge is not fully compensated (bottom). All functional groups of the polymer are adsorbed to the surface, thereby exactly compensating its charge (middle). All surface charges are compensated but the polymer has additional free groups exposed to the solution thus effectively inverting the surface charge (top). In this drawing, different stages of compensation were realized by variation of charge density along the polymer backbone. This was done only for the sake of simplicity; the same effects are also brought about by adjusting polymer concentration. Figure 3.4b shows schematic buildup of multilayer assemblies by consecutive adsorption of anionic and cationic polyelectrolytes (cyclic repetition of steps A and B). It is not implied that the symbols used for the polyelectrolytes represent their actual structure in solution or after the adsorption. For clarity, the counterions are omitted in this drawing, and the interpenetration of neighboring polymer layers is neglected. In order to attain a linear increase of thickness with an increase in the number of adsorption cycles, one has to find deposition conditions that match the criteria mentioned above. In the case f polyelectrolyte films, the surface charge must be reversed for every adsorption step and this is achieved by alternating the deposition of polyanions and polycations from their respective aqueous solution (Figure 3.4). Typical polymers used in fabrication of multilayers are shown in Figure 3.5. Water soluble Pre-PPV is converted to PPV through thermal treatment of the deposited system. Other polymers used in polyelectrolyte films include poly(vinylsulphate) (PVS), poly(-l-lysine) (PLL), biotinylated poly(-l-lysine) (PLB), poly(ethylene imine) (PEI), destransulphate, heparin, DNA and others.
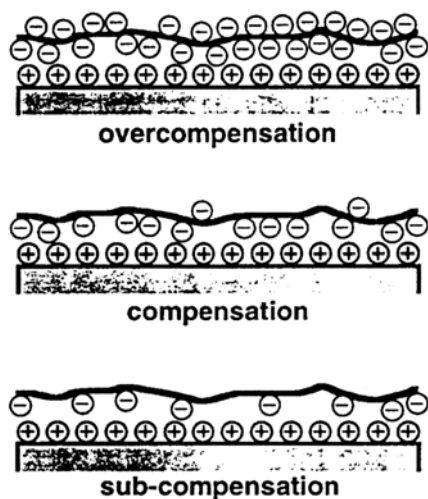


(a) Three Different Ways of Surface Modification by Adsorption of a Single Polymer Layer
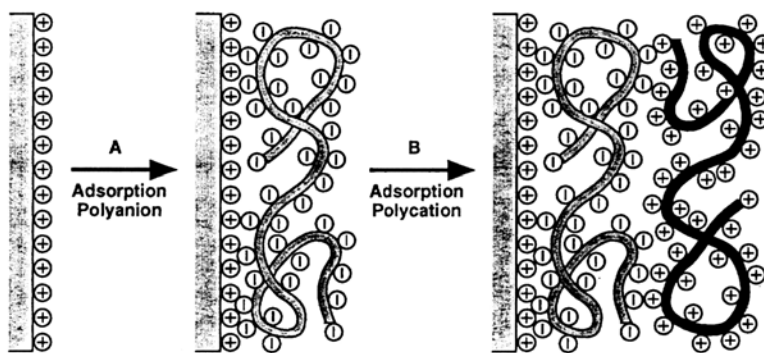
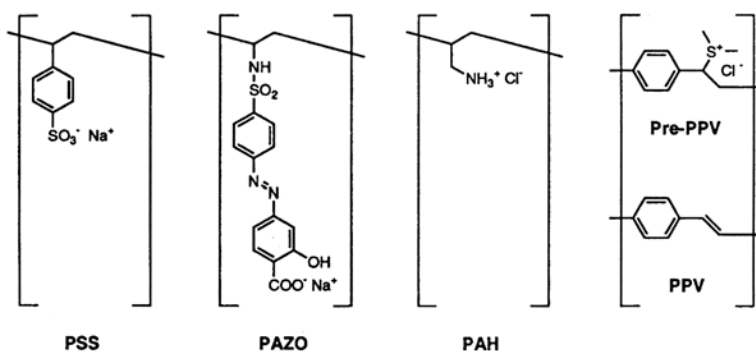(b) Build-Up of Multilayer Assemblies

*Figure 3.4.  Ionic Self-Assembly.[52]*



*Figure 3.5.  Chemical Structures of Typical Polyelectrolytes Used for Fabrication of Multilayer Filsms.[51]*

The inversion and reconstruction of surface properties, such as charge, roughness, charge density and expression of other interaction groups, can be viewed as a template controlled growth process, since the solid/liquid interface acts as a template for deposition of the very next layer.  This next layer, if adsorbed properly, will refunctionalize the surface and thus provide a new template for the adsorption of the following layer.  In the simplest case of sequential adsorption of two different compounds $(AB)_n$ this following layer restores the structure and properties of the original surface, thus allowing as many deposition cycles to be carried out as desired.  However, suitable surface properties are not the only prerequisites for successful refunctionalization.  If parameters such as polyelectrolyte concentration, adsorption time, pH, or charge density along the polymer chain are not properly adjusted, the surface functionality might be either sub-compensated, exactly compensated or overcompensated (Figure 3.4a), but only the latter provides a properly functionalized surface that allows continued growth.  It should be noted that the inversion and recreation of surface functionality does not have to be a two-step process leading to multi-layers of the $(AB)_n$ type shown in Figure 3.4b.  The only requirement for the construction of more complex architectures, such as $(ABCB)_n$ or $(ABCDEF)_n$ is that, in each adsorption step a single molecular layer mush be deposited that effectively overcompensates the previous surface functionality.

It is easy to envisage that, besides multilayers of di-, oligo-, and polyionic materials, many other materials are easily incorporated into polyanion-polycaion films.  The precision with which one can adjust the average distance between two layers of functional components makes the films interesting even for the

29

applied sciences. A tremendous advantage over other molecular deposition techniques is that no dedicated and sensitive equipment (e.g., ultrahigh vacuum apparatus or Langmur troughs) is needed and that the adsorption is carried out from aqueous solutions, which also makes the technique environmentally attractive. Therefore, a number of interesting multilayer films containing a variety of functional synthetic and biological materials have been realized. Multilayers containing DNA and biological colloids such as charged virus particles have been developed. Deposition of spherical inorganic colloids or inorganic platelets exfoliated from clay minerals is also possible. It is thought that stiff platelets might reduce the amount of interpenetration of adjacent layers. The incorporation of conducting polyelectrolytes has yielded conductivities up to 40 S/cm in a multilayer and >10 S/cm in a four-layer system. The fabrication of conducting multilayer films is now subject of major investigations, with conductivities over 300 S/cm already achieved. Polyelectrolyte multilayers can also be selectively grown on defined areas of patterned surfaces. The incorporation of polypeptide dyes and semiconductor or nanoparticles in polyelectrolyte multilayers has been reported. Fabrication of gold colloid/polyelectrolyte multilayers has also been reported.[45]

Despite a certain similarity between ionic self-assembly and chemical self-assembly (where each following molecular layer is attached to the previous one because of a specific interaction, and where a stacking fault in one of the lower layers gives rise to the avalanche-like defect formation in further growing new layers), ionic self-assembly is self-consistent. In other words, the film itself heals its defects, roughness, and other possible disturbances arising because of the introduction of any foreign particles affecting the process of film formation. The technology of ionic self-assembly allows one to design very promising molecular structures by programs that simulate possible functional use of grown system. Figure 3.6 shows the cross-section of a hybrid nanostructure combining various features provided by ionic self-assembly, and demonstrates the potential of the technology.
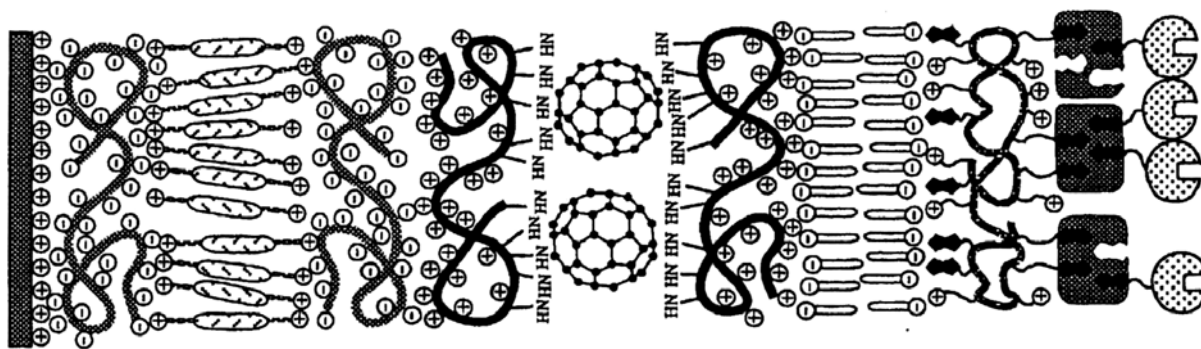


*Figure 3.6. A Hybrid Nanostructure That Can be Prepared by Ionic Self-Assembly, Comprising Polyions, Boladications, Fullerenes, Lipid Bilayers, Bioinylated Poly-L-Lsine, and Streptavidin.[56]*

Polyanion - Polycation Multilayers

The layer-by-layer adsorption of oppositely charged polyelectrolytes is a very promising approach for the fabrication of layered organic heterostructures. There are especially two facts that would make this approach interesting: (i) the ease with which one can obtain hybrid, multilayer structures; and (ii) the adsorption from aqueous solution which should allow the incorporation of charged bipolymers in a straightforward way. However, in the case of weak polyelectrolytes, one has to find polyanions and polycations whose pK values (or, in the case of proteins, isoelectric points) fit together in such a way that both polymers are sufficiently charged in order to adsorb irreversibly in a consecutive fashion. However,

let us consider what the word "layer" means in the case of a polymer at an interface before we go into the experimental details.

*What is a Polymer Monolayer?*

In contrast to monolayers of small molecules, the expression monolayer is not exactly defined in the case of polymers, since they are polydisperse materials which adopt a multitude of Guassian coils of different conformation in solution, and the situation is even more difficult at an interface (let us omit polymers with stable unique conformations such as proteins). Clearly, there are two hypothetical cases that would represent the thinnest and the thickest possible "true" monolayer of an adsorbed polymer. These would be the situations in which all polymer chains have the same length, are completely stretched out, and either adsorbed end-on (maximum layer thickness) or perfectly parallel and flat (minimum layer thickness) in a dense packing, both of which would be analogous to a "true" monolayer as in the case of small molecules.

If only a few polymer chains are attached to a unit area and the average distance between adjacent chain segments or different chains is large in comparison with the diameter of polymer chain, the resulting structures may be called "submonolayer." Starting from a coverage where the average distance between adjacent chain segments or different chains becomes smaller than the diameter of the polymer chain until the hypothetical situation in which all polymer chains are end-attached to the surface, completely extended, and densely packed, one could speak of a "monolayer." Hence, submonolayers would always be thinner than individual chains and show a substantial free surface area, and monolayers are always thicker than individual chains and have a hypothetical maximum length corresponding to the average length of the polymer in its maximum extended conformation. As a result, a multilayer composed of random coil polymers cannot exist as a structure in which individual layers can clearly be identified as blocklike tiers, simply because the surface of a polymer monolayer cannot be atomically smooth and thus two adjacent layers will always interpenetrate to some degree. Also, one can in fact prepare a "multilayer" composed of individual "submonolayers." This is possible, as long as the previously adsorbed layer exposes some of its charged groups at the film-solution interface. Then the next polymer can bind to these charges and bridge over considerable distances. The critical surface charge density must be such that there are sufficient charges on the surface for the adsorbing polymer to bind irreversibly in such a way that it itself creates a sufficient charge density for the next polyion layer to bind. All of this does not rule out that layer-by-layer adsorbed polyanion-polycation films indeed possess long-range order. It simply means that their long-range order, which is determined by the sequence of deposited materials, is not based on a periodic correlation of single atoms, but of the average segment distribution of the polymer coils. Therefore, polyelectorlyte multilayers possess structural hierarchy and represent another case (besides, e.g., lyotropic liquid crystalline phases) in which long-range (=molecular) order is present despite local (=atomic) disorder.

*Preparation, Manipulation, and Structure of Polyelectrolyte Films*

Fabrication of Polyanion-Polycation Multilayers

Multilayer suystems have been prepared in which both the anionic and the cationic layers were polyelectrolytes; the principle of layer-by-layer adsorption of polyanions and polycations was depicted schematically in Figure 3.4b. The drawing is strongly over-simplified and should only be taken as a representation of the most fundamental aspects of the process and the resulting structures. The chemical structures of the polyions poly(styrene sulfonate) (NaPSS), poly[4-vinylbenzyl)-(N,N-diethyl-,N-methyl)ammonium iodidel] (PVBDEMA) and poly(allylamine hydrochloride) (PAH) used in earlier experiments are depictd in Figure 3.7 along with the polyelectrolytes used for preparation of polyelectrolyte-containing multilayer systems.
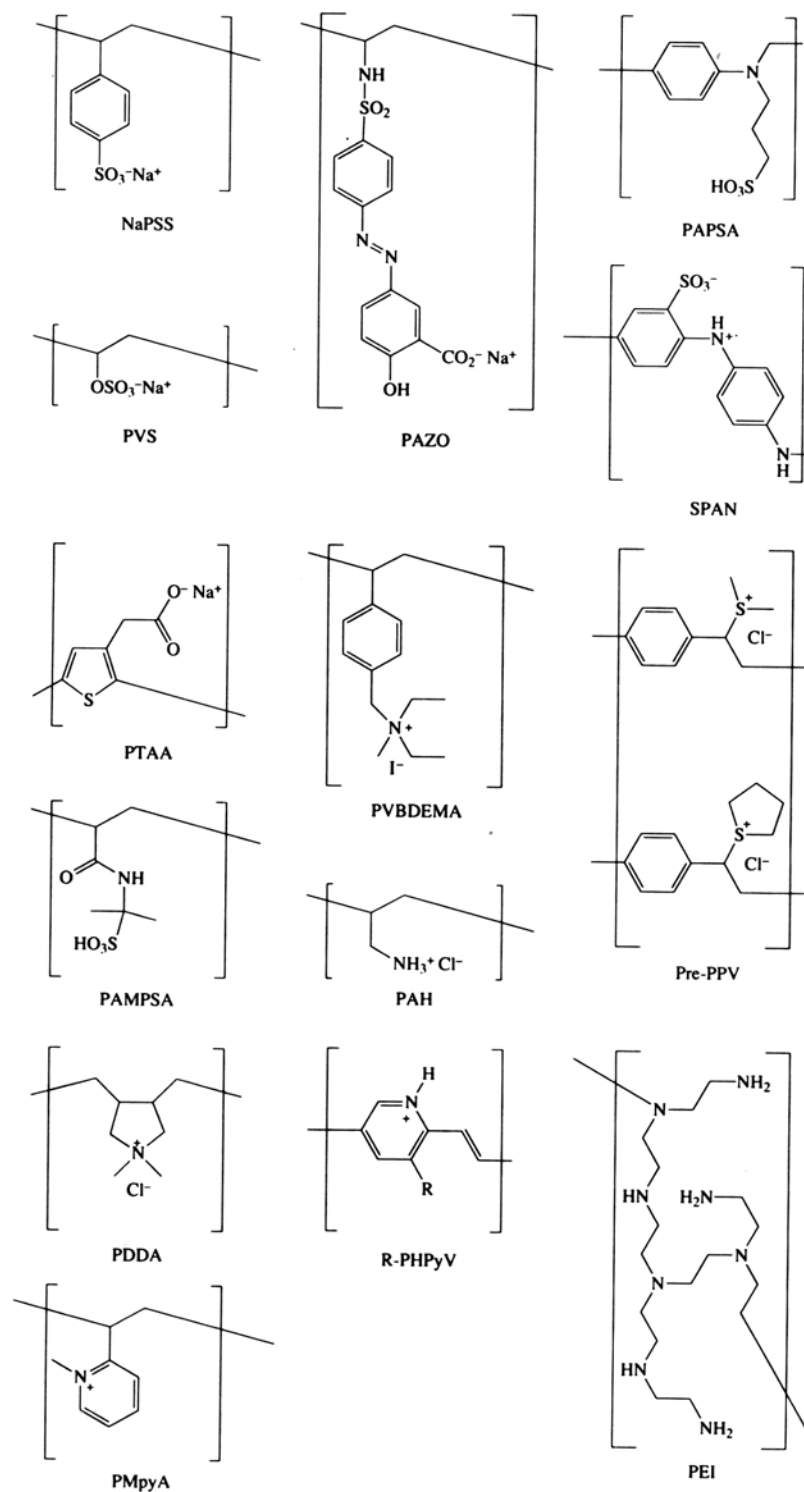
*Figure 3.7. Structure of Synthetic Polyelectrolytes Used for the Fabrication of Multilayers (there are considerably more polyelectrolytes – counterions have been omitted in some cases).*[55]

Following the general scheme of adsorption, the following conditions are common for the preparation of polyelectrolyte multilayers: adsorption solutions contain typically 2 g of polyelectrolyte per liter of ultrapure water or an aqueous solution of an appropriate salt (e.g., NaCl). Adsorption times are generally 20 min, although adsorption times of less than 1 min have also been employed. After every adsorption step, the sample is washed three times in pure water. In this way, polyelectrollyte films have been prepared composed of more than 100 layers of poly(styrene sulfonate) (NaPSS) and poly(4-vinylbenzyl-(N,N-diethyl-N-methyl)ammonium iodide) (PVBDEMA) on silicon single-crystal surfaces. Samples such as this show bright, homogeneous interference colors when viewed with the naked eye. Both polyelectorlytes contain phynyl chromophores, and their buildup on quartz substrate has been monitored by UV spectrophotometry at 225 nm up to a total of 38 layers and verified that the absorbance is linear with the number of layers (Figure 3.8). Similar results were obtained for the system poly(styrene sulfonate) (NaPSS) and poly(allylamine hydrochloride) (PAH). In the latter case, x-ray reflectivity was also registered in order to determine the increase in film thickness with increasing number of adsorbed polymer layers.
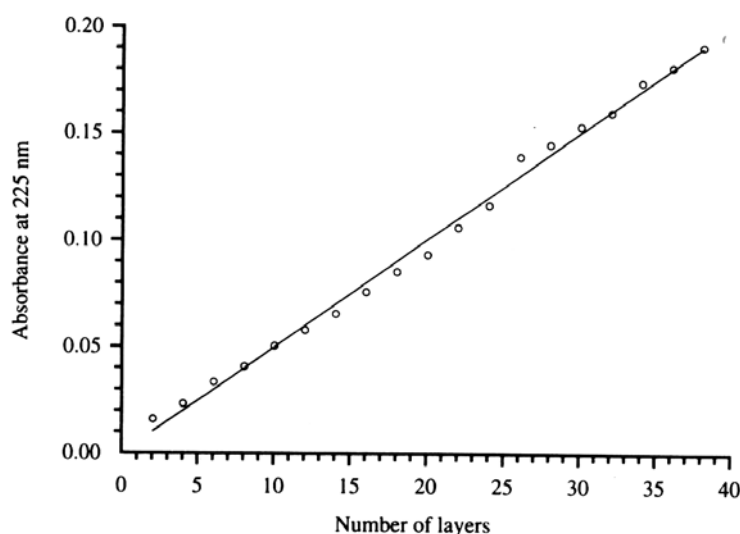


*Figure 3.8. Buildup of a Multilayer Film of NaPSS and PVBDEMA (monitored by the UV absorbance).*

Figure 3.9 shows so-called Kiessig fringes obtained by x-ray reflectivity (in x-ray scattering technique) after deposition of different number of layers. In this case, the NaPSS was deposited from a solution containing 1.0 mol/l NaCl and the PAH was deposited from pure water. The distance between the minima in the curves in Figure 3.9a allows calculation of the respective film thicknesses, which are plotted vs. the layer number in Figure 3.9b. The multilayer is composed of poly(allylamine hydrochloride) (PAH) and Sodium Poly(Styrene Sulfonate) (NaPSS); note that the curves in Figure 3.9a are linearly shifted in order to permit a better comparison of the different traces). Figure 3.9b shows the dependence of total film thickness on the number of layers for three different concentrations of NaCl in the NaPSS Solution; the triangles represent the values of the 1.0 mol/l, 1.77 nm per layer pair, thicknesses calculated from the x-ray data shown in Figure 3.9a, the circles the values of the 1.5 mol/l, 1.94 nm per layer pair, and the squares the values of 2.0 mol/l NaCl solution, 2.26 nm per layer pair; note that the PAH was always adsorbed from salt-free solution).
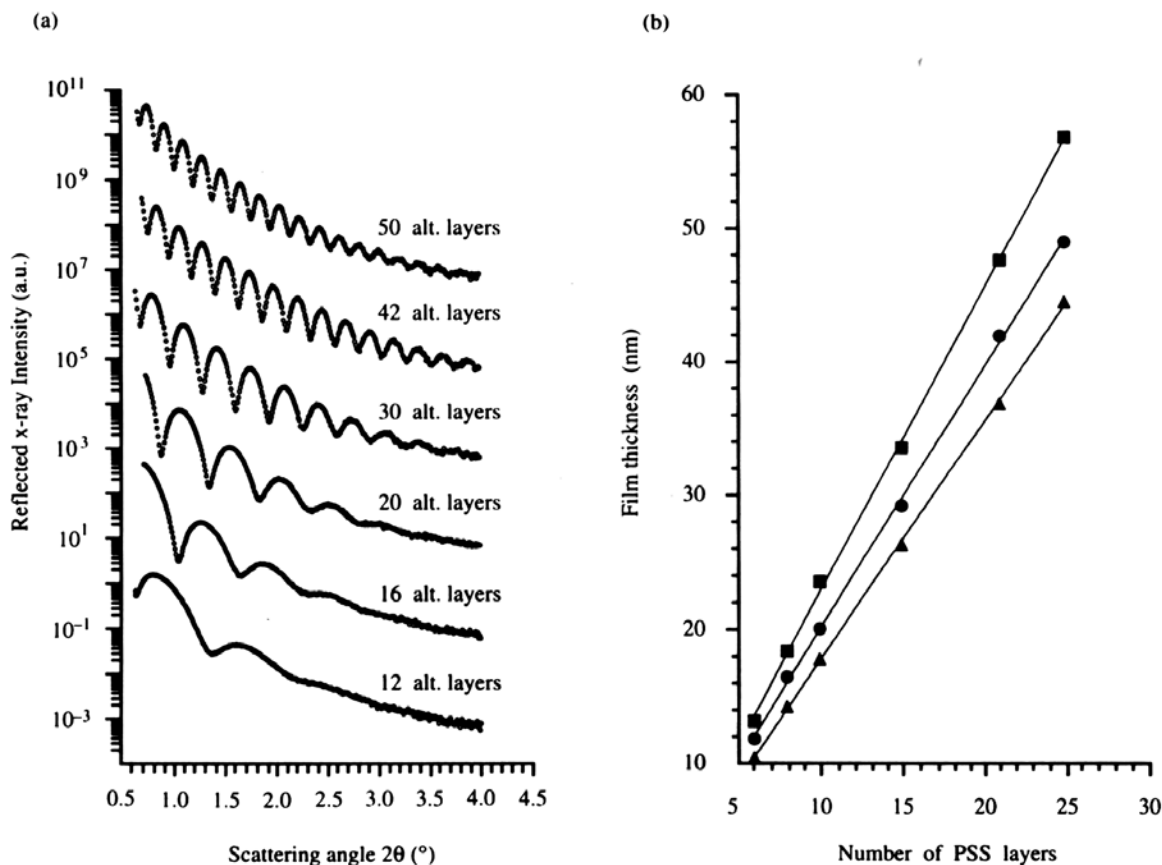
*Figure 3.9. (a) Multilayer Buildup of PAH and NaPSS; (b) Dependence of Total Thickness on the Number of Layers for Three Different Concentrations of NaCl in NaPSS Solution.[45]*

Figure 3.10 shows the schematic of molecular assembly and typical polyions used in the process. <u>First, one must charge a solid substrate. Surfaces of glass, quartz, and silicon substrates have been charged by treating them either with boladications or by applying plasma deposition.</u> As-cleaved negatively charged mica has also been used. Subsequent implementation of steps A & B in Figure 3.10a results in the formation of two layers of oppositely charged polyions on the substrate that are strongly bound to the substrate and to one another by numerious ionic bonds. Thus, the two stages above result in the formation of two layers of oppositely charged polyions on the substrate that are strongly bound to the substrate and to one another by numerous ionic bonds. The thickness increment in this cycle is called a growth step (d). The cycle can be repeated hundreds of times to increase the thickness up to the desired level. Now consider a self-assembly example involving alternating layers of poly(vinyl sulfate) potassium salt (PVS) and poly(allylamine) hydrochloride (PAA) (Figure 3.10b). Aqueous solutions of these polyions were used at a concentration of 0.01 M per liter at <u>pH 2. In an acid medium, the ionic groups completely dissociate.</u> Then the assembly was performed on glass substrates treated by boladication (glass substrates were immersed for 30 min into a solution of amphiphilic boladication. Alternating cycles of PVS and PAA adsorption were performed for 20 min each. Upon deposition of 20, 26, 32, 36, etc. molecular layers, the assembly was interrupted, and the samples obtained were dried and studied by X-ray small-angle reflectometry method. Figures 3.11a and 3.11b show the X-ray reflectivity curves obtained from the films grown at various stages of molecular assembly and calculated thicknesses of the PVS/PAA films. The reflectivity curves show oscillatioins with a period decreasing with the number of molecular layers of the film. Knowing the period of these oscillations and considering X-ray refraction, one can calculate the film thickness. It is evident that the thickness of the PVS/PAA film

increases linearly with the number of cycles of assembly; a growth step per bilayer is 13.4±0.3 Angstrom. It is much higher than the accuracy of the measured time of polyion adsorption. Moreover, even some random 3-5 min errors in adsorption times did not affect the growth step and film thickness. This indicates that the films were grown in the saturation range of polyion adsorption (here, the adsorption rate is rather high, so that a 20-min deposition is sufficient for obtaining a completely filled adsorption layer). In other words, the assembly process is self-consistent and self-regulated. Therefore, some call this process "polyion charge/charge self-assembly".
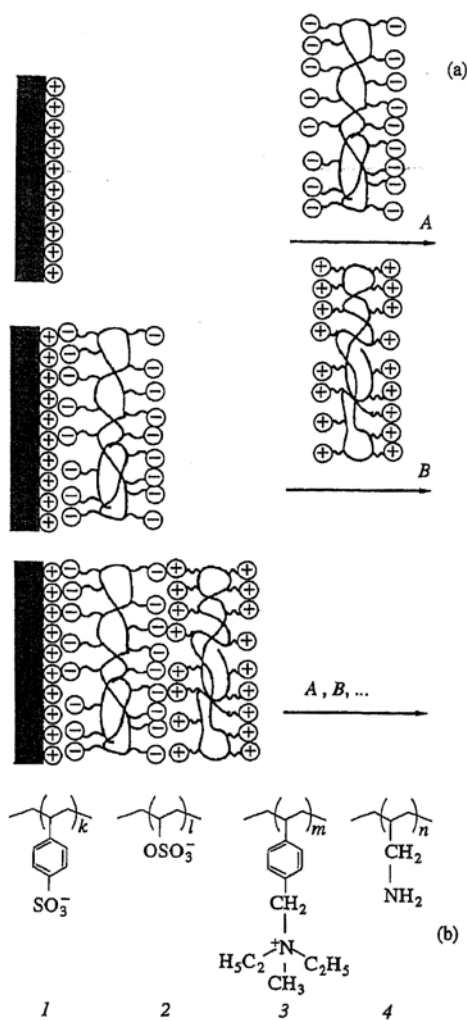


*Figure 3.10. (a) Schematic of the Build-Up of Multilayer Assemblies by Successive Adsorption: (A) Polyanion Adsorption of Polyelectrolytes Onto the Charged Substrate; (B) Polycation Adsoprtion and (AB) A Cycle of Film Growth; (b) Structure Formulas of Polyions Used: (1) PSS; (2) PVSl; (3) PVBA; and (4) PAA.[56]*
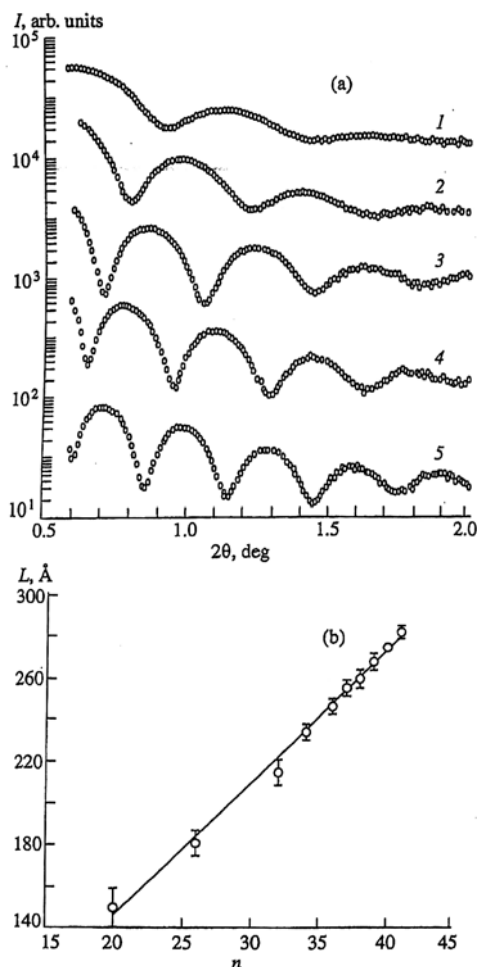
*Figure 3.11. (a) X-Ray Reflectivity Curves From Films Containing (1) 20 Alternating PVS/PAA Molecular Layers, (2) 26, (3) 32, (4) 36, and (5) 39 PVS/PAA Layers; (b) Film Thickness As A Function of the Number of PVS/PAA Adsorption Cycles.[56]*

The growth step d=13.4 Angstrom is equal to the approximate sum of the transverse dimensions of the polymer chains (see Figure 3.10b). This is typical of film assembly from polyions in solutions containing no electrolytes. Thus, for a polysterenesulfonate/polyallyamine (PSS/PAA) pair, the growth step was 10.9 Angstrom, and the the film thickness increased linearly with the number of adsorption cycles (more than 200 molecular layers were deposited). A similar linear increase of the film thickness was also observed for other alternating polycation/polyanion pairs shown in Figure 3.10b. For both PSS/PAA and ion PVS/PAA pairs, the half-steps in adsorption of each polyion were usually the same. Nevertheless, this was not always the case; there are pairs for which even an odd growth steps are different (e.g., DNA/PAA pair).

The procedure of self-assembly by alternating adsorption of charged macromolecules can depend on the pH value of the solutions and the presence of salts in these solutions, the nature of the solvents, the concentration of macromolecules and their molecular weights, time of adsorption, charge density on the substrate surface, and several other parameters. A set of these factors determines an equilibrium growth step of the film. Presently, only the effect of some of these factors on the film assembly has been studied.

The above presentation showed that the polycation/polyanion assembly provides for the obtaining of smooth homogeneous films and rigorous control for the number and alternation of molecular layers in these films. X-ray patterns from these films showed up to ten and more well-pronounced Kiessig fringes whose spacing is related to the film thickness. We also indicated the method for introducing an artificial periodicity into the films whose existence can be confirmed by recording Bragg interference reflections on the corresponding diffraction patterns. Considering multilayer films and multilayer technology of their preparation, one expects that the X-ray patterns should always show Bragg reflections corresponding to the growth step repeated cyclically dozens of times. However, in fact, all the attempts to reveal such reflections have failed. The absence of the Bragg reflections due to the growth step can be explained by several reasons. Probably, the chains of different neighboring polyions penetrate deeply into one another and become entangled, thus preventing density modulations over thickness. Another cause might be insufficient electron-density contrast between the neighboring polymer layers (having very close compositions and densities). Specially designed experiments showed that the main cause of the absence of the Bragg reflections is a low contrast between the polymer layers.

Linear Vs. Nonlinear Growth

Although all three data sets in Figure 3.9b give straight lines with good correlation coefficients for the average thickness increment of a layer pair, thus demonstrating again a reproducible refunctionalizaiton of the surface in each adsorption step, a linear relationship with the number of layers is not always observed. Imagine the case when one starts with a surface of very low charge density, which will lead to the adsorption of very few polymer chains. However, also in this case the chains will adsorb, forming "loops," "trains," and "trails," hence it is likely that, although still at submonolayer coverage, the surface charge will increase. This will continue from layer to layer until the surface charge density becomes constant and a linear correlation of the thickness with layer number is reached. Such behavior, permanently growing or shrinking of the average thickness increment per layer pair and similar surface effects (e.g., decreasing or increasing surface roughness with increasing number of layers), is indeed observed, but one can normally find conditions that lead quickly to a regular (=linear) deposition.

Salt Effects: Fine-Tuning of the Layer Pair Thickness

Figure 3.9b also shows that the average thickness increment per polyanion-polycation layer pair can be easily fine tuned with high precision, which leads to remarkable control of the film architecture, as shown in Figure 3.12. On going from 1.0 mol/l to 2.0 mol/l salt in the solution of NaPSS, one raises the average thickness per layer pair (measured through x-ray scattering) by less than 0.5 nm from 1.77 nm to 2.26 nm; the absolute precision that can be reached by adjusting the salt concentration is less than 0.1 nm. This astonishing control of individual average layer thickness is simply due to the well-known changes in the coil structure of polyions in solutions of different ionic strength. <u>At low concentrations of salt, the charged groups along the polyelectrolyte chain repel each other, the polymer adopts an extended conformation, and the chain adsorbs rather "flat." At higher concentrations of salt the repulsion of charged groups is partly screened, the polyelectrolyte conformation approaches a random coil, and the chain adsorbs rather "loopy." This behavior in solution leads to the fact that adsorbed polyelectrolyte layers are thin (~0.5 nm) if the adsorption takes place in pure water and thick (up to ~3.5 nm) if adsorbed from solutions of very high ionic strength.</u> The test data of Figure 3.12a indicates that fine tuning of the thicknesses of individual layers can indeed be used for the construction of complex architectures, even in a multilayer composed only of two materials, a single polyanion, and a single polycaiton. In this case, the polyelectrolytes NaPSS and PAH were both either adsorbed from pure water or a high concentration of salt and the resulting thicknesses per layer were 0.91 nm and 2.18 nm, respectively. That different

thicknesses per layer can be maintained in systems that have been in contact with solutions containing different amounts of salt is not trivial, as seen in Figure 3.12b. In this case, a film composed of 12 alternating layers of PAH and NaPSS, both deposited from solutions containing 0.5 mol/l NaCl, was alternately immersed for 2 h in either pure water or a solution of 0.1 mol/l NaCl. Although there is some error in the data, one generally observes that the thickness of a polyelectrolyte film increases by up to 15% when immersed in a salt solution of high ionic strength and shrinks again to about its initial value when reimmersed in pure water. The reason that two (or more) different layer thicknesses of the same material can be maintained in a single film by adjusting the ionic strength of the adsorption solution (Figure 3.12a) is simply that the effect of swelling of a polyelectrolyte film in solution of different ionic strength is only of the order of 10-15% (Figure 3.12b), whereas the thickness increment itself can be varied over a much wider range (from about 0.5 nm per layer up to about 3.5 nm per layer).
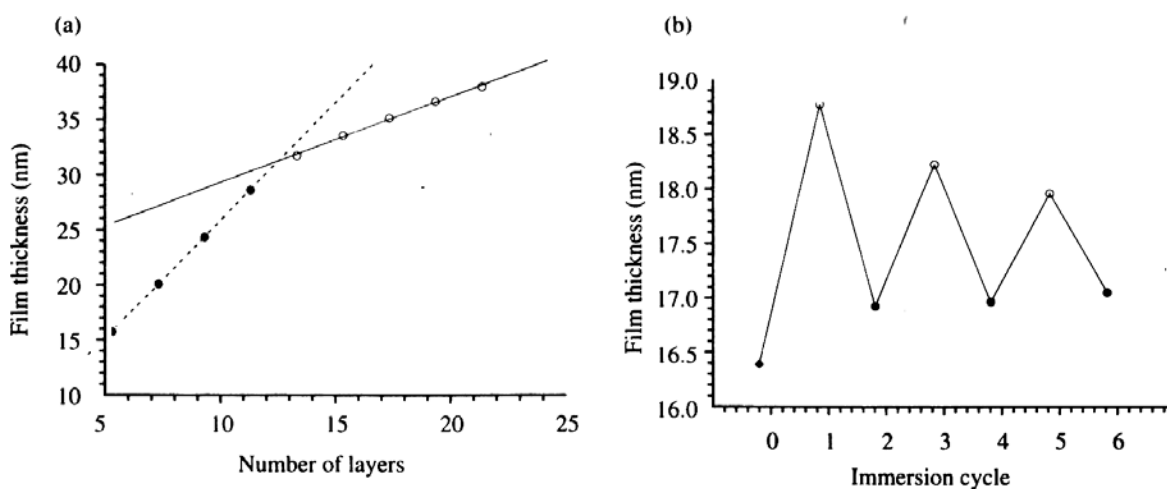


*Figure 3.12. (a) Buildup of a Two-Component (PAH-NaPSS) Multilayer Prepared With and Without Added Salt, with NaPSS adsorbed from a solution either containing salt (solid circles) or with no salt (open circles); (b) Post-Preparation increment of a polyelectrolyte Multilayer Film by 2 h Immersion in Pure Water (solid circles) and a Solution Containing 0.1 mol/l NaCl (open circle).[55]*

Temperature Effects, Reversible Changes of the Film Thickness

Although polyelectrolyte-based nanostructures have now been stored for several years, they are sensitive to certain environmental effects. Interestingly, systems composed of PAH and NaPSS can be heated to 200°C for more than 1 week without showing noticeable effects of deterioration, but they lose some water at elevated temperatures, which causes them to shrink. The effect of temperature on film thickness and surface roughness can also be followed directly, as shown in Figure 3.13. Whereas thickness shrinks by approximately 15% upon heating from ambient temperature to 110°C, roughness of the film-air interface, calculated by numerical fits to x-ray reflectivity data, stays constant. This change in film thickness is due to the loss of water and is reversible, at least in the case of PAH and NaPSS and at moderate temperatures. It should be noted that films prepared from solutions in pure water shrink less than those prepared from salt solutions. Figure 3.14a shows that polyelectrolyte lfilms that have been heated at 110°C for over 1 h return to their initial thickness (within experimental error) on equilibration at ambient conditions. It shows both experimental data and the corresponding numerical fits from which one obtains detailed information on the electron density profile of the films, equivalents of which are shown in Figure 3.14b. Both profiles are identical, given the experimental error of the two data sets in Figure 3.14a.
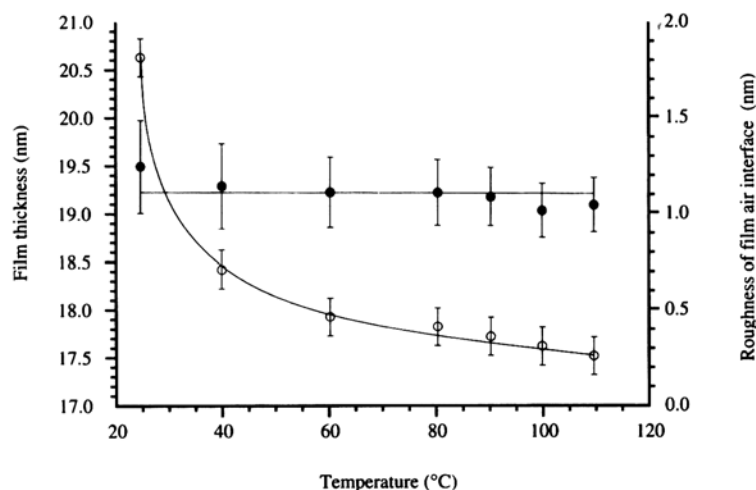
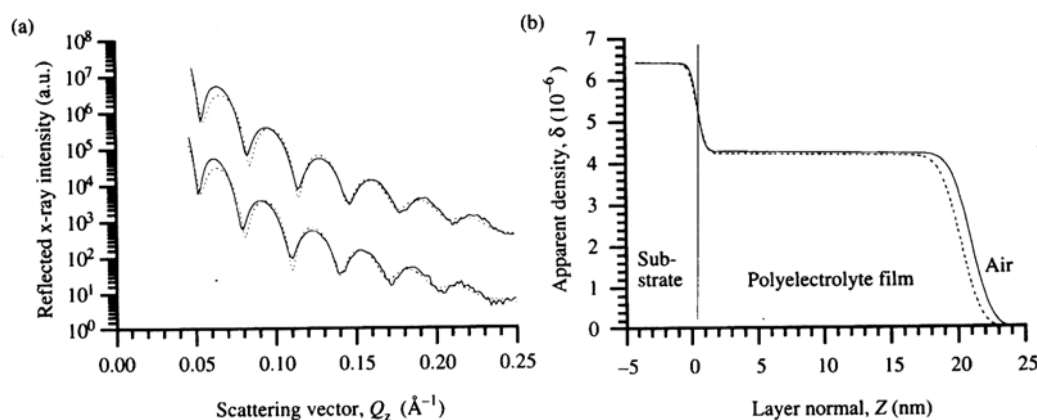*Figure 3.13. Thermal Behavior of a Polyelectrolyte Multilayer (monitored by x-ray Reflectivity).[55]*



*Figure 3.14. (a) Thermally Induced Changes in Film Thickness are Reversible (on standing in the laboratory atmosphere for some time, the original film thickness is restored): solid lines=x-ray measurements, dotted lines=numerical fits to data - before the heating experiment d=20.6±0.5 nm; (b) Apparent Film Density Profiles as Obtained From the Numerical Fits in (a) (the profiles before heating – solid line – and after heating – dotted line – are identical with respect to experimental error).[55]*

Internal Structure: Tailoring the Distance Between Molecular Sheets on the Nanometer Scale

Up to now we have only discussed structural details such as thickness and surface roughness of polyelectrolyte multilayers, and not their internal layer structure. The problem is that x-ray reflectivity is sensitive to the electron density profile of the films such as shown in Figure 3.14b. Unfortunately, the electron density differences of different polymers are only small and, as discussed above, adjacent layers penetrate into each other, thus making the small electron density gradient between the layers even more diffuse and thus difficult to observe. As a consequence, most x-ray reflectivity curves, such as those in Figures 3.9a and 3.14a or the trace at the top of Figure 3.15, show only the interferences of the substrate-film and film-air interfaces (Kiessig fringes) and no signals for the internal layer structure (Bragg peaks). Nevertheless, there are cases in which the internal structure of polyanion-polycation multilayers has been

observed by x-ray reflectivity. The fact that an internal layer structure may be present, even if x-ray reflectivity cannot resolve it, is demonstrated in Figure 3.15.

Both reflectivity experiments depicted in Figure 3.15 were performed with the same polyelectrolyte multilayer sample which was composed of 48 alternative layers of sodium poly(styrene solfunate) (NaPSS) and poly(allylamine hydrochloride) (PAH), both deposited from solutions containing 2 mol/l NaCl. The film architecture was such that every sixth polyelectrolyte layer (=every third layer of NaPSS) was perdeuterated. Due to the fact that x-ray reflectivity is sensitive to the electron density, which is identical for hydrogen and deuterium, and that neutron reflectivity is especially sensitive to the deuterium concentration, the apparent film architectures for the two techniques are different. In x-ray reflectivity the apparent layer sequence is $(NaPSS/PAH)_{24}$, yielding $120.5\pm2.0$ nm for the film thickness as derived from the Kiessig fringes, whereas in neutron reflectivity the apparent layer sequence is $((NaPSS/PAH)_2NaPSS$-$d_7/PAH)_8$, yielding $15.9\pm0.2$ nm for the layer distance of the deuterated layers as derived from the Bragg peaks. Neutron reflectivity measurements of various superlattice architectures have shown up to four Bragg peaks, indicating a well-ordered layer structure. Detailed analysis shows that layer thickness and interpenetration depend to a large extent on added salt and very little on the molecular weight of the polyelectrolytes. However, Bragg peaks have not been observed in multilayers in which every second layer was deuterated. Interestingly, a film with almost the same length of the repeat unit, but in which every fourth layer is deuterated, shows a well-resolved Bragg peak. This demonstrates again how much the structural details of polyelectrolyte multilayers can be influenced.
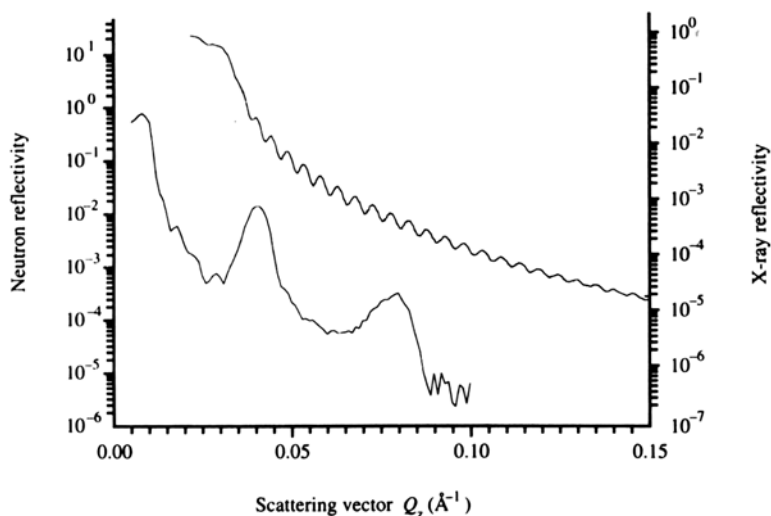


*Figure 3.15. Structural Investigation of a Multilayer Comprising 48 NaPSS/PAH Layers.*

Film Growth Close to the Substrate Surface and the Effect of Salt Additions

The growth process close to the substrate surface (the first molecular layers at a distance of up to 100 Angstrom from the surface) has some specific features. Figure 3.15 schematically illustrates the surface roughness of the PVS/PAA film calculated from the X-ray reflectometry data as a function of the number of deposited molecular layers. The roughness of the glass susbtrate used as 12 Angstrom. It is evident that, at the beginning of the process, the polyion film has a well-pronounced roughness. With an increase of the film thickness, its roughness becomes weakly marked, and by the 20th layer, the film becomes smoother than the substrate; by the 30th layer, the smoothness attains a value of 6 Angstrom, typical for films grown by this method. Figure 3.16a shows the UV absorption (proportional to the deposited

dpolyanion PSS mass) for the PSS/PAA film as a function of the number of molecular layers. One can clearly see a nonlinear segment with a reduced growth step at the beginning of the assembly (Figure 3.16b). This phenomenon was also observed in the analysis of the small-angle neutron scattering reflectometry data for other polyions. The specific structure of films close to the substrate surface is typical of ultrathin films, but presently, there is no unique interpretation of this phenomenon.
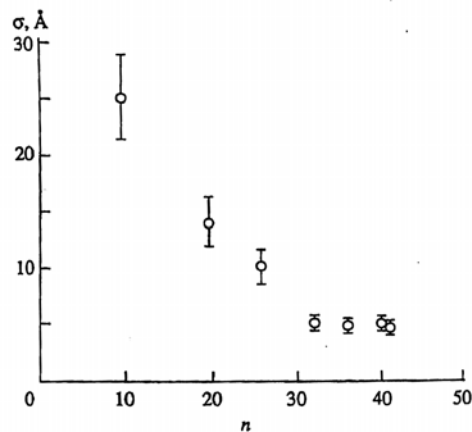


*Figure 3.15. Roughness of the PVS/PAA Film As A Funciton of the Number of Applied Molecular Layers.[9]*
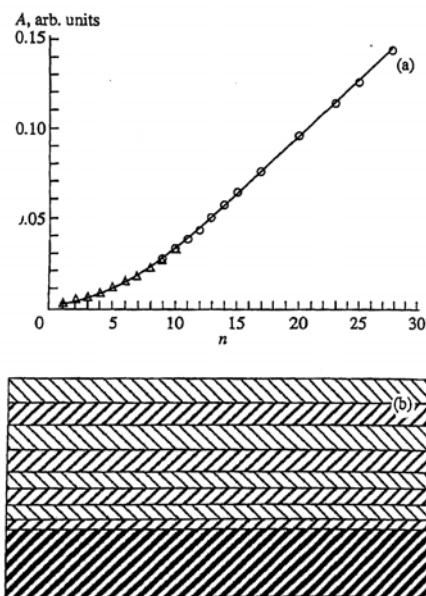


*Figure 3.16. (a) Ultraviolet Absorption At a Wavelength of 270 nm As A Funciton of the Number of Molecular Layers in the PSS/PAA Film; and (b) Cross Section of the Film (one can see reduced thicknesses of molecular layers close to the substrate).[56]*

Many samples have been deposited onto glass, quartz, or silicon substrates, preliminarily treated with boadication solutions at concentrations lower than the crucial concentration of micelle formation. A boladication molecule consists of a biphenyl nucleus with symmetrically attached (through six-membered aliphatic chain) positively charged amino groups. Thus, between the substrate and the polyion film, there is an uncharacterized boladication layer about 25 Angstrom thick whose thickness is included in the total

thickness of the gilm grown. Alternatively, a polycation has been found with a good adhesion to quartz, glass and silicon surfaces (polyethyleneimine (PEI), and can be used as the first basis layer onto which the further assembly of alternating layers of other charged molecules can be deposited in a desired sequence. In this case, a growth step for the same polymer pair at a distance of 100 Angstrom and more from the substrate surface was independent of the preliminary treatment of the substrate. Moreover, the assembly of PSS/PAA layers was performed on as-cleaved mica with a negative growth step as earlier.

Now, consider a plasma treatment of the surfaces providing further polycation/polyanion film assembly. The addition of salts to polyion solutions allows a substantial increase of the growth step (Figure 3.17a&b). The salts can be added either to one or both polyion solutions. For the PSS/PAA pair, the addition into the PSS solution of 2 M NaCl increases the growth step from 10.9 to 25 Angstrom but does not affect the film quality (surface roughness). The structure obtained is as good as in the case where these polyions are deposited from an aqueous solution (the roughness is about 6 Angstrom). Similar results were obtained when the salts of mono and divalent metals were used (NaCl, KCl, $BaCl_2$, $MnCl_2$, and $MgCl_2$). It is believed that an increase of the growth step is explained by the fact that the addition of salts leads to the formation of coils from the chains which, in turn, provides for the formation of thicker layers during adsorption. The gyration radius of a Gaussian polyelectrolyte coil in a solution increases proportionally to the square root of the ionic strength of the solution. Nevertheless, one can see from Figure 3.17 that the growth step is proportional rather to the squared ionic strength of the solution. In other words, in this case, no direct dependence of the growth step on the size of the polymer coil was observed. This result is still waiting for its interpretation. Nevertheless, the fact of possible variation of the growth step of the film seems to be very important. PSS (0.5 M $MnCl_2$)/PAA (2 M NaBr) films with a growth step of 50 Angstrom were very successfully deposited, and turned out to be very convenient for solving some problems of molecular architecture. .
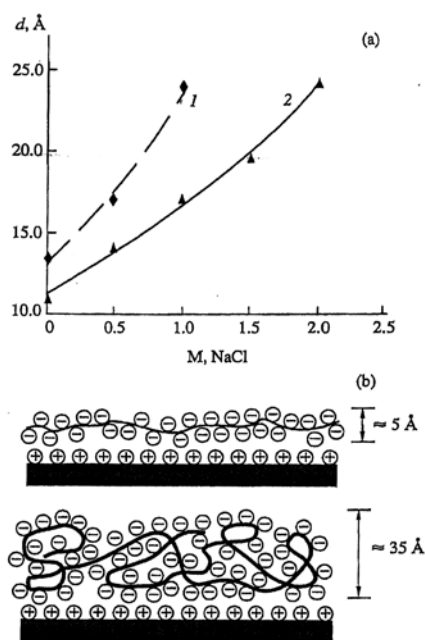


Figure 3.17. (a) Growth Step d for Various Films [(1) PVS/PAA, (2) PSS/PAA] As a Function of the Molar NaCl Concentration in the Polyanion Solution; (b) Schematic Conformation of a PSS Polyanion Adsorbed From An Aqueous Solution and From a Solution with 2 M $MnCl_2$.[56]

It is evident from Figure 3.17 that a small salt addition (less than 0.1 M) to solution almost does not influence the growth step. In other words, the technology of film assembly considered here does not

require a very high purity of the solution during the process as is the case, e.g., for the Langmuir-Blodgett or chemical assembly methods. It should also be noted that, in some cases, the addition of salts to the solutions increases not only the thickness of the saturated adsorption layer and thus the growth step, but also enhances the surface roughness and, upon two to three cycles, causes a complete cessation of the growth process. This was the case in the assembly of PVS/PAA film from the solution with more than 0.5 M NaCl in the PVS solution

Hydration and Drying of Films: Artificial periodicity induced by Drying

Despite the fact that film assembly is performed in aqueous solutions, subsequent long maintenance of the prepared film in aqueous solutions results in a 6-10% increase of their thickness (Figure 3.18). Two kinetic mechanisms can act here: (1) the mechanism with a typical 20-min long adsorption and ordering of one molecular layer; and (2) the mechanism of film swelling proceeding for 12 to 14 days. The second mechanism, swelling of films obtained from salt solutions of polyions, seemed to be more pronounced. Subsequent 7-day drying of the films at room temperature followed by 6-h holding in vacuum did not affect the film thickness. Only heating resulted in a slight and smooth variation of thickness with a more pronounced reduction at about 100$^o$C (Figure 3.19). On the whole, the decrease of the PVS/PAA film thickness within the range of 30-120$^o$C amounted to 6% and seemed to be associated with water loss during heating. In the case of slow film cooling, the film thickness remained constant, but, several days later, it acquired its initial value prior to heating. Heating and cooling of some type of films showed that they were stable at east up to 200$^o$C, whereas their thickness slightly decreased during heating.
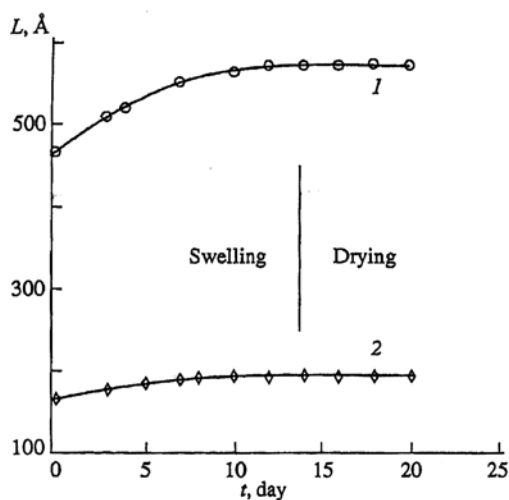


*Figure 3.18. Film Thickness L As A Function of the Duration t of Film Swelling in An Aqueous Solution and Its Drying: (1) 20 PSS (0.5 M MnCl$_2$)/PAA (2 M NaBr Layers ; and (2) 20 PSS/PAA Layers.*[56]
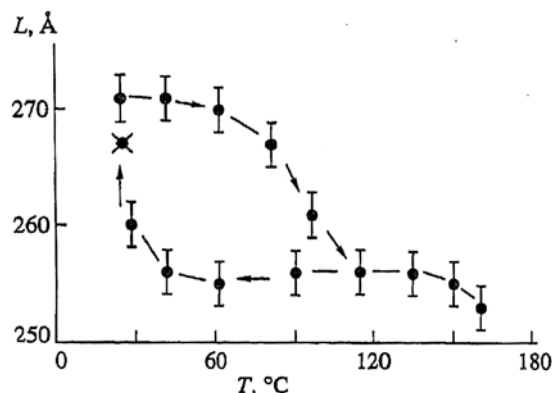
*Figure 3.19. Thickness of a PVS/PAA Film (41 molecular layers) As A Funciton of Temperature L(T) (the arrows indicate the direction of heating and cooling; filled circles denote the film thickness seven days after heating).*[56]

In one case, a PSS (0.5 M MnCl$_2$)/PAA (2 M NaBr) film was prepared with drying and making X-ray measurements on it upon each six cycles. It was revealed (Figure 3.20) that, along with an increase in the frequency of the Kiessig fringes (which is inversely proportional to the film thickness), the diffraction patterns showed Bragg interference maxima corresponding to this sixfold cyclicity. These maxima are better pronounced as the number of sixfold adsorption cycles is larger. The growth step per bilayer for the sample was 50±1 Angstrom, whereas the periodicity in the film calculated from the positions of the Bragg maximum was 150±5 Angstrom. Thus, drying changes the properties of the surface layer and, as a result, provides the formation of a periodicity. Here, two situations are possible: either the upper molecular layer somewhat shrinks during drying or drying provides a certain preferential orientation of polymer chains in the upper layer which, in turn, provides periodic variations of the electron density over the film thickness. An additional study showed that the second mechanism is more probable. Drying can also stimulate plane-parallel packing of the upper layer of polymer chains, thus preventing the mutual penetration of chain loops and ends between the neighboring molecular layers. We managed to obtain such an artificial periodicity by drying the sample after growing the 8th, 6th, and 4th molecular polyion layer. However, if the sample was dried upon the application of each second layer, no Bragg maxima were recorded. It seems that a periodicity is formed only if the depth of the mutual penetration of molecules from the neighboring layers is much less that the repetition period (which is the case for samples with large unit cells).
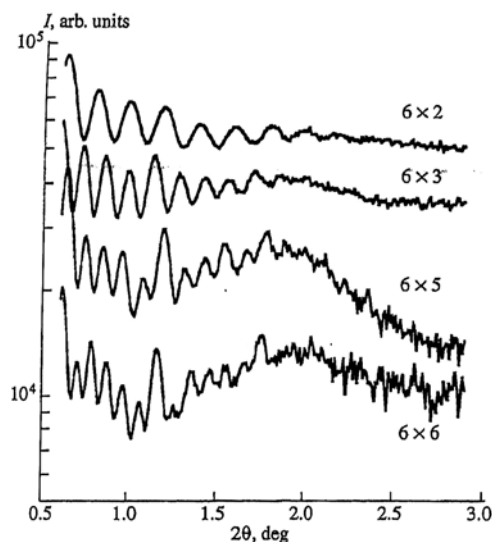
*Figure 3.20. Illustrating the Appearance of Bragg Reflection on the X-ray Reflectivity Curves for Cyclic Drying of A Sample Upon Application of Each Six PSS (0.5 M MnCl$_2$)/PAA (2 M NaBr) Layers (the number of growth cycles is indicated on the curves).[56]*

Optimization of the Assembly Process

Despite the fact that assembly of ordered ultrathin films has already been performed for many substances, the importance of process optimization is obvious. It is necessary to establish the concentration dependences, the optimum molecular weight of polyions, their kinetic characteristics, etc. Of special importance is the optimization of the charge state of polyions by varying the pH values of solutions. It has been shown that adsorption proceeds mainly for the first one to two minutes. The thickness of individual adsorbed PSS and PAA layers measured by the ellipsometric method during film assembly confirms this result. Nevertheless, the film with alternating PSS/PAA layers can be assembled only if the duration of each adsorption cycle is not shorter than ten minutes. The film assembled for a time close to this limit is of a rather poor quality and shows clearly pronounced roughness. The same also refers to the assembly of films from another pair (PVS/PAA) of polyions. For adsorption times for PVS ranging from 12 to 40 min, the ordered PVS/PAA films grew at a step of 13.4 Angstrom per bilayer (irrespective of the growth time). At shorter adsorption times, no film assembly occurred. We can assume that adsorption proceeds in two stages: at the first stage, polymer chains are anchored to the substrate; at the longer second stage, the chain packing relaxes to a denser one.

The above consideration is also true for polyion adsorption from aqueous solutions. Figure 3.21 shows the thickness of PSS/PAA multiplayer systems as a function of the number of adsorption cycles. In Curve 1, layers 1-8 represent a precursor system with the PSS/PAA alternation, and layers 9-14 were formed by the adsorption of PSS polyanions alone with the sample being dried after each deposition cycle, and layers 15-22 were formed by conventional assembly with the PSS/PAA alternation. In Curve 2 of Figure 3.21, the first eight layers were those of the precursor system with PSS/PAA alternation; altogether, five samples were prepared which were immersed for 10 min the the PSS solution, the half-time of standard 20-min cycle, the first sample for 20, the second sample for 40, the third sample for 80, the fourth sample for 100, and the fifth sample for 120 min. Thickness increased in the same way in all five casts, and it was possible to continue further assembly at a standard growth step (the right hand branch of the curve); PSS was deposited from 0.5 M MnCl$_2$ solution, and PAA from 2 M NaBr solution. If films are assembled from salt solutions (i.e., by coils), the typical adsorption times in the assembly are almost the same (Figure 3.21, Curve 2). Irrespective of the time of PSS adsorption (10, 20, 40, 80, or 120

min, i.e., from a half-cycle to six standard twenty-minute cycles), the growth step per PSS/PAA bilayer (with salt addition) is 50 Angstrom. Curve 1 in Figure 3.21 demonstrates specific features of deposition from salt solutions. Upon the tenth assembly cycle, the PSS polyion was adsorbed for 20 min, and then the film was dried to measure its thickness. The thickness increased by 40 Angstrom. The sample was immersed again into the PSS polyanion solution to be held there for twenty minutes; then it was dried again to measure its thickness, which increased by 30 Angstrom. The procedure was repeated again and again. Only upon total 120-min adsorption with periodic drying of the film did the process attain its saturation. Altogether, the film thickness increased by 100 Angstrom. This seems to be inconsistent with the independence of the growth step of the adsorption time during alternating polyion assembly (Curve 2, Fiugre 3.21). However, the measured surface potential of the film with the upper PSS layer showed that the surface charge of the films was substantially reduced during several-minute of film drying. This seems to be the cause of a new adsorption process observed when the dried sample was immersed into the PSS solution. This data recalls the packing relaxation with the formation of an artificial periodicity due to cyclic film drying discussed above.
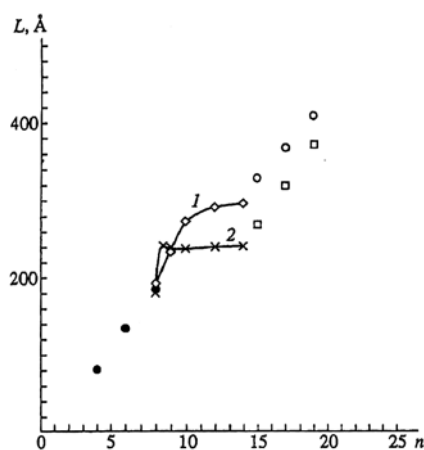


*Figure 3.21. Thickness of a PSS/PAA Film As A Function of the Number of Adsorption Cycles.*[56]

The data on the dependence of the growth step on the polyion concentration in solution is inconsistent. On the one hand, PSS (0.5 M MnCl$_2$)/PAA (2 M NaBr) films were grown from PSS solutions at concentrations of 0.1, 0.02, and 0.004 mole per liter and at a stable growth step of about 50 Angstrom per bilayer. A further four-time lowering of the PSS concentration (down to 0.001 M) resulted in the cessation of film growth (the thicknesses were controlled by X-ray reflectometry measurements). On the other hand, the studies performed for the poly-(Thiophen-3-acetate acid) (PTTA) and PAA pair showed an increase in the growth step from 10 to 19 Angstrom with an increase of the PTAA concentration from 0.0005 to 0.007 M (the ellipsometric data).

Various solvents were also investigated, including water/glycerol mixtures with 20, 30, and 50% glycerol. The assembly was steady-state, and the growth step for the PVS/PAA and PSS/PAA pairs increased by more than two times in this range in comparison with the growth step observed for the same polyions deposited from aqueous solutions. Thus, the addition to the PSS solution of 50% glycerol provided a 26 Angstrom growth step for the PSS/PAA system (this can also be attained by adding 2 M NaCl to the PSS aqueous solution). Thus, the change of solvent increases the method potential.

The pH values of the solutions could also be optimized. It is clear that the choice of pH is dictated by striving to attain the maximum degree of dissociation within the chemical conformational stability of a

macromoleclule (because the assembly was more efficient at pH ranging from 5 to 6 for some polyanions).

Self-Assembly of Heterostructures

Alternation of two oppositely charged polyions constitutes the basic step in self-assembly. It is also possible to use several polycations and several polyanions, and deposit them in any desired sequence to obtain layers of various substances. In self-assembly of alternating molecular (PSS/PAA/PVS/PAA) layers, the growth step per four molecular layers was equal to the sum of the growth steps in the films grown independently with PSS/PAA and PVS/PAA alternating layers, 13.4+10.9=24.3 Angstrom. Figure 3.22 shows the dependence of thickness on the number of molecular layers. The first twelve deposited layers were alternating PSS (0.,5 M $MnCl_2$) and PAA (2 M NaBr) layers; the growth step was 50 Angstrom. Beginning with the thirteenth step, we used aqueous PVS and PAA solutions and deposited ten more alternating molecular layers. It was evident that the change of materials did not change the linear increase in thickness, but the growth step per bilayer for the given pair of polyions slightly increased (up to 14.5 Angstrom). One can see an intermediate interval of about two molecular layers with thicknesses approximately equal to the averaged value of the growth steps at neighboring segments. We already indicated that polymer chains from neighboring layers can interpenetrate one another, but one can also see here that the film blocks are separated by at least two molecular layers having intermediate properties.[9] This experimental observation has been used to develop a method using a precursor film. Standard solutions of polyions were prepared that provided appropriate large growth steps (e.g., PSS 0.5 M $MnCl_2$/PAA 2 M NaBr; d=50 Angstrom). For reliable X-ray control, the thickness on substrate should exceed 100 Angstrom. We will indicate that, only at this film thickness, the properties and roughness of the substrate stop affecting the film properties, whereas X-ray reflectometry allows one to control the change in film parameters within an accuracy of 3-5 Angstrom. Therefore, when studying new substrates, we often performed their adsorption onto precursor films having a thickness of about 150 Angstrom and only then controlled the layer assembly and film roughness. The attempts to grow a new film without a precursor film would result in too small a growth step, and, only after several days of assembly, would it be clear if we had chosen correctly. If, for some reason, adsorbed layers had pronounced roughness, then 20-30 cycles of deposition necessary for attainment of a desirable thickness would deteriorate the surface smoothness necessary for X-ray control. Therefore, in many instances, we had to prepare a well-characterized 150-Angston-thick precursor film and then proceed to the main assembly. We used a precursor film dozens of times but only once observed a phenomenon that brought us to the idea of possible separation of a film or its part from the substrate (Figure 3.22b). In one experiment, we deposited first 12 PSS/PAA layers (with salt addition) and then 10 PVS/PAA layers (without salt addition) with a simultaneous control of two linear-growth segments. Then we made an attempt to continue the initial-type growth using the PSS/PAA pair with salt addition. Immediately after the first adsorption step, the second film block consisting of PVS/PAA is split off. In other words, the film splits along the interface between PSS/PAA blocks (with salt addition) and PVS/PAA blocks (without salt addition). Splitting of a polyion complex into individual blocks seems to be promising for further development of the technology under consideration. A similar competing reaction in the interpenetrating complexes for bulky samples has been considered.
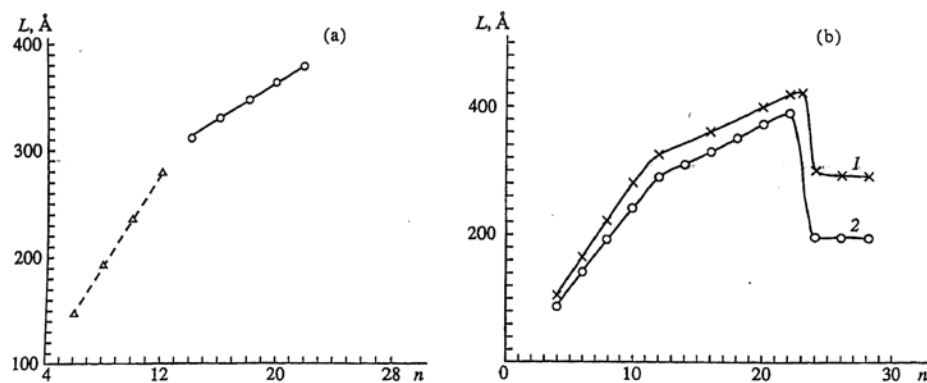
*Figure 3.22. Film thickness Versus Number of Adsorption Cycles: (1) (1-12( Alternating PSS (0.5 M MnCl₂)/PAA (2 M NaBr) and (13-22) PVS/PAA Layers; (b) (1-12) Alternating PSS/PAA Layers (with salt addition); (13-22) Alternating PVS/PAA Layers (without salt addition), and (22-28) adsorption PSS/PAA Cycles (again with salt addition); salts used: 0.5 M MnCl₂ and 2 M NaBr.*[56]

## Substrate Preparation:  Plasma Deposition Plus Self-Assembly

Looking for a universal method for charging a surface with an arbitrary shape of any area and for a material that can be used in further self-assembly, substrates have been treated by plasma of various gases (argon, oxygen, methane, polysiloxanes).  This treatment was performed in an LE-301 plasma reactor at a discharge radio frequency of 13.6 MHz by a plasma with a microwave frequency of 2.45 GHz.  The reactor allows homogeneous treatment of substrates in various modes to grow solid-state films of thicknesses ranging from several angstroms to hundreds of angstroms.  The gas pressure was about 0.01 mbar, the power of the radio frequency radiation was 98 W, the power of the microwave radiation was 600 W, and the treatment time did not exceed 15 min.

Treatment of glass and quartz substrates by argon plasma revealed no changes in the substrates (X-ray reflectometry data).  Treatment with oxygen and oxymethylsiloxane and methane plasmas resulted in deposition of thin (10-800 angstrom) solid films on the substrates.  All attempts to continue assembly by alternating polycation/polyanion (PAA/PSS) adsorption immediately upon plasma treatment failed.  Only the treatment in the polysiloxanes plus the final treatment in oxygen plasma with subsequent immersion of sample into PAA polycation solution (2M NaBr) resulted in formation of a 50-angstrom-thick polymer film on the substrate, but no further film assembly occurred.

Success was achieved by using the following scheme: alternating short treatment in oxygen plasma and then in the plasma of the methane-argon mixture plus a short final treatment in oxygen plasma.  Depending on the treatment time (1, 3 and 5 min), deposition of carbon films with thicknesses ranging from 50 to 400 angstrom was observed.  The oxygen treatment was used to provide an oxidizing reaction to form a negative surface charge (Figure 3.23).  Then the assembly was performed beginning with a positively charged PAA polycation (2 M NaBr).  In all cases, a steady-state growth of a polyion film was observed.  The growth step was 50±2 angstrom (a conventional value for these solutions).
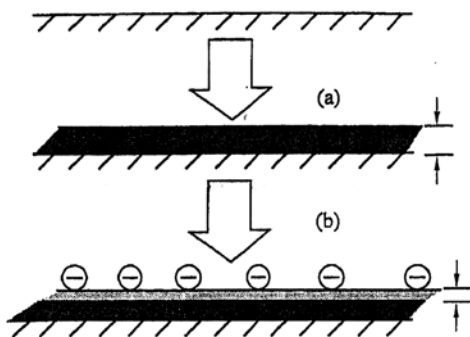
*Figure 3.23.  Stages of Plasma Deposition of Films Onto a Substrate: (a) From Methane Plasma; and (b) Subsequent Short Treatment of Film in Oxygen Plasma Providing the Formation of a Negatively Charged Surface Layer Used for Successive Deposition of the PAA Polycation.*[56]

Figures 3.24a & b show X-ray reflectivity curves and the calculated electron-density profiles of the films corresponding to the successive stages of heterostructure assembly.  A 380—angstrom-thick carbon film was assembled on the glass substrate.  On top of this film 4, 6, and 8 PAA/PSS layers were deposited (100, 150, and 200 angstrom thick).  A heterostructure consisting of carbon and organic layers was thus obtained.  It is this two-block structure than provided the beatings observed on X-ray reflectivity curves characteristic of optical experiments but never observed earlier in the range of X-ray wavelength.[56]  It is understandable because it was impossible to obtain ordered heterostructures with alternating inorganic and organic layers in the range of dozens of angstroms (the so-called nanocomposites).

The above modes of substrate treatment are universal, i.e., can be applied to any material chosen for subsequent self-assembly.  A carbon sublayer can be made rather thin (a 30-angstrom-thick sublayer has been used successfully); it will produce no effect on the properties of a formed nanocomposite.  This result offers new possibilities for modifying textile fibers or adsorbent by plasma treatment with subsequent controlled growth of macromolecular layers on fibers or in pores.
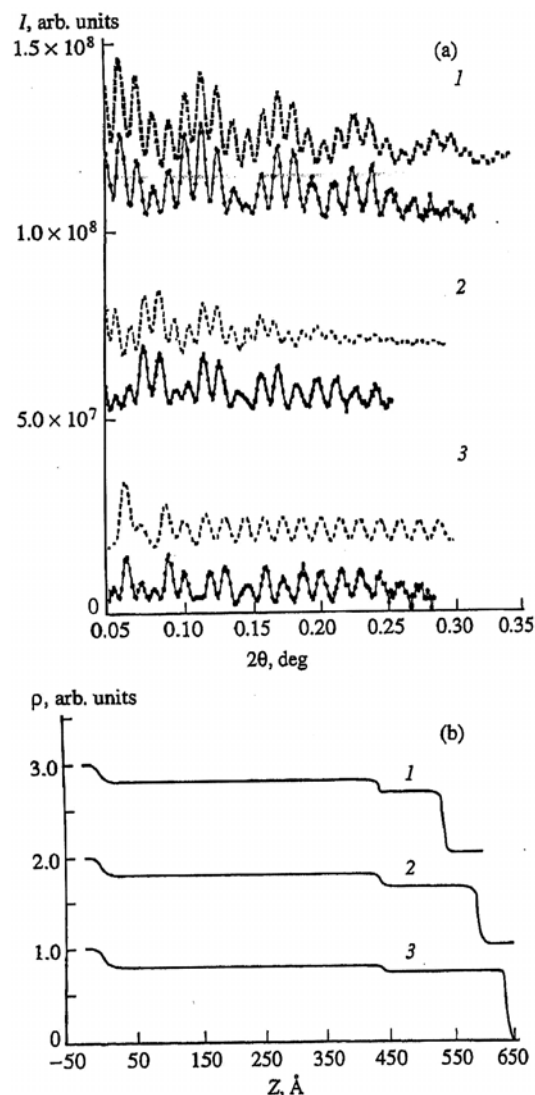
*Figure 3.24. (a) Experimental Values of X-Ray Reflection Intensities From a Nanocomposite Film (solid lines) and The Calculated Curves (dashed lines) Corresponding to the (b) Electron-Density Profiles Obtained at Successive Stages of Film Assembly: (1) Carbon Film + 4 PSS/PAA; (2) Carbon Film + 6 PSS/PAA; and (3) Carbon Film + 8 PSS/PAA (all polyions were deposited from salt solutions).[56]*

*Self-Assembly of Colloids into Nanostructured Materials*

The Colloid Chemical Approach to Nanostructured Materials

Colloid chemistry is particularly well suited to synthesis of advanced materials with enhanced or novel properties. This is because nanoparticles are, by definition, colloidal, and also because processing of advanced materials involves reactions at solid-solid, solid-liquid, or solid-gaseous interfaces. Advanced materials can be constructed from appropriately selected subunits by means of well understood chemical and colloid-chemical principles. Moreover, colloidal aggregates have served as conainers and/or templates for in situ generation and subsequent stabilization of many nanoparticles. Most importantly, utilization of a vast number of new characterization techniques and progress in theoretical descriptions have rendered colloidal chemistry to be a mature and quantitative science.

50

The construction of nanostructured advanced materials, using modern "wet" colloid-chemical techniques has been based on membrane-mimetic chemistry and inspired by biomineralization. Advantage has been taken of membrane-mimetic systems to provide chemical, spatial, and dimensionality control for the in situ generation and stabilization of ultra-small metallic, semi-conducting, and magnetic particles and particulate films. For example, reversed micelles, surfactant vesicles, bilayer lipid membranes (BLMs), monolayers, Langmuir-Blodgett films, cast and self-assembled films, lipid tubules, and other related hosts have been used as membrane-mimetic systems. Three categories of nanostructured systems are particularly highlighted (Table 3.1). Nanocrystalline particulate films, in situ grown under monolayers floating on aqueous solutions and subsequently transferred to solid substrates, represent the first system. The second system involves dispersing a range of particles, rendered hydrophobic by surfactant coating, on aqueous solutions in a procedure analogous to Langmuir monolayer preparation. The inter-particle distances are controllable and the film may be readily transferred to solid substrates. Nanoparticles, incorporated or generated in situ between the opposing headgroups of this films, constitute the third system. The preparation of oriented crystal systems is a particular challenge in the production of advanced materials. Epitaxial crystal growth, as it occurs within these three principal categories, is important.

*Table 3.1. Nanostructured Systems.*[49]

| System I<br>Langmuir Monolayers | Non-expitaxial crystal growth under monolayers. Chemical and electrochemical generation of nanoparticulate films.<br>CdS, ZnS, PbS, CdSe, PbSe, Ag, Au. |
|---|---|
| System II<br>Monoparticulate Films | Epitaxial crystal growth under monolayers.<br>PbS, PbSe, CdS |
| System III<br>Thin Films | Nanoparticles between LB films.<br>CdS, CdSe, Ag<br><br>Nanoparticles in self-assembled films.<br>CdS, $TiO_2$ |

The benefits of a colloid-chemical approach are manifold. The method is relatively simple, convenient to scale up, inexpensive, and highly versatile. It permits preparation and characterization in solution, at interfaces, and in the solid state, as well as transfers between these phases. This considerably extends the range of possible chemical and physical manipulations and allows characterization at molecular level with the armory of techniques that are available to chemists. Indeed, the chemical understanding, obtained from initial investigations, has been fueling the construction of new generations of ever more sophisticate nanostructured materials. We can confidently look forward to the development of novel nanostructured devices that are based on imaginative colloid-chemical preparations.[2]

Genesis of Wet Colloid Chemical Self-Assembly

Nanosized or nanostructured materials have dimensions, as their name implies in the 1-100 nm range. It is at this size regime that many recent advances have been made in biology, physics, chemistry, and material science. Nanostructured materials are synthesized in nature by a process known as biomineralization (the in vivo formation of inorganic crystals and/or amorphous particles in biological systems). Biomineralization is believed to be mediated by proteins acting as templates at membrane interfaces. Most naturally occurring nanostructured materials are hierarchically organized materials. This term implies an organization of materials in discrete steps, ranging from the atomic to the macroscopic scale, for optimal overall performance. The structure of abalone shell is a good illustration of a "brick-

and-mortar" hierarchial architecture.  Calcium carbonate (aragonite) bricks are bonded by soluble acidic proteins and polysaccharides (i.e., the mortar) which are present in the abalone wall.  This "brick-and-mortar" construction imparts a great deal of structural strength to the shell while reducing cracking.  The potentials of nanostructured materials are tremendous;[1] exploitation of these potentials will open the door to broad applications of these materials in diverse engineering fields.

Colloid chemists have traditionally dealt with dispersed particles, usually in the micrometer to submicrometer range.  More recently, their attention has focused upon nanometer regime.  The construction of nanostructured materials by "wet" colloid chemical methods has been inspired by mother nature's organizational ability.  The term self-assembly implies the spontaneous adsorption of molecules or of nanoparticles, in a monoparticularly thick layer, onto a substrate.  Self-assembled multilayer films are formed by the adsorption of subsequent monolayers of molecules or nanoparticles.  The evolution of self-assembled layers of molecularly nanostructured materials can be traced, at least conceptually, from simple surfactant monolayers and multilayers, through their more complex particulate analogues to the self-assembly of simple molecules and larger particulates.

Molecular level organization of surfactants has been investigated for more than a century.  Irving Langmuir and Katherine Blodgett demonstrated in the 1930s that compressed monolayers of surfactants could be transferred, layer-by-layer, onto solid substrates to form ultra-thin stable films, which are now referred to as Langmuir-Blodgett films.  These films can have properties which are not exhibited by individual monolayers.

The recognition of the potential of molecularly organized films as advanced materials has fueled the renaissance of this area in recent years.  These developments have led to the construction of self-assembling monolayers (SAMs) which obviate the need for surfactant compression in a Langmuir balance but require strong chemical interactions to anchor the appropriately functionalized surfactant to the well-cleaned substrate surface.  Self-assembling of multilayers of surfactants was accomplished by sequential steps of: (i) adsorbing thiol (or dithiol) surfactants, terminally functionalized either prior or subsequent to the adsorption, onto the coinage metal surfaces; (ii) chemically linking the second layer of functionalized surfactants to the anchored monolayer; and (iii) repeating step ii by the desired number of times.[48]  The construction of monolayered and self-assembled films has not been limited to surfactants.  The methodology has been extended to larger molecules and, indeed, to supramolecular assemblies.  Thus, Langmuir films have been formed from fullerenes, polyelectrolytes, polystyrene microspheres, silylated glass beads, and surfactant-coated metallic, semiconductor, magnetic and ferroelectric nanoparticles.  The self-assembly of supramolecular systems can be traced to the reported adsorption of negatively charged colloidal silica, or polystyrene latex particles, onto a cationic surfactant modified surface.  The adsorbed anionic colloidal particles have been shown, in turn, to adsorb a mono-particulate layer of positively charged colloids which, then adsorbed negatively charged colloidal particles from their dispersions.  Repeated adsorptions, rinsing, and drying of negatively and positively charged colloidal particles results in the buildup of films, consisting of desired number of mono-particulate layers.  Subsequently, oppositely charged polyelectrolytes and clay platelets have been self-assembled onto solid substrates.

It is instructive to compare and contrast nanostructured films prepared by the Langmuir-Blodgett technique and those formed by self-assembly.  Although both methods yield molecularly (or supramolecularly) organized films, the two dimensional compression of monolayers (or monoparticulate films) on the water surface permits a better organizational control of the LB films than that obtainable for the spontaneously self-assembled films (see Table 3.2).  Self-assembly is much more versatile, however.  A greater variety of molecules and supramolecular assemblies can be self-assembled than compressed into stable monolayers.  Furthermore, no special film balance is required for self-assembly; indeed, the method has been referred to as a molecular beaker epitaxy.  Appropriately selected oppositely charged materials are held together by strong ionic bonds and thus form long-lasting and stable self-assembled

films which are often impervious to solvents. In contrast, LB films are less stable since they are maintained by weak van der Waals interactions. They are caused by impurities and by the presence of boundaries between different domains of the substrate and of the film-forming materials. Properties of LB and self-assembled films are summarized in Table 3.2. Films can, of course, be prepared by alternating the LB technique with self-assembly for the deposition of any single layer material and any desired order.

Table 3.2. Properties of Langmuir-Blodgett and Self-Assembled Films.

|  | LB FIlm | Self-Assembled Film |
|---|---|---|
| Film-Forming Material | Subphase insoluble (usually surface active) materials which can be compressed two-dimensionally. | Any charged material which has the appropriate adsorption-desorption properties. |
| Preparation Method | Monolayers, compressed in the film balance, are transferred by repeated substrate dipping and withdrawal (X-, Y-, or Z-type deposition). | (i) Prepared substrate immersed in dispersion containing charged materials for a time optimized for adsorption; (ii) withdrawn substrate rinsed and washed; (iii) i and ii repeated for oppositely charged materials for the desired number of times. |
| Thickness, Area | Determined the thickness of the monolayer and the number of layers deposited (>300 layers reported), area is limited by the deposition equipment. | Determined the size (usually diameter) of the material and the number of layers deposited (50 layers reported), no deposition equipment is needed, thus there are few practical limitation to area. |
| Forces | Weak van der Waals interactions. | Strong ionic or coordinative bonds. |
| Order, Stability | Good layer-to-layer separation and two-dimensional order, pinholes and imperfections (decrease with thicker films), limited long-term mechanical stability in air, water and some polar solvents. | Some intermingling of layers, pinholes and imperfections (decrease for thicker films), good long-term mechanical stability in air, water and some polar solvents. |

The understanding of colloid and surface chemistry is an essential requirement for the construction of self-assembled nanostructured materials. Some key issues include the colloid and surface chemistry of stable monodisperse nanoparticles, their self-assembly into solid substrates, and the properties of the liquid adsorption layer developed at the interface of self-assembled nanoparticles in liquid mixtures. Examples of self-assembled systems incorporating colloids include alternating layers of polyelectrolyte-semiconductor nanoparticles, polyelectrolyte-exfoliated clay platelet-semiconductor nanoparticles, and polyelectrolyte-graphite platelets. While electrodeposition cannot strictly be called self-assembly, many of the recent advances in constructing chemically modified electrodes and depositing nanometer-scale layered structures by puling the applied potential during deposition are relevant to the present review.

Membrane-Mimetic Processing of Ceramic Colloids

Ceramics are made by firing non-mdetallic inorganic solids at a high temperature. The term "ceramic", originating from the Greek Keramikos, means potter's earth. Indeed, the birth of our civilization was heralded by the appearance of pottery. In the broader sense, traditional ceramics include such diverse materials as concrete and cement, in addition to fired clay products such as porcelain, pottery, tiles, and bricks. Advanced ceramic materials have been exploited in high-temperature, light-weight engines and high-temperature nuclear reactors; as heat shields in satellites; as insulators, semiconductors, superconductors, and optical and electro-optical components; and as ultra-fine fibers, artificial bones, and membranes. Their selection for these applications derives from such characteristic properties as hardness and lightness, as well as their resistance to wear, corrosion, and abrasive chemicals, even at high temperatures (1500°C or higher). However, they are also associated with such disadvantages as brittleness and low tensile strength. These problems have been overcome by embedding ceramic particles in a secondary matrix and thereby creating, for example, ceramic-metal (cermet) and ceramic-polymer (creamer) composites. Traditional ceramics are derived from naturally occurring clay minerals, silicates

and oxides. In contrast, advanced ceramics are obtained synthetically from chemicals or from highly refined, naturally occurring materials.

Conventional routes to ceramics involve precipitation from solution, drying, size reduction by milling, and fusion. The availability of well-defined monodispersed particles in desired sizes is an essential requirement for the formation of advanced ceramics. The relationship between density of ceramic materials and the sizes and packing of their parent particles has been examined theoretically and modeled experimentally. Colloid and surface chemical methodologies have been developed for reproducible formation of ceramic particles. These methodologies have included: (i) controlled precipitation from homogeneous solution; (ii) phase transformation; (iii) evaporative deposition and decomposition; and (iv) plasma- and laser- induced reactions.

Colloid chemists have greatly perfected the art of controlled precipitation to form uniform particles. In particular, in so-called "forced hydrolysis", they have employed elevated temperatures, controlled the pH of solution, and selected the most appropriate counterions. At optimal conditions, the rate of hydrolysis and, hence, the nucleation are controlled to such an extent that uniform growth and narrow particle size distribution are achieved. Using this approach, monodispersed micron-sized aluminum, chromium, titanium, iron, and cobalt (hydr)oxide particles have been prepared. Adjusting experimental conditions to control the release of anions from organic molecules (sulfide ion from thioacetamide or selenide ion from selenourea, for example) in the presence of metal-salt solutions also led to micron-sized particles with narrow size distributions. Similarly, the controlled slow release of cations from organometallic complexes in the presence of hydroxide ions was shown to yield monodispersed micron-sized metal oxides. Colloidal copper, iron, cobalt, and nickel oxides have been prepared; using these substances under highly controlled conditions can also lead to monodispersed complex colloidal particles. Controlled phase transformation of preformed particles can result in enhanced size control and increased monodispersity. The sol-gel-phase transformation, known as the sol-gel process, is the best known example of this approach. The simplest sol-gel process involves: (i) conversion of a metal salt to dispersible oxide particles; (ii) formation of a dispersed colloid (the sol) in water; (iii) removal of water and/or anions from the sol to produce a gel of desired morphology (i.e., phase transformation); and (iv) drying and sintering (or calcinating) the gel to obtain the ceramic material. Some dissolution reprecipitation or recrystallization, under optimized conditions have been found to improve the monodispersities of colloidal particles.

Evaporative decomposition of solutions and spray pyrolysis have been found to be useful in preparation of submicrometer oxide and non-oxide particles, including high temperature superconducting ceramics. Allowing uniform aerosol droplets (titanium ethoxide in ethanol, for example) to react with a vapor (water, for example) to produce spherical colloidal particles with controllable sizes and size distributions is an alternative vapor phase approach. Chemical vapor deposition techniques (CVD) have also been extended to the formation of ceramic particles.

The membrane-mimetic approach has the potential of providing superior size, morphology, and monodispersity control for ceramic particles. The relatively meager amount of published work in this area (see Table 3.3) is rather surprising. One ceramic subjected to membrane-mimetic processing is $BaTiO_3$ which is a piezoelectric ceramic. Vigorous and sustained activities, inspired by biomineralization and modeled on the incorporation of metallic, catalytic, and semiconducting particles into membrane-mimetic compartments, are fully expected.

*Table 3.3.Ceramic Materials in Membrane-Mimetic Compartments.*[48]

| Membrane-mimetic compartments | Incorporated materials | Comments |
|---|---|---|
| Vesicles prepared from egg yolk phosphatidylcholine | An aqueous solution of 0.15 M $Cu(NO_3)_3 \cdot 3H_2O:0.1$ M $Ba(NO_3)_2:0.05$ M $Y(NO_3)_3 \cdot 6H_2O:0.0125$ M $AgNO_3 = 3:2:1:0.25$ sonicated with 0.67 wt% lipid | Electron microscopy, X-ray diffraction, inductively coupled plasma emission spectra, and dynamic light-scattering measurements indicated the presence of multidomain spherical particles, containing $Ag_2O$, $Y_2O_3$, $CuO$, $Y(NO_3) \cdot H_2O$, $Cu(NO_3)_3 \cdot 6H_2O$, $Ba(NO_3)$, and $AgNO_3$, with mean diameters $34.8 \pm 13.2$ nm within the 59–99 nm diameter vesicles |
| Emulsions prepared from propylene carbonate | Alkoxides (titanium ethoxide, titanium *n*-propoxide, titanium *n*-butoxide, titanium *sec*-butoxide, titanium ethylhexoxide, aluminum *sec*-butoxide, zirconium *n*-propoxide, and their mixtures), typically 3 ml, sonicated with propylene carbonate, typically 17 ml, for 20-30 to form uniformly turbid emulsions. Immediate addition of water (10 mol excess) hydrolyzed the alkoxides. Precipitated oxide powders washed (in a Soxhlet extractor) with THF or 2-propanol for 21–30 h, dried, calcinated | Emulsion droplet size and composition determined particle sizes and compositions. The amorphous powders (spherical with diameters less than 1 μm) became crystalline upon calcination |
| Water-in-oil emulsions prepared from Tween, Span, Aerosol-OT, and Pluronic industrial type emulsifying agents | Yttrium nitrate dissolved in emulsion and evaporated in hot oil baths | 1–2 μm unagglomerated yttrium oxide particles are obtained |
| Suspensions prepared from alginic acid, obtained from *Magrocystis pyrifera* (kelp) | High purity $\alpha$-$Al_2O_3$ with 0.4 μm particle size | Low-viscosity, alginate-stabilized $\alpha$-$Al_2O_3$ is prepared |
| Films cast from poly(*n*-butylmethacrylate) and poly(methylmethacrylate) | Methylethylketone (5 g) solutions of the polymer (10 wt%) was added to isopropanol (0.2732 g) solutions of titanium isopropoxide (0.106 g, 0.3687 mmol) and barium bis-isopropoxide (0.367 g, 0.3687 mmol); the solution was cast onto microscope slides. The polymer film was dried, removed, and hydrolyzed in boiling barium hydroxide solution | Sheets, less than 30-μm thick, of $BaTiO_3$ have been produced |
| Films cast from poly(methylmethacrylate), poly(vinylidenefluoride), poly(butylmethacrylate), and poly(vinylchloride) | Polymer and precursors ($FeCl_3$, iron(III) acetate, titanium isopropoxide, silicon tetraethoxide, and copper(II) chloride) dissolved in organic solvent (acetone, ethyl acetate) and cast onto microscopic slides; precursors in situ hydrolyzed | Miscibility of the polymer and the precursor, the rate of reaction, and precipitation kinetics determine the outcome of (hydr)oxide formation |
| Triethoxysilane-capped poly(arylene ether ketone), PEK, or poly(arylene ether sulfone), PSF | THF (5 g) mixed with 0.1 ml 10 N HCl and added slowly to 5 g of titanium isopropoxide with fast stirring. This sol was then mixed with a 10 wt% solution of triethoxysilane capped PF or PEK in THF. The final solution was cast into poly(4-methyl-pentene) Petri dishes and covered for drying and curing at 60 °C for 24 h. Films were then removed and annealed at 200 °C for 15 min | The obtained materials, ceramers (ceramic polymers), had optical dispersions between organic polymers and inorganic glasses |
| Hydroxy-propyl cellulose (HPC) | Titanium tetraethoxide in ethanol is hydrolyzed in the presence of HPC | Mean particle size decreased with increasing HPC |

55

Colloid and Surface Chemistry of Self-Assembly

Developing reproducible preparations of stable dispersions containing nondispersed nanoparticles in desired compositions, sizes, and morphologies is the basic requirement for self-assembly. Equally important is the long-term stabilization of the nanoparticle dispersions. Metallic, semiconducting, magnetic and ferroelectric nanoparticles have been prepared by a large variety of different methods including hydrolysis and reduction of appropriate precursors, thermal decomposition, phtoloysis and radiolysis. New methods of preparation are being continuously developed.[48] This activity is fueled by the fundamental importance and potential applicability of nanostructured materials. Unfortunately, the mechanism of formation of monodisperse nanoprticles is not entirely understood. Careful attention to purity, to the concentrations of the reagents, to the rate and order of their addition, and to the temperature is the minimum requirement for reproducible formation of nanoparticles in desired composition and size distribution. Van der Waals attraction between unprotected nanoparticles results in their coagulation, and ultimate setting out of the particles from solution. Nanoparticle dispersions can be stabilized electrostatically and sterically. The electrostatic stabilization involves formation of an electrical double layer by the addition of counterions (citrate and chloride ions for gold and hexametaphosphate ion for sulfide semiconductor nanoparticles, for example). Agglomeration of the highly charged nanoparticles is prevented then by the screening of the Columbic repulsions which decay exponentially with increasing inter-particle distances. Displacement of the adsorbed anions by a more strongly bound neutral molecule or cation will reintroduce the van der Waals attraction and thus will result in coagulation. Coating of nanoparticles by polymers or surfactants sterically stabilizes them. Steric stabilization originates in entropic and osmotic effects. The entropy effect can be understood in terms of the required reorganization of the surfactant coating around nanoparticles if they are to be packed tighter. Decreasing the distance between nanoparticles would force the stabilizing polymers or surfactants into a smaller and more restricted space – a process which would decrease the entropy of the system. Decrease of the entropy renders a closer approach of the nanoparticles to be thermodynamically unfavorable. The osmotic effect stabilizes the nanoparticles by increased solvation of the polymer chains which are present in higher concentration in the interparticle regions. Size-quantized nanoparticles have been recently stabilized by the covalent or coordinate addition of phosphine or thiol ligands. It should be noted that the monodispersity of nanoparticles has been substantially increased by gel filtration or size selected precipitation.

Self-assembly of nanoparticles to an oppositely charged substrate surface is governed by a delicate balance of the adsorption and desorption equilibria. Efficient adsorption of one (and only one) monoparticulate layer of nanoparticles onto the oppositely charged substrate surface is the objective of the immersion step. Preventing the desorption of nanoparticles during the rinsing process is of equal importance. Optimization of the self-assembly in terms of maximizing the adsorption of nanoparticles from their dispersions and minimizing their desorption on rinsing requires judicious selection of stabilizer(s) and careful control of the kinetics of the process. Self-assembly of CdS and PhS nanoparticles was found to be most efficient, for example, if the semiconductor particles were coated by a 1:3 mixture of thiolactic acid and ethyl mercaptane. This composition of the capping agent was arrived at by many trial and error experiments. The structure and composition of porous solids profoundly influence the adsorption of liquids at their interfaces.

Layer-By-Layer Self-Assembly of Polyelectrolyte-Inorganic Nanoparticle Sandwich Films

Ultra-thin multilayer films, formed by consecutive self-assembly of cationic polyelectrolytes onto suitable substrates, were utilized as matrices in which a range of crystallites were incorporated. Alternate layers of a cationic polyelectrolite (P) and such anionic solid nanoparticles as montmorillonite clay platelets (M), $TiO_2$, and CdS were prepared on platinum and gold electrodes (Figure 3.25).[49] The substrate, S,

was prepared by immersing a clean and appropriately charged metal, platinum  or gold for example, electrode into an aqueous cationic polyelectrolyte, P, solution for a short time, rinsing with distilled water, and drying; construction of nanostructured multilayer films involves the sequential dipping of the substrate into aqueous dispersion of negatively charged clay platelets, M in Scheme i, or semiconductors, $TiO_2$ and CdS in Schemes ii and iii, and into P.  The self-assembled nano-structured films could only be removed from electrode by extensive abrasion, and showed remarkable stability.   They remained unaltered for at least three weeks, as was evidenced by their appearance, absorption spectra, electrochemical characterization, and X-ray diffraction.  The thickness of films could be controlled by the application of a potential during adsorption of M or Cd.  Spontaneous, layer-by-layer self-assembly of polyelectrolyte/clay platelet/semiconductor composite nanostructured films, further discussed in the following, well exemplifies the membrane-mimetic approach to advanced material processing.  While the dimensions, organization and deceptive simplicity of spontaneous self-assembly are analogous to the corresponding properties of biological membrane, ionic self-assembly offers a high degree of stability and relative ease of systematic chemical and physical manipulation.  Layers of clay platelets, particularly if self-assembled under an applied potential, are likely to cap imperfections and pinholes, and thus increase structural integrity of nanostructured films.  Polymerization of appropriate polyelectrolyte layers in the film provides an additional means of achieving stability and permeability control.  Significantly, judicious selection of components and their layer-by-layer self-assembly will result in nanoctructured films with the desired mechanical and physical properties.
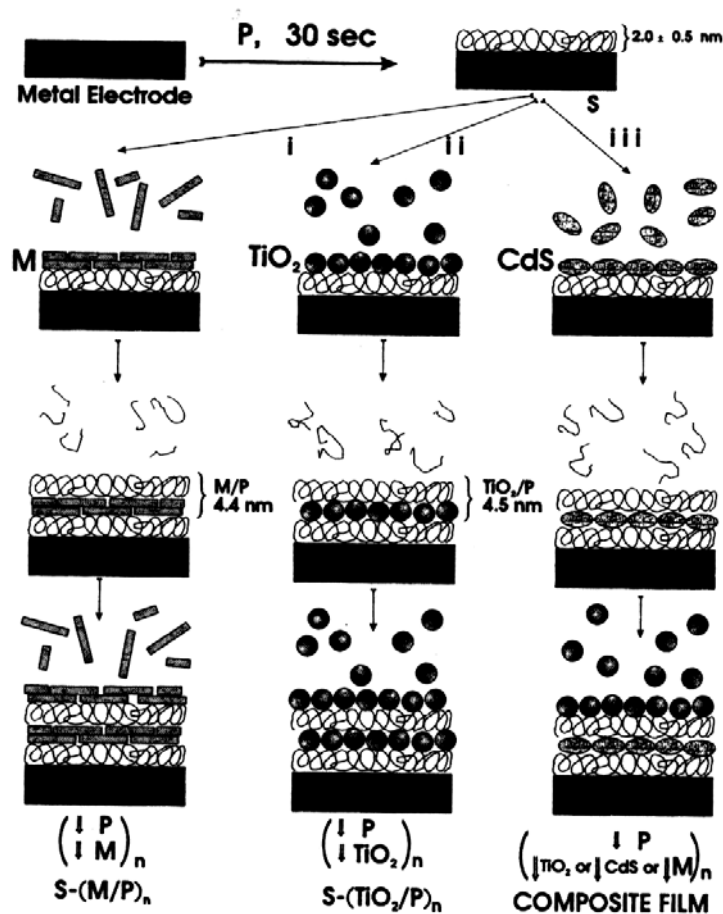


*Figure 3.25.  Schematic for Spontaneous Self-Assembly of Composite Nanostructured Films.*

The layer-by-layer self-assembly of polyelectrolyte-semiconductor nanoparticles onto substrates is deceptively simple.   A well-cleaned substrate is primed by adsorbing a layer of surfactant or polyelectrolyte onto its surface.  The primed substrate is then immersed into a dilute aqueous solution of a cationic polyelectrolyte, for a time optimized for adsorption of a monolayer, rinsed, and dried.  The next step is the immersion of the polyelectrolyte monolayer covered substrate into a dilute dispersion of surfactant-coated, negatively charged semiconductor nanoparticles, also for a time optimized for adsorption of a monoparticulate layer, rinsing, and drying.  These operations complete the self-assembly of a polyelectrolyte monolayer – monoparticle layer of semiconductor nanoparticle sandwich onto the primed substrate.  Subsequent sandwich units are deposited analogously.  The method is illustrated by the self-assembly of a poly(diallymetholammonium chloride), P, CdS nanoparticle film onto different substrates, S (gold, silver, platinum, quartz slide, highly ordered pyrolytic graphite, HOPG, mica, and Teflon).   The procedure involves the following steps: (i) immersion of the well cleaned (soaked in a concentrated sulfuric acid solution of Nocromix for 0.5-3 hours, repeatedly rinsed by ample amounts of deionized water, and dried) S into a 1.0%, w/v, aqueous solution of P, kept at pH=8.5 (no buffer), for *15 min*; (ii) rinsing with a stream of deionized distilled water, kept at pH=8.5; (iii) immersion into an aqueous CdS nanoparticle dispersion, kept at pH=9-10, for *24 h*; and (iv) washing with a stream of deionized water, kept at pH=8.5.  Each washing was followed with drying by a stream of $N_2$ for 30 s.  Thus, performing steps i-iv led to the self-assembly of one layer of polycation – one layer of CdS nanoparticle sandwich unit on the substrate, for which we adopted the S-(P/CdS) short-hand notation.  Subsequent P-CdS nanoparticle sandwich units were self-assembled by repeating steps i-v n times to produce film comprised of n number of sandwich units, S-(P/CdS)$_n$ (see Figure 3.26 for self-assembly of an S-(P/CdS)$_n$ film).  Similar methodologies (steps 9-iv) were employed for the self-assembly of many other polyelectrolyte-semiconductor nanoparticle sandwich films.
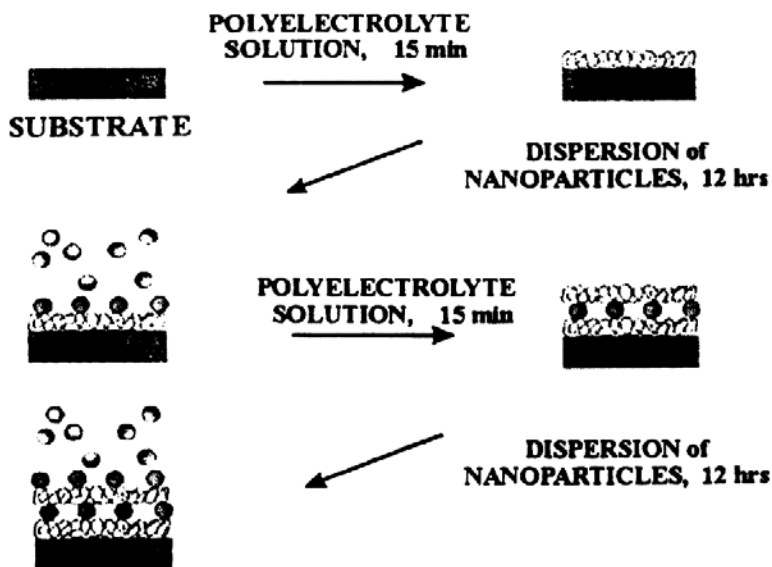


*Figure 3.26.  Schematics of the Self-Assembly of  S-(P/CdS)$_n$ Film.*

Adsorption and emission spectrophotometry, surface plasmon spectroscopy, X-ray diffractometry, scanning force microscopy, and transmission electron microscopy have been used for monitoring the self-assembly process and for characterizing the structure of self-assembled films.

Optimization of the self-assembly of initial layer of P is of particular importance. Thickness of the initial layer of P, self-assembled on a gold electrode, was found to be dependent on the concentration of polyelectrolyte and on the immersion time. Furthermore, soaking in an aqueous solution for 4 h did not remove P, as evidenced by the unaltered surface plasmon spectrum. AFM images of the polyelectrolyte film revealed featureless wavelike structures with height variations of about 0.2 nm. Apparently, multiple van der Waals forces maintain P on a variety of substrate surfaces, even in the absence of covalent bonding. Assuming P to be completely stretched on the surface of S, the mean area occupied by a positive charge on P can be estimated to be 10 (Angstrom).[49] It is this surface charge and relatively high charge density which provide the electrostatic driving force for the self-assembly of the negatively charged, surfactant-stabilized CdS, PhS, and $TiO_2$ nanoparticles onto the positive surface of P. The absorption spectra of semiconductor nanoparticle dispersions in aqueous solutions are retained in self-assembled films. Furthermore, the absorption edges (ca. 430 nm for CdS and ca. 500 nm for PbS) correspond to mean particle diameters of 35 and 100 Angstrom. AFM images of self-assmebled CdS particles revealed formation of a well-packed monoparticle layer. Successful self-assembly of a large number of repeating sandwich units of S-(P/CdS)$_{2n}$, S-(P/PbS)$_n$, and S-(P/TiO$_2$)$_n$ and S-(P/PbS)$_n$ indicate the uniformity of sandwich units that were self-assembled.

Ionic self-assembly has been adapted for layer-by-layer assembly of Zener Diodes on ITO and gold substrates from conducting polymers and CdSe Nanoparticles.[50] Both ITO and gold substrates were pretreated by an appropriate molecule which could act as anchoring agent for the semiconducting polymer by virtue of their pH sensitive terminal amino groups. The ITO substrate was pretreated by: (i) overnight (ca. 15 h) immersion into a 0.3 M solution of (4-aminobutyl)dimethylmethoxysilane in toluene (in a desiccator); and (ii) washing with toluene, ethanol, and water to provide an 8±1 Angstrom thick (determined by ellipsometry) coating. Gold substrates were pretreated by: (i) immersion into a 2% (w/v) aqueous 2-mercaptoethylamine hydrochloride solution for 12-15 h; (ii) washing by and sonicating in ethanol; and (iii) washing with water to provide an 8±1 Angstrom thick (determined by ellipsometry) coating. The electrochemical deposition of a semi-conducting thin film onto a conductive substrate is expected to produce a very rough surface. Surface roughness was decreased by the use of such anchring molecules as mercaptoethlamine, MEA (with Au substrate) and (4-aminobutyl)dimethylmethoxysilane (with ITO coated glass substrate). Surface roughness, evaluated by AFM, indicated a typical RMS value of 110 Angstrom for an electrochemically deposited 500-600 Angstrom thick film. The anchoring molecules, by virtue of providing a uniform monolayer coverage, also improved the homogeneity of the subsequent semiconductor nanoparticle layer. Polypyrrole (Ppy) layers were deposited by repeated dipping of the pretreated substrate into the filtered Ppy solution, typically for a period of 2 min, and washing extensively with deionized water. The dipping and washing sequence was repeated until the desired thickness was reached. The dipping time was increased (by a factor of 10-15) when more qualitative filtration was performed without improving the stability of the resulting Ppy solution. In a typical procedure, precoated substrates were immersed into aged (typically for 20 min) and filtered Ppy solutions for two minutes for five times and washed by deionized water between each time. Such treatment led to 100-200 Angstrom thick Ppy layers. The RMS value for the surface roughness of an 80 Angstrom thick Ppy layer, deposited onto a precoated gold substrate, was determined to be 18 Angstrom. Poly(3-methylthiophene) (PMeT) deposition was carried out in a Schlenk flask electrochemically. A potential of 10 V was applied across the pretreated ITO working electrode (the substrate), a platinum counter electrode, and a silver reference electrode in the appropriate electrolyte medium under an argon atmosphere. A potential of 1.1 V was applied across the pretreated gold working electrode (the substrate), a platinum counter electrode, and a silver reference electrode in the appropriate electrolytic medium under an argon atmosphere. In both cases the film thickness was controlled by varying the amounts of charge responsible for the *polymerization*. Because the oxidation potential at which polymerizaiton of oligomers occurs is lower than that due to the conversion of themonomer, the obtained films were directly in a p-type conducting state as characterized by their deep blue color.[50] Multilayers of CdSe nanocrystallites were prepared by using 1,6-hexanedithiol as anchoring molecule. The layering

procedure consisted of dipping successively the pretreated substrate covered with semi-conducting polymer, SCP (poly(p-phenylene vinylene), PPV, for example) into: (i) an aqueous 5 mM 1,6-hexanedithiol solution for at least 12 h; and (ii) into a CdSe nanoparticle dispersion in butanol (approximately $4\times10^{-3}$ M) for 7-8 h. The thiolated gold substrate was washed with dionized water for 20 s and then ethanol for 20 s. After dipping in a CdSe suspension the substrate was thoroughly washed with butanol (30 s) and ethanol (20 s). In some cases, negatively charged organic (PSS) and inorganic ($\alpha$-ZrP) polyelectrolytes were self-assembled onto the SCP covered pretreated substrate (Au/MEA/Ppy) prior to the self-assembly of CdSe. This self-assembly was accomplished by dipping the Au/MEA/Ppy film into a 0.02 M PSS solution (pH=1.0), for 10 h, followed by washing with deionized water (20 s) and drying under an Ar gas stream, or a diluted colloidal suspension ($6\times10^{-4}$ M) of $\alpha$-ZrP for 5 s, followed by washing with deionized water (30 s) and ethanol (20 s) and drying via Ar gas. Ellipsometric measurements indicated that a PSS layer of 6.5±2 Angstrom and an $\alpha$-ZrP film of 10±1 Angstrom (consistent with the value expected for a monolayer of sheet, thickness 6.5 Angstrom) were formed onto Au/MEA/Ppy films. All the film-supported substrates were stored in air. The work presented here[50] was prompted by the possibility of developing an ultra-thin flat-panel-display screen based on a phosphor whose electroluminescence can be triggered by "hot" electrons produced by the zener breakdown at a p-n type junction. The device fabricated consisted of two layers. The first layer contained a p-doped semiconductor polymer, SCP (polypyrrole, Ppy, for example), of variable thickness, deposited onto a pretreated (by mercaptoethylamine hydrochloride, MEA) conducting substrate (gold, for example) which served as the anode. The second layer consisted of n-type of semiconductor nanoparticles (cadmium selenide, CdSe) and 1,6-hexanedithiol, HDT, layer-by-layer self-assembled onto the first layer and coated by a thin film of aluminum (Al) which served as the cathode (Figure 3.27). Controlling the Zener breakdown by appropriate doping the SCP layer has been pivotal to this approach. The design strategy has involved the selection of the most suitable SCP and semiconductor nanoparticles by considering their energy levels, the optimization of the composition and the thickness of each layer, and the doping of the SCP layer. Self-assembly onto the derivatized substrate was mediated by two types of interactions: covalent binding, in case of using organic and inorganic polyelectrolytes. Stability in common solvents and thicknesses of CdSe layers were routinely compared in order to select the most suitable processing for self-assembly. Gold substrates were used for monitoring the thickness after each step by ellipsometry, while ITO coated glass and quartz substrates were chosen for studying the absorption properties of the different layers.
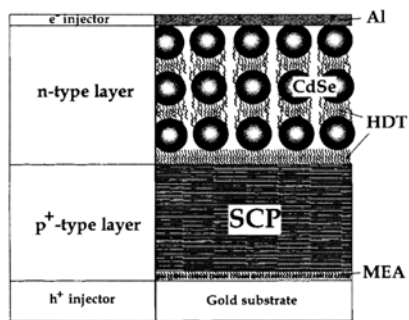


*Figure 3.27. Fabrication of $p^+$-n Junction by Layer-by-Layer Assembly and Self-Assembly, Capable of Functioning As a Rectifying Device Undergoing a Zender Breakdown.[50]*

Alternating Layers of Polyelectrolyte-Clay Platelets-Semiconductor Nanoparticles

Smectic clays, such as $Na^+$-montmorillonite, have been exfoliated into (10±2)-angstrom-thick layered silicates, often referred to as clay organicomplexes, by ion-exchange reaction with cationic surfactants. The high lateral bond strength and aspect ratios have rendered clay organocomplexes to be eminently

suitable materials for nanoconstruction. Indeed, the nanocomposites prepared by mixing polymers and clay organicomplexes had superior mechanical properties. However, a layer-by-layer assembly of nanocomposites is required for the preparation of thin films. This has prompted the spreading of clay norganicompolexes on water surfaces and their subsequent transfer to substrate by the Langmuir-Blodgett technique as well as the self-assembly of polyelectrolyte-clay platelet films. Alternating layers of polyelectrolyte (P)-clay platelet (M) sandwich films have self-assembled in a manner analogous to that shown for S-(P/CdS)$_n$ (Figure 3.26). Significantly, the thickness of a given multilayer S-(P/M)$_n$ film was found to depend on the potential which was applied during the deposition(s) of M. This behavior was established by electrochemical and surface plasmon spectroscopic measurements. In the electrochemical measurements, the working electrode was prepared by the sequential self-assembly of the required number (n) of (P/M) sandwich units on a platinum substrate (S). AgCl was used as the reference electrode. Cyclic voltammograms of 10 mM K$_3$Fe(CN)$_6$ in aqueous solutions provided useful information on the properties of the S(P/M)$_n$ film self-assembled onto the working electrode. Oxidations and reductions occurred at the metal electrode interface as a result of the diffusion-controlled penetration of the Fe(CN)$_6^{3-}$ and Fe(CN)$_6^{4-}$ ions through the self-assembled film. Increasing current drops upon deposition of successive layers of P/M are clearly seen in the cyclic voltammograms. The thickness of a given multilayer film was found to depend on the potential applied during the deposition(s) of M. Positive potentials increased the film thickness, while negative ones decreased it. Not unexpectedly, negatively charged M is attracted to a positively charged electrode more efficiently than it is to a negatively charged one. Similar behavior has been noted in the electrophoretic deposition of metal particles onto conductive substrates. The effect of an applied potential during the self-assembly also manifested itself in the changes of the surface plasmon spectra of the self-assembled films. These films were rather uniform, and the planar orientation of montmorillonite plateles in self-assembled films was readily observable. X-ray diffraction measurements indicated periodicities of 4.3±0.5 nm for the P/M repeating units. Since the thickness of polylectrolyte layer was determined by surface plasmon spectroscopy to be 2.0±0.5 nm, each self-absorbed M must contain at least two layers of clay platelets (each with a thickness of 1.0±0.1 nm).

Versatility is the major advantage of the self-assembly process described here. The method allows construction of composite films comprising different nanoparticles which can be layered in any desired order. Indeed, self-assembly of a variety of P/M/semiconductor nanoparticles has been reported.

Alternating Layers of Polyelectrolyte-Graphite Platelets

Graphite (G), like silicates, has a highly ordered layered structure. Furthermore, ultrathin G/P composites have many potentially beneficial properties, including controllable conductivity and magnetoresistance. Since G cannot be dispersed in water, a viable approach to form ultra-thin S-(P/G)$_n$ film is to prepare exfoliated graphite oxide (GO) platelets, self-assemble them onto P covered (S), and then in situ reduce the S-(P/GO)$_n$ films. This approach has, in fact, been experimentally verified. The construction of a P/GO self-assembled sandwich unit involves the following steps: (i) immersion of S into a 2.0% (w/v) aqueous P solution, kept at pH=8.5 (no buffer), for 15 min; (ii) rinsing with a stream of deionized distilled water; (iii) immersion into the aqueous GO dispersion, for 15 min; and (iv) washing with a stream of deionized water. Each washing was followed with drying by a stream of N$_2$ for 30 sec. Thus, performing steps I-iv led to self-assembly of one layer of polycation-one layer of graphite oxide platelet sandwich unit on the substrate, S-(P/GO). Subsequent P/GO sandwich units were self-assembled by repeating steps i-v n times to produce films comprised of n number of sandwich units, S-(P/GO)$_n$. Self-assembly of the successive P/GO layers onto a quarts slide was monitored by absorption spectrophotometry. The thickness of one sandwich unit of P/GO was determined to be 3.8±0.7 nm by surface plasmon spectroscopy. Reduction of GO in the S-(P/GO)$_n$ films to graphite, G, was accomplished either chemically or electrochemically. The chemical reduction involved the immersion of the self-assembled

film into a aqueous hydrazine hydride (50% w/v) solution for 1-24 h or into a 0.1 M HCl solution which contained Zn pellets (i.e., into a nascent hydrogen generator) for 2-3 h. The electrochemical reduction of GO (in the S-(P/VO)$_n$ film, self-assembled on metal or glassy carbon electrodes) was performed by scanning the potential from –0.5 to –1.5 V vs SCE for 20 min. The lateral resistivity of a (P/GO)$_{10}$ film was measured between two 3 mm wide gold stripes evaporated on a glass slide at a distance of 2 mm between them. Self-assembled graphite oxide film was deposited on top of them over the whole surface of the slide. The as-deposited (P/GO)$_{10}$ film had an R value of 32 MΩ at the 2 mm gap. After reduction by hydrogen, evolving in situ, the R value dropped to 12 KΩ, which amounts to a 27,000-fold decrease in the overall resistance. This corresponds to the change in volume conductivity from $1.2 \times 10^4$ Ω$^{-1}$.m$^{-1}$ to $3.1 \times 10^7$ Ω$^{-1}$m$^{-1}$. Roughening the substrate surface (by multiple diamond knife grooves along the electroe direction) prior to the deposition of multilayers rendered the resistivity decrease (which accompanied GO reduction) to be less pronounced (only a 370-fold increase in conductivity was observed). This was the consequence of imperfect self-assembly on a disturbed surface which resulted in broken films.

Alternating Layers of PDDA-Exfoliated Sheets of Syntetic Hectorite (Mica-Type Layered Silicate)

Ionic self assembly, with covalent bonds or ionic attraction between layers, provides high levels of stability not seen in alternative techniques such as Langmuir-Blodgett (LB) systems. This section reviews ionic self assembly of ordered multilayered films from ~1-nm thick layers of organic and inorganic macromolecules. Films with thickness greater than 0.2 μm have been prepared that have sufficient structural order to diffract x-rays. The approach involves sequential adsorption of the polyelectrolyte polydiallyl-dimethylammonium chloride (PDDA) and exfoliated sheets of synthetic hectorite, a mica-type layered silicate.[52] When stirred in water, this silicate mineral exfoliates into crystalline, quasi-two-dimensional sheets that are 0.96 nm thick and about 25-35 nm in diameter. The sheets bear a negative charge, which is balanced in the precursor by interlamellar sodium cations that can undergo ion exchange reactions with other cationic materials. The choice of PDDA for this study reflects the strong affinity of hectorite and related minerals for tetraaklylammonium compounds.[52]

To prepare a substrate for a multilayered structure, a (100)-oriented single-crystal silicon wafer bearing a native oxide was cut into small pieces (~1 cm by 2 cm) and then cleaned to provide a hydroxylated surface. A 5% (w/w) aqueous solutio nof PDDA was dripped onto this substrate, and after ~5 s, it was rinsed with water and blown dry with nitrogen. Subsequently, a 0.2% (w/w) aqueous dispersion of hectorite was dripped onto the surface, and after ~5s, it was rinsed with water and blown dry with nitrogen. By repetition of this simple two-step adsorption cycle (Figure 3.28), films thicker than 0.2 μm could be prepared in less than 2 hours. An x-ray phtoelectron survey spectrum of a silicon substrate that had been treated with PDDA, then hectorite, and then PDDA confirmed the presence of those elements in the silicate and the polymer: Si, O, Mg, C, N, and Cl. The absence of sodium, which is present in the precursor mineral as an interlamellar counterion, indicates that it had been exchanged for the catinic polymer. The low expected concentration of lighium on the surface and the low sensitivity factor of the Li 1s orbital explain the absence of this peak.

Optical ellipsometery was used to monitor the growth in thickness of the multilayer structures. In a typical cycle, ~1.1 nm of polymer and ~2.1 nm of silicate were adsorbed (Figure 3.29A). The ellipsometry indicated a linear increase in the thickness of the structures with the number of adsorption cycles (Figure 3.29B). The average thickness added per adsorption cycle increased slightly as the number of cycles ncreased, from ~3.2 nm after five cycles to ~3.6 nm after 60 cycles. The thickness of the multilayer sample was remarkably even. Ellipsometric measurements taken on any single hectorite-terminated sample typically agreed to within ±2%, and the majority of samples showed less than one-half of that variability. Sample-to-sample reproducibility was also very good. Three samples prepared on different days with 22 cycles had average thicknesses within 2% of one another. If the adsorption times

were doubled, to 10 s, the average amount of each component that was adsorbed onto the sample surface varied by ~0.1 nm or less, which is within experimental error. If adsorptions were allowed to proceed for extended times (15 min), however, the average thickness added in each of the first five cycles increased from ~3.2 nm to ~3.8 nm.
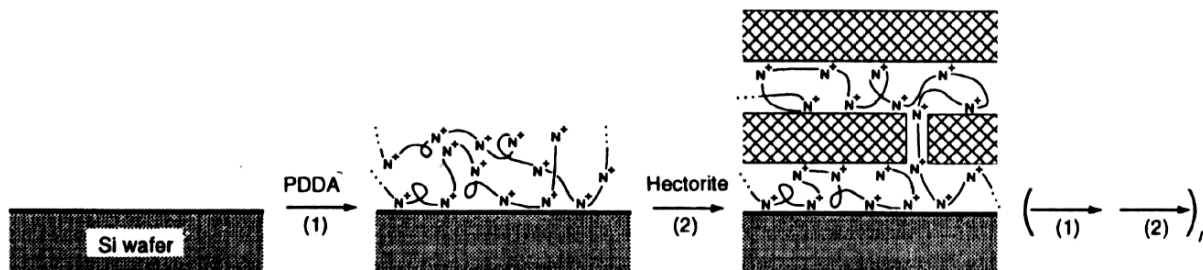


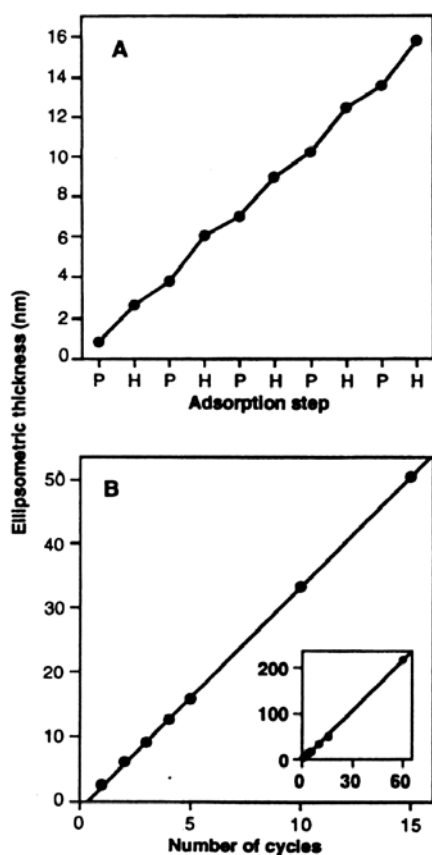*Figure 3.28.  Stepwise Assembly of PDDA/Hctorite.[52]*



*Figure 3.29.  Elecisopetric Thickness of a Multilayered Structure on a Single-Crystal Silicon Substrate as a Function of the Number of Adsorption Cycles for (A) Individual Steps in Five Cycles (P, polymer; H, hectorite); and (B) 15 and (inset) 60 Complete PPDA/Hectorite Cycles (lines shown in (B) are best fits to the data; the native oxide on silicon is not included in the reported thicknesses).[52]*

As increasing numbers of layers were adsorbed, samples progressed through a series of well-defined colors because of interference effects, as has also been noted for other (LB and SA) multilayer systems. No cloudiness was observed in the samples, and the colors were uniform, with only a small region (less than 1 mm wide) at the sample edges showing nonuniformity.

At the outset of this work, hectorite was expected to be adsorbed onto the sample surface in a controlled manner by ion exchange (of the ammonium groups of surface-bound polymer) for the alkali metal counterions of anionic hectorite sheets. Once the surface was covered with a layer of hectorite, further adsorption of the silicate should be inhibited by coulombic repulsion between the anionic sheets. The adsorption of approximately two hectorite layers (2.0-2.2 nm) per adsorption cycle indicates that some of the polymer is associated sufficiently loosely with the surface that is displaced in the subsequent hectorite adsorption and becomes the "glue" for addition of a second layer of hectorite. Consistent with this proposed mechanism, the amount of hectorite adsorbed in a particular cycle could be controlled by varying the amount of polymer adsorbed in that cycle. Furthermore, only a single layer of hectorite was adsorbed onto a single layer of monomeric ammonium salt that was covalently bound to the silicon substrate. Ion exchange has been used for the adsorption of composite films, but the combination of structural order and 1- to 2-nm lattice spacings that characterized PDDA-hectorite was a contribution of the work reported here.[52]

Because the hectorite sheets in a single adsorbed layer will have packing imperfections (that is, open space at their boundaries), the linearity of multilayer growth indicates that this system is self-healing with respect to addition of subsequent layers. It is inferred that the large lateral extent of the sheets allows coverage of regions where the underlying layer is incomplete. In contrast, other multilayer preparations that rely on the formation of each layer through reaction of individual adsorbed molecules with molecules from the contacting solution are less able to recover lost order; in such systems, defects may occur to create unreactive patches that do not participate further in multilayer growth, resulting in a decay in structural order as an increasing number of layers in added.

The tendency of exfoliated silicate sheets to restack in a parallel arrangement has been well established. The preparative method described here offers a potentially powerful strategy for building ordered organic-inorganic thin films with systematic control over both structure and thickness. It should be readily adaptable to other systems that incorporate other substrates, included molecules, and inorganic sheets. The use of gold substrate, for example, coated with an $\omega$-mercaptoalkylammonium compound to promote adsorption of the first silicate layer, would allow electrodes to be prepared with complex but controllable barrier layers and allow evaluation of the performance of these multilayered structures as electrical insulators, diffusional barriers, or mediators for electron transfer. Deposition of crystalline materials onto sheet silicates, including oxides and metals, has been demonstrated, indicating that our multilayer films may be of interest as substrates for growth of other materials. Metal-terminated structures, for example, may be of particular interest as metal-insulator-semiconductor (MIS) or metal-insulator-metal (MIM) devices. Preparation of multilayer assemblies with nonlinear optical activity may be possible for polar molecules (monomeric or polymeric) can be oriented noncentrosymmetrically between inorganic sheets. Finally, adaptation of this method to other layered materials with known intercalation chemistry, including metal dichalcogenides, metal halides, and layered metal oxides such as $V_2O_5$ and FeOCl, may allow stepwise preparation of multilayered structures with a range of electronic band gaps.[52]

Introduction of Fullerene Monolayers

At present, great interest is attracted to fullerenes, which are empty spheres built by 60 bound carbon atoms C60. A procedure has been developed in which the interaction of fullerenes with the surface containing  positively charged NH groups provided the formation of monomolecular C60 layers on the

substrate. The film growth proceeded through the formation of C-N and C-H bonds. Similar interactions have been used to assemble films with alternating molecular layers of fullerene and a polycation containing amino group. Such an assembly was successfully performed with the use of alternating C60/PEI layers; the growth step was d = 21 angstrom. Adsorption of fullerenes increased the film thickness by 9±1 angstrom (this corresponds to the diameter of the fullerene molecules C60) (Figure 3.30).[56]
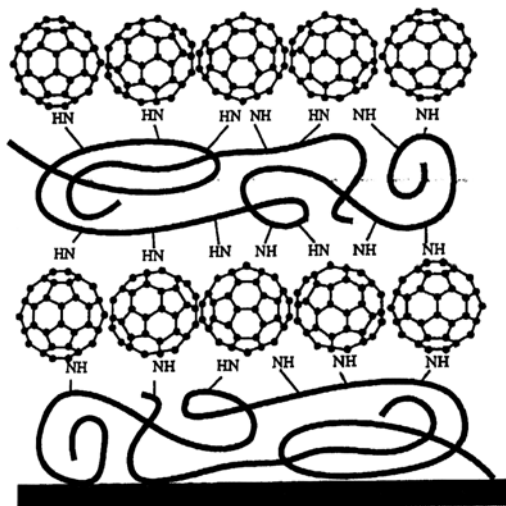


*Figure 3.30. Schematic of the Film Structure Built by Alternating Fullerene and Polyethyleneimine Layers.[56]*

**Development of Experimental Procedures for Ionic Self-Assembly of Metallic, Conductive Polymer and Piezoelectric Nanolayers**

Our hybrid composite comprise piezoelectric, conductive and metallic nanolyaers to render adaptive effects. This section reviews the experimental procedures established for ionic self-assembly of metal, conductive polymer, ceramic and piezoelectric polymer nanolayers. Ceramic nanolayers are covered in our experimental work because the offer engineering properties which are highly complementary to those of metals and polymers in the context of heterogeneous nanocomposites which are subject of our investigation.

Ionic Self-Assembly of Metal Nanoparticles

Colloidal gold with 12-18 nm particle size was used to demonstrate the potential for ionic self-assembly of metal nanoparticles. Colloidal gold/Polyelectrolyte multilayer systems were prepared by first preparing a charged surface (Figure 3.31) and then depositing alternating poly(styrene sulfonate sodium salt), PSS (molecular weight 168,000) and PAH (molecular weight 50,000-65,000) layers onto a poly(ethyleneimine) (PEI)-modified substrate (Figure 3.32). These polyelectrolyte layers were deposited from $3 \times 10^{-3}$ M aqueous solutions containing 1 M NaCl, using immersion times of 20 min., followed by rinsing with deionized water and drying after each second layer. The uppermost layer of PAH provides a positively charged surface for subsequent self-assembly of a monolayer of gold particles using an immersion time of 5 hours. Repeated cycled of PE and colloidal Au deposition (with a final capping layer of PAH) yield multi-layer architectures of the form PEI/[(PSS/PAH)$_m$Au/PAH]$_n$ (Figure 3.33). In the exploratory work, the number of PEI layer pairs (m) varied between 0 and 5, and the total number of polymer/Au layers (n) ranged from 1 to 4.

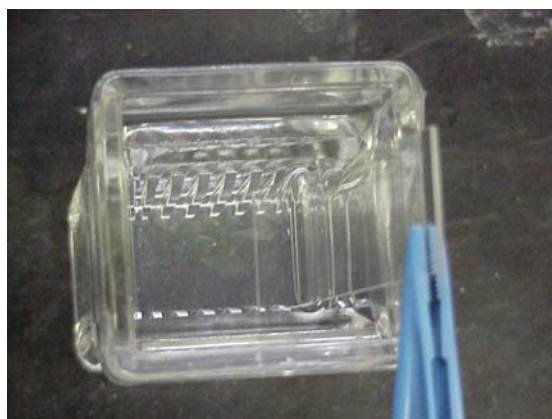*Figure 3.31.   Substrate Surface Modification.*


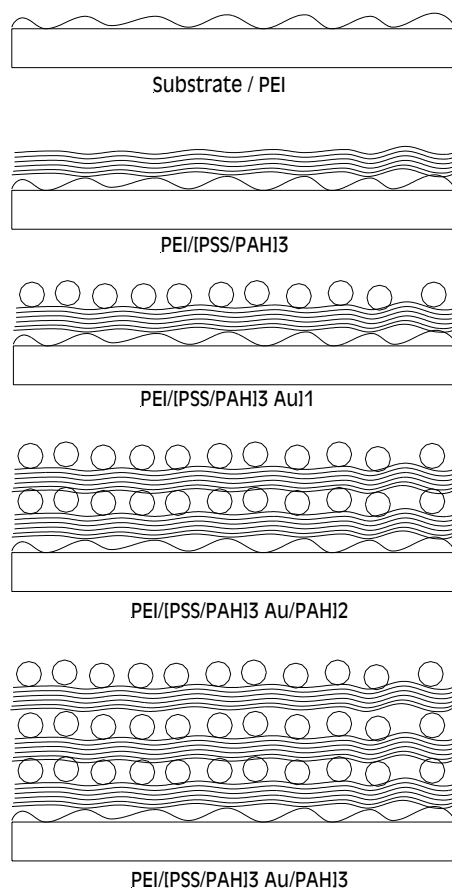
*Figure 3.32.   Ionic Self-Assembly in Solution*



*Figure 3.33.  Ionic Self-Assembly of Colloidal Gold/Polyelectrolyte Multilayers to a Final Structure with m=3 and n=2.*

UV-vis spectroscopy of the n=4 multilayers shows large changes in absorption peak maxima as m increases from 0 to 2; a very slight additional shift is observed for m=3, and no further spectral changes

are observed for multilayers with m values from 3 to 5. These trends indicate that inter-particle interactions that give rise to the long wavelength peaks are effectively eliminated by the separation of Au layers with 5-7 individual Polyelectrolyte layers. Au particles seem to form an initial monolayer on PEI that is limited to about 30% surface coverage, presumably due to electrostatic repulsions. Slight differences in colloid packing (or partial aggregation) in Au monolayer ncrease interparticle interactions, which result in the appearance of a long wavelength band attributed to plasmon resonance. The structural characteristics of the Au/polyelectrolyte multilayer are controlled by the number of polyelectrolyte interlayers between Au layers. As PE layers are deposited, they most likely fill voids between, and then form a physical buffer layer on top of Au particles; hence, the increasing difference in layer spacing for multilayers with increasing number of polyelectrolyte interlayers, m. The calculated layer spacings for multilayers with n=4 are 12.5 nm (m=2), 16.3 nm (m=3), 22.0 nm (m=4) and 29.0 nm (m=5), compared to Au particle size of 12.7-17.9 nm. When the layer thickness is comparable to or exceeds the particle size, the increased separation of Au layers effectively eliminates the induced dipole interactions (both within the same layer or between layers) that give rise to the long wavelength band.

In summary, the above work demonstrates the feasibility of ionic self-assembly of multalayer superlattices that incorporate colloidal metal nanoparticles. Using this approach, multilayers with isotropic, anisotropic, or graded properties could be produced with various other polymers and particles to yield a wide range of new heterostructured materials. Ionic self-assembly can yield particle/polymer multilayers with a well-defined layered structure by adjusting the relative spacing of polyelectrolyte interlayers and metal particles, which can in turn lead to rational design of nanocomposites with tunable engineering properties.

Ionic Self-Assembly of Ceramic Nanoparticles

Like metals, ceramics are available in the form of colloids comprising cluster of molecules with 2-50 nanometer particle size. These nanoparticles offer superior engineering properties when compared with their coarse-grained conventional counterparts. Ionic self-assembly of zirconia nanoparticles is discussed in the following.

The objective of this experimental work was to fabricate dense, polycrystalline zirconia through ionic self-assembly. Poly(allylamine hydrochloride) (PAH) and poly(sodium-4-styrenesulfonate) (PSS) as well as a molecular dye (PS119) were used in conjunction with the zirconia nanocluster solution with 5-10 nanometer particle size. Solutions of PAH and PS119 were prepared by separately dissolving 50 mg of each polymer in 25 ml of deionized water. The PAH and PS119 solutions were used to provide the cationic and anionic polyelectrolytes, respectively. Solutions of PSS were prepared by dissolving 200 mg of the polymer in 100 ml of deionized water. This solution was used to provide the anionic polyelectrolytes, opposite in charge to the nanoclusters in zironia solution. A zirconia solution of 10 mg/ml was prepared and used to provide the cationic polyelectrolytes. Prior to construction of the $ZrO_2$/polymer multilayers, four bilayers of PAH/PS119 were deposited on cleaned and negatively sharged silicon wafer substrate to promote adhesion between the surface and the first monolayer of $ZrO_2$. Since the substrate surface was negatively charged, it was first immersed in the PAH solution for 3 minutes, rised, and then immersed in the PSS119 solution with an immersion time of 3 minutes. The uppermost layer of PS119 provided a negatively charged surface for subsequent assembly of alternating $ZrO_2$ and polymer layers. Zirconia/polymer nanocomposites were deposited in the same manner as the PAH/PS119 multilayers. The immersion time for each solution was 5 minutes. By repeating the above procedure in an alternating fashion, multilayer assemblies of $ZrO_2$/polymer thin films were fabricated on the substrates (Figure 3.34).Close to 200 bilayers of $ZrO_2$ and PSS were deposited.
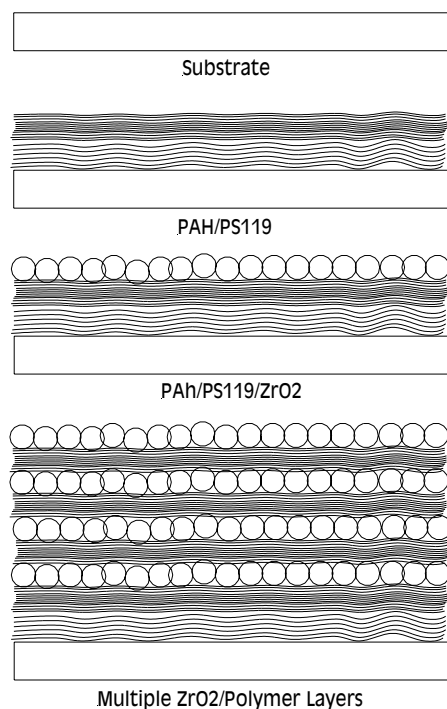
*Figure 3.34. Schematic Presentation of Ionic Self-Assembly of ZrO₂/Polymer Nanocomposite.*

Thickness measurements after each bilayer deposition, through ellipsometry, indicated that each bilayer of $ZrO_2$/polymer was about 2 nanometer. The Vickers microhardness of $ZrO_2$/polymer nanocomposites was also measured prior to and after heat treatment. The heat treatments employed involved exposure to $450^oC$ and $900^oC$ for two hours and one hour, respectively. For an indentation depth of 100 nanometer, as-deposited nanocomposites exhibites a Vickers hardness of 2.5 GPa, which was increased to 20 GPa after heat treatment at $450^oC$ for one hour, and to 26 GPa after heat treatment at $900^oC$ for two hours. The ionically self-assembled nanocomposites incorporating $ZrO_2$ exhibited substantially higher levels of physical integrity and microhardness when compared with similar systems developed using other processing techniques. For example, in the case of sputter-deposited $ZrO_2$, failure during microhardness measurements occurred by peeling before indentation. The high physical integrity of ionically self-assembled nanocomposites reflects on the high molecular packing density of the system and the small particle size of zirconia nanoclusters. Ionic self-assembly allows formation of closely packed nanoclusters in a single layer, and their separation from adjacent layers by ultra-thin polymer spacers. This procedure mitigates extension of voids beyond single monolayer thickness due to the self-healing nature of polymer mnonlayers. Hence, macroscopic voids are avoided, and the resulting particle packing density is very large. Additionally, heating of the nanocomposite decreases the size of microvoids through burnout of polymer interlayer binders, and further increases packing density and microhardness. Due to the very small grain size of zirconia nanoclusters, a large fraction of zirconia molecules occur near the large number of cluster-to-cluster boundaries, thus promoting very strong intermolecular interactions between clusters in individual layers and to clusters between pairs of adjacent parallel layers.

In another experimental work, the ionic self-assembly technique was adapted to develop nanocomposites of nanosized particles of titanium dioxide with ionic polystyrene molecules on different substrates. Poly(sodium 4-styrenesolfonate) ($M_w$=70,000) (PSS), poly(allylamine hydrochloride) ($M_w$=50,000) (PAH), and N-2-(20aminoethyl)-3-aminopropyltrimethoxysilane) (94%) (APS), and colloidal dispersion of $TiO_2$ with 2-5 nanometer particle size were the raw materials used in the process. Solutions containing

PSS were prepared by dissolving 120 mg of the polymer in 60 ml of HCl in order to set the same pH as that of the polycation solution. The solutions were then filtered through a 0.5 micon filter. The pH oaf rinsing water was adjusted with HCl to the same as those of polycatin and polyanion solutions. THe substrates of quarts, silicon and glass were cleaned and then dipped in a solution of 5% APS in pure toluene for 15 hours, and then ultrasonically agitated for 30 min each in toluene, methanol/toluene (1:1), and methanol. Finally, they were extensively rinsed to remove residual APS, and then dried. Such APS-modified surfaces are positively charged.

Ionic self-assembly of $TiO_2$/polymer multilayer film (Figure 3.35) started with immersion of an APS-modified substrate in the anionic solution of PSS for 10 min, rinsing with water, blowing out with nitrogen gas, and dipping into the cationic solution of $TiO_2$ for 15 min followed by rinsing with water and drying out with nitrogen gas. By repetition of this two-step process, layered nanocomposites comprising about 100 $TiO_2$/polymer bilayers were produced. UV-vis spectroscopy results confirmed a linear and consistent deposition pattenr of about 100 bilayers, with no molecular aggregation between adjacent layers. These fundings further confirm the potential fo ionic self-assembly as a powerful, low-cost and high-throughput means of fabricating, at room temperature, high-performance polymer/$TiO_2$ layered nanocomposites with controlled thickness and molecular architecture on different modified substrates, which could eventually include plastics and metals.
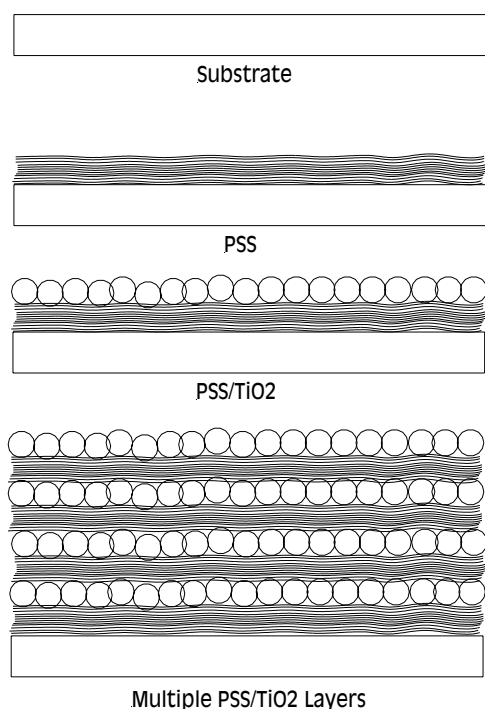


Substrate

PSS

PSS/TiO2

Multiple PSS/TiO2 Layers

*Figure 3.35. Schematic Presentation of Ionic Self-Assembly of $TiO_2$/Polymer Nanocomposite.*

In yet another experimental work, nanosized iron exide ($Fe_3O_4$) particles and polyimide molecules were ionically self-assembled on quartz and glass substrates. For this purpose, poly(diallyldimethylammonium chloride) (PDDA)-coated $Fe_3O_4$ particles with 8 nanometer particle size (dispersed in water) were used together with a thermoplastic polyimide precursor polyamic acid salt (PAATEA) with molecular weight ($M_w$) of 30,000 g/mole after imidization. The substrates were cleaned and themn immersed in a 1% volume solution of (N-2-aminoethyl1-3-aminopropyl) trimethoxysilane (APS) in toluene for two hours at

a temperature of 45°C. After silanization, the substrates were ultrasonically agitated for two minutes each in pure toluene, a toluene/methanol (1:1) mixture twice, and pure methanol twice, then thoroughly rinsed. This process covalently anchored a monolayer of APS with amine functionalities onto the substrate, yielding a positively charged surface in proper pH range. The substrate was then immersed in a 1% (by weight) aqueous solution of PAATEA with pH of 8.5 for a peiod of 10 min, rinsed and blown dry with nitrogen gas, dipped into the cationic solution of (Fe$_3$O$_4$:PDDA)/H$_2$O (3/1.5/50, by weight) with a pH of 8.5 for 10 minutes, and then rinsed and dried using nitrogen gas. Repetition of this two-step process yielded a nanocomposite with close to 50 bilayers. The process is schematically presented in Figure 3.36. UV-vis spectroscopy indicated a linear build-up of bilayers, confirming that each layer adsorbed contributes an equal amount of material to the layered nanocomposite. The remarkably simple ionic self-assembly technique with molecular-level control over thickness is thus capable of producing layered nanocomposites with complicated multilayer architecture.
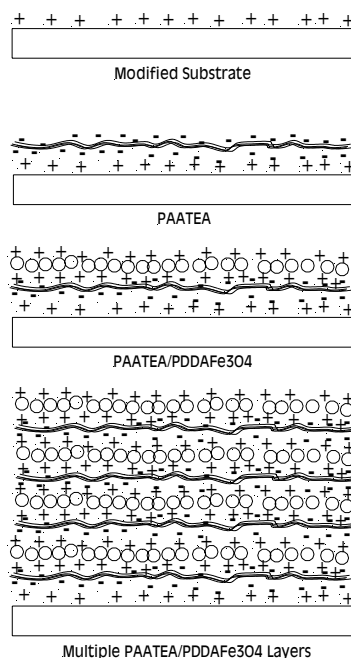


*Figure 3.36. Schematic Presentation of Ionic Self-Assembly of PDDA-Fe$_2$O$_3$/Polymer Nanocomposite.*

Ionic Self-Assembly of Piezoelectric Polymers

Piezoelectric nanolayers, through conversion of mechanical energy to electrical energy, drive the adaptive phenomena in our new material system. The mechanical energy is generated in the material system by loads applied on the system during service. Ionic assembly of piezoelectric nanolayers is thus critical to successful development of the new material system.

This experimental work investigated ionic self-assembly of multi-layer polymer (sodium 4-styrenesulfonate)/poly(diallyldimethulammonium chloride) (PSS/PDDA) piezoelectric nanocomposite. PSS was selected because its charged $-SO_3^-$ functional group effectively gives it a non-centrosymmetric dipolar structure. PDDA was used as the counterion to self-assemble PSS. PSS and PDDA had molecular weights ($M_w$) of 70000 and 400000-500000 (20 wt% in water), respectively. Indium tin oxide (ITO)-coated glass was used as a negatively charged substrate. For the purpose of ionic self-assembly,

the cleaned substrate was first immersed in a 1% PDDA (v/v) solution for 5 min, and then rinsed extensively with ultrapure water, thus anchoring a  monolayer of PDDA with positively charged groups onto the substrate.  The system was then dipped into the anionic aqueous solution of negatively charged PSS with a concentration of 2 mg/ml at pH = 6-7 for 3 min, followed by thorough washing with water and drying with nitrogen gas.  By repetition of this simple two-step process, the multilayer nanocomposite system was self-assembled.  Optical UV-visible spectroscopy of multilayer nanocomposites indicated that the self-assembled layer-by-layer system was built uniformly by alternate assembly of each layer of PDDA and PSS, which suggests that a high-quality nancomomposite was synthesized by the ionic self-assembly process.

The normal load method was employed to characterize the piezoelectric coefficient $d_{33}$ of the multi-layer PSS/PDDA system on an ITO-coated glass substrate, once it was synthesized without electric field poling.  Figure 3.37 shows a schematic diagram of the set-up used for measurement of piezoelectric coefficient.  An electrically conducting ITO coating on the substrate material formed one electrode, and a metal test weight, which made contact with the opposite side of the deposited film, was used as the other electrode.  By dropping the weight onto the film from a known height and measuring the resulting charge using an electrometer, the $d_{33}$ piezoelectric coefficient may be determined.  A standard PVDF film was used as a reference to verify the measurement procedure.  The $d_{33}$ value for the PVDF was 34.6 pC/N, or within 15% of the nominal $d_{33}$ value of 30 pC/N for PVDF.  The piezoelectric response of the self-assembled, 60 bilayer PSS/PDDA system with the thickness of about 70 nm is shown in Figure 3.38.  A linear relationship is observed between the output voltage of the ionically self-assembled PSS/PDDA and the applied force.  This demonstrates that the self-assembled PSS/PDDA system has piezoelectric properties.  The experiment was carried out under quasi-static conditions.  According to hydrostatic equations, the piezoelectric coefficient charge constant $d_{33}$ resulting from direct piezoelectric effect and measured by the normal load method can be calculated as:

$$d_{33} = D_3 / T_3 = Q / F = C_0 . V / F$$

where, $D_3$ is the electric displacement and $T_3$ is the stress in the 's' direction; Q is the induced charge in the film within the electrode area for an applied force F; and $C_0$ is the capacitance of the standard capacitor used in the set-up (Figure 3.37).

The normal load tests indicated that the ionically self-assembled PSS/PDDA multi-layer system (as deposited) with thickness of 70 nm provided a piezoelectric coefficient $d_{33}$ of about 7.0 pC/N without any electric field poling treatment.  Hence, piezoelectric systems can be synthesized by ionic self assembly, with the resulting system exhibiting piezoelectric response directly without poling.
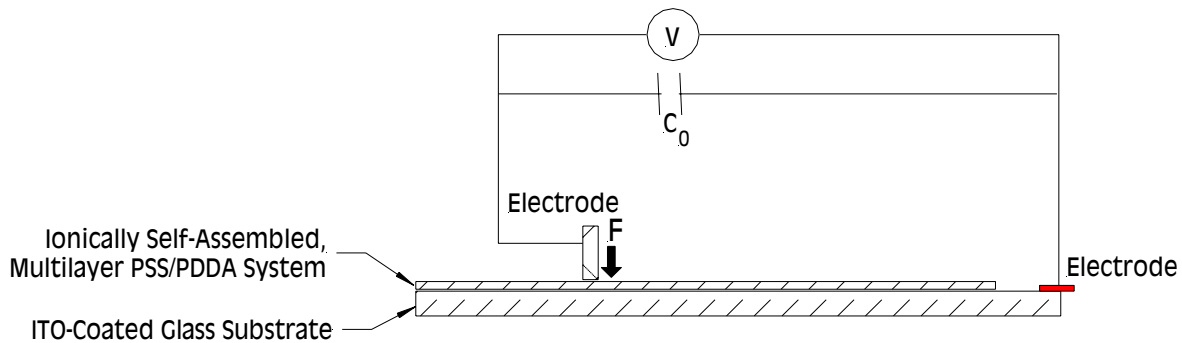


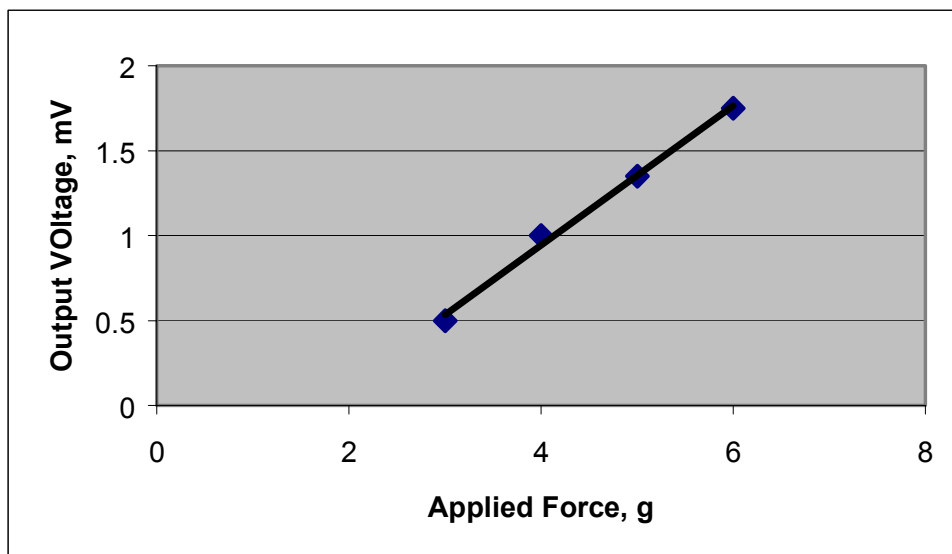*Figure 3.37.  Schematic Presentation of the Normal Load Set-Up for Measuring the Piezoelectric Coefficient $d_{33}$*

*Figure 3.38. Output Voltage Associated with the Piezoeelctric Effect in Ionically Self-Assembled PSS/PDDA System Vs. Applied Force ($C_0$=15- pF).*

For the layered nanocomposite system presented above, the '3' direction is considered to be perpendicular to the planar surface. Meanwhile, the piezoelectric response of the system in the '3' direction with respect to the stress over the electrode area induced by the applied force (the weight of the electrode) is in the direction of the net polarization of the system.[14] From the principle of piezoelectricity, the surface charge density that remains due to the applied force is numerically equal to the polarization, or net dipole moment per unit volume. The piezoelectric response of the as-deposited system indicates that the PSS polymer molecules are mostly aligned in a geometrical order, resulting from the regular geometric assembly of the positively charged PDDA molecules. Statistically, this arrangement of PSS piezoelectric molecules leads to average molecular orientation parallel to the '3' direction. Hence, a net macroscopic polarization of the self-assembled system is created once the piezoelectric molecules are assembled during the ionic self-assembly process, and this polarization may remain permanently due to the existence of the electrostatic force resulting from the oppositely charged polymer PDDA molecules in the system. This discussion suggests that the ionically self-assembled PSS/PDDA system has piezoelectric properties although it has quite a different structure in comparison to conventional piezoelectric systems.

Ionic Self-Assembly of Conducting Polymers

Conduction of electrons and ions using the piezo-induced electric charge is central to implementation of the adaptive phenomena occurring in the new material system. Ionic self-assembly of conducting polymers is thus critical to success of our approach.

Figure 3.39 presents two p-type-doped conducting polymers (polypyrrole and polyaniline) that we processed, through ionic self-assembly, into multilayer nanocomposites. Our key challenge was to create the chemistry needed to produce dilute solutions of these materials in their doped forms. It is well recognized that non-derivatized, doped conducting polymers are insoluble in most solvents, particularly water, which is the preferred solvent in ionic self-assembly. Two basic approaches have been identified for generating water-soluble forms of p-type-doped conducting polymers. In one approach, conducting polymer chains are formed in situ in a dilute aqueous solution comprised primarily of a monomer and an oxidizing agent. In this case, the conducting polymer is actually created in the solution and subsequently

spontaneously adsorbed onto the substrate surface in uniform thickness. In the second approach, preformed conducting polymers are used directly by forming dilute solutions of their doped forms in suitable solvent systems. In this case, it is necessary to control the type of solvent system and the level and type of chemical doping of the polymer chains.
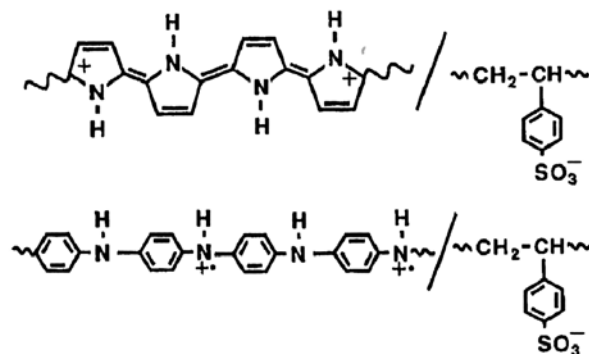


*Figure 3.39. Examples of p-Type-Doped Conducting Polymers.*

In the case of in situ polymerized, p-type-doped conducting polymers, polypyrrole dipping solutions were prepared by adding polypyrrole polypyrrole monomer to an aqueous ferric chloride solution which had been pH adjusted to a desired level (typicall pH 1.0) using concentrated Hcl. The dipping solution was aged for 15 min and filtered prior to use. Typical dipping solutions comprised 0.02 mol/l pyrrole monomer and 0.006 mol/lo FeCl$_3$. TO ensure controlled deposition, dipping solutions were typically used for only 2-3 hrs. Ionic self-assembly of multilayer systems involved alternate dipping of a substrate into the in situ polymerized polypyrrole solution and a polyanion solution. The substrates were dipped in the polypyrrole solution for 5 min and in the polyanion solution for 10 min. Between dips the substrate was vigorously washed with water and dried under a steam of compressed air. Sulfonated polystyrene solution (0.001 M, pH 1.0) was generally used as the polyanion dipping solution. The substrate was glass with positively charged surfaces. Optical absorption data generated during self-assembly of alternating layers of doped polypyrrole and sulfonated polystyrene indicated a linear build-up of the conducting polypyrrole polymer. The bilayer was observed to reproducibly contribute about 35 Angstrom to total thickness. Multilayer systems yielded good environmental stability, and exhibited conductivities as high as 50 S/cm after build-up of 15 bilayers. This confirms that highly conductive layered nanocomposites could be produced through ionic self-assembly.

In the alternate approach, it is necessary to first identify a suitable solvent system for the conductive polymer in its deped form. For polyaniline, dilute aqueous solutions can be formed by first dissolving the nonconducting emeraldine-base form of this polymer in DMAc, and subsequently diluting this solution with acidic water such that the final solution has a 90:10 water-DMAc volume ratio. The net result is a stable, water-based solution (90% water) of doped polyaniline that is quite well suited for ionic serl-assembly via alternate deposition with polyanions. In this exploratory work, solutions containing doped polyaniline were prepared by first dissolving 0.47 g of the emeraldine-base form of this polymer in 25 ml of dimethyllacetamide (DMAC); vigorous stirring and subsequent ultrasonic treatment to ensure complete dissolution. After all the polymer was dissolved, 3 ml of this solution was slowly added with stirring to 26 ml of pH 3.5 acidic water (acidified with methane sulfonic acid, MeSO$_3$H, or hydrochloric acid). The pH of the final polyaniline dipping solution was then adjusted to a level of 2.5 using 1 ml of pH 1.0 and 0.33 ml of pH 3.5 acidic water (acidified with methane sulfonic acid or hydrochlorid acid). Dipping solutions with polyaniline concentration of 0.01 M and a pH level of 2.5 were used. Sulfonated polystyrene (SPS, M$_w$=70,000 g/mol) solutions were made by stirring the SPS in MeSO$_3$H or HCl aqueous solutions. A 0.01 M, pH 2.5 SPS solution was used for diping. All solutions were filtered with

2-4 micron filter paper before use.  Multilayer nanocomposites were self-assembled by alternately dipping a substrate into the polyaniline-DMAC solution and SPS solution.  The substrate was dipped in each solution for 15 minutes and subsequently washed and rinsed with pH 2-4 solutions for 15 sec.  After each deposition and cleaning step, the system was blown dry with a gentle flow of compressed filtered air.  Optical absorption data confirmed linear build-up of multilayers (with sulfonated polystyrene used as polyanion); electrical conductivities of about 2 S/cm were obtained with only four layers of polyaniline deposited.

**Automation of Ionic Self-Assembly**

Our adaptation of ionic self-assembly requires build-up of multiple nanolayers of complex heterostructure to render structure and functional effects.  Manual build-up of this complex, multilayered nanocomposite is tedious and prone to error.  In order to ensure accuracy and expedient implementation of the ionic self-assembly process, we designed and fabricated an automatic system which offers substantial flexibility in selection of process variables.  This system (Figure 3.40) comprises a specimen container (Figure 3.41) designed with multiple valves (connected to different containers) which allows for filling the container with different solutions, emptying the container, and rinsing of specimens after exposure to various solutions.  The system can be programmed (Figure 3.42) to provide broad ranges of processing variables, including the number, sequences and durations of applications of various solutions, and the intensity and replication of rinsing processes.  This automated system allows for recycling of solutions.



*Figure 3.40.  Automated Self-Assembly System.*

Figure 3.41.  Specimen Container with Multiple Valves.

*Figure 3.42.  Programming Module of the Automated Self-Assembly System.*

The automated system shown in Figures 3.40 through 3.42 has been calibrated by comparing products of automated and manual self-assembly.  The automated system has been fine-tuned based on our experience in preliminary runs, and it has been used for ionic self-assembly of cellular structures and adaptive systems presented in later chapters.  Several options are being added to system in order to enhance its versatility, reliability and ease of use.

# CHAPTER 4

## SELF-ADAPTATION & SELF-HEALING THROUGH PIEZO-DRIVEN ELECTROLYSIS: REVIEW OF RELEVANT PRINCIPLES, AND DEVELOPMENT OF EXPERIMENTAL & THEORETICAL PROCEDURES

## Introduction

Service loads build mechanical energy into structural systems; structures are generally designed to withstand stresses and strains which are manifestations of this energy input. Our approach makes use of this energy input to transfer mass within the system to render adaptive and self-healing effects. Mechanical energy is converted to electric energy using the piezoelectric phenomenon; electrolysis processes in the context of a solid electrolyte are then used to transfer mass through electro-stripping and electro-deposision phenomena. The electrical signals also guide the mass transfer process toward producing a desirable stress distribution which yields self-healing and adaptation effects. Integration of various constituents into one hybrid system at proper proportions and with appropriate topology to meet both structural and functional requirements is a key challenge in development of the material system. This chapter presents reviews of piezoelectricity, electrolysis and solid electrolyte, and reviews our experimental and theoretical efforts towards integration of these principles in a self-healing and adaptive structural material.

## Piezoelectricity

### Introduction

Piezoelectricty, Greek for "pressure" electricity, was discovered by Curie brothers more than 100 years ago. They found that quartz changes its dimensions when subjected to an electrical field, and conversely, generated electrical charge when mechanically deformed. One of the first practical applications of the technology was made in the 1920's when a quartz transmitter/receiver system was developed for underwater sound – the first sonar. Before World War II, researchers discovered that certain ceramic materials could be made piezoelectric when subjected to a high polarizing voltage, a process analogous to magnetizing a ferrous material. By the 1960's, researchers had discovered a weak piezoelectric effect in whale bone and tendon. This began an intense search for other organic materials that might exhibit piezoelectricity. In 1969, Kawai found very high piezo-activity in the polarized fluoropolymer, Polyvinylidene fluoride (PVDF). While other materials like nylon and PVC exhibit the effect, none are as highly piezoelectric as PVDF and its copolymers. Like some other ferroelectric materials, PVDF is also highly pyroelectric, producing electrical charge in response to a change in temperature.

### Basic Principles of Piezoelectricity

For ordinary solids, a stress T merely causes a proportional strain S, related by an elastic modulus, $T = Y.S$. Piezoelectricity is the additional creation of an electric charge by the applied stress. This is the direct piezoelectric effect. The charge is proportional to the force, and it is therefore of opposite sign for compression and tension. In terms of dielectric displacement D (charge Q per unit area) and stress T, we may write $D = Q/A = d.T$, where d is expressed in coulombs/Newton. There is a converse effect. An applied field E produces a proportional strain S, expansion or contraction depending on polarity: $S = d.E$, where d is expressed in meters/Volt.

For both effects, the proportionality constant is the piezoelectric constant d, which is numerically identical for both direct and converse effects: $d = D/T = S/E$. High d constant is desirable for materials intended to develop motion or vibration, such as sonar or ultrasonic cleaner transducers.

Another frequently used piezoelectric constant is g, which gives the field produced by a stress. Its usual units are meter.volts/Newton, presented in simplified form $(V/m) / (N/m^2)$. The g constant is related to the d constant by the permittivity: $g = d/\varepsilon' = d/K.\varepsilon_o$. High g constant is desirable in materials intended to generate voltage in response to a mechanical stress, as in phonograph pickup.

Additional piezoelectric constant which are only occasionally used are e which relates stress T to field E, and h which relates strain S to field E:

$$T = -e.E$$
$$E = -h.S$$

The piezoelectric constants can be defined as partial derivatives evaluated at constant stress (subscript T), constant field (subscript E), constant displacement (subscript D) or constant strain (subscript S). We may think of these boundary conditions as "free", "short circuit", "open circuit", and "clamped", respectively. The actual definitions are:

$$d = (\partial S/\partial E)_T = (\partial D/\partial T)_E$$
$$g = (-\partial E/\partial T)_D = (\partial S/\partial T)_D = (\partial S/\partial D)_T$$
$$e = (-\partial T/\partial E)_S = (\partial D/\partial S)_E$$
$$h = (-\partial T/\partial D)_S = (-\partial E/\partial S)_D$$

These are derived from the equations of state of a solid body. The elastic, dielectric and piezoelectric constants may differ along different axes.

Possibly the best single measurement of the strength of a piezoelectric effect is the electromechanical coupling factor k. When an electric field is applied, it measures the fraction of the electrical energy converted to mechanical energy (or vice versa when a crystal or ceramic is stressed). The actual relationship is in terms of $k^2$:

$k^2$ = (electrical energy converted to mechanical energy) / (input electrical energy)

or

$k^2$ = (mechanical energy converted to electrical energy) / (input mechanical energy)

Since the conversion of mechanical to electrical energy is always incomplete, $k^2$ is always <1, and thus k is also <1. Typical values of k are 0.10 for quartz, 0.4 for barium titanate ceramic, 0.5-0.7 for $Pb(Ti, Zr)O_3$ ceramic, and as much as 0.9 for Rochelle salt at its 24$^o$C curie point.[59]

Our material system employs piezoelectricity to convert mechanical energy to electrical energy. Like water from a sponge, piezoelectric materials generate charge when squeezed. The amplitude and frequency of the signal is directly proportional to mechanical deformation of the piezoelectric material. The resulting deformation causes a change in surface charge density of the material so that a voltage appears between the electroded surfaces. When the force is reversed, the output

voltage is of opposite polarity. A reciprocating force thus results in an alternating output voltage. Piezoelectric materials are dynamic materials that develop an electrical charge proportional to a change in mechanical stress. Piezoelectric materials are not suitable for static measurements (true dc) due to their internal resistance. The electrical charge developed by piezoelectric materials decay with a time constant that is determined by the dielectric constant and the internal resistance of the material, as well as the input impedance of the interface electronics to which the film is connected. Practically speaking, the lowest frequency measurable with piezo film is in the order of 0.001 Hz. There are methods to achieve true dc response, but these require using the piezoelectric material as both an actuator and sensor, monitoring change in the actuation resulting from the dc event. The fundamental piezoelectric coefficients for charge or voltage predict, for small stress (or strain) levels, the charge density (charge per unit area) or voltage field (voltage per unit thickness) developed through the piezoelectric effect.

*Charge Mode of Behavior*

Under conditions approaching a short circuit, the general charge density is given by:

$$D = Q / A = d_{3n} . X_n \qquad (n = 1, 2, \text{ or } 3)$$

The mechanical axis (n) of the applied stress (or strain), by convention, is: 1 = length (or stretch) direction; 2 = width (or transverse) direction; 3 = thickness direction. In above equation, D = charge density developed; Q = charge developed; A = conductive electrode area; $d_{3n}$ = appropriate piezoelectric coefficient for the axis of applied stress or strain; n = axis of applied stress or strain; and $X_n$ = stress applied in the relevant direction. It is important to note that the $d_{3n}$ coefficient is commonly expressed in pico-Coulombs per Newton (pC/N), but the more correct form would be $(pC/m^2)/(N/m^2)$ since the area $(m^2)$ upon which the stresses or strains apply are very often different and cannot be "canceled".

*Voltage Mode Behavior*

The open-circuit output voltage is given by:

$$V_o = g_{3n}.X_n.t \quad (n = 1, 2, \text{ or } 3, \text{ as above})$$

where, g = appropriate piezoelectric coefficient for the axis of applied stress or strain; $X_n$ = applied stress in the relevant direction; and t = the film thickness.

*Piezoelectric Coefficients*

The most widely used piezoelectric coefficients, $d_{3n}$ and $g_{3n}$ for charge and voltage respectively, possess two subscripts. The first refers to the electrical axis, while the second subscript refers to the mechanical axis. Because piezo electric polymer film is thin, the electrodes are only applied to the top and bottom film surfaces. Accordingly, the electrical axis is always "3", as the charge or voltage is always transferred through the thickness (n=3) of the film. The mechanical axis can be either 1, 2, or 3, since the stress can be applied to any of these axes, as shown in Figure 3.1. Typically, piezoelectric polymer films ar eused in the mechanical 1 direction for low frequency sensing and actuation (<100 kHz) and in the mechanical 3 direction for high ultrasound sensing and actuation (>100 kHz).
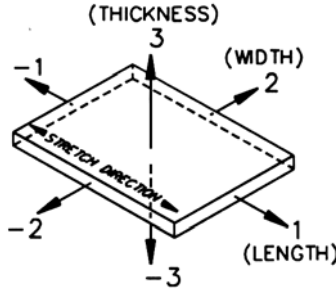
*Figure 4.1. Numerical Classification of Axes.*[60]

Piezoelectric materials are anisotropic; this means that their electrical and mechanical responses differ depending upon the axis of applied electrical field or axis of mechanical stress or strain. Calculations involving piezo activity must account for this directionality.

Table 4.1 presents some basic properties of piezoelectric polymer PVDF and piezoelectric ceramics PZT and $BaTiO_3$. Table 4.2 lists a more complete set of properties for piezoelectric polymers (PVDF and copolymer). Table 4.3 presents piezoelectric, elastic and dielectric constants of some PZT formulations. Measured effects on a $BaTiO_3$ ceramic show strains as large as 0.15% before rupture. The rate of creep depends on the applied stress, and the total deformation depends strongly on time. Typical behavior is shown in Figures 4.2 and 4.3. For fast loading, the samples were elastic; with maintained stress, anelastic effects were observed. Gamma and neutron irradiation up to the order of $10^8$ roentgens or $10^{12}$ nvt have been found to leave the piezoelectric properties of ceramics intact. The ceramics, therefore, appear to be suitable for use in space. Capacitance is a measure of any component's ability to store electrical charge, and is always present when two conductive plates are brought close together. In our case, the conductive plates are the conductive layers applied onto each surface of the film. The capacitance of the device is strongly affected by the properties of the insulator serving to space the plates apart, and the measure of the insulator's capacity to store charge is given by the dielectric constant or permittivity. PVDF has a high dielectric constant compared with most polymers, with its value being about 12 (relative to the permittivity of free space). Obviously, the capacitance of an element will increase as its plate area increases, so a large sheet of film will have a larger capacitance than a small element. Capacitance also increases as the film thickness decreases, so for the same surface geometry, a thin film will have a higher capacitance than a thick film. These factors are formally related in the equation:

$$C = \varepsilon\, A/t$$

where, C is the capacitance of the film, $\varepsilon$ is the permittivity (which can also be expressed in the form $\varepsilon = \varepsilon_t . \varepsilon_o$, in which $\varepsilon_t$ is the relative permittivity (about 12 for PVDF), and $\varepsilon_o$ is the permittivity of free space (a constant, $8.854 \times 10^{-12}$ F/m), A is the active (overlap) area of the film's electrodes, and t is the film thickness. The units of capacitance are Farads (F), but usually much smaller sub-multiples are encountered: microfarads ($\mu$F or $10^{-6}$F), nanofarads (nf or $10^{-9}$F) and picofarads (pF or $10^{-12}$F).

*Table 4.1.  Comparison of Piezoelectric Materials.*[60]

| Property | Units | PVDF Film | PZT | BaTi0$_3$ |
|---|---|---|---|---|
| Density | 10$^3$kg/m3 | 1.78 | 7.5 | 5.7 |
| Relative Permittivity | $\varepsilon/\varepsilon_0$ | 12 | 1,200 | 1,700 |
| $d_{31}$ Constant | (10$^{-12}$)C/N | 23 | 110 | 78 |
| $g_{31}$ Constant | (10$^{-3}$)Vm/N | 216 | 10 | 5 |
| $k_{31}$ Constant | % at 1 kHz | 12 | 30 | 21 |
| Acoustic Impedance | (10$^6$)kg/m$^2$-sec. | 2.7 | 30 | 30 |

*Table 6.1.  Typical Properties of Piezo Film.*[60]

| Symbol | Parameter | | PVDF | Copolymer | Units |
|---|---|---|---|---|---|
| t | Thickness | | 9, 28, 52, 110 | Various | μm (micron, 10$^{-6}$) |
| $d_{31}$ | Piezo Strain Constant | | 23 | 11 | 10$^{-12}$ $\frac{m/m}{V/m}$ or $\frac{C/m^2}{N/m^2}$ |
| $d_{33}$ | | | -33 | -38 | |
| $g_{31}$ | Piezo Stress constant | | 216 | 162 | 10$^{-3}$ $\frac{V/m}{N/m^2}$ or $\frac{m/m}{C/m^2}$ |
| $g_{33}$ | | | -330 | -542 | |
| $k_{31}$ | Electromechanical Coupling Factor | | 12% | 20% | |
| $k_t$ | | | 14% | 25-29% | |
| C | Capacitance | | 380 for 28μm | 68 for 100μm | pF/cm$^2$ @ 1kHz |
| Y | Young's Modulus | | 2-4 | 3-5 | 10$^9$ N/m$^2$ |
| $V_0$ | Speed of Sound | stretch: | 1.5 | 2.3 | 10$^3$ m/s |
| | | thickness: | 2.2 | 2.4 | |
| p | Pyroelectric Coefficient | | 30 | 40 | 10$^{-6}$ C/m$^2$ °K |
| $\varepsilon$ | Permittivity | | 106-113 | 65-75 | 10$^{-12}$ F/m |
| $\varepsilon/\varepsilon_0$ | Relative Permittivity | | 12-13 | 7-8 | |
| $\rho_m$ | Mass Density | | 1.78 | 1.82 | 10$^3$kg/m |
| $\rho_e$ | Volume Resistivity | | >10$^{13}$ | >10$^{14}$ | Ohm meters |
| $R_\square$ | Surface Metallization Resistivity | | 2.0 | 2.0 | Ohms/square for CuNi |
| $R_\square$ | | | 0.1 | 0.1 | Ohms/square for Ag Ink |
| tan $\delta_e$ | Loss Tangent | | 0.02 | 0.015 | @ 1kHz |
| | Yield Strength | | 45-55 | 20-30 | 10$^6$ N/m$^2$ (stretch axis) |
| | Temperature Range | | -40 to 80 | -40 to 115...145 | °C |
| | Water Absorption | | <0.02 | <0.02 | % H$_2$O |
| | Maximum Operating Voltage | | 750 (30) | 750 (30) | V/mil(V/μm), DC, @ 25°C |
| | Breakdown Voltage | | 2000 (80) | 2000 (80) | V/mil(V/μm), DC, @ 25°C |

Table 4.3. *Piezoelectric, Elastic and Dielectric Constants of Several Lead Titanate Zirconate Compostitions.*[59]

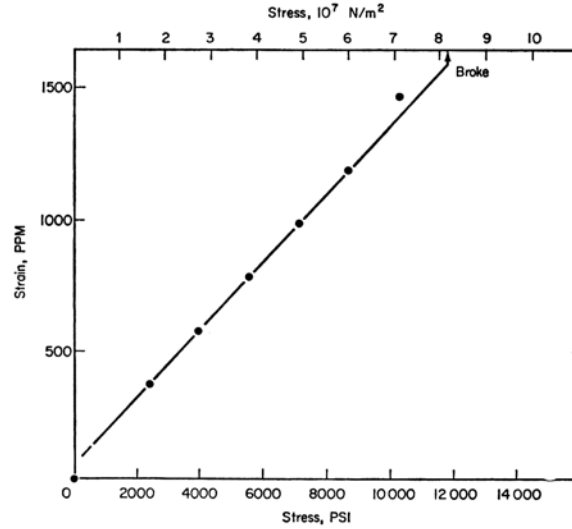| | $Pb(Ti_{0.48}Zr_{0.52})O_3$ | $(Pb_{0.94}Sr_{0.06})$ $(Ti_{0.47}Zr_{0.53})O_3$ | $Pb_{0.988}(Ti_{0.48}Zr_{0.52})_{0.976}$ $Nb_{0.024}O_3$ |
|---|---|---|---|
| Curie point, °C | 386° | 328° | 365° |
| $K_1^T$ | 1180 | 1475 | 1730 |
| $K_1^S$ | 612 | 730 | 916 |
| $K_3^T$ | 730 | 1300 | 1700 |
| $K_3^S$ | 399 | 635 | 830 |
| Dissipation factor | 0.004 | 0.004 | 0.02 |
| $k_p$ | $0.52_9$ | 0.58 | 0.60 |
| $k_{31}$ | $0.31_3$ | $0.33_4$ | $0.34_4$ |
| $k_{33}$ | $0.67_0$ | 0.70 | $0.70_5$ |
| $k_{15}$ | $0.69_4$ | 0.71 | $0.68_5$ |
| $d_{31}$, $10^{-12}$C/N | $-93.5$ | $-123$ | $-171$ |
| $d_{33}$ | 223 | 289 | 374 |
| $d_{15}$ | 494 | 496 | 584 |
| $g_{31}$, $10^{-3}$Vm/N | $-14.5$ | $-11.1$ | $-11.4$ |
| $g_{33}$ | 34.5 | 26.1 | 24.8 |
| $g_{15}$ | 47.2 | 39.4 | 38.2 |
| $h_{31}$, $10^8 V/m$ | | $-9.2$ | $-7.3$ |
| $h_{33}$ | | 26.8 | 21.5 |
| $h_{15}$ | | 19.7 | 15.2 |
| $e_{31}$, C/m² | | $-5.2$ | $-5.4$ |
| $e_{33}$ | | 15.1 | 15.8 |
| $e_{15}$ | | 12.7 | 12.3 |
| $s_{11}^E$, $10^{-12}$m²/N | 13.8 | 12.3 | 16.4 |
| $s_{33}^E$ | 17.1 | 15.5 | 18.8 |
| $s_{12}^E$ | $-4.07$ | $-4.05$ | $-5.74$ |
| $s_{13}^E$ | $-5.80$ | $-5.31$ | $-7.22$ |
| $s_{44}^E$ | 48.2 | 39.0 | 47.5 |
| $s_{66}^E$ | 38.4 | 32.7 | 44.3 |
| $s_{11}^D$ | 12.4 | 10.9 | 14.4 |
| $s_{33}^D$ | 9.35 | 7.90 | 9.46 |
| $s_{12}^D$ | $-5.38$ | $-5.42$ | $-7.71$ |
| $s_{13}^D$ | $-2.56$ | $-2.10$ | $-2.98$ |
| $s_{44}^D$ | 25.0 | 19.3 | 25.2 |
| $c_{11}^E$, $10^{10}$N/m² | | 13.9 | 12.1 |
| $c_{12}^E$ | | 7.78 | 7.54 |
| $c_{13}^E$ | | 7.43 | 7.52 |
| $c_{33}^E$ | | 11.5 | 11.1 |
| $c_{44}^E$ | | 2.56 | 2.11 |
| $c_{66}^E$ | | 3.06 | 2.26 |
| $c_{11}^D$ | | 14.5 | 12.6 |
| $c_{12}^D$ | | 8.39 | 8.09 |
| $c_{13}^D$ | | 6.09 | 6.52 |
| $c_{33}^D$ | 13.4 | 15.9 | 14.7 |
| $c_{44}^D$ | | 5.18 | 3.97 |
| $Q_M$ | 500 | 500 | 75 |

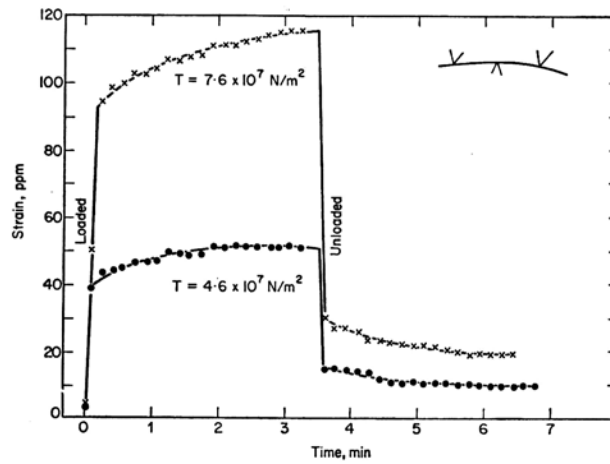*Figure 4.2.  Stress-Strain Relations for BaTiO₃ Ceramic, Fast Loading.*[59]



*Figure 4.3.  Tensile Strain As a Function of Time for Constant Loading (the measurements of strain were made with three point flexural loading – upper fight; maximum tensile strain and stress, T, are shown).*[59]

Equivalent Circuits

There are two equally valid "models" for electrical equivalent of the piezoelectric effect – one is a voltage source in series with a capacitance, the other a charge generator in parallel with a capacitance – but the latter is uncommon in electrical circuit analysis and we will concentrate on the voltage source (Figure 4.4).  The dashed line represents the "contents" of the piezo film component.  The voltage source $V_S$ is the piezoelectric generator itself, and this source is directly proportional to the applied stimulus (pressure, strain, etc.); voltage thus will absolutely follow the applied stimulus (it is a "perfect" source).  It should be noted that the node marked "X" in Figure4.4 can never be accessed.  The film's capacitance $C_o$ will always be present and connected when we monitor the "output" of the film at the electrodes.
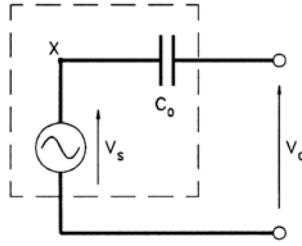
*Figure 4.4. Piezoelectric Polymer Film Element As a Simple Voltage Generator.*[60]

We can add the effect of connecting up the piezoelectric polymer film to an osciclloscope by adding a resistive load (Figure 4.5). The oscilloscope and its probe are modeled simply as a pure resistance, although in reality there will be a very small capacitance associated with the probe and the cable (usually in the region of 30 to 50 pF). This can be neglected if the film capacitance is significantly higher in value. The voltage measured across the load resistor $R_L$ will not necessarily be the same voltage developed by the "perfect" source ($V_S$). To see why, it is helpful to redraw this circuit in another way.
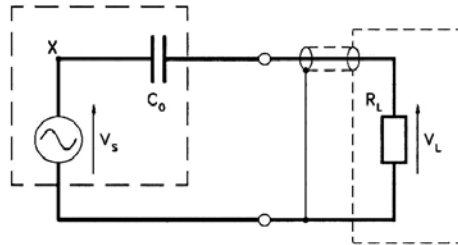


*Figure 4.5. Adding the Oscilloscope as Resistive Load.*[60]

With the circuit shown in Figure 4.5 redrawn as in Figure 4.6, it is easier to see why the full source voltage does not always appear across the resistive load. A potential divider is formed by the series connection of the capacitance and the resistance. Since the capacitance has an impedance which varies with frequency, the share of the full source voltage which appears across $R_L$ also varies with frequency. The proportion ($V_L$) of $V_S$ which appears across $R_L$ is given by $V_L = R_L / (R_L + Z_C)$, in which $Z_C = -j.X_C = -j / (2\pi.f.C)$, j denoting $\sqrt{-1}$, and $X_C$ being the reactance of the capacitive element. For simplicity, we ignore any resistive component of the film's impedance. These equations may be used in simple ways to calculate the voltage level expected to be observed in simple cases where the frequency of excitation is constant, and so a value of f can simply be substituted. In many real-world cases, however, there may be a distribution of signal energy over a band of frequencies. Then it becomes useful to consider the "frequency response" of the network, which is illustrated in the following.
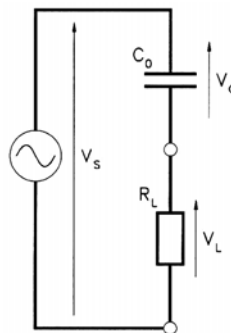


*Figure 4.6. Potential Divider.*[60]

**Electrolysis**

An electrolytic cell uses electrical energy to produce chemical change. The process of electrolysis involves forcing a current through an electrochemical cell to produce a chemical change for which the cell potential is negative; that is, electrical work causes an otherwise nonspontaneous chemical reaction to occur. Electrolysis has great practical importance; for example, charging a battery, producing aluminum metal, and chrome plating an object are all done electrolytically.

To electrochemical cell shown in Figure 4.7 has a galvanic potential of 1.10 V; it runs spontaneously (without any voltage application) to produce the following anodic and cathodic reactions: $Zn \rightarrow Zn^{2+} + 2e^-$ (anode); $Cu^{2+} + 2e^- \rightarrow Cu$ (cathode). In Figure 4.7, however, an external power source is applied, forcing electrons through the cell in the opposite direction of galvanic cell. This requires an external potential greater than 1.10 V, which must be applied in opposition to the natural cell potential. This device is an electrolytic cell. Notice that since electron flow is opposite in the two cases, the anode and cathode are reversed between the two cases. Also, ion flow through the salt bridge is opposite in the two cells. The fact that each $Cu^{2+}$ ion carries two electrons can be used to determine the amount of copper electrodeposited by the following equation upon transfer of a particular level of charge through the cell:
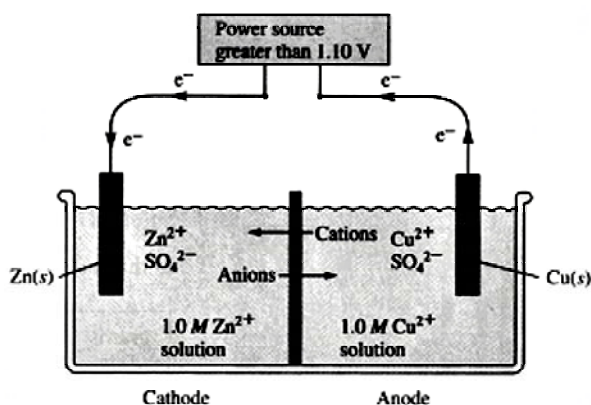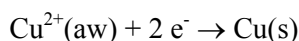
$$Cu^{2+}(aw) + 2\ e^- \rightarrow Cu(s)$$



*Figure 4.7. Electrolytic Cell.*[63]

Our approach uses the same electrode (e.g., copper) in the electrochemical cell; hence, the galvanic potential to be overcome (the sum total of reduction and oxidation potentials) is zero. This is because reduction and oxidation potentials are equal in value and opposite in sign, and thus cancel each other (as far as we neglect the relatively small effect of concentration on potential).[62] Even in this case, however, electrolysis would occur only if a minimum "overvoltage" is exceeded. The sources of this overvoltage are rather complex. Basically, the phenomenon is caused by difficulties in transferring electrons from the species in electrolyte to atoms on the electrode across the electrode-electrolyte interface. This phenomenon is further described below; it is critical to our application because we should design the piezoelectric system not only to provide sufficient charge for mass transfer but also sufficient voltage to overcome the overvoltage of the system.

*Double-Layer Effects*

We have assumed in above discussion that the potential drop between the electrode and electrolyte occurs entirely within the immobile Helmholtz layer and that a molecule or ion experiences no variation in potential as it approaches the electrode. This ideal situation is rarely, if ever, obtained and a correction is usually required. Thus the apparent electron-transfer rate constant determined using equations $i_0 = i_{c,e} =$

$F.A.k_0.C_O{}^*.\exp[-\alpha F(E_e-E^o)/(RT)]$   and   $i_0 = -i_{a,e} = F.A.k_0.C_R{}^*.\exp[\beta F(E_e-E^o)/(RT)]$ (presented earlier) should be corrected by:

$$k_0 = (k_0)_{app}.\exp\{[-(\beta.z_0+\alpha.z_r).F.\Phi_a]/(RT)\}$$

where, $\Phi_a$ is the surface potential (at x=0) relative to the bulk solution. The difference in the work terms due to the double-layer effect is:

$$\omega_o - \omega_r = F.\Phi_a$$

so that there may be a contribution to the transfer coefficients.. For $E \approx E^o$:

$$\alpha = \tfrac{1}{2} - F.\Phi_a/4\lambda$$

The double-layer contributions to the exchange current and transfer coefficients depend on the sign and magnitude of the surface potential $\Phi_a$. $\Phi_a$ is expected to go through zero at the potential of zero charge. Thus, for example, the potential of zero charge for mercury is about –0.43 V (vs. s.c.e.) so that $\Phi_a$ is positive for an electrode potential E > -0.43 V. The potential of zero charge can be determined, at least approximately, by the maximum in electro-capillary curve (for liquid electrodes) or by the minimum in double-layer capacitance vs. potential curve.

*Current-Overpotential Curve*

When the over-potential $\eta$ is sufficiently large, $|F\eta/RT| \gg 1$, one of the exponential terms in equation $i = i_0.\{\exp[(-\alpha F\eta/(RT)] - \exp[\beta F\eta/(RT)]\}$ (presented earlier) will be negligible compared with the other. For example, when the over-potential is large and negative, the anodic component of the current is negligible and we have:

$$i = i_0.\exp[-\alpha F\eta/(RT)]$$
$$\ln i = \ln i_0 - \alpha F\eta/(RT)$$

or, at 25$^o$C,

$$\log i = \log i_0 - 16.90\ \alpha\eta$$

The above logarithmic, $\ln i = \ln i_0 - \alpha F\eta/(RT)$, current-potential relationship (Tafel equation) suggests the means by which the exchange current and the transfer coefficient may be determined. If, for an equilibrium mixture of O and R, the current is measured as a function of over-potential and then plotted as log i vs. $\eta$, a linear region should be found. Extrapolation of the linear portions of the plot to zero over-potential yields the log of the exchange current as the intercept; the slopes should be –16.90 $\alpha$ and 16.90 $\beta$. Such a plot is shown in Figure 4.8. The Tafel equation and Figure 4.8 suggest that the current increases exponentially with increasing over-potential. There must be a point at which the current becomes limited by the rate of transport, and log i vs. $\eta$ plots begin to flatten out. The point at which this happens depends on the efficiency of stirring and on the diffusion coefficients of the electro-active species, but more critically on the electron-transfer rate. For slow electron-transfer processes such as the reduction of $H^+(aq)$ at a mercury cathode, the exchange current is so small that the rate of transport is rarely a problem. For faster processes, however, the Tafel plot approach may be impractical because, with increasing over-potential, transport limitation sets in before the linear Tafel region has been established.
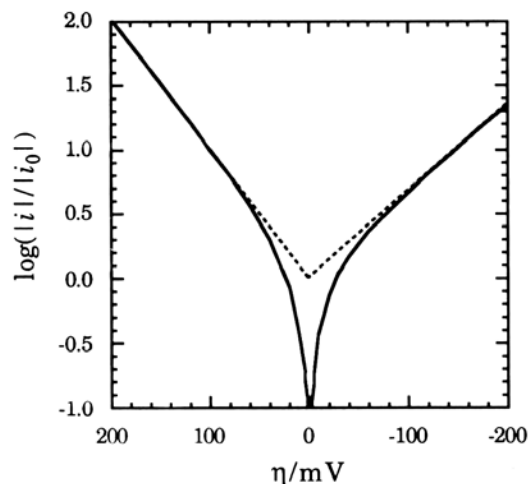
*Figure 4.8.  Tafel Plot: $log(|I|/i_0)$ vs. $\eta$ for $\alpha=0.4$; the slopes of the dashed lines are $\beta F/2.3RT=10.14$ $V^{-1}$ and $-\alpha F/2.3RT=-6.76$ $V^{-1}$.*

*Meausres of Electrolyte Conductivity*

Molar Conductivity

The observation that current increases with increasing salt concentration led to the notion of molar conductivity, which approximately factors out the concentration dependence.  Molar conductivity is defined by    $\Lambda = \kappa / C$, with C denoting concentration in mol/m$^3$ (1 mol/m$^3$ = 10$^{-3}$ mol/l = 1 mM).  The units of $\Lambda$ are S.m$^2$/mol.  The molar conductivities of several salts are plotted as functions of concentration in Figure 4.9.  The molar conductivity depends on concentration; the magnitude of dependence varies from one salt to another, but in every case the variation is greatest at low concentrations.  Various empirical equations have been tried to fit this concentration dependence, with the conclusion that the limiting behavior for strong (i.e., completely ionized) electrolytes is:

$$\Lambda = \Lambda^o - s.C^{0.5}$$

where, $\Lambda^o$ is the molar conductivity extrapolated to infinite dilution, and the slope s depends on the electrolyte and solvent.
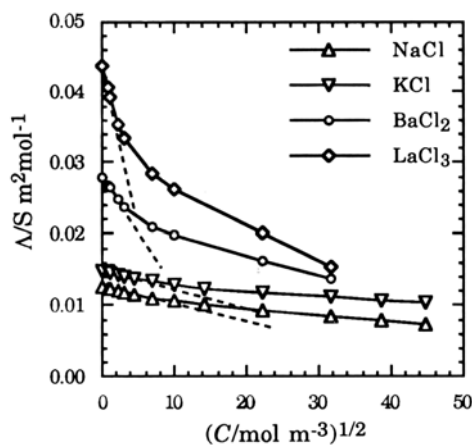


*Figure 4.9.  Molar Conductivities of Several Salts at 298$^o$K Vs. Concentration (the dashed lines represent the linear extrapolation to infinite dilution using the equation presented above).*

86

## Ionic Conductivities

If, at infinite dilution, the behavior of electrolytes is indeed ideal (i.e., we can neglect inter-ionic interactions), and if electrolytes are completely ionized, then the molar conductivity of an electrolyte should be the sum of the molar conductivities of the individual ions. If one mole of the salt produces $v_+$ moles of cations with molar conductivity $\Lambda_+^0$ and $v_-$ moles of anions with molar conductivity $\Lambda_-^o$, then:

$$\Lambda^o = v_+ . \Lambda_+^o + v_- . \Lambda_-^o$$

The molar conductivity of an individual ion cannot be measured directly, but if the above equation is correct, then subtracting the molar conductivities of NaCl and KCl, for example, should give the difference between the molar conductivities of the sodium and potassium ions. Comparing KCl and NaCl, the difference is $23.2 \times 10^{-4}$ $S.m^2/mol$, for KI and NaI, the difference is $23.82 \times 10^{-4}$ $S.m^2/mol$, and for $KbrO_3$ and $NaBrO_3$ the difference is $23.32 \times 10^{-4}$ $S.m^2/mol$; the agreement is thus quite good.

## Transference Numbers

When current passes through an electrolyte solution, it is carried in part by cations moving toward the cathode and in part by anions moving toward the anode. The fractions of total current carried by positive and negative ions are called the transference numbers:

$$t_+ = v_+ \Lambda_+ / \Lambda \qquad\qquad t_- = v_- \Lambda_- / \Lambda$$

where, since $v_+ \Lambda_+ + v_- \Lambda_- = \Lambda$, the transference numbers must sum to 1: $t_+ + t_- = 1$. There are several experimental methods for determination of transference numbers.[1] With transference numbers available, the above equations can be used to separate molar conductivities into the contributions of positive and negative ions. If transference numbers are known over a range of concentrations, they can be extrapolated to infinite dilution in order to obtain the infinite dilution ionic conductivities, $\Lambda_+^o$ and $\Lambda_-^o$.

## Ionic Mobilities

It is sometimes useful to think of the transport of an ion in terms of its mobility. The mobility of an ion is defined as the velocity per unit electric field strength:

$$u_i = \frac{|v_i|}{|E|}$$

To see how mobility is related to molar conductivity, we start with Ohm's law, written in the form $i = \Delta\Phi/R$. If the potential difference across a conductance cell of length L is $\Delta\Phi$, the field strength is $E = -\Delta\Phi/L$. With $\kappa = L / (R.A)$ rearranged to $R = L/A\kappa$, we have:

$$i = -\kappa.A.E$$

Now consider 1 $m^3$ of solution containing $C_i$ moles of ions carrying charge $z_i.F$ coulombs $mol^{-1}$ and moving with an average velocity $v_i$. The contribution to the current density across the end of the cubic meter is the product of these three factors:

$$(i/A)_I = C_i.z_i.F.v_i$$

Combining the above two equations we have:

$$v_i = -\frac{\kappa_i.E}{C_i.|z_i|.F}$$

or, with $u_i = \dfrac{|v_i|}{|E|}$, $\qquad u_i = -\dfrac{\kappa_i}{C_i.|z_i|.F}$

Finally, with the definition of molar conductivity $\Lambda = \kappa / C$, we have:

$$u_i = -\frac{\Lambda_i}{|z_i|.F}$$

Thus ionic mobilities at infinite dilution can be obtained from molar ionic conductivities such as those given in Table 4.4.

*Table 4.4. Molar Ionic Conductivities.*[62]

| Ion | $\Lambda°$ | Ion | $\Lambda°$ | Ion | $\Lambda°$ |
|---|---|---|---|---|---|
| $H^+$ | 349.8 | $Pb^{2+}$ | 139.0 | $IO_3^-$ | 40.5 |
| $Li^+$ | 38.7 | $Mn^{2+}$ | 107. | $IO_4^-$ | 54.6 |
| $Na^+$ | 50.1 | $Fe^{2+}$ | 107. | $MnO_4^-$ | 62.8 |
| $K^+$ | 73.5 | $Co^{2+}$ | 110. | $HCO_3^-$ | 44.5 |
| $Cs^+$ | 77.3 | $Ni^{2+}$ | 108. | $H_2PO_4^-$ | 36. |
| $NH_4^+$ | 73.6 | $Al^{3+}$ | 189. | $HCO_2^-$ | 54.6 |
| $(CH_3)_4N^+$ | 44.9 | $Cr^{3+}$ | 201. | $CH_3CO_2^-$ | 40.9 |
| $(C_2H_5)_4N^+$ | 32.7 | $Fe^{3+}$ | 204. | $C_2H_5CO_2^-$ | 35.8 |
| $(C_3H_7)_4N^+$ | 23.4 | $OH^-$ | 199.2 | $C_6H_5CO_2^-$ | 32.4 |
| $Ag^+$ | 61.9 | $F^-$ | 55.4 | $CO_3^{2-}$ | 138.6 |
| $Mg^{2+}$ | 106.1 | $Cl^-$ | 76.3 | $SO_4^{2-}$ | 160.0 |
| $Ca^{2+}$ | 119.0 | $Br^-$ | 78.1 | $S_2O_3^{2-}$ | 174.8 |
| $Sr^{2+}$ | 118.9 | $I^-$ | 76.8 | $CrO_4^{2-}$ | 170. |
| $Ba^{2+}$ | 127.3 | $CN^-$ | 78. | $HPO_4^{2-}$ | 114. |
| $Cu^{2+}$ | 107.2 | $NO_2^-$ | 72. | $C_2O_4^{2-}$ | 148.3 |
| $Zn^{2+}$ | 105.6 | $NO_3^-$ | 71.5 | $P_3O_9^{3-}$ | 250.8 |
| $Cd^{2+}$ | 108.0 | $ClO_3^-$ | 64.6 | $Fe(CN)_6^{3-}$ | 302.7 |
| $Hg^{2+}$ | 127.2 | $ClO_4^-$ | 67.4 | $Fe(CN)_6^{4-}$ | 442. |

Frictional Coefficients

When an ion moves through solution, it is subject to a viscous drag force proportional to the ion's velocity:

$$F_i = -f_i.v_i$$

where, the proportionality constant $f_i$ is called a frictional coefficient. Under steady-state conditions, the ion moves at constant velocity so that the viscous drag force exactly cancels the electrical driving force, $z_i.e.E$, and the net force is zero: $F_i = z_i.e.E - f_i.v_i = 0$ or $u_i = \left|\frac{v_i}{E}\right| = \frac{|z_i|.e}{f_i}$ , or, using the previously

presented equation $u_i = -\frac{\Lambda_i}{|z_i|.F}$, one gets: $\Lambda_i = \frac{z_i^2.F.e}{f_i}$

The motion of an ion through solution can thus be described equivalently in terms of molar ionic condutivities, ionic mobilities, or frictional coefficients.

Stokes' Law Radii

Still another way of thinking about the rate at which ions move through solution is by imagning the ion to be a hard sphere of effective hydrodynamic radius $r_i$ and frictional coefficient given by Stokes' law:

$$F_i = 6\pi.\eta.r_i$$

Substituting the above equation into $u_i = \left|\frac{v_i}{E}\right| = \frac{|z_i|.e}{f_i}$, we solve for the Stokes' law radius $r_i$:

$$r_i = \frac{|z_i|.F}{6\pi\eta.N_A.u_i}$$

where, e has been replaced by $F/N_A$.

Faster moving ions, of course have smaller Stokes' law radii, and slower ones have larger radii. While Stokes' law is not really valid for small ions in ordinary solvents, Stokes' law radii do give a rough measure of the effective size of ionic species as they move through a solution. Some Stokes' law radii are compared with ionic radii from crystal structure data. Several insights can be obtained from examination of these data. In the first place, it is hard to imagine a hydrodynamic radius being smaller than the crystal radius of the same ion. The Stokes' law radii are probably systematically underestimated, perhaps by about a factor of 2. However, within a related series of ions, e.g., the alkali metal cations, the trends are interesting. The crystal radii increase, as expected, in the series $Li^+ < Na^+ < K^+$, but the Stokes' law radii go in the opposite direction. This must mean that the small, highly polarizing $Li^+$ ion tightly binds a lot of solvent molecules which must move with the ion as a unit. The same effect is seen in comparison of the alkaline earth cations $Mg^{2+}$, $Ca^{2+}$, and $Ba^{2+}$. The three halide ions, $Cl^-$, $Br^-$ and $I^-$ all have about the same Stokes' law radii despite an increase in the crystal radii; this again is consistent with larger, less polarizing ions binding fewer solvent molecules or binding them less tightly so that fewer move as a unit. Comparing the isoelectronic ions $Na^+$, $Mg^{2+}$ and $Al^{3+}$, we see an even more dramatic effect which has the same qualitative explanation. Extending the comparison to $F^-$, which is isoelectronic with $Na^+$ and has about the same crystal radius, we see that the solvation sheath is apparently greater for $Na^+$ than for $F^-$, consistent with the idea that cations are rather more specifically solvated (formation of coordinate covalent bonds) than are anions (orientation of water dipoles and/or hydrogen bonding).

From crystal structure data, $OH^-$ and $F^-$ would be expected to be nearly the same size, but the Stokes' law radius of $OH^-$ is 47 pm, much less than the radius of any other anion. A similar discrepancy is found for $H^+$, which has a Stokes' law radius of 26 pm. Structural evidence suggests that $H^+(aq)$ is better represented by $H_3O^+$, which might be expected to have a Stokes' law radius comparable to $Li^+$ or $Na^+$, say about 200 pm. The anomalously high conductivities of $H^+$ and $OH^-$ in water can be understood if we recall that these water-related ions are part of an extensive hydrogen-bonded network involving solvent water molecules. A small shift in hydrogen bonds thus can move the charge from one oxygen center to another, and several such shifts can move the charge much faster than any of the nuclei travel. \Thus the conductivity is much higher than might have been expected from the size of the $H_3O^+$ or $OH^-$ ions.

Theoretical Treatment of conductivity

Kohlrausch's discovery that molar conductivity varies as the square root of concentration, $\Lambda = \Lambda^o - s.C^{0.5}$, attracted the attention of several theoreticians, most notably Onsager, who derived a conductance limiting law starting from the Debye-Huckel treatment of the ion atmosphere. Onsager's result can be written as:

$$\Lambda = \Lambda^o - \frac{|z_1.z_2|.F^2.\Lambda^o}{12\pi\varepsilon\varepsilon_o x_A RTN_A}.\frac{q}{1+\sqrt{q}} - \frac{(|z_1|+|z_2|).F^2}{6\pi\eta N_A x_A}$$

where, $x_A$ is the ion atmosphere thickness, $\eta$ is the solvent viscosity, $z_1$ and $z_2$ are the positive and negative ion charges, and

$$q = \frac{z_1.z_2}{(z_1 - z_2).(z_2.t_1 - z_1.t_2)}$$

where, $t_1$ and $t_2$ are the transference numbers. When $z_1 = -z_2$ (a 1:1 or 2:2 electrolyte), $q=1/2$ and is independent of the transference numbers. The other parameters have their usual significance. Both

correction terms are proportional to $1/x_A$, which in turn is proportional to the square root of ionic strength, matching the $C^{0.5}$ dependence discussed earlier.

The first term in the Onsager limiting law arises from the so-called ion atmosphere relaxation effect. When an ion is attracted by an electric field, it is also subject to an opposite force exerted by its ion atmosphere, which tends to restrain the ion and thus lowers its contribution to the solution conductance. The effect increases with the density of ions in the atmosphere, i.e., inversely proportion to $x_A$. The second correction term results from the electrophoretic effect. When the ion in question moves through the solution, it tends to take its ion atmosphere with it, resulting in a viscous drag force opposing the motion, thus the dependence on viscosity. Like Debye-Huckel theory from which it is derived, Onsager's theory is a limiting law valid only at very low concentrations, usually less than 0.001 M.

Basic Theory of Electrolysis

*Bulk electrolysis*

In 1833, Farady summarized the quantitative aspects of electrolysis experiments in two statements which have come to be known as Faraday's laws of electrolysis: *"The weight of metal plated on the cathode during passage of current through a solution of the metal salt is proportional to: (1) the charge passed through the solution; and (2) the equivalent weight (atomic weight/oxidation number) of the metal."* In modern terms, we would say that one mole of electrons (one Faraday) will reduce one mole of $Na^+$, one-half mole of $Ca^{2+}$, or one-third mole of $Al^{3+}$. Faraday's work not only put electrolysis on a quantitative basis but laid the groundwork for the more complete understanding of the role of electrons in chemistry which began to emerge 50 years later.

*Exhaustive Electrolysis*

When an electrolyte solution is subjected to electrolysis, either to separate a component of the solution or to oxidize or reduce a substrate, rather large amounts of electrical charge must be passed through the cell. Hence, the first concern is to see how current can be increased to obtain significant net electrolysis in a reasonable time. One obvious way to increase the current through an electrolysis cell is to stir the solution, thus increasing the rate of mass transport. In a stirred solution, the diffusion layer thickness can be reduced to as little as tens of microns. Suppose that the electrode process is $O + N\ e^- \rightarrow R$, and that a linear concentration gradient in O is set up across a diffusion layer of constant thickness. If the potential of the working electrode is sufficiently negative that the concentration of O is zero at the electrode surface, then the current is given by $i = n.f.A.k_D.C_O^*$ where, $k_D = D/x_D$ is the mass transport rate constant. The number of moles of O reduced is related to charge transferred by $dn_O = -dQ/(n.F)$. Since $dQ = i.dt$ and $dn_O = V.d.C_O^*$ (V is the solution volume), the change in bulk concentration on passage of current for a time interval dt is $dC_O^* = -[i/(n.f.V)].dt$. Substituting $n.f.A.k_D.C_O^*$ for i, we have $dC_O^* = -[(A.k_D.C_O^*)/V].dt$. Integration of this expression gives:

$$C_O^*(t) = C_O^*(0).exp(-kt)$$

where, $k = k_D.A/V$. Hence, we expect the bulk concentration $C^*$ to fall exponentially with a rate proportional to the rate of mass transport and to the ratio of the electrode area to solution volume. Thus if the process is to be completed in minimum time, the general strategy for exhaustive electrolysis should include efficient stirring and a high area-to-volume ratio. Since the stirring must be particularly efficient at the working electrode surface, careful attention to electrode geometry is required for optimum performance.

An example explaining the above principles considers 250 cm$^3$ of 0.1 M CuSO$_4$ to be electrolyzed using a cathode area of 250 cm$^2$ and an initial current of 5A. The time required for removal of 99% of the copper from solution is to be found in this example, assuming that the cathode process is rate limiting, From

equation $i=n.f.A.k_D.C_o^*$ we obtain the diffusional rate constant $k_D=i/2FAC_O^*$. Substituting the electrode area and the initial current and concentration, we have $k_D=1.04\times10^{-5}$ m/s. With the area-to-volume ratio of 100 $m^{-1}$, equation $k=k_D.A/V$ gives $k=1.04\times10^{-3}$ $s^{-1}$. To reduce the copper concentration from 0.1 M to 0.001 M thus requires a time $t=-[\ln(0.01)]/k=4440$ s (74 minutes). To reduce the concentration to $10^{-5}$M amounts to another factor of 100 decrease in concentration and thus will require another 74 minutes or 140 minutes in all.

*Electroplating*

An important application of electrodeposition is the plating of a layer of metal on an object to improve the appearance or to impart hardness or corrosion resistance. Metals commonly used in electroplating include Cr, Ni, Zn, Cd, Cu, Ag, Au, Sn, and Pb. Some alloys such as brass (Cu/An) and bronze (Cu/Sn) also can be electroplated.

The basic theory of electroplating is extremely simple For example, to plate copper on a steel substrate, the object to be plated is made cathode in an electrolysis cell where a piece of copper is used as the anode. There are many subtleties, however, which must be considered in practice. Thus, in plating copper on steel, for example, we immediately recognize that the reaction $Cu^{2+}(aq) + Fe(s) \rightarrow Cu(s) \_ Fe^{2+}(aq)$ is spontaneous. To prevent the dissolution of iron from substrate, the activity of $Cu^{2+}(aq)$ must be reduced by the addition of a complexing agent which coordinates strongly to Cu(II) but much less so than Fe(II).

In electroplating applications, it is usually desirable to deposit a layer of uniform thickness. This requirement is not difficult to meet if the substrate has a simple geometry. If there are holes or recesses, however, a uniform layer can be quite difficult to achieve.

When a potential is applied across an electrolysis cell, the potential drop is the sum of several contributions:[62]

1. the equilibrium anode-solution and solution-cathode potentials (i.e., the equilibrium cell potential);
2. the activation and polarization overpotentials at the anode and cathode; and
3. the solution iR drop.

Since the iR potential drop is proportional to the length of the current path, it will be smallest at that part of the cathode which is closest to the anode. Since the total cell potential is constant, this means that the cathodic overpotential will be greatest at that closest part of the cathode. The current density – and the deposited layer thickness – will be greatest, therefore, at exposed parts of the cathode.

Electroplaters refer to the ability of a plating bath to deposit metal at hard to reach spots in terms of the throwing power of the bath. The throwing power of a plating bath can be controlled (to some extent) in three ways: (1) by adding a large concentration of an inert electrolyte, the solution resistance is lowered and differences in iR drop to various points on the cathode surface are reduced; (2) by operating the bath under conditions for which $H_2(g)$ evolution occurs at exposed points where the overpotential is large, the iR drop is increased locally, thus reducing the overpotential and slowing the rate of plating at these exposed points; (3) by adding a complexing agent, the electrode process is converted to: $ML_x^{n+} + n\ e^- \rightarrow M + x\ L$. It is generally found that complexing agents decrease the slope of a Tafel plot (log i vs. $\eta$), so that current variations with overpotential are smaller. In addition, throwing power is usually found to be a function of temperature through the temperature dependences of various rate processes involved. Plating baths with good throwing power usually have optimized all these parameters, most commonly through trial-and-error investigations.

The nature of an electroplated metal deposit can be modified by the addition of organic additives to perform one or more of the following functions: (1) wetting agents facilitate the release of bubbles of $H_2(g)$ from the surface, preventing the occlusion of hydrogen in the deposit and enhancing current density control by hydrogen evolution; (2) Levelers are preferentially adsorbed at surface dislocations and sharp corners and thus inhibit current flow at the points at which the current density would otherwise be highest; (3) Structure modifiers and brighteners change the nature of the deposited layer, perhaps changing the crystal growth pattern or reducing the crystallite size in the deposited layer.

In most commercial electroplating operations, the current efficiency (i.e., the fraction of current which produces the desired metal deposit) is high, 90% or better. The most notable exception is in chromium plating, where chromium is added to the bath as $CrO_3$ and the plating process is based on the six-electron reduction of Cr(VI). Here Cr(III) is an unwanted by-product, unreducible under normal experimental conditions. The detailed electrode process is not well understood, but there are apparently several current-consuming side reactions.

Organic polymer coatings can be applied to metal surfaces by a technique called electrophoretic painting, which is closely related to electroplating. The polymer to be deposited is soluibilized with charged functional groups. In anodic electropainting, negatively charged groups, usually $-CO_2^-$, cause the polymer molecules to move toward the anode, where water is oxidized to $O_2$ and $H^+$. The local decrease in pH leads to neutralization of the carboxylate groups and the polymer precipitates. In cathodic electropainting, positively charged polymers with $-NH_3^+$ groups are attracted to the cathode, where water is reduced to $H_2$ and $OH^-$, the ammonium groups are neutralized, and the polymer deposited on the surface. Electropainted polymer coatings adhere exceptionally well, apparently because of coordination of surface metal atoms by the polar functional groups. The technique is commonly used to impart corrosion resistance to automobile parts.

Electrical Work

The first law of thermodynamics may be states as $\Delta U = q + w$, in which $\Delta U$ is the change in the internal energy of the system, q is the heat absorbed by the system, and w is the work done by the system. In elementary thermodynamics, we usually deal only with mechanical work, for example the work done when a gas is compressed under the influence of pressure (dw=-P.dV) or the expansion of a surface area under the influence of surface tension (dw=$\gamma$.dA). However, other kinds of work are possible and here we are especially interested in electrical work, the work done when an electrical charge is moved through an electric potential difference.

Consider a system which undergoes a reversible process at constant temperature and pressure, in which both mechanical (P-V) work and electrical work are done, w=-P.$\Delta$V + $w_{ele}$. Since, for a reversible process at constant temperature, q=T.$\Delta$S, equation $\Delta U = q + w$ becomes $\Delta U_{T,P} = T.\Delta S - P.\Delta V + w_{elec}$. At constant pressure, the system's enthalpy change is $\Delta H_P = \Delta U_P + P.\Delta V$, and at constant temperature, the Gibbs free energy change is $\Delta G_T = \Delta H_T - T.\Delta S$. Combining the above three equations, we have:

$$\Delta G_{T,P} = w_{elec}$$

Now let us see how electrical work is related to the experimentally measurable parameters which characterize an electrochemical system. Consider an electrochemical cell (the thermodynamic system) which has two terminals across which there is an electric potential difference, E. The two terminals are connected by wires to an external load (the surroundings), represented by a resistance R (Figure 4.10). When a charge Q is moved through a potential difference E, the work done on the surroundings is E.Q. The charge passed in the circuit is the product of the number of charge carriers and the charge per charge carrier. If we assume that the charge carries are electrons, then:

$$Q = \text{(number of electrons) x (charge/electron)} = N.e$$

or

$$Q = \text{(number of moles electrons) x (charge/mole)} = n.F$$

where, F is the Faraday constant, the charge on one mole of electrons, 96,484.6 coulombs (C), and n is the number of moles of electrons transferred. Thus the work done by the system on the resistor (the resistor's energy is raised) is simply $n.F.E$. However, according to the sign convention of equation $\Delta U = q + w$, work done on the system is positive so that the electrical work is negative if the system transfers energy to the surroundings:

$$W_{elec} = -n.F.E$$

Substituting the above equation into equation $\Delta G_{T,P} = w_{elec}$, we obtain the change in Gibbs free energy of the system:

$$\Delta G_{T,P} = -n.F.E$$

If E is measured in volts (V), F in $C\ mol^{-1}$, and n is the number of moles of electrons per mole of reaction $(mol\ mol^{-1})$, then $\Delta G$ will have the units of joules per mole $(J\ mol^{-1})$ since $1\ J = 1\ V\text{-}C$. This quite remarkable result immediately demonstrates the utility of electrochemical measurements. We have a direct method for the determination of changes in the Gibbs free energy without recourse to measuring equilibrium constants or enthalpy and entropy changes.
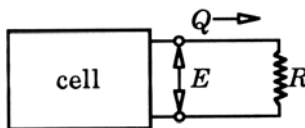


*Figure 4.10. Electrochemical Cell Doing Work on An External Resistance.*

**Solid Electrolytes**

Introduction

It has been known for many years that polyethers and various salts are capable of direct interaction and, indeed, these complexing properties have been widely used in organometallic chemistry. In 1973, Dr. P. V. Wright first reported the conducting properties of "solvent-free" poly(ethylene oxide)-slat systems, but it was in 1978 that Professor M.B. Armand highlighted the potential of these materials as a new class of solid electrolytes for energy storage applications. Most of early work carried out on polymer electrolytes concentrated on poly(ethylene oxide) (PEO) and related homopolymers as the host for a number of salt species. Although a wide variety of polymer structures have now been made in an attempt to optimize electrical properties and/or mechanical and electrochemical stability, many of these incorporate PEO as the coordinating component.

It is possible to dissolve appropriate salts into some polymers, but then the dissolved salt is not completely dissociated into single ions only. Ion pairs, triplets and even higher aggregates exist in equilibrium with dissociated ions. The issue of ion association is important because it is common for most polymers to be poor salt solvents due to their low electrical permittivity. If we focus on monovalent salts, ion pairs will be neutral species with a permanent dipole moment that may be stronger than that of other types of aggregates. Since the polymer itself is a low permittivity material, the permittivity contribution from the ion pairs can be detected in dielectric measurements.[64]

Common Preparation Methods of Polymer Electrolyte Films

By far the most common method of producing polymer electrolyte thin films is by solvent casting. This involves preparing a solution of the polymer and salt; for PEO-salt systems, a 4% solution of the

components in acetonitrile or methanol is most commonly used. This solution is cast into formers on a polytetrafluoroethylene (PTFE) surface, the solvent is removed by slow evaporation, and the final film is heated under vacuum to remove residual solvent. Many polymer electrolytes are semicrystalline, and crystal formation may be significantly affected by the nature of the solvent, by the rate of solvent removal, and by traces of residual solvent which is capable of acting either as nucleation sites or as a plasticizer. In addition, the temperature at which films undergo final drying is important. Higher temperatures usually induce the formation of high-melting spherulites as the sample cools. Consistency in casting techniques is important as demonstrated by the problems associated with phase diagram construction, but in practice, no common criteria are universally observed.

To eliminate the effects of solvent, a grinding/hot pressing technique has been developed for film preparation. This involves grinding the polymer to a fine powder under liquid nitrogen and subsequently milling appropriate quantities of the polymer and salt together to form an intimate mixture. CHN microanalysis has indicated that a homogeneous distribution can be achieved for O:cation concentration ratios as low as 50:1. After the samples were annealed at 120 to 150$^{\circ}$C, they were cooled under pressure to form thin films. Conductivities were found to be significantly higher than those of solvent cast material, also annealed in this temperature region. A similar technique has also been employed where KI and PEO were milled on a two-roll mill at 80$^{\circ}$C. A good distribution was achieved after 10 to 15 min. Changes in melting point, $T_g$, and stiffness modulus of the material, after various quantities of salt were milled into the polymer, were interpreted as association of the KI with PEO.

One-micon films of PEO-LiCF$_3$SO$_3$ have been prepared by evaporating the components onto a silica substrate in a $1 \times 10^{-4}$ Pa vacuum. The molecular weight of the polymer was initially $4 \times 10^6$, and after deposition, gel permeation chromatography indicated the molecular weight range to be 200 to 2000. The materials were wax-like and exhibited conductivities comparable to those of fully amorphous systems. Differential scanning calorimetry (DSC) traces showed diffuse endotherms in the temperature region –20 to 50$^{\circ}$C.

Ultra-thin polymer electrolyte films of the order of 1 micron in thickness have been prepared by plasma polymerizaiton of tris(2-methoxyethoxy)vinyl silane. A layer of plasma-polymerized monomer was first deposited on a stainless steel, nickel or gold substrate. This was sprayed with a 3% LiClO$_4$ solution in methanol followed by deposition of a further polymer layer. The resulting layered structure was heated at 80$^{\circ}$C for 24 h under vacuum to produce a homogeneous salt distribution. The plasma parameters had to be optimized to achieve maximum conductivity. The polymer contained Si-O-Si crosslinks and these increased in number as the radio frequency (RF) power to monomer flow rate and molecular weight ratio increased.

Solvent-cast PEO-based films tend initially to have crystal lamellae 15 to 20 nm in thickness. Annealing high-molecular-weight PEO-based systems at temperatures close to the melting point of the particular crystalline phase leads to rapid lamellar thickening and to well-defined lamellae 40 to 60 nm in thickness. More complex "banded" structures may be observed, arising from the formation of stacks of lamellar fragments. Melt recrystallized phases have different morphologies from solvent cast materials, suggesting that there is a difference in fibril formation. For example, PEO-NaI films go through a series of morphological states on melt-recrystallization cycles, reducing lamellar thickness to about 20 nm. Extended annealing of this cannot bring about lamellar thickening which occurs rapidly in solution-cast films. At least three crystalline structures have been observed by X-ray crystallographic studies that depend on the method of sample preparation. It is also worth noting that the melting point of the polymeric system is dependent on crystal size, as well as crystal type, increasing with increasing annealing time.

It has been shown that the solvent influences the morphology of polymer electrolyte systems, producing material predominant in either high-melting, highly ordered (phase I) or low-melting, partially ordered (phase II) crystalline phases from the same stoichiometry. It is, however, difficult to generalize the effects of solvent type and rate of solvent removal as these are properties of the polymer-salt system.

## The Interaction Between Polymer and Salt

### Ion Solvation by the Polymer

The existence of polar groups in polymers is a common feature; thus, it may be expected that they will behave as high-molecular-weight solvents and dissolve salts to form stable ion-polymer complexes. A salt dissolves in a solvent only if the associated energy and entropy changes produce an overall reduction in free energy of the system. This arises when the interaction between the ionic species and the coordinating groups on the polymer chain compensates for the loss of salt lattice energy. The gain in entropy is brought about by destruction of the crystal lattice and also by gross deformations in the polymer structure host by the ions. The enthalpy of solvation is essentially the result of electrostatic interactions between the cation positive charge and the negative charge on the dipolar groups of the polymer or of partial sharing of a lone pair of electrons on a coordinating atom in the polymer, leading to a coordinate bond. The lattice energy effects may be compensated for by such factors as a low value of cohesive energy density and vacancy formation, favored by a low glass transition temperature, Lewis acid-base interaction between coordinating sites on the polymer and the ions, and long-range electrostatic forces such as cation-anion interaction energies. In addition, for a particular cation-polymer coordination group, the distance apart of the coordinating groups and the polymer's ability to adopt conformations that allow multiple inter- and intramolecular coordination are important. Neither poly(methylene oxide), $(CH_2O)_n$ nor poly(trimethylene oxide), $(CH_2CH_2CH_2O)_n$, for example, tend to form polymer electrolytes. Both the rigidity of chains in the former and the inability of either polymer to adopt low-energy conformations to maximize polymer-cation coordinations can account for this. Similarly, poly(propeleyen oxide) (PPO) is known to form less stable ion-polymer systems than poly(ethylene oxide) (PEO), because of the steric hindrance of the $CH_3$ group. In addition, intra-molecular coordinations are more effective in poly(ethylene succinate), $(-OH_2CH_2OCOCH_2CH_2CO-)_n$, which coordinates lithium ions more effectively than poly(ethylene sebacate), $-OCH_2CH_2OCO(CH_2)_8CO-$ where the coordinating groups are separated by eight methylene groups, leading to greater dissociation. PEO, for example, is able to solvate an extremely wide range of metal salts, including alkali, alkaline earth, lanthanide, and transition metals. The majority of these complexes are only partially characterized.

### Hard-Soft Acid-Base Principle

The hard-soft acid-based (HSAB) principle has been suggested as a means of accounting for and predicting the stability of complexes formed between Lewis acids and bases. Those acids and bases that are small, are highly electronegative, are of low polarizability, and are hard to oxidize are termed hard, that is, they tend to hold their electrons tightly; soft acids and bases are of low electronegativity, tend to be large, are highly polarizable, and are easy to oxidize, that is, they hold their valence electrons loosely. In general, a preference is found for complexes to be formed between hard acids and bases or soft acids and bases. In addition to classifying acids and bases according to the properties of the donor atom, it is also possible to group any given acid or base as hard or soft by its apparent preference for hard or soft reactants. For example, a base B may be categorized by the behavior of the following equilibrium:

$$BH^+ + CH_3Hg \leftrightarrow CH_3HgB + H^+$$
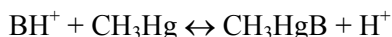
In this competition between a hard acid ($H^+$) and a soft acid ($CH_3Hg^+$), a hard base will cause the reaction to go to the left but a soft base will cause it to proceed to the right. Molecules such as ethers and some amines that have donor atoms with high electronegativity and low polarizability are therefore hard bases.

Consequently, PEO and PEI may be regarded as regular arrays of hard bases. Thioethers including poly(ethylene sulfide), on the other hand, are examples of soft bases.

*Anions*

In polar solvents such as water or methanol, hydrogen bonding is important for specific anion solvation, whereas aprotic liquids and solvating polymers have negligible anion stabilization energies. Differences in general solvation energies of anions do occur as the dielectric constant of the solvent varies. On passing from a polar, protic medium through to a less polar one, most anions are destabilized, the destabilization being greatest when the charge density and basicity of the ion are low:

$$F^- >> Cl^- > Br^- > I^- \sim SCN^- > ClO_4^- \sim CF_3SO_3^- > BF^- \sim AsF6^-.$$

The most suitable choices of anion for aprotic, low-dielectric-constant dipolar polymer-based polymer electrolytes are those to the right of the preceding series. These are large anions, with delocalized charge, are very weak bases, and possess low ion-dipole stabilization energies. In addition, their lattice energies are relatively low and they have little tendency to form tight ion pairs. These particular anions may be either soft ($I^-$) or hard ($ClO_4^-$) bases.

In general, the formation of polymer electrolytes is controlled by the cation solvation energy in opposition to the salt lattice energy. It is thus understandable that strongly solvated ions such as $Li^+$ can be complexed by PEO, even when the counterion is relatively small, like $Cl^-$, and there is an associated high lattice energy. The larger $I^-$ anion is required for the heavier, less solvated $K^+$ ion. Divalent and trivalent cations again have sufficiently large solvation energies to induce the formation of complexes, even with the smaller Br anion. In addition, salts formed from a soft cation and anion, for example, AgI, are not complexed by the ether oxygens, but a weaker hard-soft interaction allows for competition between the anion and the complexing polymer: AgCF3SO3 forms polyether-based polymer complexes but AgBr, and AgCI do not. The chloride, bromide, and iodide salts of $Hg^{2+}$, which is a much softer cation, all complex with ether oxygens; however, mercury halides are too covalent to allow the free $Hg^{2+}$ ion to form in solution and therefore complexes are between polymer and molecular salt. Crystallographic studies of PEO-HgCl$_2$ complexes show the linear salt molecule to be slightly bent in the complex as a result of unsymmetrical interaction. It is difficult to predict solely in terms of the HSAB principle which salts are likely to form polymer-ion complexes, but it does give a good indication as to the stability of the complex once it is formed.

Much useful information can be obtained on ion-polymer interactions from studies carried out on polyether-salt systems in solutions. Many of these were carried out prior to the initiation of studies on "polymer electrolytes" as such. Addition of salts to aqueous PEO solutions generally leads to a salting out of the polymer. Ionic hydration is too strong for competitive ion-polymer interactions to be significant in this system. Conversely, studies have been reported of the interactions of potassium salts with PEO and PPO in anhydrous methanol using dialysis and viscosity measurements. Methanol is a nonsolvent for PEO but addition of salts such as KI results in a salting-in effect. Other studies of methanolic solutions have been reported. One study investigated the binding of potassium and sodium thiocyanates and iodides to PEO in anhydrous methanol by fluorescence and ultrafiltration techniques along with conductivity measurements. It was shown conclusively that in addition to normal electrostatic forces, specific interactions led to a fraction of the anions binding to the PEO-cation unit. The solvation of $Na^+$, $K^+$, and $Cs^+$ by PEO has been investigated in nitromethane which only weakly solvates cations. The equilibrium constants of the formation of polymer solvates were evaluated for different polymer molecular weights and were shown to increase with increasing chain length and decreasing cation radius. Estimates of the number of -(CH$_2$CH$_2$O)- groups involved in the solvation shell was given as 6 to 12 depending on the cation. Many studies of PPO salt interactions have also been reported in the literature. The effects of adding up to 24.5% by weight of lithium perchlorate on the

specific volume and viscoelastie behavior of low- and high-molecular-weight PPO have been investigated. The glass transition temperature of PPO-$ZnCl_2$ solutions has also been studied, through which the rise in $T_g$ with salt concentration has been explained by intermolecular coordination of the zinc ions which yield crosslinking. Such studies in liquid solution have been valuable for shedding light on the nature of ion-solvent interactions in solvent-free polymer electrolytes.

*Complex Formation*

The term comp1ex tends to be applied rather loosely when referring to polymer electrolytes. It is generally taken to mean the material formed when the polymer host interacts with the salt to form a new polymeric system. At high enough temperatures or in systems where crystallization is prevented, the ions are solvated by the polymer to form a homogeneous polymer-salt solution. With host materials such as high-molecular-weight linear PEO, however, the system crystallizes to form spherulites of well-defined stoichiometries. These "crystalline complexes" are often recognized by their melting points which can be well in excess of $1000^o$ C. The amorphous regions within the spherulites of complex material can be of a very different stoichiometry and it is therefore somewhat inappropriate to refer to the entire system as a "complex." Computational procedures have been used to determine criteria for complex formation in PEO-sodium halide systems. Formation of PEO-NaX crystalline complexes involves the reaction of 1 mol of salt with 3 mol of ethylene oxide (EO) units. The lattice energy of the crystalline complex comprises several contributions:

$$E_{complex} = \varepsilon(NaX) + \varepsilon(3EO\text{-}NaX)_{intra} + \varepsilon(3EO\text{-}NaX)_{jnter} + \varepsilon(3EO)$$

where, $\varepsilon(NaX)$ is the lattice energy of the salt within the complex, $\varepsilon(3EO\text{-}NaX)_{intra}$ is the energy of interaction of the 3EO segment with ion pairs within the same polymer-salt molecular adduct, and $\varepsilon(3EO\text{-}NaX)_{inter}$ is the energy of interaction of the segment with ion pairs of neighboring molecular adducts. $\varepsilon(3EO)$ is the interaction of the segment with neighboring PEO helices in addition to changes in internal energy of this reference segment on compexation with the salt. A crystalline polymer-salt complex will thus form provided that:

$$\varepsilon(3EO\text{-}NaX)_{intra} + \varepsilon(3EO\text{-}NaX)_{inter} + \varepsilon(3EO) < \varepsilon(NaX) + \varepsilon(3EO) - \varepsilon(NaX)$$

where, $\varepsilon(NaX)$ and $\varepsilon(3EO)$ are the salt and polymer segment lattice energies, respectively. A value of –39.7 kJ (mol of 3EO unit)$^{-1}$ was calculated for the latter parameter. Crystallographic data were used to compute the terms on the left-hand side of the preceding equation and the lattice energy of the ions within the complex. The computed results are plotted as functions of the partial electronic charges on the carbon atom, $q_c$, ($q_o$, the partical charge on the oxygen - $-2q_c$), in Figure 4.11. It can be seen that if a partial electronic charge of +0.2 to 0.23 on the carbon atom is assumed, then complex formation will occur as the total of the left-hand side terms is more negative than the right-hand side total. This value was taken from the charge distribution in the C-O bond employed in treatment of the dipole moments of PEO oligomers. The oxygen atom has been considered to have a partial charge of –0.6, that is, $q_c = 0.3$ in 18-crown-6 complexes with cations, thus allowing a greater stability margin for PEO-NaI. Estimates of corresponding energetic parameters for PEO-NaBr and PEO-NaCl also have plausible interpretations in terms of (as observed) complex formation in the former electrolyte and phase separation of the salt and polyether in the latter. A semi-quantitative explanation for the solubility and insolubility of salts in polymers can thus be obtained in terms of lattice energies, although further calculations on other polymer-salt systems are obviously needed before a fully satisfactory theoretical prediction can be given.
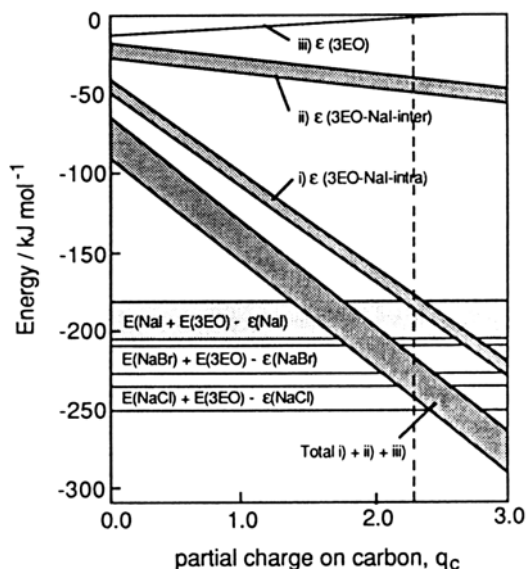
*Figure 4.11. Computed Values for Components of the Lattice Energy of PEO-NaI As a Funciton of the Partical Charge on Carbon, $q_x$ (the dard dashed area denotes the results for "high" and "low" van der Waals parameters; the "total" corresponds to the left-hand side of equation $E_{complex} = \varepsilon(NaX) + \varepsilon(3EO-NaX)_{intra} + \varepsilon(3EO-NaX)_{jnter} + \varepsilon(3EO)$ between "calculated and "thermochemical cycle" values for E(NaI); estimates for PEO-NaBr and PEO-NaCl are given in the lightest shading).*

Conductivity Studies

Dielectric and conductivity studies have been performed on poly(propylene glycol) with a molecular weight of 4000 complexed with 0.01 to 6 mol% $AgCF_3SO_3$. The highest conductivity value at 70°C, $8 \times 10^{-5}$ S.cm$^{-1}$, was obtained for 6 mol% $AgCF_3SO_3$. The equivalent conductivity, $\Lambda$, plotted against $AgCF_3SO_3$ concentration shows a minimum and a maximum, similar to that found in other salt-poly(propylene glycol) complexes. The dielectric relaxation studies reveal two loss peaks: a primary peak which may be attributed to ion pairs and a secondary, low intensity peak only visible at low salt concentrations, that is assumed to be due to a relaxation attributed to the polymer chain.[64]

When performing dielectric measurements on materials with high ionic conductivity, it has to be taken into consideration that there is a contribution to relative permittivity not only from the dipoles but also from mobile ions. For time-dependent electric fields, the current density, $j_{tot}$, in the Maxwell-Ampere equation is split up into two parts: the conduction current density and the current density due to the displacement field D, according to:

$$j_{tot}(t) = \sigma_0.E(t) + \frac{\partial D(t)}{\partial t}$$

where, Ohm's law j=σ.E has been used and $\sigma_o$ is the bulk conductivity of the material. By taking Fourier transform, the frequency-domain relation becomes:

$$j_{tot}(\omega) = \sigma_o.E(\omega) + i.\omega.D(\omega)$$

Since the relative permittivity, $\varepsilon_r$, is a complex quantity dependent on frequency, i.e., $\varepsilon_r(\omega)=\varepsilon'_r(\omega)-i.\varepsilon''_r(\omega)$ and D=$\varepsilon_r.\varepsilon_o$.E, the measured relative permittivity, $\overline{\varepsilon}_r(\omega)$, is related to electric fields and current density through:

98

$$j(\omega) = i\omega\,\bar{\varepsilon}_r(\omega)\varepsilon_o E(\omega) = i\omega\left[\varepsilon'_r(\omega) - i\left(\frac{\sigma_o}{\omega\varepsilon_o} + \varepsilon''_r(\omega)\right)\right]\varepsilon_o E(\omega)$$

To obtain the true dielectric loss, it is thus necessary to subtract the term $\sigma_o/(\omega\varepsilon_o)$ from the dielectric loss measured by the instrument. Although simple in principle, this subtraction is often difficult to perform accurately for high conductivity materials since, at low frequencies, both $\sigma_o/(\omega\varepsilon_o)$ and $\bar{\varepsilon}_r(\omega)$ are almost equal and very large in magnitude, i.e., the true dielectric loss $\varepsilon''_r$ is small compared to $\bar{\varepsilon}_r''$. Investigation of a broad range of salt concentrations would make it easier to evaluate the true dielectric loss.[1]

Preparation of ion-conducting samples for the purpose of certain electrical studies used poly(propylene glycol)(PPG) with a weight average molecular weight of 4000 (PPG 4000) complexed with $AgCF_3SO_3$. The salt was first dried at 75°C for 24 h and then at 90°C for another 24 h in a vacuum oven. The polymer was dried in the vacuum oven at room temperature for 24 h followed by freeze-drying using 10 to 15 freeze-pump-thaw cycles under a vacuum of 1 MPa. While still under vacuum, the polymer was transferred into an argon atmosphere dry box where it was heated to 70-80°C . The salt was then dissolved directly into the polymer. For samples with lowest concentrations, a solution was mixed with the pure polymer in one or two steps. The unit used in the figures for concentration, c, is mole of salt per kg of solution (salt + solvent). Since silver salts often are sensitive to light, we tested the samples for electronic conductivity, but these tests showed that the electronic contribution to the conductivity was negligible.[64]

Electrical measurements were performed using a cell made of quartz with stainless steel electrodes, 10.3 mm in diameter and 1.1 mm apart. Loading of the cell was performed in a dry argon atmosphere in order to avoid moisture affecting the conductivity of polymer/salt complex. The loaded cell was put in a shielded container immersed in a temperature controlled water bath. To maintain a dry atmosphere inside the container, a steady flow of dry nitrogen gas was provided. The sample temperature was measured using a Platinel II thermocouple placed close to the cell. Complex impedance measurements were performed; the signal applied to the sample was 0.1 V. The ionic conductivity was calculated from the bulk resistance determined in the complex impedance plot as the distance from the origin to the intersection of the high frequency semicircle and the real axis.[64]

Figure 4.12 presents the ionic conductivity as a function of temperature for $AgCF_3SO_3$ concentrations in the range from 0.010 – 5.9 mol%. The results show trends similar to those measured for PPG complexed with $LiCF_3SO_3$ and $NaCF_3SO_3$ or $NH_4CF_3SO_3$, but the conductivity is somewhat higher for $AgCF_3SO_3$-PPG complex. For example, at the relatively low concentration of 0.17 mol/kg (O.M.=100) conductivity is $3.2\times10^{-7}$ S/cm for $LiCF_3SO_3$-PPG, while it is $1.3\times10^{-6}$ S/cm for $AgCF_3SO_3$-PPG at 25°C.[64]

Relatively few studies have been reported on polymers complexed with silver salts. The reported conductivities are all within the range $10^{-8}$ – $10^{-5}$ S/cm, except $AgNO_3$-Poolyethylene oxide (PEO) where conductivities as high as $9\times10^{-3}$ S/cm have been found for extremely high concentration of silver salt. For the silver ion conducting polymer-salt composite material $RbAg_4I_5$-PEO a high room temperature conductivity of $2\times10^{-3}$S/cm was obtained, but this material contained high-conductivity crystalline $RbAg_4I_5$ grains in addition to the polymer and should thus not be directly compared to polymer-salt complexes. The conductivity values reported for $AgCF_3SO_3$-PEO are close to the values for $AgCF_3SO_3$-PPG presented above.
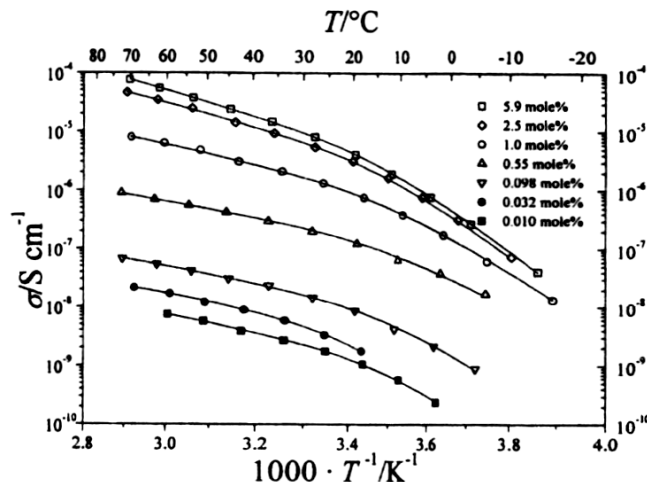
*Figure 4.12. Conductivity Vs. Reciprocal Temperature for Seven Different Concentrations of AgCF$_3$SO$_3$ (solid lines are the best fits to the VTF equation in a least square sense).[1]*

The measured conductivity data were least square fitted to the Vogel-Tamman-Fulcher equation:

$$\sigma(t) = \frac{A}{\sqrt{T}} \cdot \exp\left[ -\frac{E_p}{k_a \cdot (T - T_o)} \right]$$

where, $\sigma$ is the conductivity, T the absolute temperature, $k_B$ the Boltzmann constant, and A, $E_p$ and $T_o$ are fitting parameters.   An anomalously high value of the fitting parameter $T_o$ was obtained at low concentration.  This type of behavior, observed earlier, has been attributed to a deficiency of the VTF equation to describe accurately the conductivity of polymer electrolytes.  The maximum conductivity is obtained for the highest AgCF$_3$SO$_3$ concentration measured (Figure 4.13).  However, it is often useful to plot the equivalent conductivity, $\Lambda = \sigma/c$, versus the square root of concentration for these materials (see Figure 4.14).  For some other polymer complexes, three rgions have been identified in such a plot: region I where $\Lambda$ decreases with increasing concentration of salt, region II where $\Lambda$ increases with concentration, and region III in which $\Lambda$ again decreases with increasing salt concentration.  Ions associating into electrically neutral ion pairs provide one of the reasons for the decrease in $\Lambda$ in region I.  The increase of $\Lambda$ values in region II has been suggested to be due to an increasing amount of charge carrier either due to the formation of ion triplets or to an increasing fraction of "free" ions at intermediate concentrations, so-called dissociation.  Percolation effects may also contribute to the conductivity enhancement.  Finally, in region III, $\Lambda$ is decreasing due to formation of large aggregates and to a drop in the ionic mobility due to an increase in viscosity as a result of transient cross-linking.  Although region I is not fully developed in Figure 4.13, AgCF$_3$SO$_3$-polypropylene oxide (PPO) shows a similar behavior to that observed in other polymer systems.
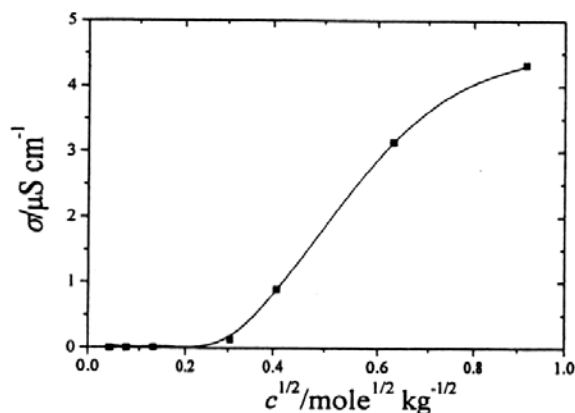
*Figure 4.13. Conductivity Vs. the Square Root of AgCF₃SO₃ Concentration at 283°K (the square root of concentration is taken in order to better distinguish details at low concentration; the curve is drawn to guide the eye).[64]*
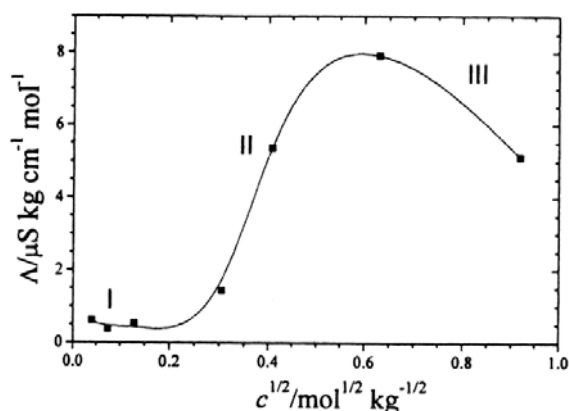


*Figure 4.14. Equivalent Conductivity Λ for PPG 4000 Plotted Against the Square Root of AgCF₃O₃ Concentration at 293°K (the curve is drawn as a guide to eye).[64]*

*Physical Properties*

An essential prerequisite for significant cation mobility is a high lability of the cation-polymer bond. Hence, while strong cation-polymer bonds are necessary for polymer electrolyte formation, labile bonds are necessary for cation mobility. The rate of exchange of solvent cooridinated to a cation is affected by many factors: cation radius and charge are important, but for transition metal ions, the dominant factor is often the change in d-orbital energy on going from a ground-state solvation structure (e.g., octahedral coordination) to a transition state (e.g., square pyramidal or bipyramidal coordination). It has been shown that $Hg^{2+}$ has the fastest exchange rate with water of all the divalent cations. Its exchange rate is $\sim 5 \times 10^8$ $sec^{-1}$. Because of the similar donicities of the oxygen in water and ethers, exchange rates in ethers can be expected to follow a similar trend. It has been predicted that $Hg^{2+}$ might therefore be mobile in PEO. $Ca^{2+}$ with a water exchange rate of approximately $4 \times 10^8$ $sec^{-1}$ is also expected to be mobile. On the other hand, $Mg^{2+}$ has a water exchange rate of approximately $10^5$ $sec^{-1}$ and should be much less mobile. The trivalent cations of the lanthanide group have water exchange rates of the order of $10^7$ to $10^8$ $sec^{-1}$ and may on this premise be again expected to exhibit mobility in an anhydrous polymer electrolyte. Conductivity and transference number measurements have shown that although $Hg^{2+}$ is indeed mobile and $Mg^{2+}$ immobile, $Ca^{2+}$ and $La^{3+}$ are also immobile. On the basis of the hard-soft acid-base principle,

hardness of divalent cations follows the trend $Mg^{2+}, Ca^{2+} > Ni^{2+}, Cu^{2+}, Zn^{2+}, Co^{2+}, Pb^{2+} > Cd^{2+}, Hg^{2+}$. Therefore, in this instance, one might expect both $Mg^{2+}$ and $Ca^{2+}$ to be immobile and $Hg^{2+}$ to be mobile. $La^{3+}$ is one of the hardest of the lanthanide ions but, in addition, the charge in the $La^{3+}$ ion will undoubtedly contribute further to its lack of mobility. That $Hg^{2+}$ is a soft cation and shows very high lability may account for the very reasonable conductivities observed for anhydrous PEO-$Hg(ClO_4)_2$ system.

Other factors such as electronegativity and ionic radius may also affect the mobility of ions. More important, the mobile species are likely to be associated (as in 1:1 electrolytes) and the nature of these species and degree of association will depend on the anion, cation, and salt concentration. The majority of studies on divalent cation polymer electrolytes have involved divalent halides as the salt. This series of salts has an associated problem in that results may not be directly comprable because there is considerable variation in the character of anion-cation bond. For example, the chlorides of zinc, cadmium, and mercury show a shart transition from ionic to covalent character. Likewise, the tendency of, for example, zinc halides, to form complexes decreases on going from the chloride to the iodide. Cadmium halides in general form auto complex ions such as $CdX^+$, $CdX_3^-$, and $CdX_4^{2-}$ in concentrated solutions and the iodides dissociate in solution as: $2\ CdI_2 \leftrightarrow Cd^{2+} + CdI_4^{2-}$ to give totally anomalous transference number data. Mercury halides are too covalent to allow the free $Hg^{2+}$ ion to form in solution. Thus, $HgCl_2$ dissociates only slightly to give: $HgCl_2 \leftrightarrow HgCl^+ + Cl^-$. These factors are important considerations when interpreting data as mobile species may vary from electrolyte to electrolyte. In addition to the species, the morphology of the polymer electrolyte is important when determining transference number data. Many of the electrolytes containing divalent or trivalent cations include high-melting complexes melting at $18^oC$ and upward. In many instances, measurements may have been made in heterogeneous systems.

*Alkaline Earth Metal Cations*

PEO complexes of $MgCl_2$, $Mg(ClO_4)_2$, $Mg(SCN)_2$, and $Mg(CF_3SO_3)_2$ have been reported in the literature. $P(EO)_4MgCl_2$ electrolytes were found to contain crystalline PEO, indicating that the crystalline complex has a composition in which EO:$MG^{2+}$ is less than 4. For a 16:1 complex, at $100^oC$, conductivities were found to be $1.5 \times 10^{-5}$ S/cm for PEO-$MgCl_2$, $1.6 \times 10^{-4}$ S/cm for PEO-$Mg(CF_3SO_3)_2$, $2 \times 10^{-4}$ S/cm for PEO-$Mg(ClO_4)_2$, and $4 \times 10^{-6}$ S/cm for PEO-$Mg(SCN)_2$. Apart from the thiocyanate complex, conductivities are comparable to those of PEO-$LiCF_3SO_3$ complexes above $80^oC$. As the $Mg^{2+}$ transference number was found to be essentially zero it can be concluded that these are anion conductors.

Transference number measurements have been carried out on PEO-$Ca(CLO_4)_2$ and PEO-$CaI_2$ and it is found that the cation is effectively immobile. X-ray absorption fine-structure (EXAFS) studies on PEO-$CaI_2$ systems have shown the $Ca^{2+}$ ion to be trapped within a cage of 10 ether oxygens, which may account for its immobility. Conductivity data have been reported for a number of calcium salt-PEO electrolytes where the anion is $SCN^-$, $CF_3SO_3^-$, $ClO_4^-$, or $I^-$. Some discrepancy is noted between studies of the perchlorate systems but this may be caused by moisture as only one study was carried out under anhydrous conditions. The conductivities are shown in Figure 4.15. As observed in a number of divalent cation-containing electrolytes, unusual behavior is observed at high salt content. As with magnesium systems, the thiocanate complexes show conductivities lower by a factor of approximately 10 than the other electrolytes.
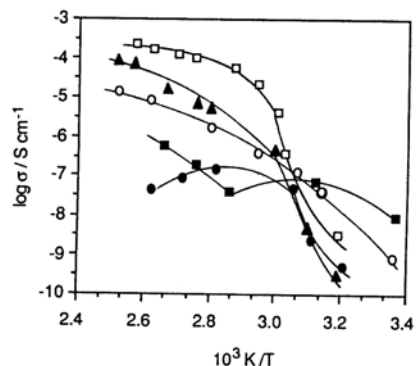
*Figure 4.15. Temperature Dependence of the Conductivity of P(EO)$_x$Ca(ClO$_4$)$_2$, x=50 (□), 20 (▲, 12 (O), 8 (■), and 4  (●).*

X-ray diffraction and differential scanning calorimetry studies of PEO-Ca(ClO$_4$)$_2$ films indicated the presence of two eutectics, one with a composition between 20:1 and 12:1 and a second with composition near 8:1.  Both crystalline complexes are high melting (>200$^o$C).  Conductivity data have been reported for MEEP-Sr(CF$_3$SO$_3$)$_2$ and PEO-Sr(ClO$_4$)$_2$ electrolytes which are similar to PEO-MG9ClO$_4$)$_2$ systems. The latter electrolytes were prepared from the hydrated salt and were dried at room temperature only.

Zinc(II)

Electrolytes containing ZnX$_2$, where X = Cl, Br, ClO$_4$, and CF$_3$SO$_3$ have been described for a wide range of salt concentrations.   Highest conductivities were found for P(EO)$_{16}$ZnI$_2$ (3.6x10$^{-4}$ C/cm) and P(EO)$_{20}$Zn(CF$_3$SO$_3$)$_2$ (3.1x10$^{-4}$ S/cm) at 140$^o$C.  P(EO)$_8$ZnI$_2$ has been suggested from local structure analysis carried out using EXFAS.  It has been reported that in P(EO)$_n$ZnCl$_2$ electrolytes, two defined complexes and two eutectics at compositions n=30 and 14 exist.

Copper

Of all the divalent systems studied to date, PEO-containing copper salts have revealed the most intriguing properties.  Films that have been solvent cast were reported to be blue, whereas hot-pressed materials that had never been in contact with solvent were found to be yellow-green.  The former showed absorption in the ultraviolet-visible spectrum at 750 nm, and the latter materials absorbed at 825 nm.  This is most likely a solvent effect: where a hexacoordination with a Cu$^{2+}$ ion is expected for small molecules such as CH$_3$CN, this is much less likely for large PEO molecules and the lower coordination results in a wavelength shift.  It has also been found that when left in a drybox atmosphere for many months, blue solvent-cast films turn yellow.  Heating these electrolytes under vacuum to remove solvent poses a problem in itself as decomposition of the electrolyte results from prolonged heating at temperatures above approximately 110$^o$C.

**Experimental Evaluation of Electrolysis Through Solid Electrolyte**

Our approach uses electrolysis in the context of a solid electrolyte to transfer mass (through electrostripping and electrodeposition) in response to altered stree fields, thereby rendering self-healing and adaptation effects.  Transport of ions through solid electrolytes has been thoroughly investigated; the above review of solid electrolytes provided substantial information on this topic.   Solid electrolyte-electrode interfaces, however, require further investigation; electrostripping and electrodeposition phenomena occur and these interfaces, and they determine the overpotential needed to drive the electrolysis process in our application.  We conducted an experimental study to make a preliminary assessment of electrolysis process within solid

electrolytes, and to provide further insight into interface phenomena. The experimental set-up is depiected in Figure 4.16. This set-up seeks to electrostrip and electrodeposit copper in the context of a solid electrolyte comprising polystyrene sulphonic acid complexed with paratoulene sulphonate copper. This ion-conducting polymer was synthesized in our laboratory using the following ingredients: polystyrene sluphonic acid, paratoulene sulphonic acid, and $Cu(OH)_2$. The actual planar dimensions of the cell were 1x1 cm. Cyclic voltammetry tests were conducted with voltage changing at a rate of 10 mV/s. The resulting voltammogram of Figure 3.49 is indicative of the occurrence of electrostripping and electrodeposition phenoemena. This votammogram is particularly significant in determining the sum total of activation and polarization overpotentials at interfaces, noting that when a potential is applied across an electrolysis cell, the potential drop is the sum of several contributions: (1) the equilibrium anode-electrolyte and electrolyte-cathode potentials (i.e., the equilibrium cell potential); (2) the activation and polarization overpotentials at the anode and cathode; and (3) the electrolyte iR drop. In our electrochemical cell, where anode and cathode are both copper, the anode-electrolyte and electrolyte-cathode potentials cancel each other. The electrolyte iR drop is also rather small in our case $[(8x10^{-3} \text{ S/m})^{-1}.(0.12x10^{-3} \text{ m}) / (1x10^{-4} \text{ m}^2) = 0.0096 \text{ } \Omega]$. The voltammogram indicates a resistance of about 50 $\Omega$, which can be largely attributed to anode-electrolyte and electrolyte-cathode overpotentials.

In order to provide physical evidence for the occurrence of copoper electrodeposition within solid electrolyte, we prepared a test set-up similar to that shown in Figure 4.17, except that in cathode the copper foil was replaced with stainless steel mesh; current was not reversed in this case so that electrodeposition on stainless steeel mesh was not followed by electrostripping. Micrographs of Figure 4.18 compare the stainless steel mesh prior to and after electrodeposition, providing physical evidence for electrodeposition of copper in the context of a solid electrolyte. The charge applied during this electrolysis process was of the order of 10 Coulmbs (per $cm^2$ area of the cell). Close to 2.3 mg of copper was electrodeposited in the process; this is within the rage of theoretical value [=10*63.546/(2*96485)=0.0033 g].
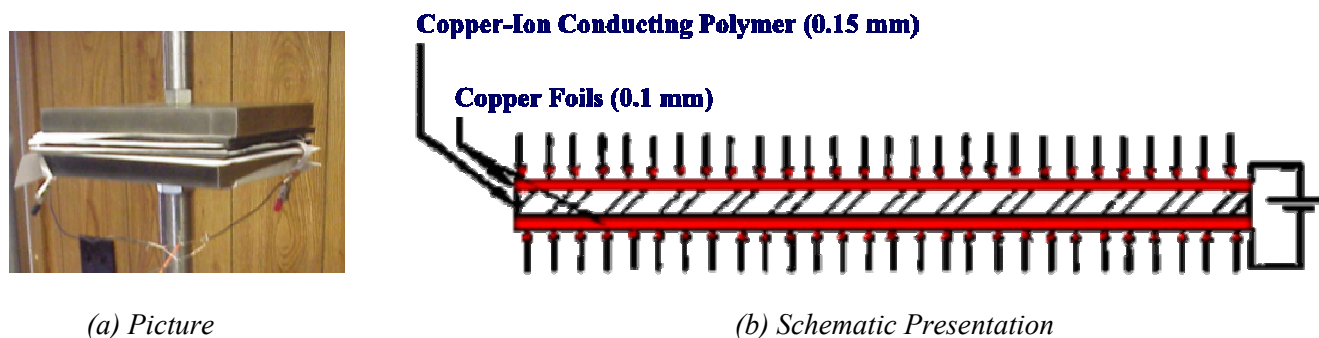


*(a) Picture*         *(b) Schematic Presentation*

*Figure 416. Experimental Set-Up for Assessment of the Overpotential in Electrolysis Through Solid Electrolyte.*
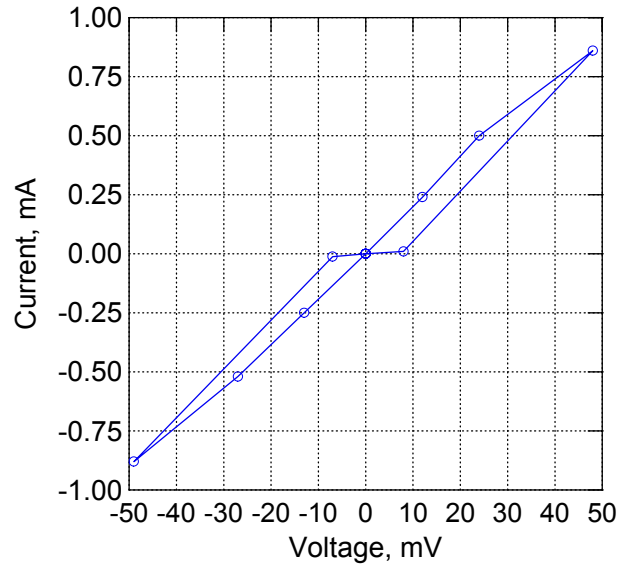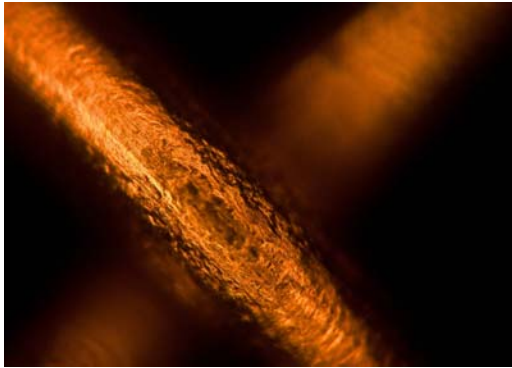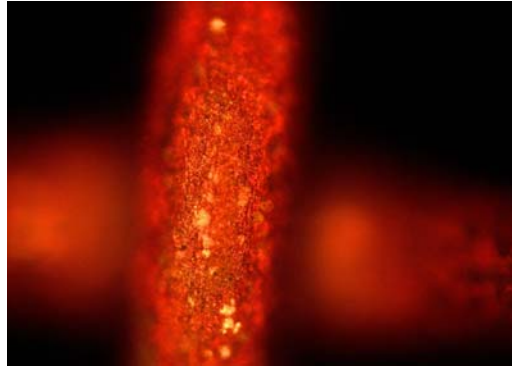
*Figure 4.17. Voltammogram for the Cyclic Copper Plating-Stripping Process in Solid Electrolyte Cell.*



*(a) Stainless Steel Mesh Prior to Electrolysis*



*(b) Stainless Steel Mesh After Electrolysis in Solid Electrolyte (depicting electrodeposited copper)*

*Figure 4.18. Microscopic Pictures of Stainless Steel Mesh Prior to and After Electrolysis in Solid Electrolyte.*

**Design and Experimental Validaiton of a Piezo-Driven Electrolytic Cell**

Piezoelectricity is employed in our approach to convert mechanical energy to electrical energy in order to drive the electrolysis process (which renders self-healing and adaptation effects). It is therefore important to validate piezoelectricity as a viable means of driving electrolytic cells. The set-up we designed to validate this concept is schematically presented in Figure 4.19. This set-up comprises 10 piezoelectric polymer (PVDF) sheets with thickness of 0.1 mm and planar dimensions of 50x50 mm. The sheets are separed from each other by thin plastic films; electrical connections are made between surfaces developing similar charge in order to accumulate their

charges (at the voltage offered by each piezoelectric sheet). The piezoelectric stack was subjected to 30 MPa compressive stress at a frequency of 3 Hz, and it was used to drive a cell similar to that presented earlier (Figure 4.16, but with a stainless steel mesh replacing copper foil at cathode).
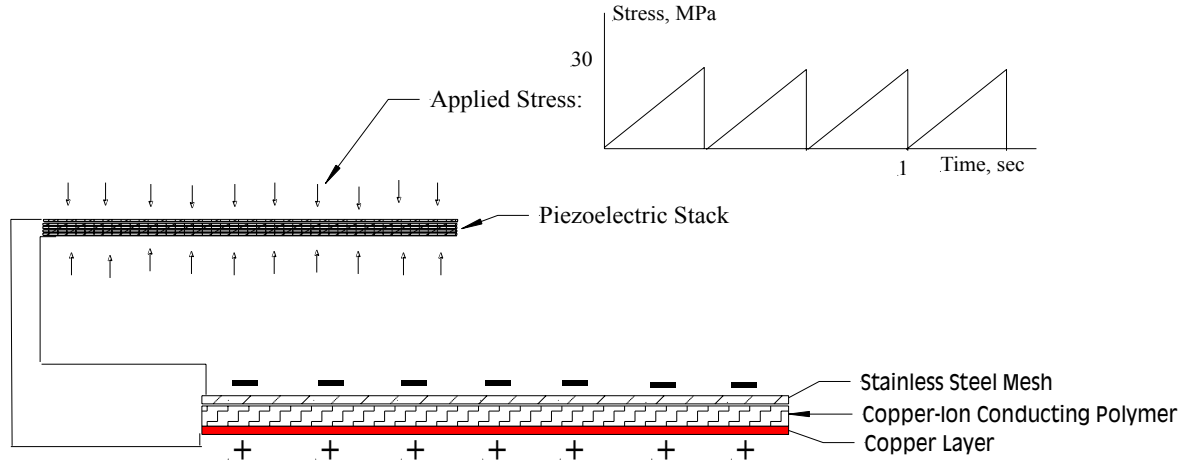


*Figure 4.19. Schematic Presentatino of the Piezo-Driven Electrolytic Cell.*

Under each application of the 30 MPa stress (s), the piezoelectric stack (of 10 sheets) develops the following levels of voltage (V) and charge (Q):

$$V = g_{33}.s.t = 330x10^{-5}(30x10^6).(0.1x10^{-3}) = 9.9 \text{ volts}$$

$$Q = d_{33}.s.A = 33x10^{-12} (30x10^6).(10x0.05x0.05) = 2.475x10^{-5}$$

The voltage level developed is sufficient to overcome the interfacial overpotential of the cell. The charge developed per stress application (at 3 Hz frequency) generates $2.475x10^{-5}$ x $(3x60x60) = 0.2673$ coulmbs per hour. The mass of copper that can be transfered per hour would thus be: $0.2673$ ($\frac{1}{2}$ *63.546 / 96485)x1000 = 0.088 mg/hr.

One remaining question concerns electrical resistance of the system, which determines electrical current and thus the time required for transfer of the charge generated under each stress application. The votammogram generated for the electrochemical cell (Figure 4.39) indicated an overpotential (plus bulk electrolyte resistance) of about 50 $\Omega$. This implies that the current generated under the applied potential of 9.9 V would be 0.2 A. Hence, the generated current of $2.475x10^{-5}$ would be transferred in a time period of $(2.475x10^{-5}) / (0.2) = 0.00012$ seconds. The selected frequency of 3 Hz would allow ample time for this charge transfer to take place.

In order to validate the above calculations, we developed an experimental set-up (Figure 4.20) comprising the cell and piezoelectric stack of Figure 4.19. This set-up was run continuously for 48 hours, after which the weight gain of cathode (stainless steel mesh) was determined to be to 2.9 mg when compared with the theoretical prediction of 0.088x48 = 4.22 mg. This

experimental finding validates the ability of driving electrolytic cells using the piezoelectric phenomenon.



*Figure 4.20.  Experimental Set-Up for Validaiton of Piezo-Driven Electrolytic Cell.*

# CHAPTER 5

## DESIGN AND EXPERIMENTAL VALIDATION OF INTEGRATED ADAPTIVE STRUCTURAL MATERIALS

### Introduction

Our ultimate goal in this project is to consolidate basic functional (piezoelectric, solid electrolyte, metallic) and supporting (structural/functional) constituents into integrated structural elements with adaptive and self-healing attributes. Consolidation of these constituents into a (compact) structural element introduces various topological and geometric constraints; design of the integrated system within these constraints proved to be a defining step in the project. It is only in the context of a hybrid nanostructure that adaptive and self-healing qualities can be realized in light of the relevant topological and geometric constraints. The simple and economical process of ionic self-assembly ideally suits production of the new hybrid nanocomposite.

### Design of Adaptive Nanocomposites

A basid Design for Feasibility Studies

As a first step towards design of adaptive structures, we considered a basic system design (Figure 5.1) comprising repeated assemblies of piezoelectric, ionically conductive, metallic, conductive polymer, and insulative polymer layers. The system is subjected to bearing stresses on a fraction of its surface. Adaptive qualities of the system would be mobilized to transfer mass (of metallic layers) from stress-free regions to stressed regions. As noted earlier, this adaptive process involves conversion of mechanical energy to electrical energy which drives an electrolytic cell to electrostrip metal, transport metallic ions through the solid electrolyte, and electrodeposite the metal in stressed areas. The total thickness (T) of the system shown in Figure 5.1 is built-up with n replication of insulative/conductive/piezoelectric/solid electrolyte/metallic layers. Given the thickness symbols introduced in Figure 5.1, the number of replications (n) would be:

$$n = T / (T_i + T_c + T_p + T_s + T_m)$$

As a preliminary step towards design of a viable system, two alternative designs are investigated here (see Table 5.1). The two systems have the same dimensions (T=0.25 mm; L=W=20 mm; L1=W1=15 mm). System I is processed using conventional techniques and have layer dimensions in micrometer range. System II, on the other hand, is processed through ionic self-assembly and has layer thicknesses in nanometer range.

*Table 5.1. Alternative System Designs (see Figure 5.1).*

| System | $T_i$ | $T_c$ | $T_p$ | $T_s$ | $T_m$ |
|---|---|---|---|---|---|
| I (conventional) | 50 μm | 50 μm | 50 μm | 50 μm | 50 μm |
| II (nanocomposite) | 5 nm | 5 nm | 50 nm | 40 nm | 40 nm |

Replicated Multilayers of:
    Insulative Layer (Ti)
    Conductive Layer (Tc)
    Piezoelectric Layer (Tp)
    Solid Electrolyte Layer (Ts)
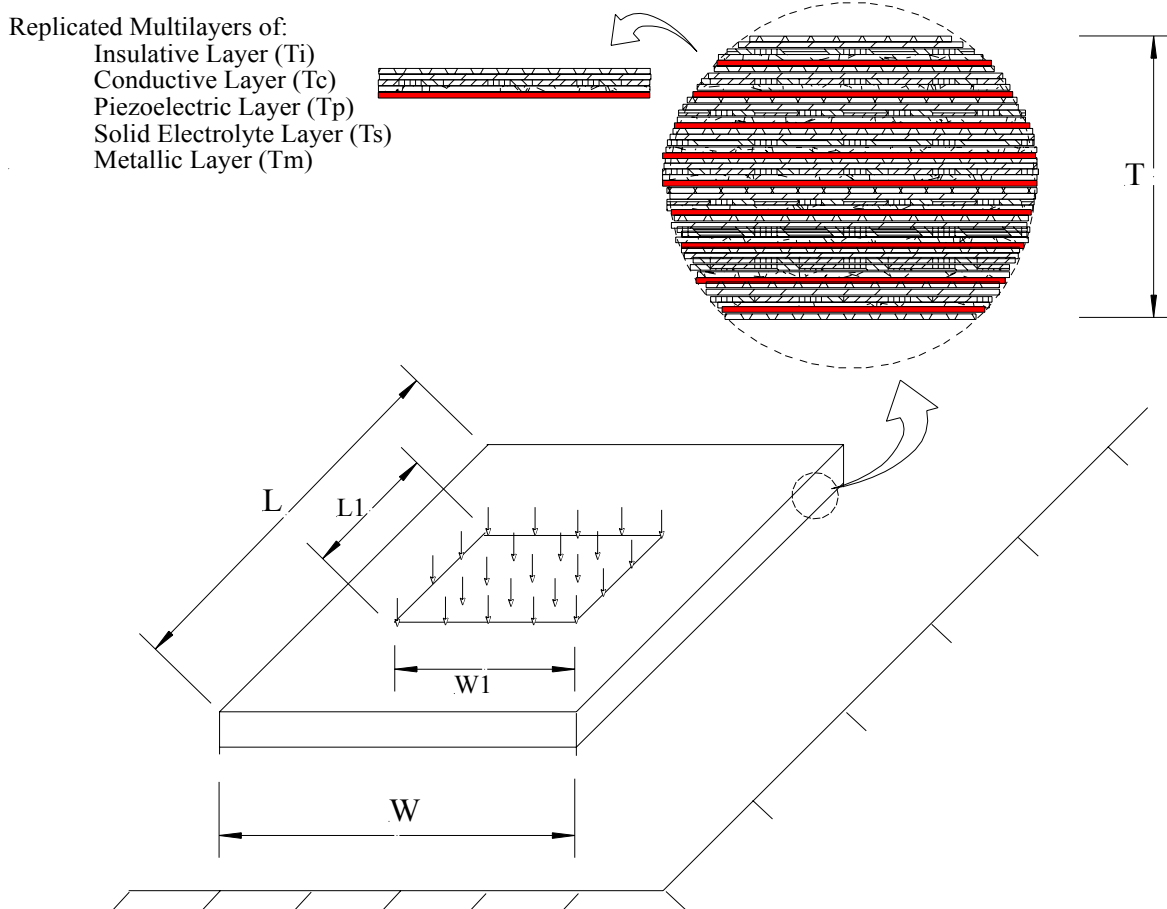    Metallic Layer (Tm)

*Figure 5.1.  Schematic Presentation of the Basic Adaptive System.*

The following expressions can be used to derive the voltage (V) and total charge (Q) generated in the basic adaptive system of Figure 5.1 under one application of 30 MPa stress (s):

$$V = g_{33}.s.T_p$$

$$Q = d_{33}.s.(n.L_1.W_1)$$

The above expressions yield (using the piezoelectric coefficients of PVDF) voltages of 4.95 V and 500 mV and charges of $8.91 \times 10^{-7}$ C and $3.99 \times 10^{-4}$ C in systems I and II, respectively.  Our basic work on electrolytic cells based on solid electrolyte indicated that a voltage exceeding 50 mV is required to activate the electrochemical process.  Both systems provide voltages exceeding this level, noting that voltage output of piezoelectric layers is proportainoal to their thickness. Once the threshold voltage level is reached, it is the generated charge which decides the quantity of mass transferred.  With metallic layers made of copper, the relationship between transferred mass (m in grams) and generated charge (Q in coulombs) would be as follows:

$$m = Q (63.546) / (2 \times 196,485) = 0.000162 \, Q$$

The above equation implies that each application of stress generates sufficient charge in systems I and II for transfer of $1.44 \times 10^{-10}$ g and $6.46 \times 10^{-8}$ g of copper, respectively. The rate of mass transfer in the nanocomposite system (II) is thus about 450 times greater than that in conventional system (I). Systems I and II both have close to 100 mg of copper occurring outside the stressed area. In order to transfer 10% of this mass, at a stress application rate of 3 cycles per second, we woud require 6,400 hrs and 14 hrs in systems I and II, respectively. Hence, the mass transfer phenomenon can occur rather rapidly for a nanolayered composite; in the case of conventional composite, however, the required time period for mass transfer seems to be prohibitively long. This conclusion proved to be true for diverse structural configurations we have considered so far. The simple reason explaining this conclusion is that the charge generated in piezoelectric layers is proportional to their surface area. Multiple piezoelectric nanolayers would thus generate more charge than a limited number of micrometer-thick layers. The fact that our approach would be viable in the context of a nanolayered composite highlights the significance of ionic self-assembly as a practical and low-cost means of processing structural elements for our application.

An Elaborate Structural Element Design

The self-adaptation phenomenon in bone can be mobilized by the introduction of flexural stresses (in addition to axial compressive stresses), which introduce tensile effects and stress gradients. Through transfer of mass from tensile to compressive zones, bone seeks to reduce eccentricity (flexural effect), thereby approaching a pure axial effect with normalized stress distribution. This section presents a system design which mimics this adaptive quality of bone. Figure 5.2a presents schematics of this system; it has a nanolayered structure similar to that shown in Figure 5.1. The stresses generated in piezoelectric nanolayers of the system shown in Figure 5.2a, however, are not bearing-type but axial stresses. It is the stress gradient (i.e., the difference in axial stress on the two sides of neutral axis) that generates electric potential in this case. The stress gradient is generated because flexural stresses are introduced (in addition to axial compressive stresses); our system, like bone, seeks to minimize these flexural stresses (i.e., minimize the stress gradient) through mass transfer. Figures 5.2b through 5.2e summarize this process. Figure 5.2b shows the ideal force condition where concentric loading produces uniform compressive stresses within the system. Eccentric loading (Figure 5.2c), however, produces flexural effects which generate stress gradient, increasing compressive stresses and potentially introducing tensile stresses. This stress gradient mobilizes the piezoelectric effect (Figure 5.2d – top) which drives mass transfer (Figure 5.2d – bottom) towards compression zone. This mass transfer makes the section centroid move towards the eccentric force, thus lowering the eccentricity and stress gradient, thereby normalizing the stress condition (Figure 5.2e). Specifics of the system design and the impact of mass transfer on stress distribution are presented below.
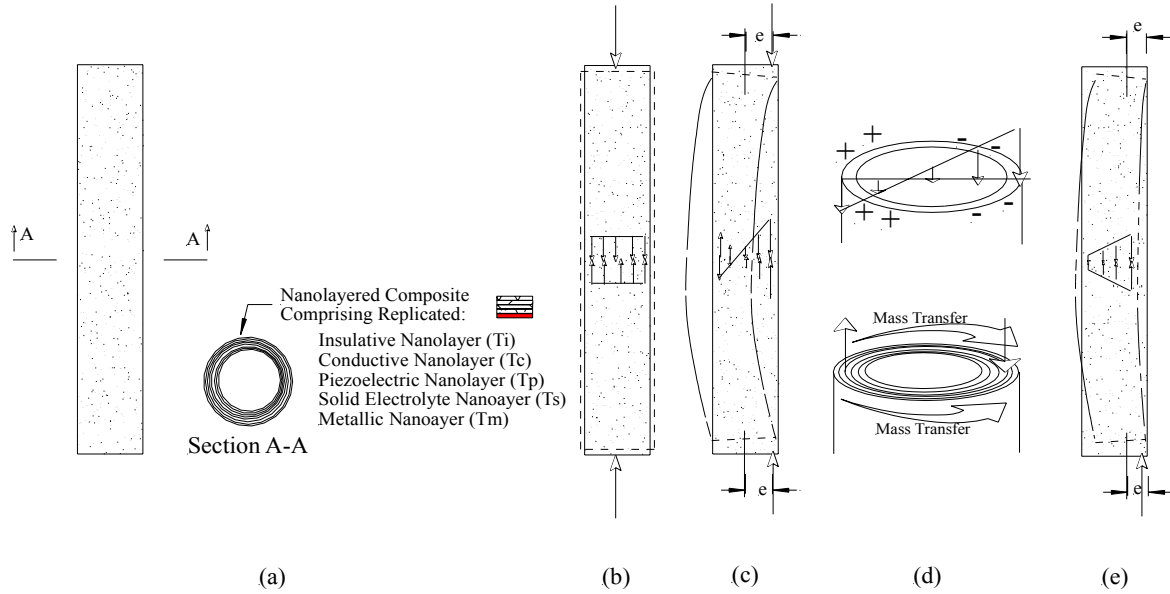
*Figure 5.2. Self-Adaptive System with the Biomimetic Capability to Mitigate Flexural Effects and Normalize Stresses Through Mass Transfer In Response to Stress Gradient.*

Figure 5.3 presents the cross-secitonal dimensions of the nanolayered composite system which is subject of this investigation. This system design utilizes piezoelectric ceramic to drive electrolysis processes which electrostrip copper from tensile zones, which is transported towards and electrodeposited at compression zone. Piezoelectric ceramic is chosen over piezoelectric polymer because ceramics offer a higher elastic modulus which is more compatible with that of metals (copper in this case). Comparable levels of elastic moduous are needed for both metals and piezoelectric ceramic developing high stress levels under axial-flexural effects, thus fully mobilizing their potential structural and functional capabilities. Collids of piezoelectric ceramic $BaTiO_3$ are available for use in the ionic self-assembly process. For the purpose of this preliminary design, we assumed that copper and piezoelectric ceramic both have an elastic modulus of 130 GPa. Both copper and piezoelectric ceramic can safely develop close to 45 MPa axial stress in service. The elastic modulus of polymers (about 3 GPa) is two order of magnitude smaller than those of piezoceramics and copper; hence, stress calculations should be based on a transformed cross section. Transformation of the section shown in Figure 5.3 (to 130 GPa equivalent elastic modulus) yields a moment of inertia (I) of $3.2 \times 10^{-10}$ m$^4$ and an area of $3 \times 10^{-5}$ m$^2$. The buckling load ($P_{cr}$) of the element is (assuming hinged end supports):

$$P_{cr} = (\pi^2.E.I) / l^2 = 411 \text{ N}$$

Under the effect of 250 N axial compression applied concentrically (Figure 5.4a), the element develops a uniform compressive stress of 8.33 MPa in structural constituents (ceramic and metal); no lateral deformations occur under concentric loading. When this axial compression (of 250 N) is applied at an eccentricity of 3 mm, axial-flexural effects produce lateral deformations (Figure 5.4b)with maximum value (at mid-height), d, expressed in terms of $k=(P/EI)^{0.5} = 2.45$ as follows:

$$d = e.[\cos kl/2 + (1 - \cos kl).\sin kl/2 / \sin kl -1) = 1.95 \text{ e} = 5.85 \text{ mm}$$

At mid-height, where the effective eccentricity is e + d = 8.85 mm, the peak compressive and tensile stresses would be 43 MPa and 26 MPa, respectively.  Each application of these stresses generate the following voltage (V) and charge (Q) through piezoelectric effect in the element:

$$V = g_{31}.s.t = 0.0518 \text{ V} \quad (51.8 \text{ mV})$$

$$Q = d_{31}.s.A = 0.3406 \text{ C}$$

The total mass of copper in the element adds up to 12 g.  At a stress application rate of 3 Hz, the piezo-driven electrolysis process can transfer 0.5959 g of copper per hour.  Hence, the system can transfer 6 g of copper from tension to compression half of the element in about 10 hours.  This mass transfer reduces the eccentricity of the system from 3 mm to 0 (Figure 5.4c), thus restroring the original pure axial behavior of the system with stresses back to the original uniform level of 8.33 MPa, which represents a five-fold reduction of compression (and elminiation of tension) resulting from the self-adaptation qualities of the element.

Nanolayered Composite
Comprising Replicated:

Insulative Nanolayer (Ti = 5 nanometer)
Conductive Nanolayer (Tc = 5 nanometer)
Piezoelectric Nanolayer (Tp = 150 nanometer)
Solid Electrolyte Nanoayer (Ts = 40 nanometer)
Metallic Nanoayer (Tm = 150 nanometer)

1 m

1 mm

A

A

10 mm

Section A-A
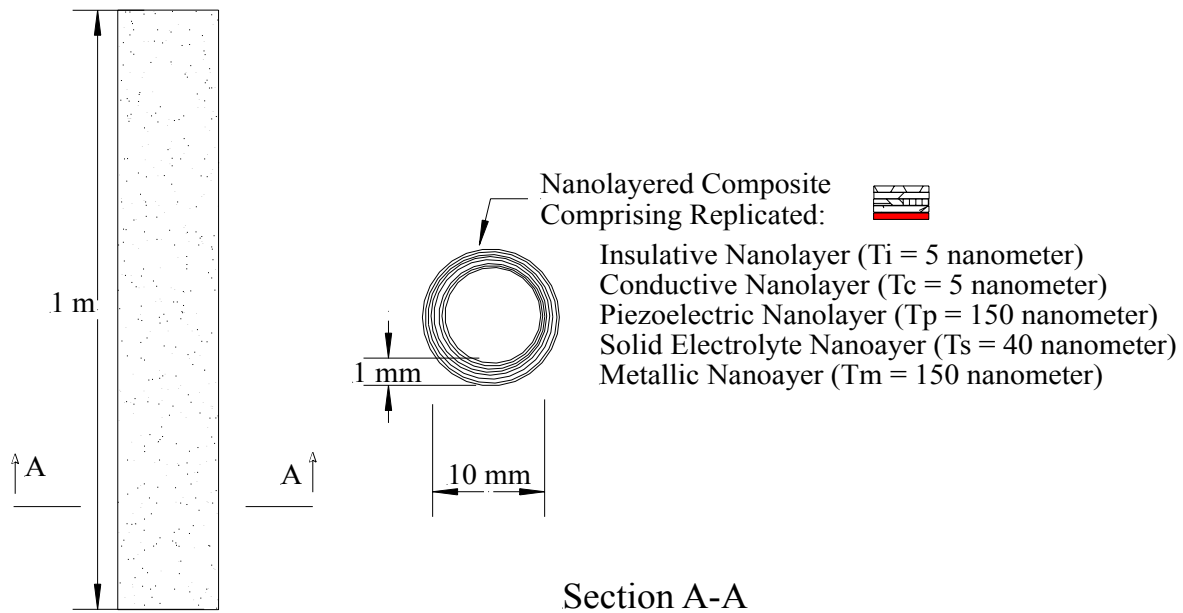
*Figure 5.3.  Specifics of System Design.*

112

<div align="center">

(a) Concentric Loading     (b) Eccentric Loading     (c) Concentricity Restored by Self-Adaptation

</div>
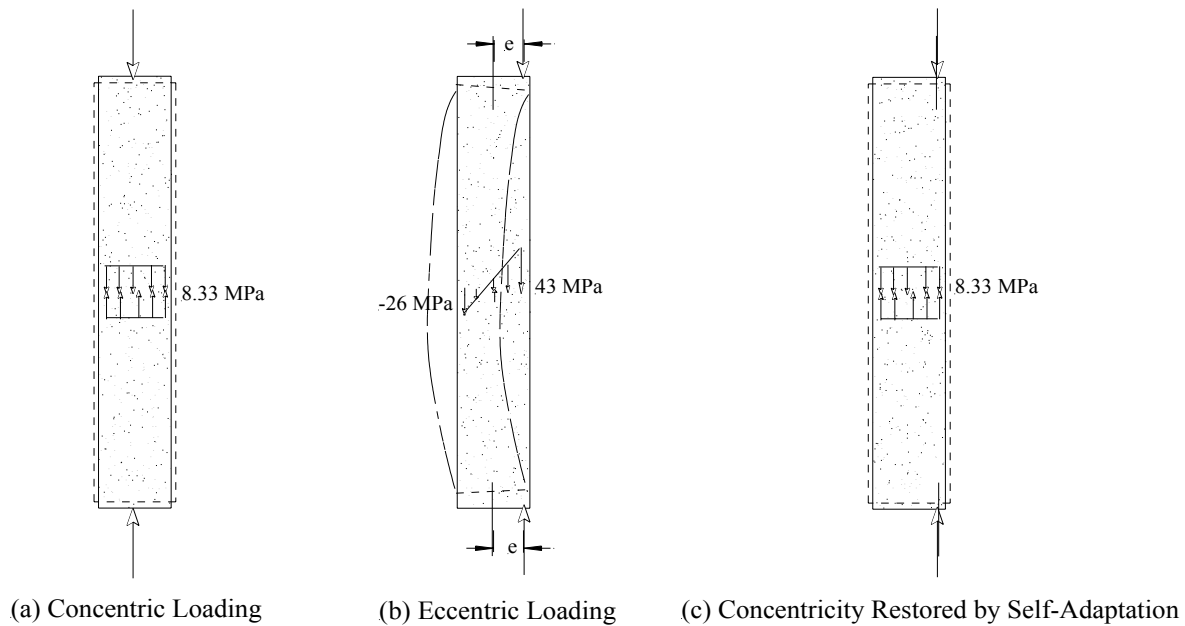
*Figure 5.4. System Performance Under Concentric Load, After Introduction of Eccentricity, and After Self-Adaptation Restores Concentric Behavior.*

A Preliminary Analysis of Structural Implications

The structural implications of the self-healing and self-adaptive qualities of the new material system were investigated conceptually through a series of simple analyses. A truss system is subject of this preliminary study (Figure 5.5). All members are modeled with hinged ends ,and have a length to thickness ratio of ten. The system is initially subjected to a uniform compressive stress state as shown in Figure 5.5.

Figure 5.6 shows the system response to an accidental eccentric loading which produces bending. Flexural behavior is clearly seen from the deformed configuration as well as the asymmetric axial load demand on the truss system. Under the eccentric loading, the stresses on the left members are 72% greater than those on the right vertical member. A self-adaptive material system would seek to minimize the newly imposed bending behavior. The analysis results shown in Figure 5.7 show that material transfer from the most severely tensioned (or least compressed) regions to the most compressed regions minimizes the bending response and equalizes bending stresses. This can be seen from observing the deformed geometry of the "self-adapted" truss in Figure 5.7b. In addition, while the axial force levels remain the same, the cross sectional area of the members are changed, thus achieving a more uniform stress demand in all members. Through a trial and error procedure, the stresses in the left and right vertical truss members assume equal values when 12.5% of the material from the right members (now weak struts) transfers to the left members (now strong struts).

The "self-adaptive" process seeks to normalize the stress distribution and then ceases to operate until another event generates stress gradient. As discussed above, the process is initiated by the presence of bending. Figure 5.8 shows the condition that would be created if too much material

(50%) were transferred from the severly tensioned members to compressed members. The deformed shape configuration shows how this "over-correction" leads again to a bending behavior and excess member stresses.

The potential for the system to exhibit "self-healing" effects is described in Figures 5.9 through 5.11. Figure 5.9 presents the response of a truss system similar to that shown in Figure 5.5 with the difference that additional load paths have been provided (cross members). The presence of "damage" to the member is modeled by the removal of a member. The response of the "damaged" system under the same uniform compressive load is shown in Figure 9.10. It can be clearly seen that the damage introduces significant bending deformations. In addition, stress demands on the members increase by as much as 11 times (cross members). A "self-healing" process would then be mobilized with material transferred from the bending tensile region to other members, thereby creating an alternate load path. The results of this exercise are shown in Figure 5.11. In the trial and error process, 70% of material from the left vertical members (weak struts) was transferred to the right vertical members and selected cross members, increasing their cross sectional area by 35% (strong struts). It can be seen that alternative load paths created by the material transfer can minimize bending deformations and establish a more balanced state of stress. This can be qualitatively observed in the deformed shape of the system and in the evaluated stresses, which particularly show how the cross members decrease their stress demand.



(a) Model            (b) Deformed Shape           (c) Axial Load Diagram
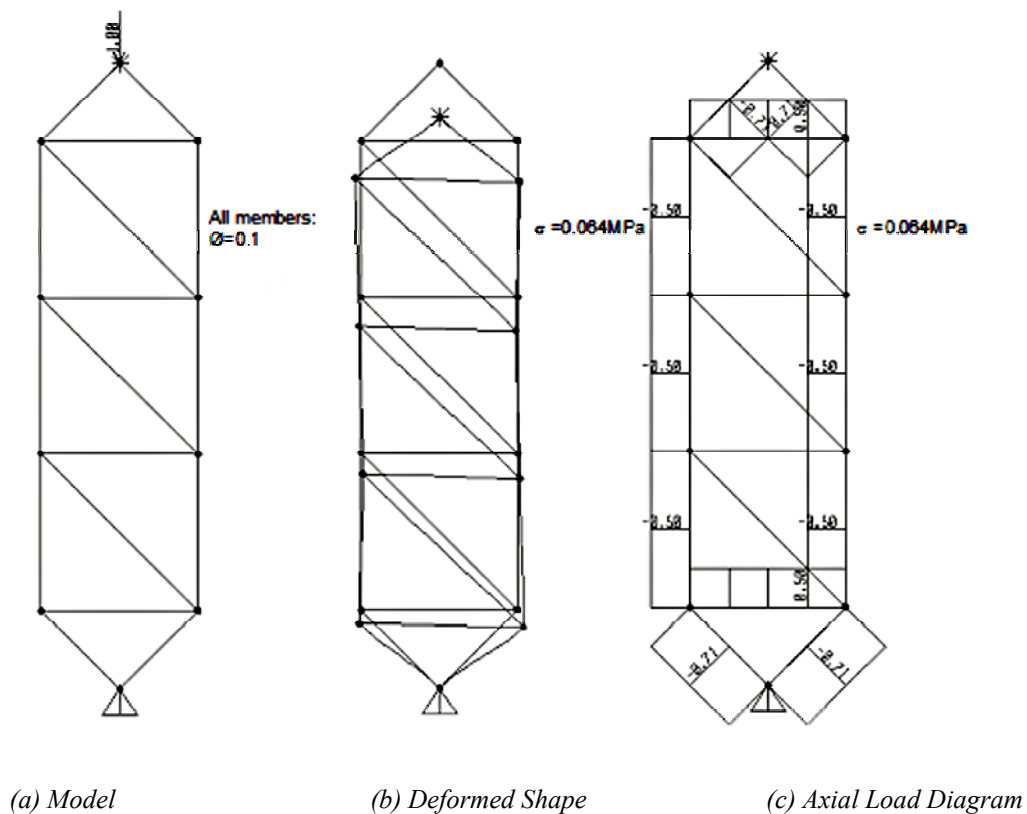
*Figure 5.5. The Truss Subjected to Uniform Compressive Load*
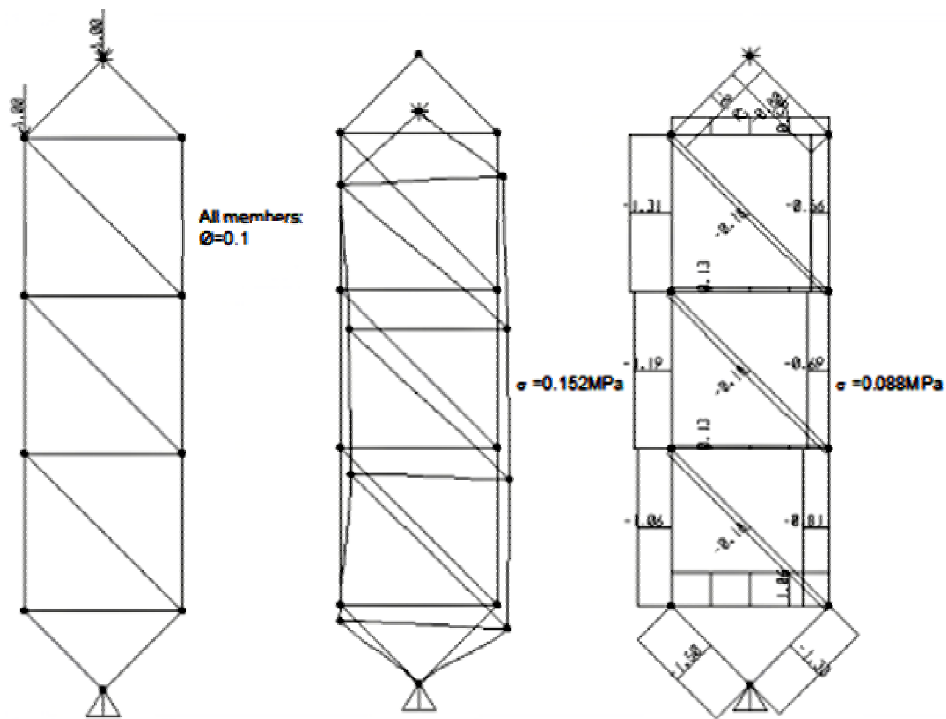
| (a) Model | (b) Deformed Shape | (c) Axial Load Diagram |

*Figure 5.6. Strut Subjected to Accidental Load Causing Bending*
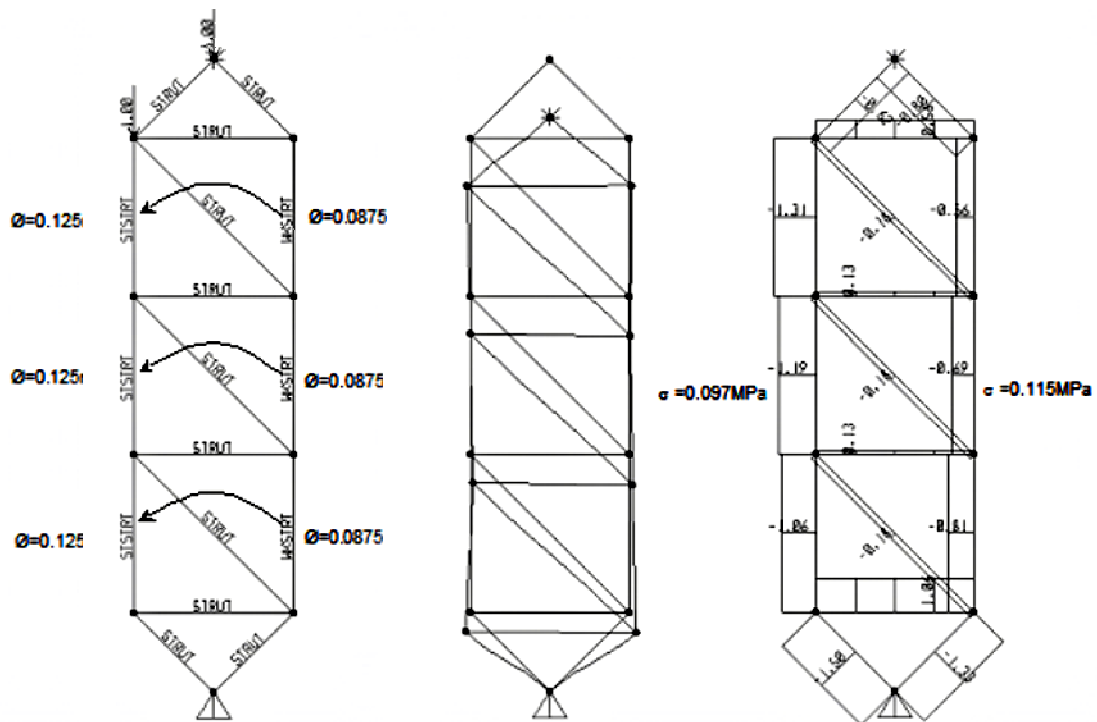


| (a) Model | (b) Deformed Shape | (c) Axial Load Diagram |

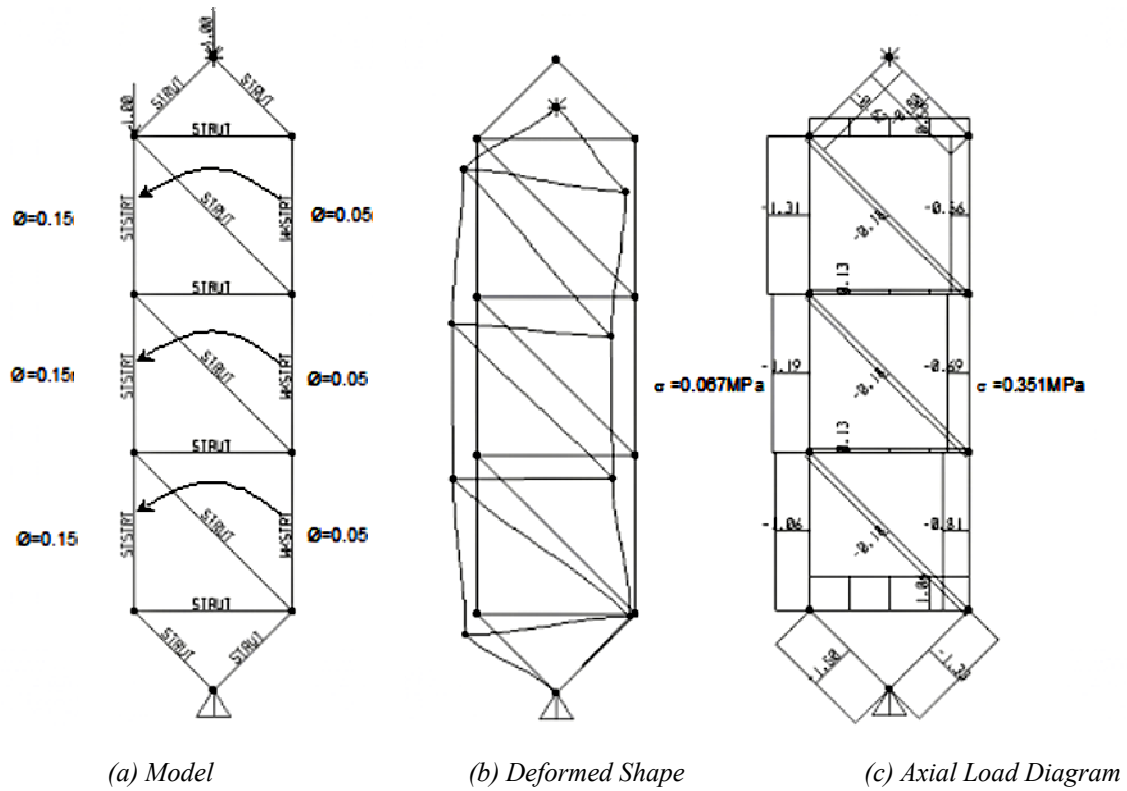*Figure 5.7. Member Self-Adaptation to Minimize Bending Effects*

|(a) Model|(b) Deformed Shape|(c) Axial Load Diagram|

*Figure 5.8. Self-Induced Bending Behavior with Excessive Material Migration*



|(a) Model|(b) Deformed Shape|(c) Axial Load Diagram|
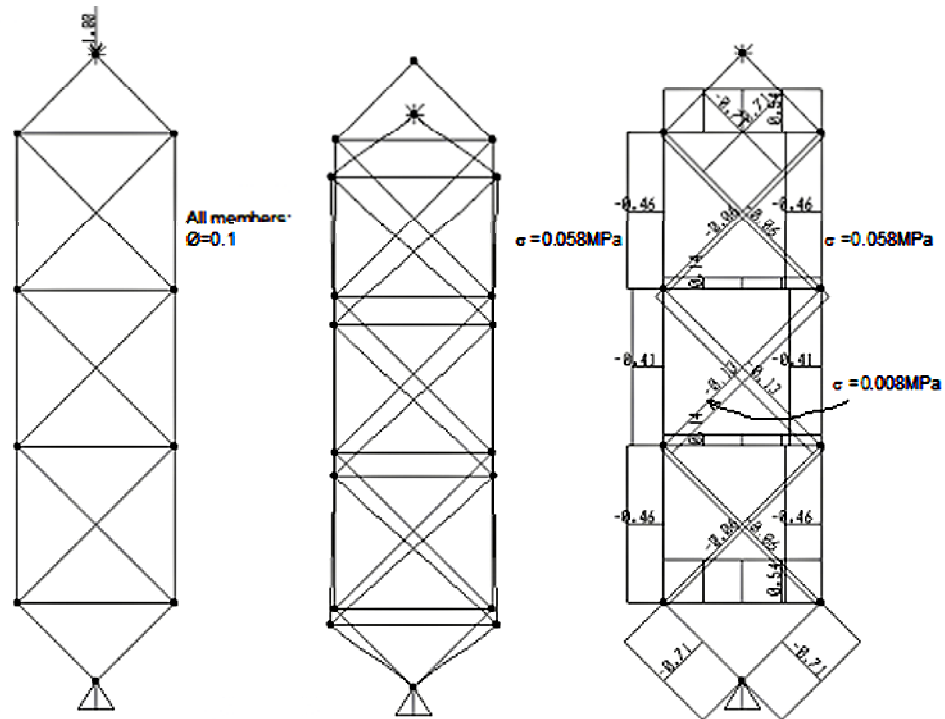
*Figure 5.9. Uniformly Compressed Strut Modeled with Additional Load Paths*

116
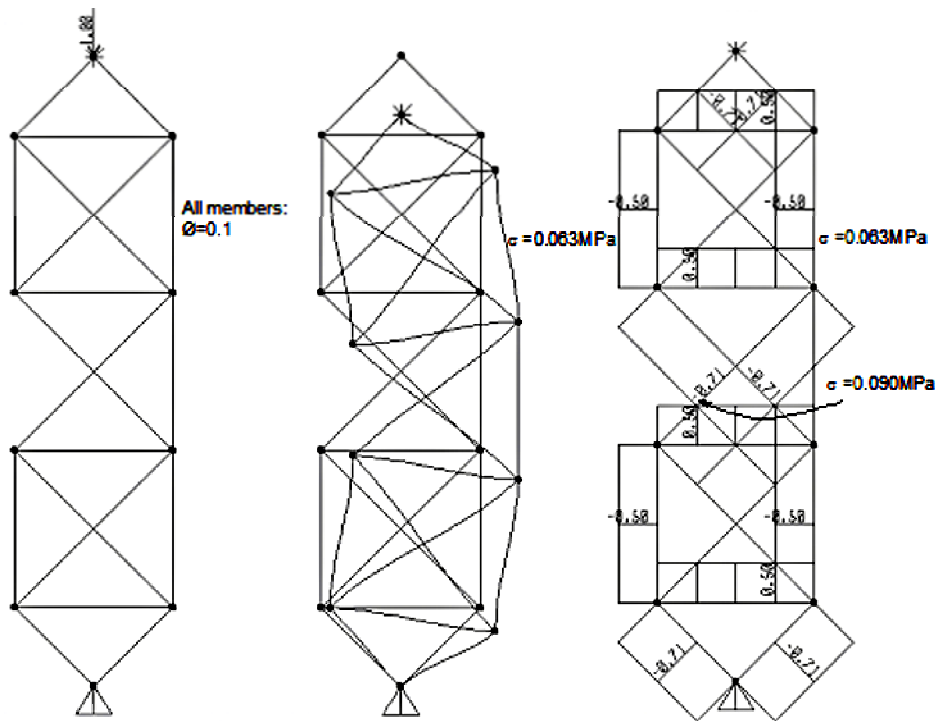
*(a) Model*        *(b) Deformed Shape*        *(c) Axial Load Diagram*

*Figure 5.10. Strut Subjected to Damage Causing Bending*
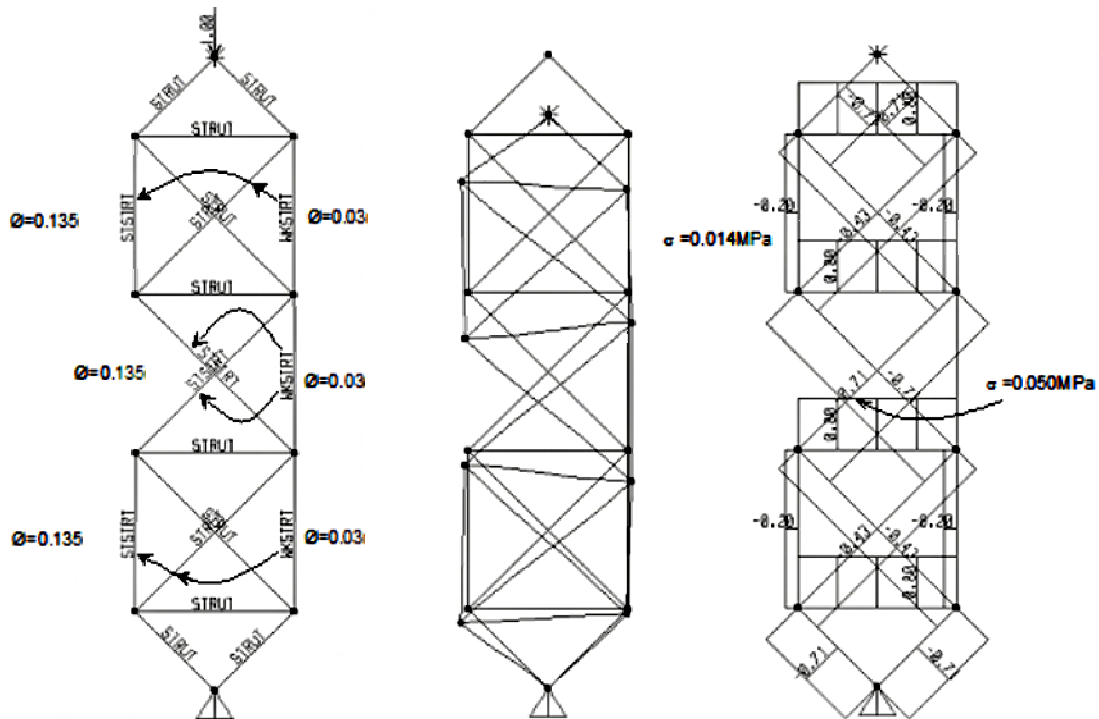


*(a) Model*        *(b) Deformed Shape*        *(c) Axial Load Diagram*

*Figure 5.11. Member Self-Adaptation to Minimize Bending Effects due to Damage*

117

**Experimental Validaiton of An Integrated System**

Our preliminary efforts to validate the concept of adaptive and self-healing systems focused on the basic design of Figure 5.12 (introduced earlier). This system is subjected to bearing stress on a fraction of its surface. Adaptive qualities yield mass transfer from unstressed to stressed areas. This system was built-up through ionic self-assembly (Figure 5.13a), and was subjected to a bearing stress of 30 MPa at a rate of 3 cycles per second (Figure 5.13b) for a total period of 14 hours. Weight of the system was measured prior to test; after test the unstressed and stressed areas were cut and weighed separately. These measurements indicated that 6.4 mg of mass was transferred from unstressed to stressed area, confiming that the adaptive process has actually occurred. There is, however, a discrepancy between the predicted level of mass transfer (close to 10 mg) and the measured one. More elaborate modeling of complex interface phenomena could yield a more accurate prediction of test results.

Replicated Multilayers of:
    Insulative Layer (5 nm)
    Conductive Layer (5 nm)
    Piezoelectric Layer (50 nm)
    Solid Electrolyte Layer (40 nm)
    Metallic Layer (40 nm)

0.5 mm

20 mm

15 mm

15 mm

20 mm
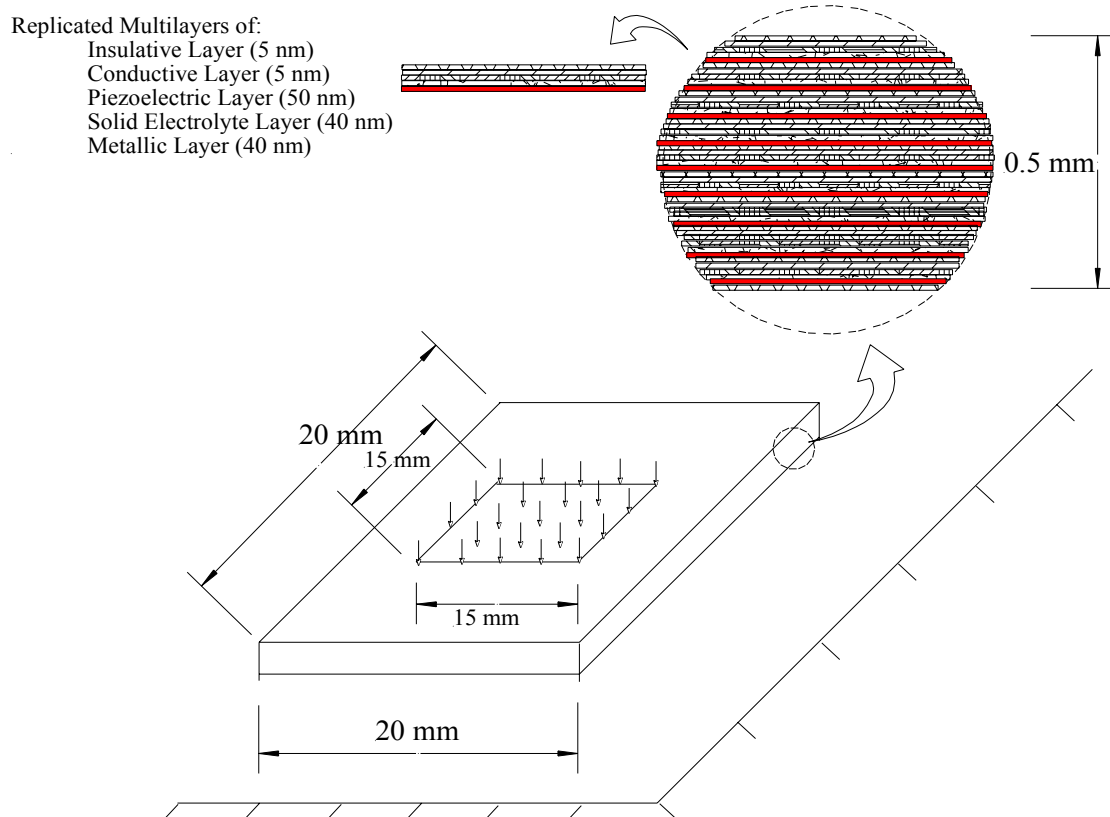
*Figure 5.12.  The Basic System Design for Experimental Validation.*



*(a) Ionic Self-Assembly*



*(b) System Under Bearing Test*

*Figure 5.13.  Processing and Testing of the Basic System.*

119

# CHAPTER 6

## THEORETICAL MODELING AND EXPERIMENTAL VALIDATION OF STRUCTURAL QUALITIES

### Introduction

Structural systems embodying the adaptive and self-healing principles introduced earlier can assume diverse forms. Our focus in this project is on self-assembly of nanolyaers on open-cell structures to develop lightweight composites with the potential to yield tremendous levels of structural efficiency by complementary use of the precursor (base cellular) and hybrid nanolayered composite materials. A cellular solid may be regarded as an interconnected network of solid struts or plates that form the edges and faces of cells, see Figure 6.1. Due to their high performance index (large structural properties with respect to their density), open-cell cellular solids, or foams, like that shown in Figure 6.1 are of particular interest. While polymers, metals, ceramics, glasses, and even composites can be fabricated into cells, the properties of the resulting foam is dictated by the (usually homogeneous) composition of the cell struts. The structural component of our project seeks to demonstrate that development of nanocomposite struts by the self assembly of nanolayers can lead to improved performance of cellular systems.
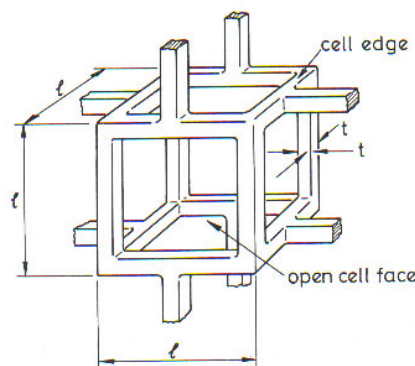


*Figure 6.1. Cubic Model for Open-Cell Solid.[69]*

Although the cell arrangement for the multi-layered cellular material under study has not been finalized, its geometry is expected to follow well-identified patterns that can be studied using unit cells similar to that shown in Figure 6.1. The most important difference, however, is the multi-layered composite architecture of the cell wall/strut cross-section. The assembly of monolayers and multi-layered stacks of polymer, metal, or ceramic colloidal solutions can allow gradual composition of composite cross sections. A base low-density (homogeneous) cellular foam is use as the precursor for buildup of the section, yielding a layered cross-section with a center core and outer layered rings as shown in Figure 6.2. Deposition of layers requires staggering of layers with alternating ionic charge. This requires deposition of alternating ceramic, metal, and polymer layers as schematically shown in Figure 6.2.
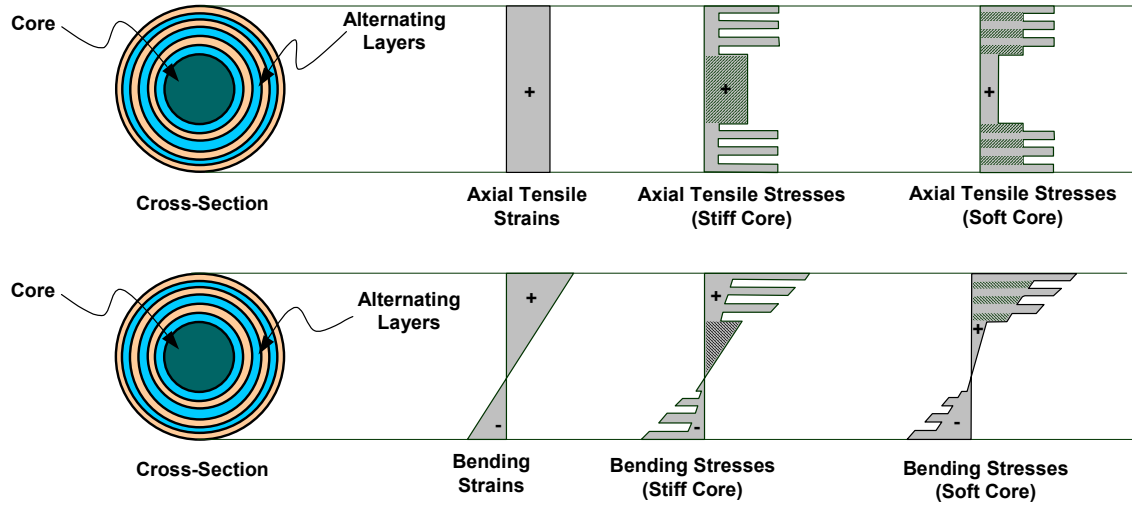
*Figure 6.2. Schematic of Axial and Bending Strains and Stresses in Laminated Cross-Section.*

Unit-cell approaches proposed by Gibson and Ashby (1988)[69] to characterize open-cell materials seems to adequately describe the behavior of cellular solids. However, they directly apply only to systems composed of a homogeneous material. The goal of our computational studies is therefore to extend the models to cover open-cell materials with multi-layered, hybrid composite walls/struts. This progress report focuses on *section-level analysis,* where computational models were developed to evaluate the section behavior of multi-layered walls/struts in tension, compression, and bending.

## Material Selection and Modeling

Our effort focuses on the development of a nanocomposite cell strut architecture that best takes advantage of the properties inherent to different classes of materials. Hence, the three basic categories of materials (ceramics, metals, and polymers) are considered. Within these material types, a pair of choices is selected for each category of materials. These choices cover representative ranges of material properties for each category of materials, and also reflect on current availability of open-cell foam materials to be used as precursors in developed of our hybrid nanocomposite system. A summary of the selected materials and their properties is given in Table 6.1.

*Table 6.1. Material Properties for Analysis of Multi-Layered Struts.*

| Material | Density $(Mg/m^3)$ | Elastic Modulus $(nN/nm^2)$ | Elastic Tensile Limit $(nN/nm^2)$ | Elastic Comp. Limit $(nN/nm^2)$ | Ultimate Strength $(nN/nm^2)$ |
|---|---|---|---|---|---|
| Ceramics | | | | | |
| RVCarbon | 1.54 | 35 | 0.058 | 0.58 | |
| Silicon Carbide | 3.20 | 410 | 0.35 | 0.35 | 0.35 |
| Metals | | | | | |
| Aluminum Alloy | 2.70 | 74 | 0.3635 | 0.3635 | 0.50 |
| Copper | 8.90 | 124 | 0.060 | 0.060 | 0.40 |
| Polymers | | | | | |
| Polyurethane (Rigid) | 1.20 | 1.60 | 1.27 | 1.27 | 1.30 |
| Polyurethane (Flexible) | 1.20 | 0.045 | na | na | na |

Given the complex structure of the material system, comprising multiple nanolayers built upon an open-cell structure, two different geometric regimes are considered in analysis: the core, and the built-up layers. The core component is defined by the geometric characteristics of the open-cell foam precursor. At this point, the geometry of the core is assumed to be circular. The built-up layers are those added to the precursor foam through the self-assembly process. While the thicknesses of these layers vary depending on the material type and self-assembly conditions, this preliminary analysis assumes a constant thickness for all assembled nanolayers. The manufacturing process, however, depends on the assembly of oppositely charged colloidal and dissolved substances. In general, ceramics and metals are positively charged, while polymers could be either negatively or positively charged. The analyses assume a layered assembly that repeats a basic combination of ceramic-polymer-metal-polymer layers.

Constitutive Properties of Materials

*Ceramics*

Ceramics are brittle materials, and thus their behavior is linear (Eq. 1) up to failure at maximum compressive and tensile strains. In Equation (1), $E_c$ is the ceramic elastic modulus, and $\varepsilon_c$ is the strain in the ceramic material.

$$f_c = E_c \varepsilon_c \tag{1}$$

Due to their brittle nature, the tensile behavior of ceramics is typically inferior to their compressive response. Local flaws and microcracks tend to concentrate tensile stresses; the low fracture toughness of ceramics undermines their ability to mitigate propagation of these flaws and microcracks under tensile stresses. The response of brittle materials can be significantly improved by the provision of reinforcement and through transverse confinement. Bonding of polymer and metal layers to the ceramic core and/or ceramic layers on strut thus bring about improvements in tensile behavior. This phenomenon parallels steel reinforcement of concrete, and is referred to as "tension stiffening." The relationship defining this phenomenon is:

$$\textit{If } \varepsilon_x > \varepsilon_{cr}, \textit{ then}$$
$$f_t = \frac{f_{cr}}{1 + \sqrt{500\varepsilon_x}} \tag{2}$$

where $f_{cr}$ is the cracking stress, $\varepsilon_{cr}$ is the cracking strain, $f_t$ is the tensile stress and $\varepsilon_t$ is the tensile strain.

It is also well known that transverse confinement enhances the compressive strength and ductility of brittle materials. While several models exist for this phenomenon, their applicability to generic ceramic materials, especially at the dimensional scales of our material system, is questionable. However, it is believed, that the presence of metal layers surrounding a ceramic core and/or ceramic layers will produce trends similar to those predicted by these models. For this reason, the following assumptions are made for modeling the response of confined ceramics:

(a) An elasto-plastic stress-strain response is assumed with a maximum stress equal to the peak compressive strength; and
(b) The ultimate compressive strain is made dependent on the amount of metal layers confining the ceramic core and/or ceramic layers according the following equation:

$$\varepsilon_{cu} = \varepsilon_{co} + \frac{5.6t_j f_{my} \varepsilon_{mh}}{D_j f_{cu}} \tag{3}$$

where, $\varepsilon_{cu}$ = the ultimate compressive strain, $\varepsilon_{co}$ = the compressive strain at peak stress, $t_j$ = the additive metal layer thickness providing confinement, $f_{my}$ = the metal yield stress, $\varepsilon_{mh}$ = the metal ultimate tensile strain, $D_j$ = the diameter of the confining metal layer, and $f_{cu}$ = the ultimate compressive stress of the ceramic material.

*Metals*

The stress-strain response is characterized by a distinct elastic region, a yield plateau, a strain-hardening region, fallowed by a falling branch after peak stress up to failure. The response is considered similar in tension and in compression.

Equations describing the monotonic uniaxial stress-strain curve up to ultimate strain are:

For the elastic range, i.e., $\varepsilon_s \leq \varepsilon_y$:

$$f_m = E_m \varepsilon_m \tag{4}$$

where, $e_m$, $f_m$ = axial strain and stress in metal, respectively; $e_y$ = yield strain of metal; and $E_m$ = modulus of elasticity of metal.

For the yield plateau, i.e., $\varepsilon_y \leq \varepsilon_m \leq \varepsilon_{sh}$:

$$f_m = f_y \tag{5}$$

where, $\varepsilon_{sh}$ = axial strain at the onset of strain-hardening.

For the strain-hardening range, i.e., $\varepsilon_{sh} \leq \varepsilon_m \leq \varepsilon_{su}$:

$$f_m = f_y \left( \frac{m(\varepsilon_m - \varepsilon_{sh}) + 2}{60(\varepsilon_m - \varepsilon_{sh}) + 2} + \frac{(\varepsilon_m - \varepsilon_{sh})(60 - m)}{2(30r_s + 1)^2} \right) \tag{6}$$

$$m = \frac{(f_{su}/f_y)(30r_s + 1)^2 - 60r_s - 1}{15r_s^2} \tag{7}$$

$$r_s = \varepsilon_{su} - \varepsilon_{sh} \tag{8}$$

where, $\varepsilon_{su}$, $f_{su}$ = ultimate strain and stress in metal, respectively.

Based on the above model, two different types of response are modeled: metals with large ductile response, and high-strength metals with low ductility:

For ductile metal response: $\qquad\qquad \varepsilon_{sh} = 14\ \varepsilon_y$
$\qquad\qquad\qquad\qquad\qquad\qquad\qquad\quad \varepsilon_{su} = 0.14 + \varepsilon_{sh}$

For high-strength metal response: $\qquad \varepsilon_{sh} = 5\ \varepsilon_y$
$\qquad\qquad\qquad\qquad\qquad\qquad\qquad\quad \varepsilon_{su} = 0.12$

*Polymers*

The constitutive behavior of polymer materials is more variable than those of ceramics and metals. In general, three types of behavior are identified: (a) a linear elastic brittle behavior (similar to ceramics); (b) a ductile type of behavior (similar to metals); and (c) a plastic or rubber-type behavior (similar to post-yield metal behavior). All these three types of polymer response are considered in our analyses as discussed below.

The response of linear elastic brittle polymers follows the model described for ceramic materials, except that no consideration for confinement or tension stiffening is provided. The behavior of ductile polymers follows the model described for metals, comprising an elastic branch, a yield plateau, and a strain-hardening region. Finally, the plastic/rubber type of polymer behavior follows an elastic-homogeneous plastic response:

$$f_p = K\varepsilon^n \tag{9}$$

where, $f_p$ = stress in the polymer; $K$ = a material constant, typically between *G/100* and *G/1000*, $G$ = shear modulus of the polymer; $\varepsilon$ = axial strain; and $n$ = strain-hardening coefficient, usually taken at *0.2*.

Equation 9 is commonly used to define the plastic (from the onset of yielding to the maximum response) behavior of metals. Thus, the strain term ($\varepsilon$) typically refers to the true plastic strain. In our case, we use this model to represent the plastic-type response of soft , and thus the strain term is simply the actual strain in polymer. The model neglects the elastic portion of response.

**Section Analysis Procedures**

This section describes the analytical procedure for modeling the response of multi-layered cell struts in open cell structures. The models were developed primarily to guide design of the new material system. The approach devised here is based on evaluation of section-level behavior using the material constitutive models presented above.

The type of member considered is presented in Figure 6.3. A prismatic element of constant cross sectional area over its length is considered. The cross section is assumed to be symmetrical about the vertical axis. The built-up layers are assumed to be concentric with the circular cross sectional core. It is also assumed that the section is only subjected to normal strains, and that these strains are uniform over the width of the section and vary linearly through the depth of the section (i.e., plane sections remain plane). Finally, it is assumed that perfect bond exists between the core and the built-up layers and also between individual layers.
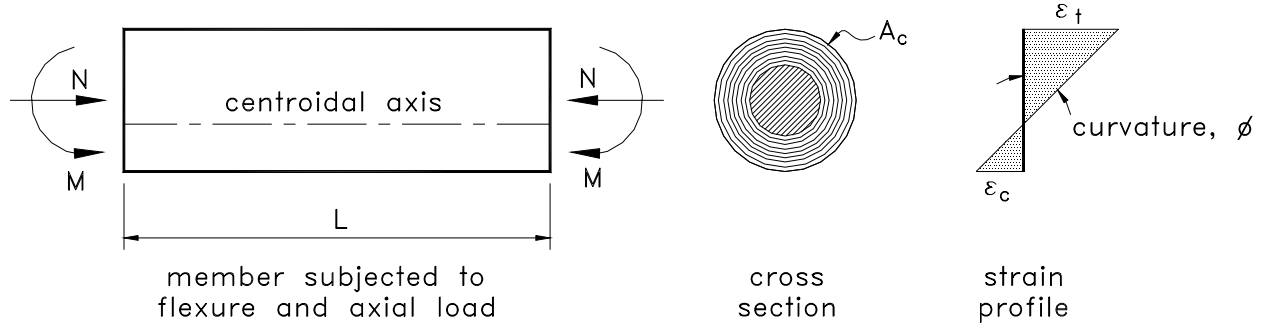
*Figure 6.3. Multi-Layered Cell Strut Element under Flexure and Axial Load*

Section-level analysis (Figure 6.4), commonly termed moment-curvature analysis, allows evaluation of the axial-flexural response of a section by considering force equilibrium for a given strain distribution. The linear strain distribution can be defined simply by one value, that is the slope of the strain distribution profile (i.e., curvature). Thus, with reference to Figure 6.4, the strain at any level $y$ is given by:

$$\varepsilon_y = \varepsilon_{co} - \phi y \qquad (10)$$
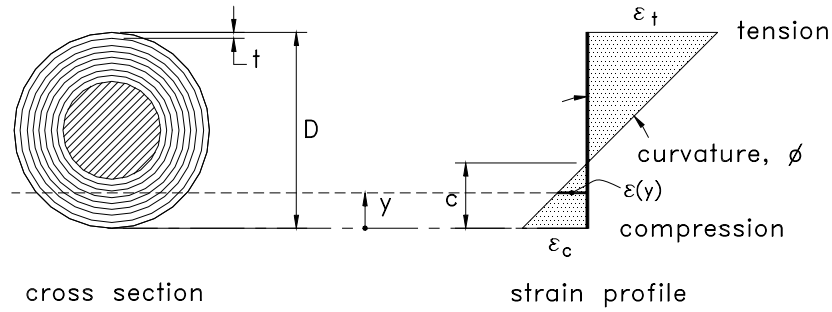


*Figure 6.4. Axial-Flexural Strain Distribution at Strut Cross Section.*

Equilibrium conditions yield the stress state along the cross section for a given curvature. At any section, by integrating the stress resultants and by enforcing equilibrium, the axial and flexural forces ($N$ & $M$, respectively) can be found:

$$\int_{A_c} f_c dA_c + \int_{A_l} f_l dA_l = N \qquad (12)$$

$$\int_{A_c} f_c y dA_c + \int_{A_l} f_l y dA_l = M \qquad (13)$$

The approach followed to determine the moment-curvature response of the section consists of choosing a value for the extreme compressive strain of section and the applied axial force, and then finding the corresponding curvature that equilibrates the axial resultant of internal stresses

125

against the applied axial force. The moment associated with the resulting strain distribution is then determined. The complete section response is obtained by repetition of these calculations for incremental levels of extreme compressive strain.

Due to the difficulty in evaluating the integrals of Equations (12) and (13), the problem is solved using the "fiber-based section analysis" The cross section is idealized as a series of rectangular or trapezoidal "fibers," with strain is assumed to be constant within the fiber, and equal to the actual strain at center of the layer (see Figure 6.5). Since only uni-directional bending is being investigated (noting that for circular sections biaxial bending can be analyzed as a uni-axial bending), the section core can be simply subdivided into horizontal layers. The built-up layers are assumed to have uniform thickness and are placed concentrically around the center core. The built-up layer fibers are discretized around the circular geometry in angular increments thus creating a string of rectangles around the layer perimeter.

With the above section discretization and the assumption of uniform strain over the rectangular fibers, the stress resultants will also be uniform over the layer. The force in each layer is simply found as the product of stress by its area. The moment contribution of each layer is determined by multiplying its force by the distance between the centroid of the layer and a reference axis. The resulting section axial force and moment are obtained by summating all of the layer forces and moments. Obviously, the idealization becomes more accurate as the fibers become smaller. A computer program for evaluating the axial force-strain and moment-curvature response of the multi-layered struts was developed.
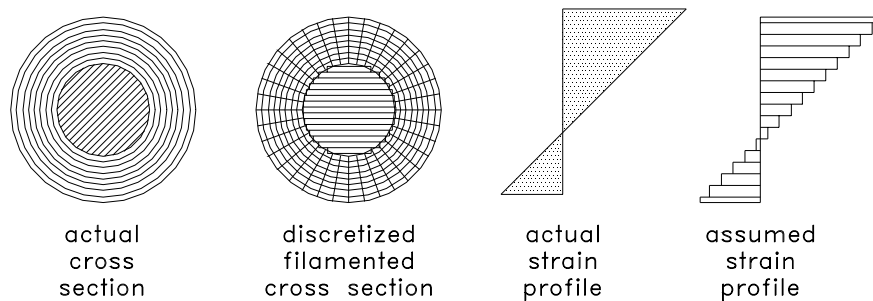


| actual cross section | discretized filamented cross section | actual strain profile | assumed strain profile |

*Figure 6.5. Multi-Layered Strut Section Idealization for Numerical Computation.*

**Numerical Results and Assessment of Section-Level Behavior**

This section summarizes results of numerical computations conducted so far on laminated composite strut sections (of a cellular material system). The objectives of the section-level analyses were to :

(1)     provide guidance to the manufacturing efforts in regard to optimal material lamination arrangements and selection for the precursor core material; and

(2)     demonstrate the potential benefits of the proposed material system in terms of enhanced performance.

Development of this new cellular composite material system is based on the structure of cancellous bone. Hence, the cell sizes are of the order of 1 mm, and the strut cross sectional dimensions are of the order of 0.01 mm. Under the currently considered manufacturing process, alternating material layers may have a thickness of about 10 nm (this thickness can be controlled by adjustment of solution chemistry; it tends to be smaller for polymer layers). In order to have an assessment of the overall benefits of the proposed material design, system combinations of Table 6.2 were considered in our preliminary analyses.

*Table 6.2. Material System Combinations Considered in Preliminary Analyses.*

|  | Core | Ceramic Layers | Metal Layers | Polymer Layers |
|---|---|---|---|---|
| **Case 1** | RVC | RVC | Copper | Polyurethane (F) |
| **Case 2** | Copper | RVC | Copper | Polyurethane (F) |
| **Case 3** | Polyurethane (F) | RVC | Copper | Polyurethane (F) |

Figures 6.6 through 6.23 present the tensile, compressive, and flexural responses for system combinations of Table 2 (Cases 1 through 3). All figures present three traces, one for the initial core precursor with a diameter of 0.05 mm (solid cross section), one for a built-up layered composite section with total diameter of 0.1mm, and one the homogeneous core material if its section diameter was increased to match the total built-up diameter of layered composite.

Evaluation of the figures shows that the deposition assembly of different material layers on the solid material precursor has major positive effects on the response of section in tension, compression, and bending. While this improved performance might be considered a direct consequence of the increase in section diameter and thus material substance available, improved performance is also observed in comparison with the a solid cross section of equal diameter made solely of the precursor material. This enhancement is clearly due to the mechanical advantages provided by the complementary material characteristics of the hybrid system built-up on the section.

While all material precursors were enhanced by the build-up of the hybrid system, the improvements were different for each case. The performance of flexible polyurethane precursor material is most dramatically improved with the deposition of addition of multiple layers, followed by the reticulated vitreous carbon, and lastly the copper precursor. Strength enhancements of the layered section over the initial core section varied 200% - 900% for Cases 1 and 2, and 3000% - 15000% for Case 3. The improvements in ductility and energy absorption capacity were as dramatic. Versatility of the process allows engineering of built-up layers and core materials to achieve diverse balances of strength, stiffness and ductility in tensile, compressive and flexural modes of behavior.
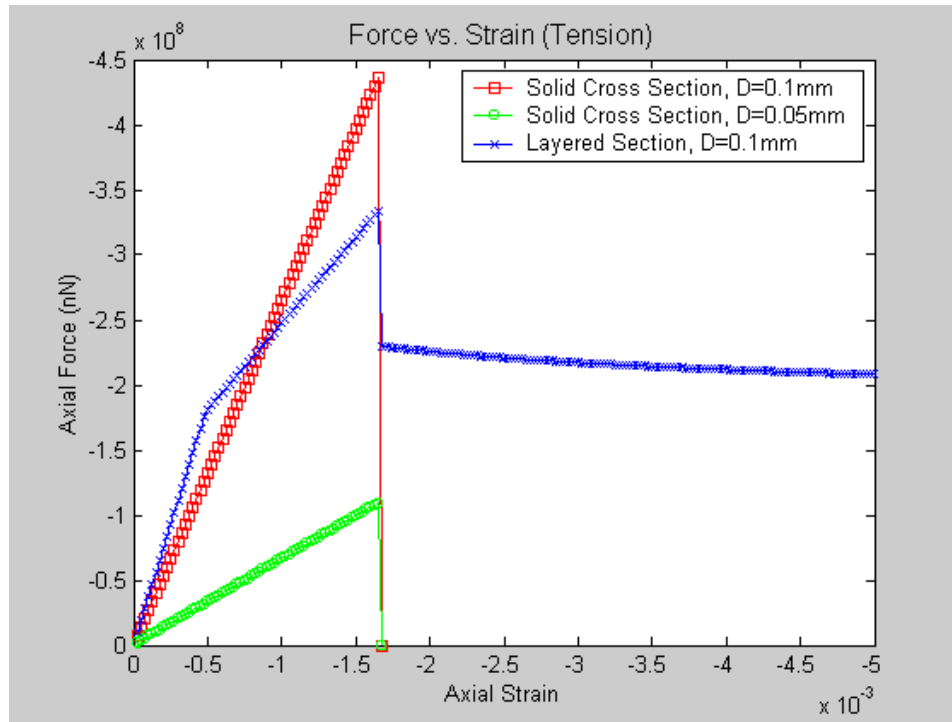
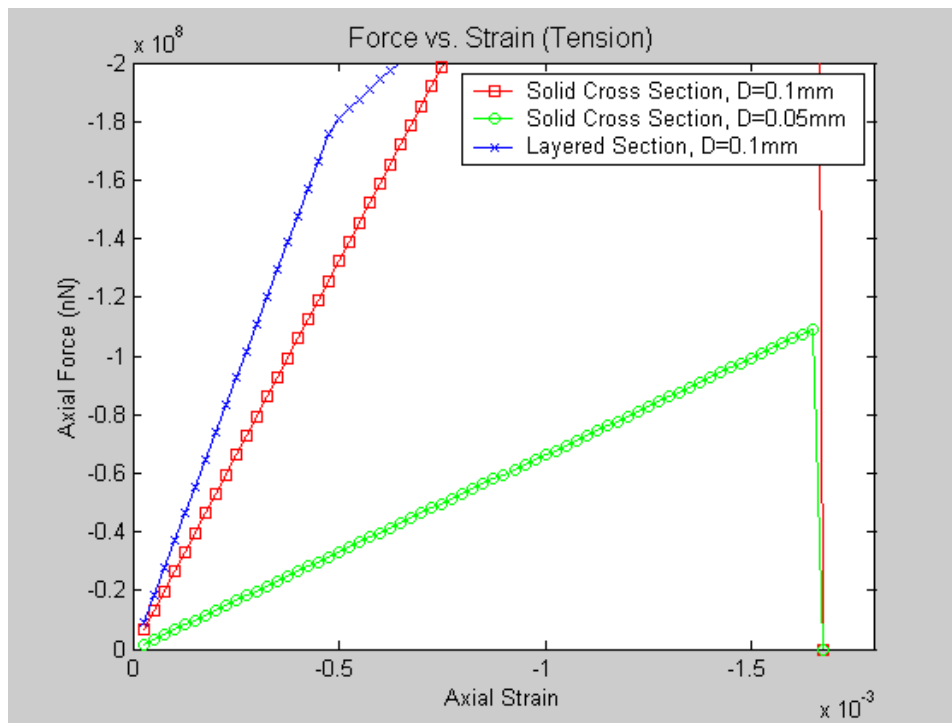*Figure 6.6. Tensile Response for Case 1 (RVC core)- Total Response.*



*Figure 6.7. Tensile Response for Case 1 (RVC core)- Initial Part of Response.*
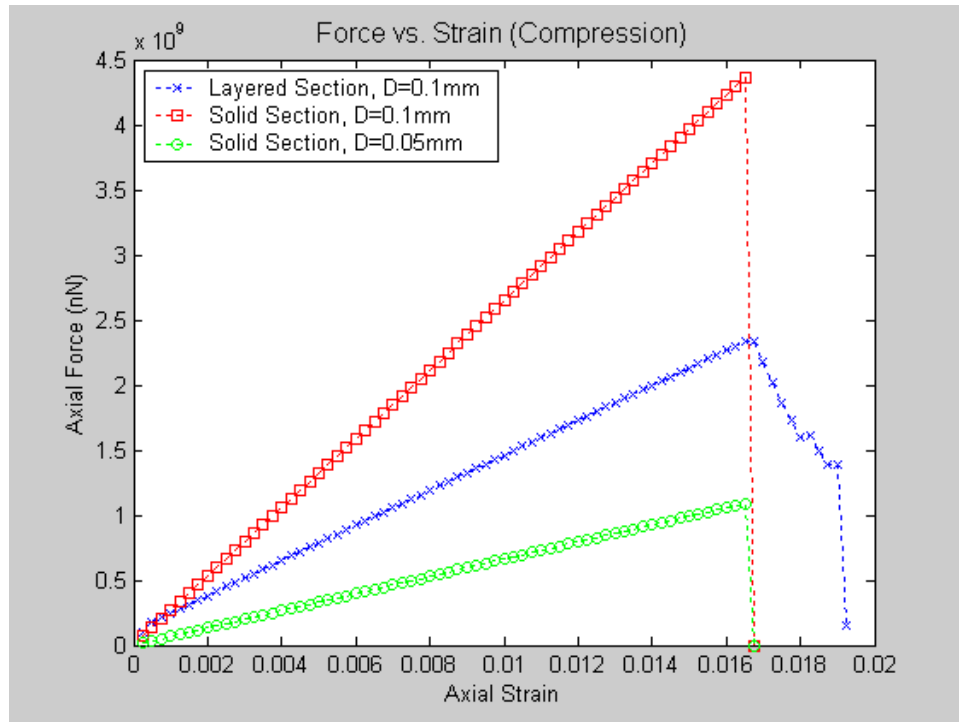
*Figure 6.8. Compressive Response for Case 1 (RVC core) – Total Response.*
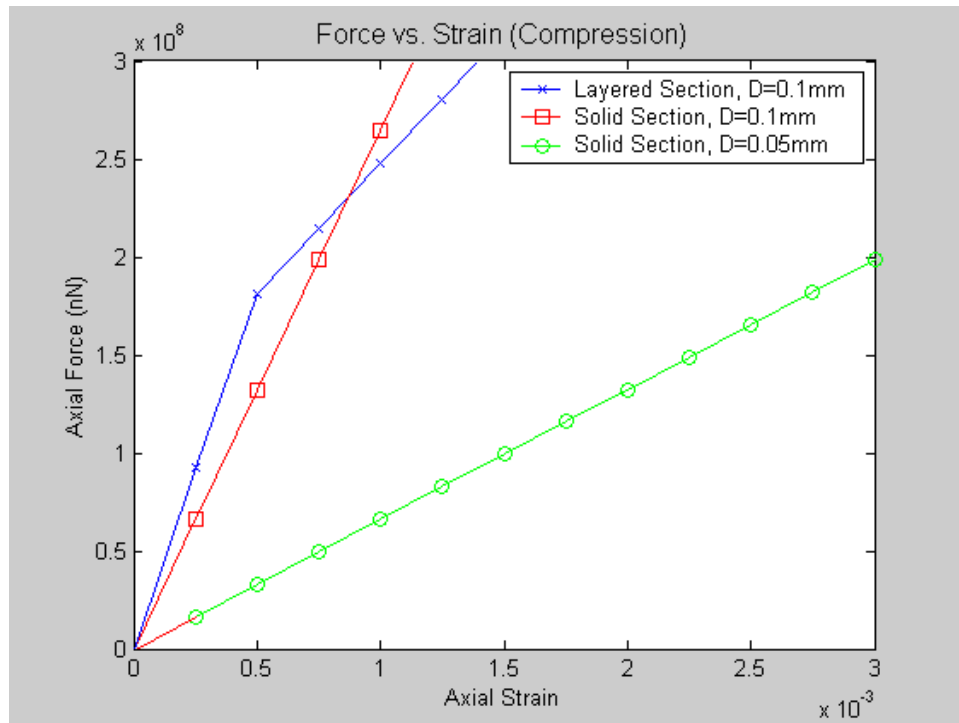


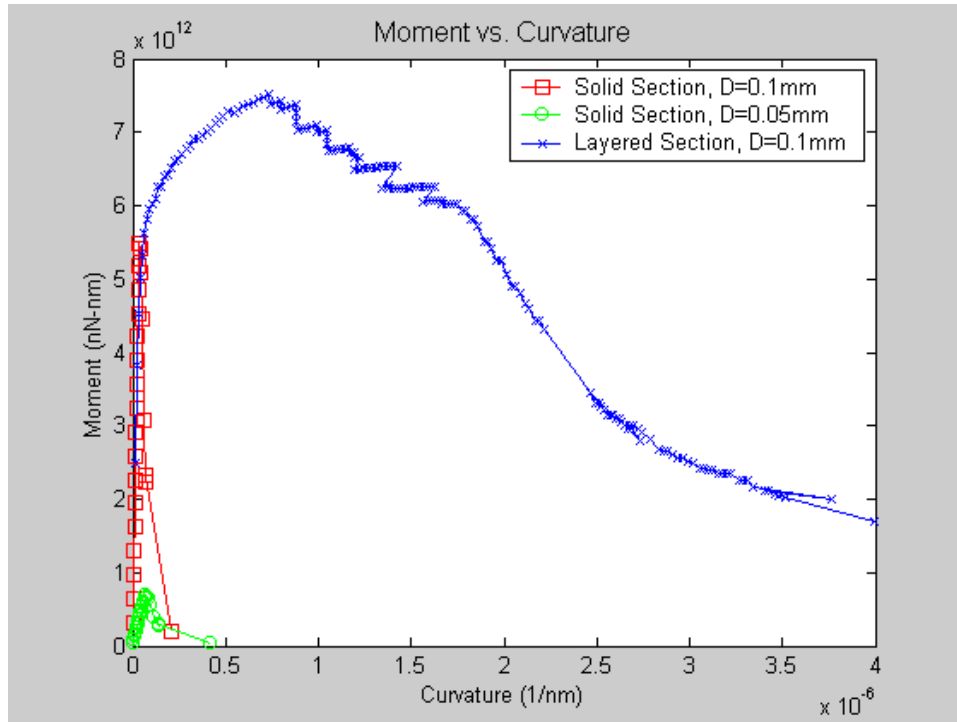*Figure 6.9. Compressive Response for Case 1 (RVC core) – Initial Part of Response.*

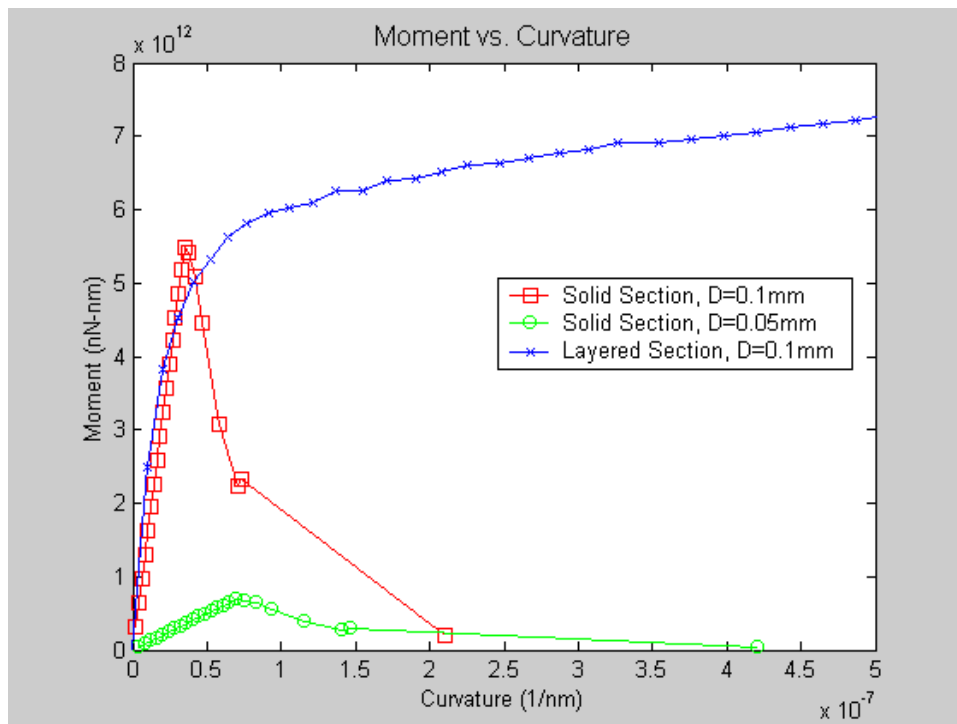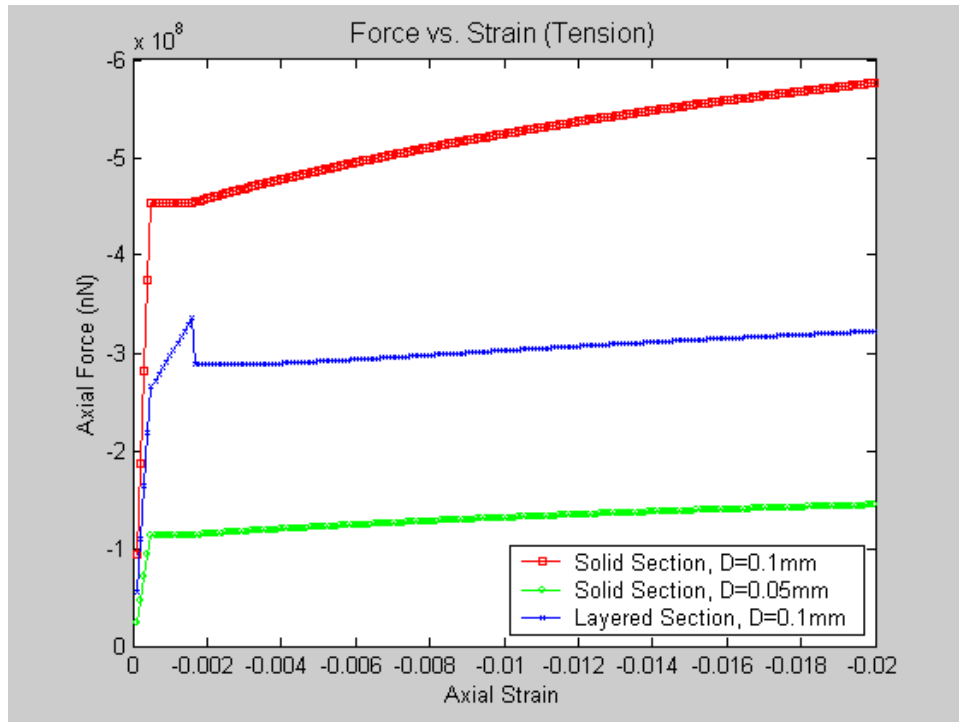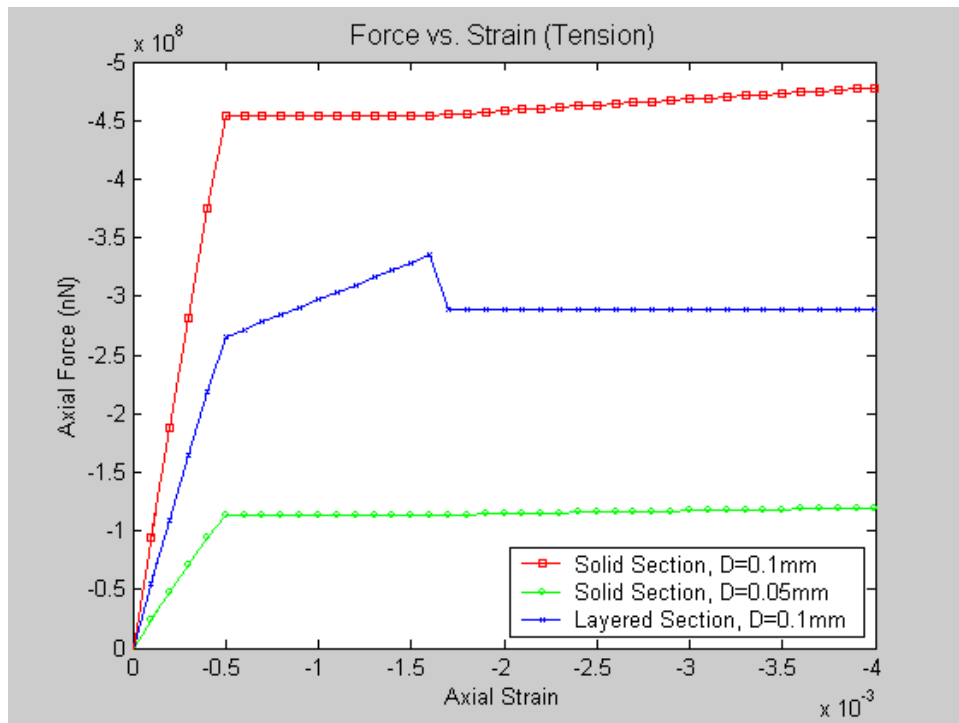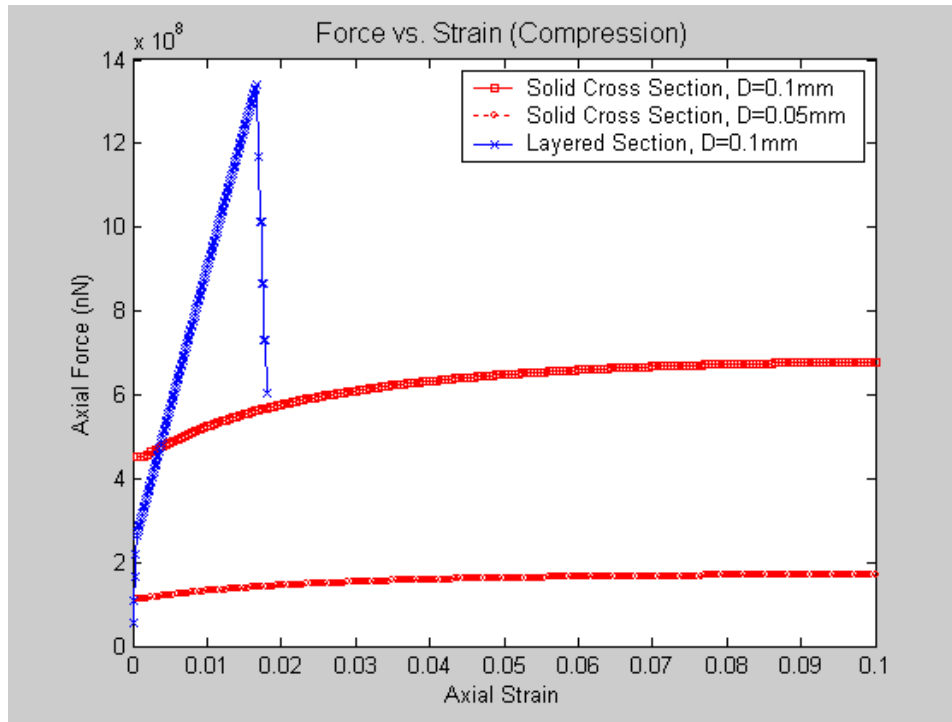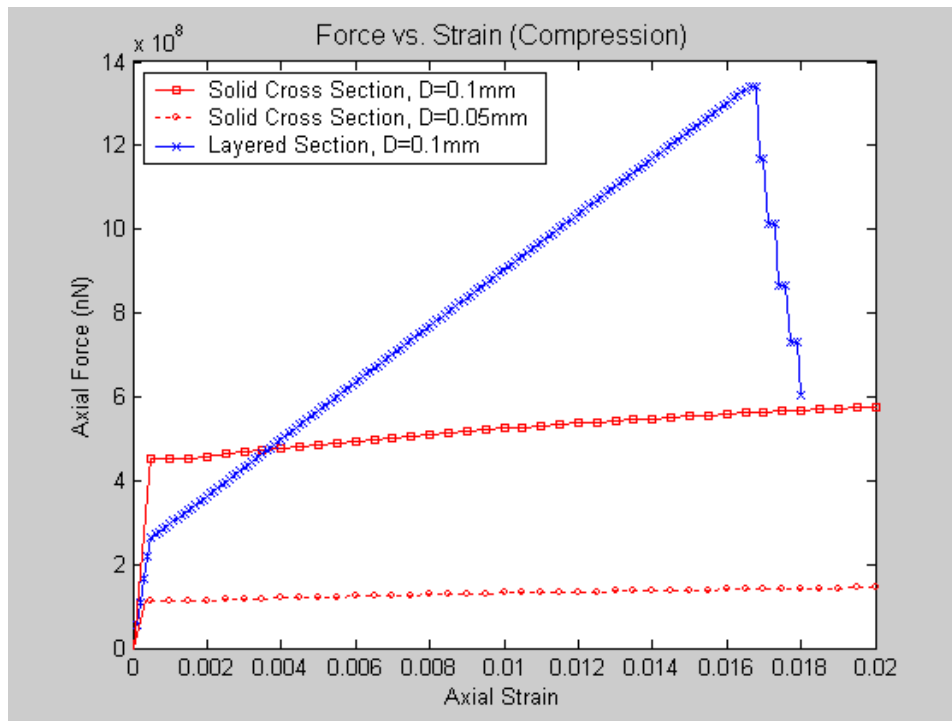*Figure 6.10. Flexural Response for Case 1 (RVC core) – Total Response.*



*Figure 6.11. Flexural Response for Case 1 (RVC core) – Initial Part of Response.*

130

*Figure 6.12. Tensile Response for Case 2 (Cu core) – Total Response.*



*Figure 6.13. Tensile Response for Case 2 (Cu core) – Initial Part of Response.*

131

*Figure 6.14. Compressive Response for Case 2 (Cu core) – Total Response.*



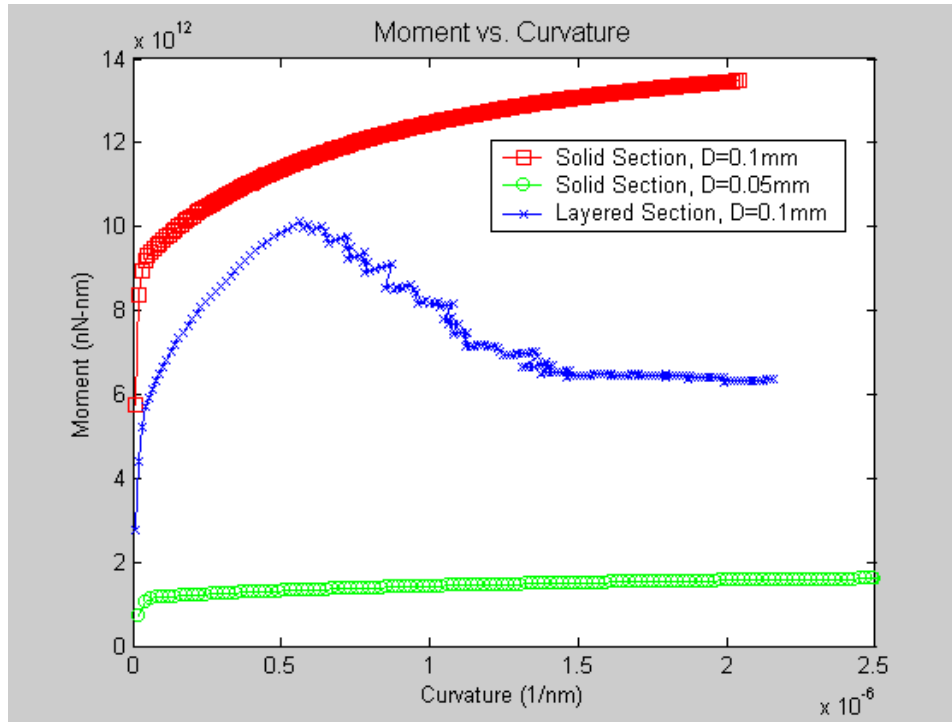*Figure 6.15. Compressive Response for Case 2 (Cu core) – Initial Part of Response.*

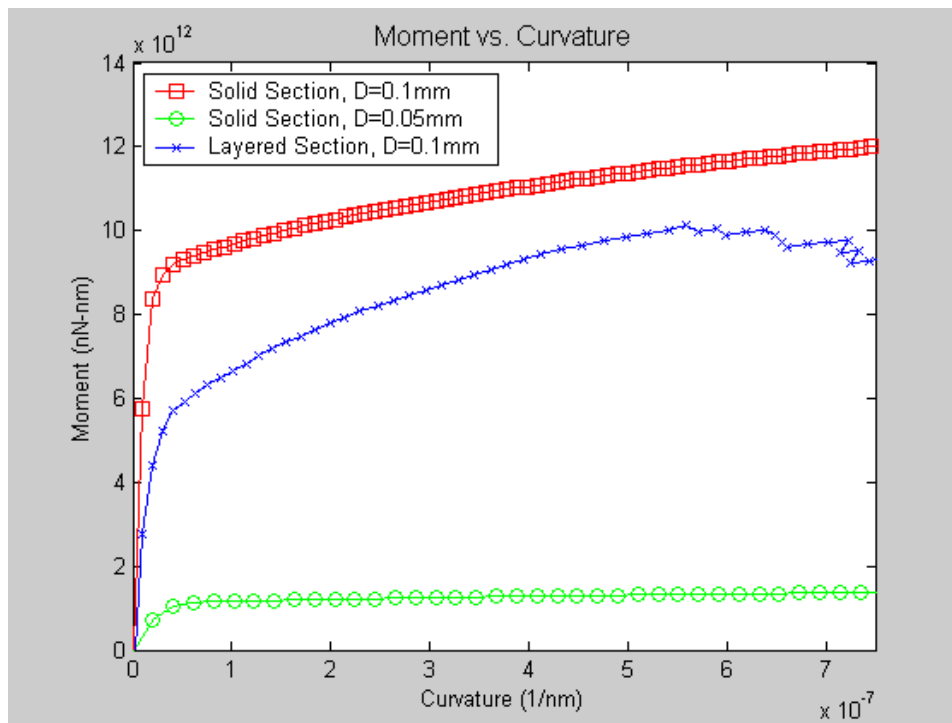*Figure 6.16. Flexural Response for Case 2 (Cu core) – Total Response.*



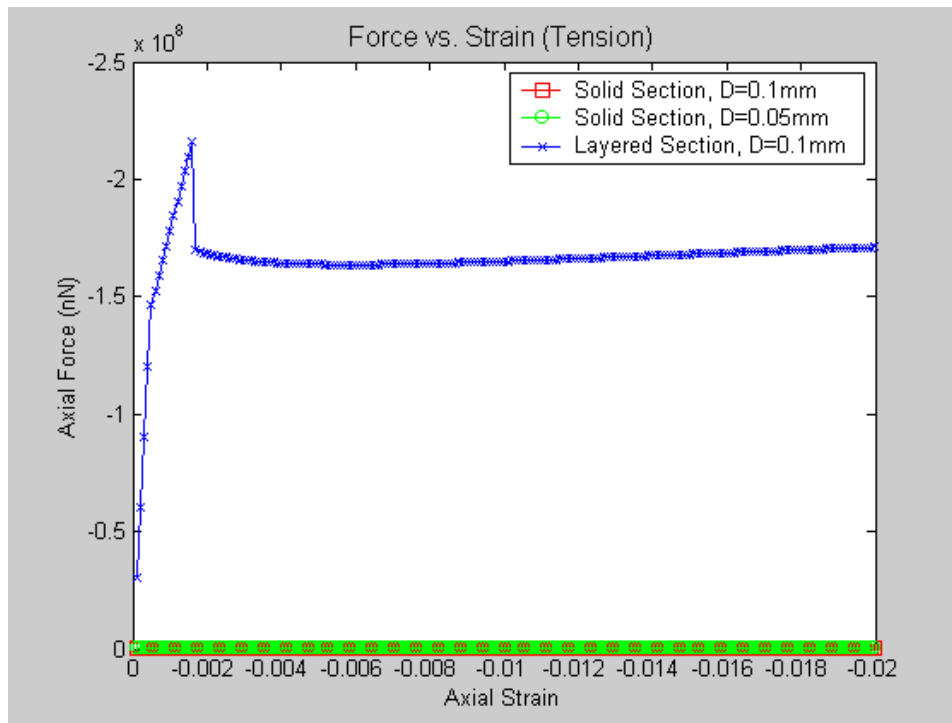*Figure 6.17. Flexural Response for Case 2 (Cu core) – Initial Part of Response*

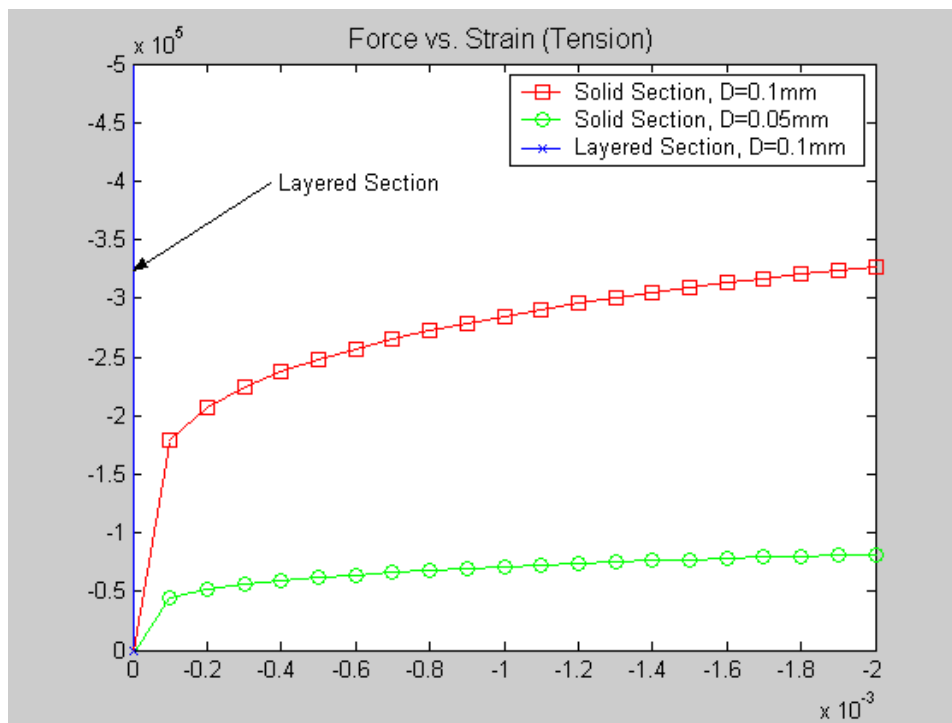*Figure 6.18. Tensile Response for Case 3 (PU core) – Total Response.*



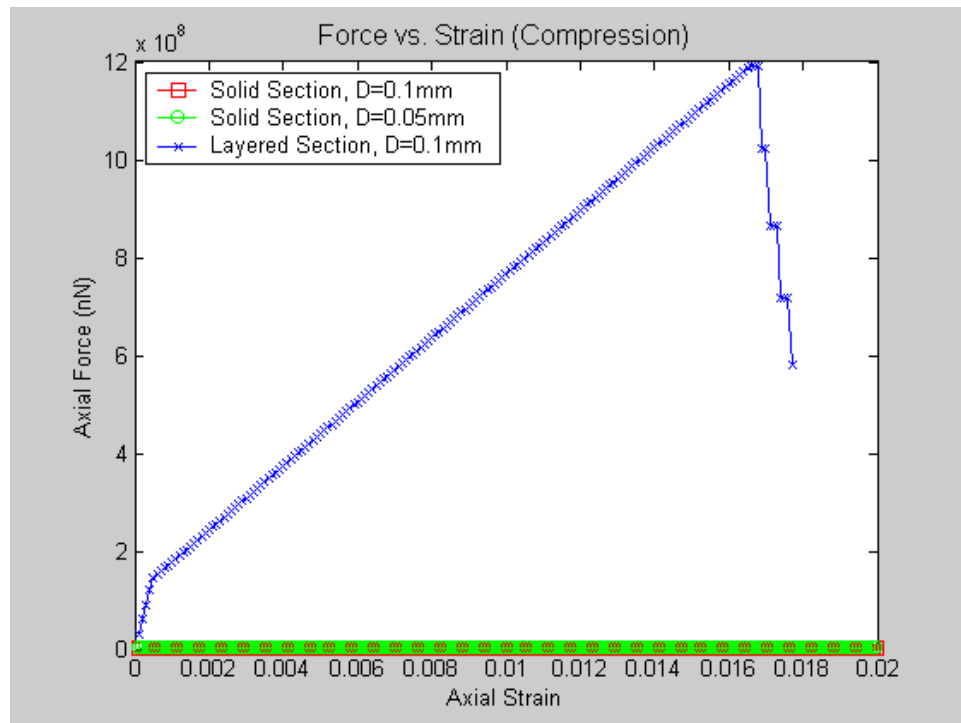*Figure 6.19. Tensile Response for Case 3 (PU core) – Initial Part of Response.*

134

*Figure 6.20. Compressive Response for Case 3 (PU core) – Total Response.*
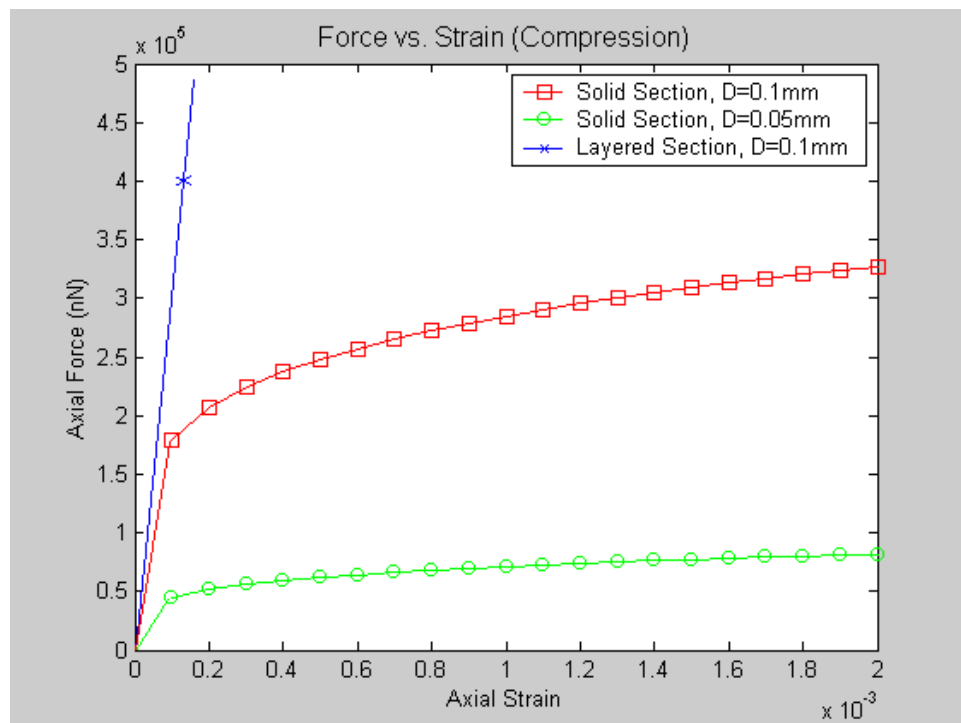


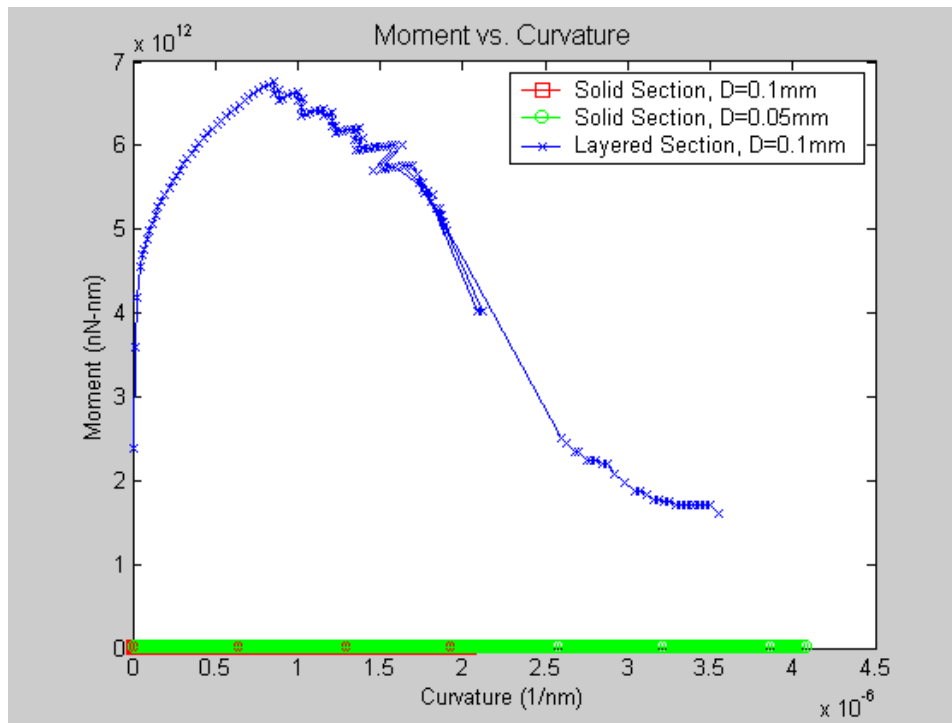*Figure 6.21. Compression Response for Case 3 (PU core) – Initial Part of Response.*

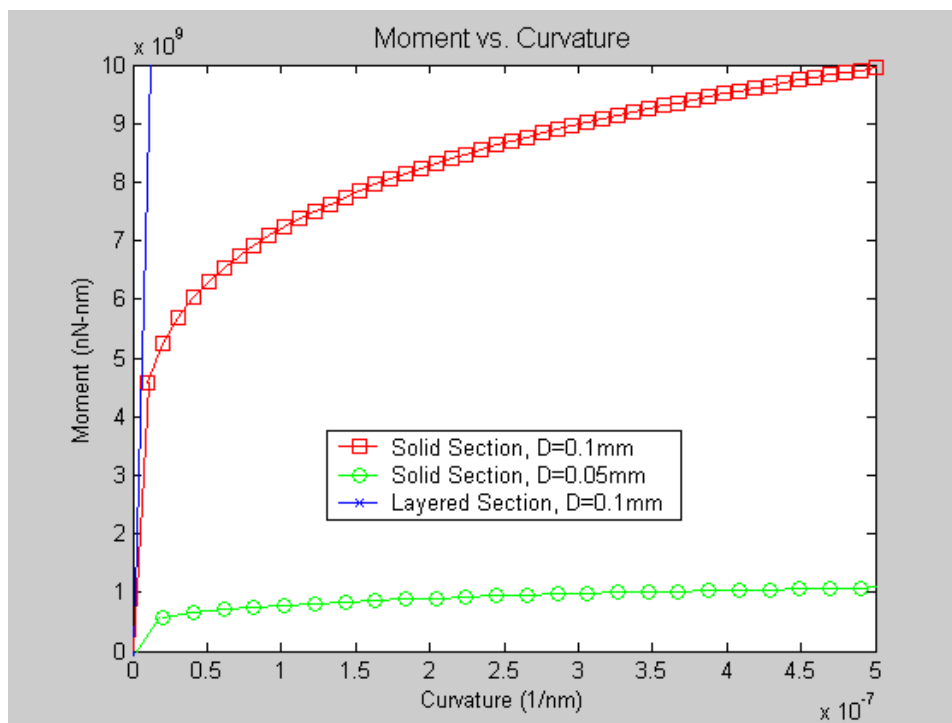*Figure 6.22. Bending Response for Case 3 (PU core) – Total Response.*



*Figure 6.23. Bending Response for Case 3 (PU core) – Initial Part of Response.*

**Cell Characterization**

Enhancement of section properties through deposition of nanolayers was summarized above. A preliminary assessment of the effects of such section enhancements on the unit cell response and the bulk cellular material behavior is presented in this section. The simple cell modes of behavior shown in Figure 6.24 are most common with open-cell systems. Expressions to describe the properties (i.e., density, stiffness) and capacities (i.e., stability, strength) of open-cell solids have been shown to have the general form:[69]

$$\frac{S^*}{S_s} = K\left(\frac{\rho^*}{\rho_s}\right)^m$$

where $S^*$ is the property of the cellular system, $S_s$ is the property of the solid from which the cell struts are made, $\rho^*$ is the density of the cellular material, and $\rho_s$ is the density of the solid from which the cell struts are made. The constant of proportionality $K$ has been determined from experimental data.[69] Despite their simplicity, these models have been shown to successfully model open-cell foams and they have provided the basis for more complex modeling assumptions and failure theories.[70,71]
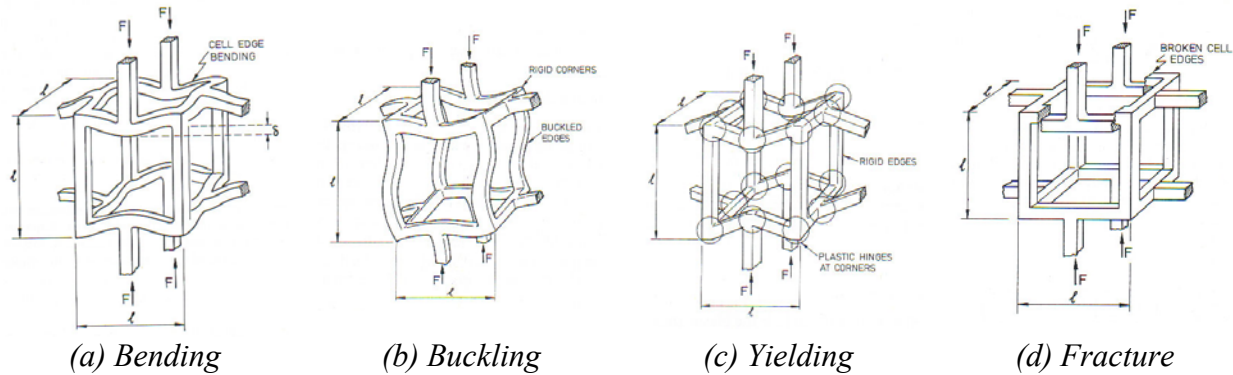


| (a) Bending | (b) Buckling | (c) Yielding | (d) Fracture |

*Figure 6.24. Behavior and Failure Mechanisms in Open Cell Foams.[69]*

The formulae proposed by Gibson and Ashby[69] were used to evaluate the enhancement of the new composite cellular material at the cell and bulk material levels. The example summarized herein is for a Reticulated Vitreous Carbon cellular foam precursor strengthened with sequential deposition of polyurethane, copper, and RVC nanolayers. The section response of the cell struts was presented earlier. The section behavior was used to determine the effective modulus, tensile strength, compressive strength, and bending (yield and maximum) strength of the cell struts.

As previously discussed, the precursor RVC cellular material is assumed to have strut length of 1 mm and strut cross-sectional diameter of 0.05 mm at a relative density ($\rho^*/\rho_s$) of 0.023. The layered composite increases the section diameter to 0.1 mm for a relative density of 0.09. A summary of the mechanical properties for both the RVC precursor and the composite cellular material is provided in Table 6.3. The table also summarizes the corresponding formulae used to evaluate each of the mechanical properties and the ratio of the property values of the composite to precursor cellular material.

As expected, the precursor material has lower properties because of its lower material content (lower relative density). However, while the ratio of relative densities of the composite to precursor is approximately four, the mechanical properties of the composite are 6 to 22 times greater than those of the precursor cellular material. This suggests considerable enhancement of material properties that are possible through multiple deposition of hybrid nanolayer on the struts of cellular materials.

*Table 6.3. Mechanical Properties for Precursor and Composite Cellular Materials.*

| Property | Formulae[69] | Precursor Material (RVC) | Composite Cellular Material | Ratio of Composite to Precursor |
|---|---|---|---|---|
| Relative Density | $\dfrac{\rho^*}{\rho_s}$ | 0.023 | 0.09 | 3.9 |
| *Compressive/Tensile Linear Elastic Properties* | | | | |
| Modulus of Elasticity, E [GN/m²] | $E^* = E_s\left(\dfrac{\rho^*}{\rho_s}\right)^2$ | 0.019 | 0.39 | 21 |
| Shear Modulus, G [GN/m²] | $E^* = 0.375 E_s\left(\dfrac{\rho^*}{\rho_s}\right)^2$ | 0.007 | 0.15 | 21 |
| Poisson's Ratio | $\upsilon^* = \dfrac{E^*}{2G^*} - 1$ | 0.33 | 0.33 | 1.0 |
| *Compressive Mechanical Properties* | | | | |
| Compressive Elastic Strength [MN/m²] | $\sigma^*_{el} = 0.03 E_s t^3 \left(\dfrac{\rho^*}{\rho_s}\right)^2 \left(1+\left(\dfrac{\rho^*}{\rho_s}\right)^{1/2}\right)^{1/2}$ | 0.60 | 13 | 22 |
| Compressive Plastic Strength [MN/m²] | $\sigma^*_{pl} = 0.23 \sigma_{ys} \left(\dfrac{\rho^*}{\rho_s}\right)^{3/2} \left(1+\left(\dfrac{\rho^*}{\rho_s}\right)^{1/2}\right)^{1/2}$ | 0.019 | 0.23 | 12 |
| Compressive Crushing Strength [MN/m²] | $\sigma^*_{cr} = 0.65 \sigma_{fs} \left(\dfrac{\rho^*}{\rho_s}\right)^{3/2}$ | 0.074 | 0.84 | 11 |
| *Tensile Mechanical Properties* | | | | |
| Tensile Plastic Stiffness [GN/m²] | $E_A = E_s\left(\dfrac{\rho^*}{\rho_s}\right)^2$ | 0.81 | 4.3 | 5.4 |
| Tensile Plastic Collapse [MN/m²] | $\sigma^*_a = \sigma_{ys}\left(\dfrac{\rho^*}{\rho_s}\right)$ | 0.50 | 2.8 | 5.7 |
| Tensile Brittle Strength [MN/m²] | $K^*_{IC} = 0.65 \sigma_{fs}\sqrt{\pi l}\left(\dfrac{\rho^*}{\rho_s}\right)$ | 0.13 | 1.49 | 11 |

**Experimental Evaluation of Nanolayered Composites Built Onto Open-Cell Structures**

A preliminary assessment of the structural value of hybrid nanolayers built onto the struts of open-cell structures was made using RVC (carbon) struts with cell size of about 1 mm and density ratio (to solid) of about 0.35% were subject of this experimental study. An as-received sample with 25 mm square cross section and 50 mm length is shown in Figure 6.25(a). These RVC foams were subjected to tension test (Figure 6.25b) either in as-received form or after deposition of 300 polymeric (PAH/PSS) nanolayers. Figure 6.26 presents a typical comparison of the tensile stress-strain relationships of RVC open-cell structures prior to and after deosition of polymeric nanolayers. The microcrack control and toughening effects of polymer nanolayers, covered earlier under structural modeling, are observed in Figure 6.26 to enhance the tensile strength and especially the post-peak ductility of RVC open-cell structures.



*(a) Carbon Foam Sample*          *(b) Tension Test Set-Up*

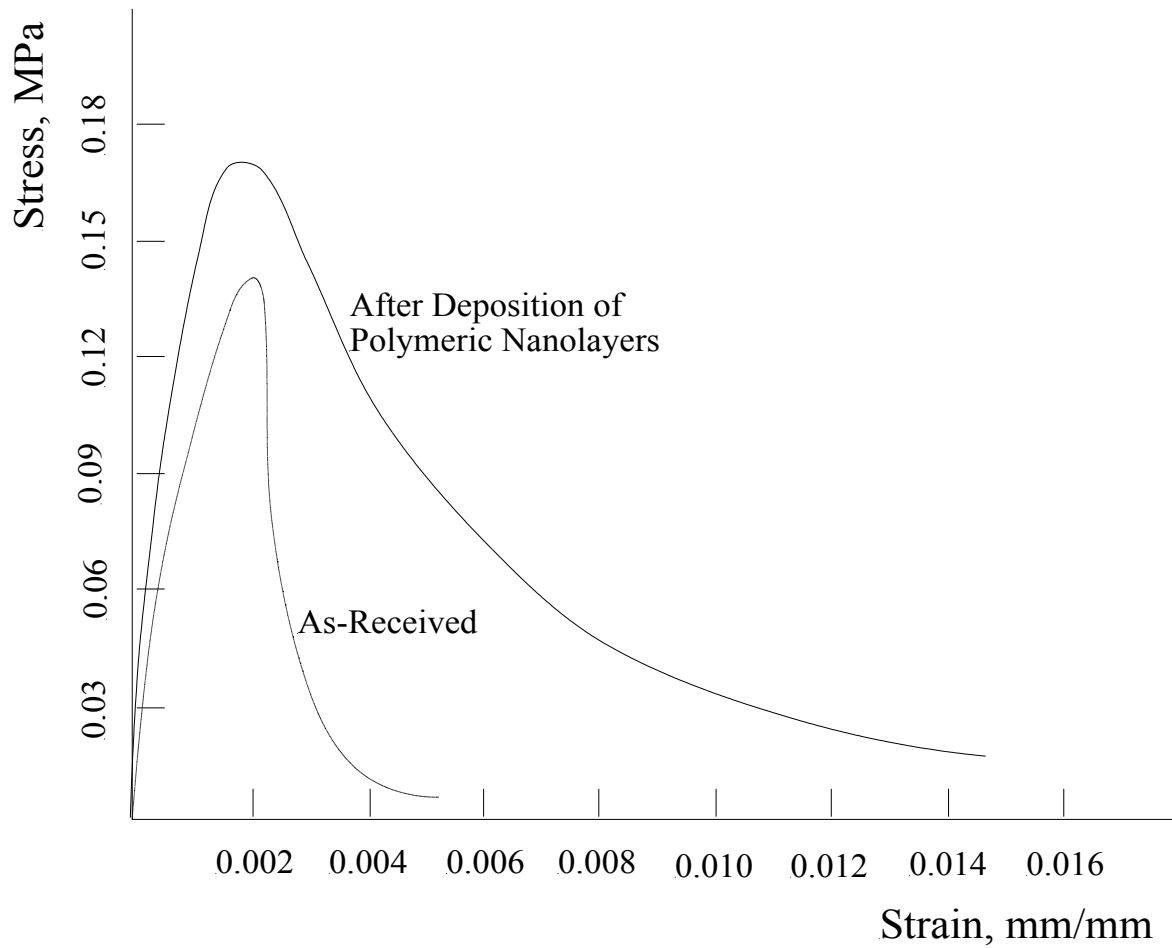*Figure 6.25.  The Open-Cell Carbon Foam Sample and Tension Test Set-Up.*

*Figure 6.26. Representative Stress-Strain Curves of RVC Open-Cell Structures Prior to and After Deposition of Polymeric Nanolayers (stress calculated over gross area).*

# CHAPTER 7

## SUMMARY AND CONCLUSIONS

A new generation of biomimetic structural materials and systems are under development which exhibit novel adaptive and self-healing qualities, and offer distinctly high levels of structural efficiency. The adaptive qualities of these systems involve conversion of the mechanical energy input of service loads to electrical energy which, in turn, drives the adaptive process of electrostripping, transport and electrodeposition of structural substant to normalize stress conditions. This adaptive process is guided by electric potentials which reflect on stress gradients. Piezoelectric constituents use the mechanical energy to produce electric potential and charge. A solid electrolyte provides the medium through which the electrostripping, mass (ionic) transport, and electrodeposition phenomena take place.

An integrated analytical/experimental project was implemented to validate the basic principles of the approach, and to demonstrate the viability of developing material systems embodying these principles. This effort addressed key issues relevant to structural/functional design, processing, system integration, and experimental validation of the new concepts and structural systems. The following conclusions were derived.

1. Solid electrolytes provide viable media for electrostipping and electrodeposition phenomena.

2. The piezoelectric effect can be used to drive electolysis processes within solid electrolytes through conversion of mechanical energy to electrical energy.

3. Adaptive requirements impose constraints on system architecture; most importantly, a nanolayered assembly of piezoelectric, solid electrolyte and structural systems is needed for adaptive effects to occur within reasonable time frames.

4. The adaptive and self-healing phenomena can be synchronized at local (material) and global (structural system) levels.

5. The biomimetic concept of hybrid nanolayered composited built onto open-cell precursors provides a strong basis for development of new generations of structural componets and systems with streamlined load paths and distinctly high levels of structural efficiency.

6. Ionic self-assembly provides a powerful, low-cost and energy-efficient means of assembling piezoelectric, solid electrolyte and structural nanolayers onto different open-cell base systems, complementing excellent interfacial bonds with tremendous versatility at micro- and macro-structural levels.

7. Integrated systems embodying our principles can be designed to dynamically tune their structure to imposed loads and damaging effects, yielding highly efficient use of material resources and improved levels of structural safety and system reliability.

8. The processing methodologies and system architectures developed here are quite versatile and can yield multi-functional structural systems contributing to various aspects of system performance.

# CHAPTER 8

## REFERENCES

1. Dickerson, R.E. and Geis, I., "The Structure and Action of Proteins," Menlo Park: Benjamin, 1969.
2. Wheeler, E.J. and Lewis, D., "An X-Ray Study of the Paracrystalline Nature of Bone Apatite," Calcified Tissue Research Vol. 24, 1977, pp. 243-248.
3. Glimcher, M.J., "Composition, Structure and Organizaiton of Bone and Other Mineralized Tissues and the Mechanisms of Calcification," Handbook of Physiology (G.D. Aurbach, editor), Section 7, Vol. 7, American Physiology Society, 1976, pp. 25-116.
4. Boyde, A., "Electron Microscopy of the Mineralizing Front," Metabolic Bone Disease and Related Research 2 (Supplement), 1980, pp. 69-78.
5. Enlow, D.H., "A Handbook of Facial Growth," W.B. Saunders, Philadelphia, 1975.
6. Minaire, P., Meunier, P., Edourd, C., Bernard, J., Coupron, P. and Bourret, J., "Quantitative Histological Data on Tissue Osteoporosis," Calcified Tissue Research, Vol. 17, 1976, pp. 57-73.
7. Voge, , J.M., Whittle, M.W., Smith, M.C. and Rambaut, P.C., "Bone Mineral Measurement – Experiment MO 78," Biomedical Results from Skylab (R.S. Johnson and L.R. Diethein, editors), NASA SP 377, 1977.
8. Morey, E.R. and Baylink, D.J., "Inhibition of Bone Formation During Space Flight," Science, Vol. 201, 1978, pp. 1138-1141.
9. Spengler, D.M., Morey, E.R., Carter, D.R., Turner, R.T. and Balink, D.J., "Effect of Space Flight on Bone Strength," Physiology, Vol. 22, 1979, pp. 75-76.
10. Jones, H.H., Priest, J.D., Hayes, W.C., Tichenor, C.C. and Nagel, D.A., "Humeral Hypertrophy in Response to Exercise," Journal of Bone and Joint Surgery, Vol. 59A, 1977, pp. 204-208.
11. Niven, J.S.F., "The Development in vivo and in vitro of the Avian Patella," Roux Archiv, Vol. 128, 1933, pp. 480-501.
12. Goodship, A.E., Lanyon, L.E. and McFie, H., "Functional Adaptation of Bone to Increased Stress," Journal of Bone and Joint Surgery, Vol. 61-A, 1979, pp. 539-546.
13. Lanyon, L.E., Goodship, A.E., Pye, C.J. and MacFie, J.H., "Mechanically Adaptive Bone Remodeling," Journal of Bone and Joint Surgery, Vol. 61-A, 1982, pp. 141-154.
14. Woo, S.L-Y., Kuei, S.C., Amiel, D., Gomez, M.A., Hayes, W.C., White, F.C. and Akeson, W.H., "The Effect of Prolonged Physical Training on the Properties of Long Bone: A Study of Wolff's Law," Journal of Bone and Joint Surgery, Vol. 63A, 1981, pp. 780-787.
15. Becker, R.O., "Significance of Electrically Stimulated Osteogenesis – More Questions Than Answers," Clinical Orthopaedics and Related Research Vol. 141, 1979, pp. 266-274.
16. Eridsson, C., "Electrical Properties of Bone," Biochemistry and Physiology of Bone (G.H. Bourne, editor), Vol. 4, Academic Press, New York, 19767, pp. 329-384.
17. Korostoff, E., "A Linear Piezoelectric Model for Characterizing Stress Generated Potentials in Bone," Journal of Biomechanics, Vol. 12, 1979, pp. 335-337.

18. Lanyon, L.E. and Hartman, W., "Strain Related Electrical Potential Recorded in Vitro and in Vivo," Calcified Tissue Research, Vol. 22, 1977, pp. 315-327.

19. Cochran, G.V.B., Pawluk, R.J. and Bassett, C.A.L., "Electromechanical Characteristics of Bone Under Physiologic Moisture Conditions," Clinical Orthpaedics and Related Research, Vol. 58, 1968, pp. 249-270.

20. Jendrucko, R.J., Hyman, W.A., Newell, P.H. and Chakraborty, B.K., "Theoretical Evidence for the Generation of High Pressure in Bone Cells," Journal of Biomechanics, Vol. 9, 1976, p. 87-91.

21. Bassett, C.A.L., "Comment on Theoretical Evidence for the Generation of High Pressure inBone Cells," Journal of Biomechanics, Vol. 9, 1976, p. 485.

22. Frost, H.M., "Bone Modeling and Skeletal Modeling Errors," Springfield: Charles C. Thomas, 1973.

23. Pauwels, F., "Kruzer Uberbick Uber Die Mecanische Beanspruchung des Knochens Und Ihre Bedeutung Fur Die Funktionelle Anpassung," Zeitschrift Fur Orthopadie Und Ihre Grenzgebiete, Vol. 111, 1973, pp. 681-705.

24. Lisdova, M. and Hert, J., "Reaction of Bone to Mechanical Stimuli. Part 2. Periosteal and Endosteal Reaction of the Tibial Diaphysis in Rabbit to Intermittent Loading," Folia Morphologica, Vol. 19, 1971, pp. 301-317.

25. Lanyon, L.E. and Hartman, W., "Strain Related Electrical Potentials Recorded in Vitro and in Vivo," Calcified Tissue Research, Vo. 22, 1977, pp. 315-327.

26. O'Connor, J.A., Goodship, A.E., Rubin, C.T. and Lanyon, L.E., "The Effect of Externally Applied Loads on Bone Remodeling in the Radius of the Sheep," Mechanical Factors and the Sekleton (I.A.F. Stokes, editor), John Libby, London, 1981, pp. 83-90.

27. Lanyon, L.E. and Rubin, C.T., "Funcitonal Adaptation in Skeletal Structures," Functional Vertebrate Morphology (Hildebrand, editor), Harvard University Press, 1983.

28. Vasciaveo, F. and Bartoli, E., "Vascular Channels and Resorption Cavities in the Long Bone Cortex. THe Bovine Bone," Acta Anatomica, Vol. 47, 1961, pp. 1-33.

29. Enlow, D.H., "A Handbook of Facial Growth," W.B. Saunders, Philadelphia, 1975.

30. Cohen, J.and Harris, W.H., "The Three-Dimensional Analtomy of Baversian Systems," Journal of Bone ad Joint Surgery, Vol. 40-A, 1958, pp. 419-434.

31. Martin, R.B. and Burr, D.B., "A Hypothetical Mechanism for the Stimulation of Osteonal Remodeling by Fatigue Damage," Journal of Biomechanics, Vol. 15, 1982, pp. 137-139.

32. Churches, A.E. and Howlett, C.R., "The Response of Mature Cortical Bone to Controlled Time-Varying Loading," Cowin, 1981, pp. 69-80.

33. Bouvier, M. and Hylander, W.L., "Effect of Bone Strain on Cortical Bone Structure in Macaques," Journal of Morphology, Vol. 167, 1981, pp. 1-12.

34. Hert, J., Lisdova, M. and Landgrol, B., "Microstructure of the Compact Bone of Rabbit Tibia After Intermittent Loading," Acta Anatomica, Vol. 82, 1972, pp. 218-230.

35. Sevitt, S., "Bone Repair and Fracture Healing in Man," Churchill Livingston, London, 1981, 315 pp.

36. Leaver, A.G., Triffit, J.T. and Holbrook, I.B., "Newer Knowledge of Non-Collagenous Protein in Dentin and Corical Bone Matrix," Clin. Orthop., Vol. 110, 1975, pp. 268-292.

37. Lokietek, W., Pawluk, R.J., Bassett, C.A.L., "Muscle Injury Potentials: A Source of Voltage in the Undeformed Rabbit Bone," J. Bone Jt Surg, Vol. 56B, 1974, pp. 361-369.

38. Yasuda, I., "Fundamental Aspects of Fracture Treatment," J Kyto Med Sci, Vol. 4, 1953, pp. 395-406.

39. Harris, W.H., Moyen, B.J.L., Trasher, E.L., Davis, L.A., et al, "Differential Response to Electrical Stimulation. A Distinction Between Induced Osteogenesis in Intact Tibia and the Effect on Fresh Fracture Defects in Radii," Clin Orthop, Vol. 124, 1977, pp. 31-40.

40. Becker, R.O. and Murray, D.G., "The Electrical Control System Regulating Fraction Healing in Amphibians," Clin Orthop, Vol. 73, 1970, pp. 169-198.

41. Bassett, C.A.L., "Biophysical Principles Affecting Bone Structure,"Biochemistry and Physiology of Bone (G.H. Bourne, editos), Vol. 3, Academic Press, New York, 1971, pp. 1-76.

42. Becker, R.O., Bassett, C.A.L. and Bachman, C.H., "Bio-Electric Factors Controlling Bone Structure," Bone Biodynamics (H.M. Frost, editor), Little Brown, Boston, 1964, p. 209.

43. Friedenburg, Z.B., Roberts, P.G., Didizian, N.H. and Brighton, C.T., "Stimulation of Fracture Healing by Direct Current in the Rabbit Fibula," J Bone Jt Surg, Vol. 48A, 1971, pp. 299-310.

44. Piekarski, K., Demetriades, C. and Mackenzie, A., "Osteogenetic Stimulation by Externally Applied ED Current," Acta Orthop Scand, Vol. 49, 1978, p. 113-120.

45. Connolly, J.F., Hahn, H. and Jardon, O.M., "The Electrical Enhancement of Periosteal Proliferation in Normal and Delayed Fracture Healing," Clin Orthop, Vol. 124, 1977, pp. 97-105.

46. Friedenburg, Z.B. and Brighton, C.T., "Bio-Electrical Potentials in Bone," J Bone Jt Surg, Vol. 48A, 1966, pp. 915-923.

47. Lokietek, W., Pawluk, R.J. and Bassett, C.A.L., "Muscle Injury Potentials: A Source of Voltage in the Undeformed Rabbit Bone," J Bone Jt Surg, Vol. 56B, 1974, pp. 361-369.

48. Fendler, J.H., "Self-Assembled Nanostructued Materials," Chem. Mater., Vol. 8, 1996, pp. 1616-1624.

49. Fendler, J.H. and Meldrum, F.C., "The Colloidal Chemical Approach to Nanostructured Materials," Advanced Materials, Vol. 7, No. 7, 1995, pp. 607-632.

50. Casssagneau, T., Mallouk, T.E. and Fendler, J.H., "Layer-by-Layer Assembly of Thin Film Zener Diodes from Conducting Polymers and CdSe Nanoparticles," J. Am. Chem. Soc., Vol. 120, 1998, pp. 7848-7859.

51. Decher, G., Lehr, B., Lowack, K., Lvov, Y. and Schmitt, J., "New Nanocomposite Films for Biosensors: Layer-By-Layer Adsorbed Films of Polyelectrolytes, Proteins or DNA," Biosensors & Bioelectronics, Vol. 9, 1994, pp. 677-684.

52. Kleinfeld, E.R. and Ferguson, G.S., 'Stepwise Formation of Multilayered Nanostructural Films from Macromolecular Precursors," Science, Vol. 265, July 15, 1994, pp. 370-373.

53. Cheung, J.H., Fou, A.F. and Rubner, M.F., "Molecular Self-Assembly of Conducting Polymers," Thin Solid Films, Vol. 244, 1994, pp. 985-989.

54. Fendler, H., "Membrane-Mimetic Approach to Advanced Materials," Springer-Verlag, 1994, 236 pp.

55. Decher, G., "Layered Nanoarchitectures Vis Directed Assembly of Anionic and Cationic Molecules," Chapter 14, pp.507-528

56. Lvov, Y.M. and Gecher, G., "Assembly of Multilayer Ordered Films by Alternating Adsorption of Oppositely Charged Macromolecules," Crystallography Reports, Vol. 39, No. 4, 1994, pp. 628-647.

57. Schmitt, J., Decher, G., Dressick, W.J., Brandow, S.L., Geer, R.E., Shashidhar, R. and Calvert, M., "Metal Nanoparticle/Polymer Superelastic Films: Fabrication and Control of Layer Structure," Adv. Mater., Vol. 9, No. 1, 1997, pp. 61-65.

58. Feng, Y., Teo, W., Siow, K., Gao, Z., Tan, K. and Hsieh, A., "Corrosion Protection of Copper by a Self-Assembled Monolayer of Alkanethiol," Journal of Electrochemical Society, Vol. 144, No. 1, January 1997, pp. 55-64.

59. Jaffe, B., Cook, W.R. and Jaff, H., "Piezoelectric Ceramics," Academic Press, 1971, 317 pp.

60. Measurement Specialties, Inc., "Piezo Film Sensors Technical Manual," www.msiusa.com, August 1998.

61. Egusa, S. and Iwasawa, N., "Piezoelectric Paints as One Approach to Smart Structural Materials with Health-Monitoring Capabilities," Smart Materials and Structures, Vol. 7, 1998, pp. 438-445.

62. Rieger, P.H., "electrochemistry," Chapmen & Hall, New York, NY, 1994, 483 pp.

63. Zumdahl, S.S. and Zumdahl, S.A., "Chemistry," Houghton Mifflin, 2000, pp. 837-887.

64. Eliasson, H., Albinsson, I. and Mellander, B.E., "Dielectric and Conductivity Studies of a Silver Ion Conducting Polymer Electrolyte," Electrochemica Acta, Vol. 43, Nos. 10-11, 1998, pp. 1459-1463.

65. Gray, F.M., "Solid Polymer Electrolytes – Fundamentals and Technological Applications," VCH Publishers, Inc., 1991, 245 pp.

66. Owen, J.R., Maskell, W.C. and Steele, B.C.H., "Thin Film Lithium Aluminum Negative Plate Material," Solid State Ionics, Vol. 13, 1984, pp. 329-334.

67. Rao, S.S., Rao, K.V.S., Shareefuddin, M., and Rao, U.V.S., "Ionic Conductivity and Battery Characteristic Studies on PEO+AgNO$_3$ Polymer Electrolyte," Solid State Ionics, Vol. 67, 1994, pp. 331-332.

68. Bonino, F., Scrosati, B. and Selvaggi, A., "The Lithium-Polymer Electrolyte Interface. I. Lithium Cyclability," Solid State Ionics, Vols. 18 & 19, 1986, pp. 1050-1053.

69. Gibson, L., and Ashby, M.F., "Cellular Solids – Structure & Properties", Pergamon Press, 1988.

70. Gibson, L.J., Ashby, M.F., Zhang, J., and Triantafillou, T.C., "Failure Surfaces for Cellular Materials under Multiaxial Loads – I. Modeling," International Journal of Mechanical Science, Vol. 31, No. 9, 1989, pp. 635-663.

71. Triantafillou, T.C., Zhang, J., Shercliff, T.L., Gibson, L.J., and Ashby, M.F., "Failure Surfaces for Cellular Materials under Multiaxial Loads – II. Comparison of Models with Experiment," International Journal of Mechanical Science, Vol. 31, No. 91989, pp. 635-663.